Macrophysical and Microphysical Influences on Radiative Transfer in Two-Dimensional Marine Stratus

By
David P. Duda and Graeme L. Stephens

Department of Atmospheric Science
Colorado State University
Fort Collins, Colorado

Research was supported by NIGEC grant #91-S01, DOE contract #466535,
and ONR grant #N00014-91-J-1422..

Colorado State University

Department of Atmospheric Science

Paper No. 565

MACROPHYSICAL AND MICROPHYSICAL INFLUENCES ON RADIATIVE TRANSFER IN TWO DIMENSIONAL MARINE STRATUS

David P. Duda and Graeme L. Stephens

Research supported by NIGEC grant #91-S01, DOE Contract #466535,
& ONR Grant # N00014-91-J-1422.

Principal Investigator: Graeme L. Stephens

Department of Atmospheric Science
Colorado State University
Fort Collins, CO 80523

November, 1994
Atmospheric Science Paper No. 565

ABSTRACT

Recent estimates of the effects of increasing amounts of anthropogenic sulfate aerosol on global climate have indicated that its impact on the radiative forcing of the atmosphere may be comparable in magnitude to the effect from increases in CO_2. Much of this impact is expected from the indirect effects of the aerosol on global cloud microphysics and the subsequent impact on cloud albedo. However, internal horizontal variations in cloud optical properties are also known to affect cloud albedo and reflectance, and thus affect the remote sensing of cloud microphysics.

A broadband solar radiative transfer model (SHSG) capable of simulating the radiances and fluxes in a medium that varies both vertically and horizontally was used to quantify the effects of both cloud microphysical changes and cloud inhomogeneity changes on the radiative properties of marine stratus. Two dimensional cross sections of cloud physics data taken from a set of three dimensional RAMS/LES simulations of marine stratus provided realistic optical property data for radiative transfer simulations. Along with a control run using typical marine CCN concentrations, two studies using enhanced concentrations of CCN were examined.

The results of the radiative transfer calculations indicated that in unbroken marine stratus clouds the *net* horizontal transport of photons over a domain of a few km was nearly zero, and the domain average broadband albedo computed in a two dimensional cross section was nearly identical to the domain average calculated from a series of independent pixel approximation (IPA) calculations of the same cross section. This matches the findings from Cahalan et al. (1994) for monochromatic calculations in a simple cloud model, and suggests that accurate computation of domain averaged albedos in unbroken marine stratus can be made using IPA calculations with one dimensional radiative transfer models.

However, the horizontal inhomogeneity does affect the cloud albedo due to the nonlinear relationship between albedo and optical depth and the reduction in cloud albedo could be related to the variability of the distribution of the logarithm of cloud optical depth. The effects of cloud inhomogeneity on the broadband albedo of unbroken marine stratus were found to be nearly as large as the effects from the microphysical changes induced by the enhanced CCN concentrations. Like the broadband albedos, the local differences between the 2D and IPA computed heating rates were significant but the domain averages were very similar.

Using a simplified two channel retrieval method that compared the cloud top reflectances computed from the two dimensional RAMS/LES cross sections with tabulated results from a set of plane parallel calculations, the cloud optical depth and effective radius were estimated and compared to the actual cloud properties. The results showed that the effects of cloud inhomogeneity produced local fluctuations in the reflected radiances that could be significantly different than those computed from plane parallel calculations. Horizontal inhomogeneity within a satellite pixel will also affect the retrievals due to the nonlinear relationships between the reflectance functions and the retrieved optical properties. Improved multidimensional radiative transfer models and measures of cloud inhomogeneity will be needed to account for the effects of cloud inhomogeneity on remote sensing of cloud optical depth and effective radius.

ACKNOWLEDGEMENTS

We are indebted to many others for their support during the preparation and writing of this paper. We would especially like to thank Dr. K. Franklin Evans for providing the source code for the SHSG method, and Paul Stackhouse, Jr. for supplying his k distribution data and two-stream model. We also have benefitted from their helpful comments about their radiative transfer models. We also acknowledge the help of Bjorn Stevens and the modeling group under the direction of Dr. William Cotton, who provided the RAMS/LES data in the dissertation. Thanks is also given to Dr. Philip Gabriel for his discussions about multidimensional radiative transfer modeling, and to Darren Jackson, Sue Lini and Heather Jensen, who all helped in the preparation of this report.

This research was supported by NIGEC 91-S01, Department of Energy Contract 466535 and Office of Naval Research Grant N00014-91-J-1422. Some of the computer calculations in this dissertation were carried out using the Academic Computing and Networking Services (ACNS) computing facilities at Colorado State University.

CONTENTS

LIST OF FIGURES

LIST OF TABLES

Chapter 1

INTRODUCTION

Global climate change has become an important area of study in atmospheric science. Popular interest in topics such as greenhouse warming has led scientists to consider the possible influences of mankind's activities on climate. The interactions between the many parts of the earth-atmosphere system make such an analysis difficult and many questions about global climate change remain unanswered.

One area where mankind's influence on climate change may be important, but where our present knowledge is incomplete is the influence of anthropogenic aerosols on large scale cloud systems (including marine stratus cloud systems). Such cloud systems are believed to have a strong influence on climate since they have profound effects on the radiative energy budget over the subtropical oceans, and significant changes in the albedo of these systems would produce far ranging effects on climate. Twomey (1977) hypothesized that increasing concentrations of cloud condensation nuclei (CCN) in the atmosphere as the result of increasing levels of pollution would tend to make clouds brighter. The brightening would result from the creation of more numerous but smaller droplets in a cloud which would be more efficient at reflecting solar radiation. More recently, other researchers have suggested that natural sources of CCN from the production of dimethyl sulfide (DMS) by oceanic phytoplankton could also have profound effects on cloud albedo (Charlson et al., 1987; Meszaros, 1988).

Although the "Twomey effect" has been quantified by observations of ship tracks in marine stratus cloud decks (Coakley et al., 1987), the global impact of increased CCN concentrations on clouds is difficult to assess. Since large scale marine stratus and stratocumulus cloud systems have a significant influence on solar radiative forcing over the

ocean, even relatively small changes in the optical properties of these cloud systems may have significant effects on global climate. For example, Charlson et al. (1992) have estimated that a 15% increase in the global mean droplet concentrations in marine stratus and stratocumulus would result in a radiative cooling effect comparable and opposite to current estimates of greenhouse warming. Also, Slingo (1990) estimated from a global circulation model (GCM) study that decreasing the mean effective radius of low clouds across the entire planet from 10 to 8.5 μm would result in a global cooling that could offset the expected warming due to doubling the CO_2 content of the atmosphere. Recent studies by Jones et al. (1994) and Boucher and Rodhe (1994) using the parameterized effects of aerosol on clouds in a GCMs show that the radiative forcing from the effects of aerosol on cloud albedo (-1.3 W m^{-2}) may be comparable to the 2 to 2.5 w m^{-2} forcing from the addition of carbon dioxide since 1850 (Houghton et al., 1990). Figure 1.1 shows the aerosol-induced radiative forcing computed from Boucher and Rodhe (1994), where local extremes reach -5 W m^{-2}.

Since marine stratus systems have a potentially large impact on climate, the radiative transfer in stratus has been an important subject of study for many years. The physical properties of the cloud, which ultimately determine the radiative transfer, can be loosely defined in terms of their microphysical properties (the properties of the individual droplets) and their macrophysical properties (the properties of the whole cloud). Since one dimensional, plane parallel radiative transfer models have primarily been used to study radiative transfer in clouds, much effort has been spent on evaluating the effects of microphysics on radiative transfer. Quantities such as effective radius and droplet concentration have been used to help incorporate microphysical effects into radiative transfer models (RTMs).

The effects of the large scale structure (especially the horizontal inhomogeneity) of a cloud system on radiative transfer are less understood. Although some macrophysical quantities (for example, total liquid water content) are commonly used in RTMs, parameters that measure the structure throughout the entire cloud cannot be used and their effects cannot be evaluated by plane parallel models. Also, several

different flux and radiance measurements from aircraft and satellite platforms have been made that have shown discrepancies from 1D model results. Measurements of the absorptivity of clouds in visible and near infrared wavelengths have consistently shown larger amounts of absorption than can be accounted for by plane parallel radiative transfer theory (Stephens and Tsay, 1990). Satellite observations of radiances at far from nadir angles have also shown discrepancies with model predictions, even when the near nadir radiances show good agreement (Stuhlmann et al., 1985; Smith et al., 1989). Finally, Cahalan et al. (1994) have recently shown that the effects of internal horizontal inhomogeneity in unbroken layers of marine stratus may reduce the albedo of the cloud system by fifteen percent compared to a plane parallel, perfectly homogeneous cloud with the same mean optical properties. These results suggest that macrophysical properties possibly may influence the radiative transfer in large scale cloud systems. Such an influence would be far-reaching, and affect many aspects of atmospheric radiative transfer. In particular, macrophysical effects on the remote sensing of cloud optical properties may affect such retrievals significantly and necessitate the development of new or modified remote sensing techniques. The possible impacts of cloud inhomogeneity on remote sensing can be seen in Figures 1.2 and 1.3. Figure 1.2 is a retrieval of cloud optical depth from Nakajima and Nakajima (1994), while Figure 1.3 is the corresponding effective radius retrieval. In both figures, the areas of broken cloudiness to the west and east of the flight path (in the center of the figures) have lower reflectances than the surrounding overcast regions. The lower reflectances result in the smaller retrieved optical depths and larger retrieved effective radii. While some of the variation in retrieved optical properties in Figures 1.2 and 1.3 are likely the result of microphysical differences, some may be caused by cloud inhomogeneity. Several radiative transfer modeling studies (see Barker, 1992) have shown that cloud inhomogeneity suppresses cloud reflectance, and thus much of the difference in retrieved values in the broken cloud areas in Figures 1.2 and 1.3 may be due to macrophysical differences rather than microphysical differences. In addition to the effects of cloud inhomogeneity on remote sensing, the results of Cahalan et al. (1994) suggest that the effects of cloud structure may significantly modify the

Gabriel et al. (1993) for a summary of past methods) but in previous attempts some simplifying assumptions in the radiative transfer models had to be made to save computational time. Advances in the speed of computers, however, have made multi-dimensional computations more feasible and in the past few years several new methods (Stephens, 1988; Gabriel et al., 1993; Evans, 1993) have been developed to compute radiances and fluxes in a two or three dimensional medium.

This dissertation makes quantitative assessments of the effects of both macrophysics and microphysics on the radiative transfer applied in three areas: remote sensing of cloud optical properties by satellites, the distribution of broadband radiative heating in stratus, and the relationship between changes in broadband cloud albedo and changes in CCN concentrations in the cloud system. This assessment is accomplished by using a newly developed multi-dimensional radiative transfer model with cloud field data produced by a sophisticated, three dimensional large eddy simulation (LES) model.

1.1 Dissertation Objectives

1.1.1 Remote sensing of cloud optical properties

Many retrieval methods have been used to estimate cloud optical properties (specifically effective radius and cloud optical depth) from aircraft and satellite radiometer measurements (Curran and Wu, 1982; Twomey and Cocks, 1982; Twomey and Cocks, 1989; King, 1987; Foot, 1988; Wielicki et al., 1990; Nakajima and King, 1990; Han et al., 1994). Satellite retrievals are not only necessary to obtain the large-scale information needed in research programs like FIRE or ASTEX (Albrecht et al., 1988), but are also needed to monitor change in cloud physical and radiative properties for long-term climate studies. A determination of the importance of cloud macrophysics is crucial in evaluating the overall accuracy and effectiveness of satellite climatological observations and retrievals.

The techniques mentioned above are based on the principle that the reflection function of clouds at a non-absorbing channel in the visible wavelength region is mostly a function of cloud optical thickness, while the reflection function at a channel where liquid

water absorbs is mostly a function of effective radius, which is a parameter related to the absorption at this wavelength. All of the schemes presently used to retrieve optical properties are based on 1D radiative transfer models. It is unknown how much horizontal heterogeneity may affect the reflected radiances measured by satellites. Some of the issues involved with the effects of macrophysics on satellite retrievals that will be discussed in the following chapters include:

- How does horizontal inhomogeneity affect the retrieval of effective radius and optical depth (What are the differences between the calculated reflected radiances in the 1D and 2D models)?
- How does the sun-viewing geometry affect the differences in calculated reflected radiances between the 1D and 2D models?

1.1.2 Distribution of broadband radiative heating in stratus

It is commonly believed that the thickness of the layer of cloud-top radiative longwave cooling and solar heating has an important effect on the dynamics of the marine cloud layer, and may have a critical role in the breakup of the cloud systems. Diurnal decoupling and subsequent clearing of the marine boundary layer is one of several hypotheses suggested to explain the breakup of stratocumulus. Decoupling of the cloud layer from the subcloud layer caused by the stabilizing effects of solar heating has been observed in mid-latitude marine stratus (Nicholls, 1984) and in FIRE-I (Betts, 1989). In a broken cloud layer, the contribution of horizontal fluxes to the solar heating rates may complicate the decoupling process and lead to cloud breakup under different conditions than in a horizontally uniform layer. A broadband, multi-dimensional RTM would allow us to learn more about how the macrophysics of a cloud system affect the depth and magnitude of broadband heating/cooling rates in the system. It is possible that dynamical models could incorporate parameterizations of solar heating in horizontally inhomogeneous clouds derived from multi-dimensional RTM calculations and improve our understanding of cloud breakup. Some of the questions concerning the relationship between cloud structure and radiative heating rates that will be addressed in this dissertation are:

- How do the horizontal variations in solar radiative heating compare in magnitude to the vertical variations in heating?
- Does the lateral transport of photons in the the 2D model affect the net flux convergence (and thus the amount of absorption) throughout the entire cloud layer?
- How do the vertical profiles of heating rate compare between the 1D and 2D models?
- How do changes in solar zenith angle affect the solar heating rate differences between the 1D and 2D models?

1.1.3 CCN-cloud physics-cloud albedo relations

Since marine stratus cloud systems are known to have a large effect on the radiative budget of the earth-atmosphere system, it is crucial that the most important factors that influence the radiative properties of these clouds be identified. Previous estimates of the impact of CCN on cloud albedo such as those in Jones et al. (1994) are ultimately based on plane parallel RTMs. Kim and Cess (1993) have reported higher values of low level cloud albedo in near coastal boundaries compared to similar mid-ocean clouds and attribute the difference to changes in CCN concentrations. However, this conclusion is based on gross assumptions about the macrophysical properties (including cloud optical depth) of the coastal and mid-ocean clouds. The influence of cloud structure on broadband albedos must be studied before a more accurate assessment of the sensitivity of cloud albedo to CCN concentrations can be made. Multi-dimensional RTMs can be used to quantify more accurately the link between CCN concentrations and cloud albedo. A similar evaluation of the link between CCN and cloud emissivities will lead to the development of improved radiative parameterizations in GCMs that include the effects of micro/macro structure. Toward this goal, the following questions about the effects of microphysical and macrophysical changes on cloud albedo will be addressed:

- How large are the albedo changes produced by typical variations in the cloud structure of marine stratus?

- What is the magnitude of the albedo changes produced by increases in CCN concentrations? How much of the albedo change results from microphysical changes? Do the enhanced CCN concentrations produce macrophysical changes in the cloud and how do these changes affect cloud albedo?

- Observations of CCN concentrations during FIRE-I (Hegg et al., 1990) and ASTEX (Martin et al., 1994) have shown significant CCN concentrations above cloud level. Does the location of the enhanced CCN concentrations have an impact on its overall effect on cloud albedo changes? More specifically, how do the albedo changes compare when equal amount of CCN are introduced from either above or below the cloud layer?

1.2 Outline

The numerical models used in this dissertation are described in the three following chapters. The two dimensional SHSG radiative transfer model is presented in chapter 2, while chapter 3 presents the modifications to this model that were necessary to calculate broadband fluxes. Chapter 4 briefly summarizes the changes made to RAMS for this study and describes the various CCN/LES experiments that were conducted to supply input to the radiative transfer model. Chapters 5 and 6 contain most of the original research of this dissertation. Chapter 5 presents the results of the broadband calculations including the heating rate and albedo results. This chapter includes estimates of the effects of microphysical changes by increased CCN concentrations on the cloud albedo and estimates of changes in albedo due to changes in the horizontal variability of the cloud optical properties. Chapter 6 presents the results of radiance calculations in a two dimensional medium and shows how the horizontal inhomogeneity in an unbroken marine stratus cloud affects the retrieval of cloud optical depth and effective radius from satellite reflectance measurements. The final chapter summarizes the important results of the dissertation and provides a discussion on how the effects of cloud inhomogeneity may be modeled in future studies.

Chapter 2

SHSG RADIATIVE TRANSFER MODEL

The multi-dimensional radiative transfer calculations in this dissertation were made using the spherical harmonic spatial grid (SHSG) method. This method has been developed by Evans (1993) and it offers some advantages that make it particularly useful for evaluating the effects of cloud structure on radiative transfer. The SHSG model is an accurate and efficient model that is faster than other general multi-dimensional RTMs. The model gains much of its speed from the efficient way it discretizes the radiative transfer equation. The model expands the angular part of the radiance field in a spherical harmonic series and represents the spatial part of the of the radiance field on a discrete grid. The coupled linear system resulting from this discretization (and the appropriate boundary conditions) is solved iteratively with the conjugate gradient method. Unfortunately, even with this model, the computational resources necessary for 3D radiative transfer modeling greatly limit the size of the model domain, and only two dimensional radiative transfer calculations were used in this dissertation. Although the results from a 2D model will not be as general as those from a 3D model, much can still be learned about the effects of cloud inhomogeneity.

The SHSG method described in Evans (1993) is monochromatic, and in order to do broadband calculations it was modified to include multi-band calculations. The k-distribution method was used to account for gaseous absorption, and parameterizations for Rayleigh scattering and e-type continuum absorption were also included. The development of this broadband model represents one of the major contributions of this dissertation and its description is presented in Chapter 3.

2.1 Monochromatic Model Description

The monochromatic radiative transfer equation in a two dimensional medium can be expressed as:

$$\mu\frac{\partial I}{\partial z} + (1-\mu^2)^{1/2}\cos\phi\frac{\partial I}{\partial x} = -kI + \frac{k\tilde{\omega}}{4\pi}\int_0^{2\pi}\int_{-1}^{1} P(\mu,\mu',\phi,\phi')I(\mu',\phi')d\mu' d\phi' + S, \quad (2.1)$$

where μ is the cosine of the zenith angle (positive for upward angles), ϕ the azimuthal angle, z the vertical coordinate, and x the horizontal coordinate. In this model, the radiance field $I(\mu,\phi,x,z)$ and sources of radiation $S(\mu,\phi,x,z)$ depend on angle and location, while the phase function $P(\cos\Theta,x,z)$ depends on scattering angle and location, and the extinction $k(x,z)$ and single scattering albedo $\tilde{\omega}(x,z)$ depend only on location.

Solar radiation is divided into the direct collimated beam and diffuse radiation. The Beer-Bouger-Lambert law defines the attenuation of the direct beam. The scattering of the direct beam produces a source of diffuse radiation (often called the "pseudo-source") that is written as:

$$S(\mu,\phi,x,z) = \frac{F_0}{\mu_0}\frac{k\tilde{\omega}}{4\pi}\exp\left[-\tau_s(x,z)\right]P(\mu,\phi,\mu_0,\phi_0), \quad (2.2)$$

where $\tau_s(x,z)$ is the optical path of the collimated solar beam from the sun to location (x,z), F_0 is the solar flux, and (μ_0,ϕ_0) is the direction of travel of the solar beam.

For infrared wavelengths, the thermal source term is

$$S(x,z) = k(1-\tilde{\omega})B(T), \quad (2.3)$$

where $B(T)$ is the Planck function.

2.1.1 Spherical harmonic expansion

In general, the two dimensional radiative transfer equation cannot be solved analytically, thus numerical methods are used to solve the equation to a desired accuracy. In the SHSG method, the angular part of the radiance field at each grid location is expressed as a truncated spherical harmonic series:

$$I(\mu,\phi) = \sum_{m=0}^{M}\sum_{l=m}^{L+m} I_{lm}Y_{lm}(\mu,\phi). \quad (2.4)$$

The spherical harmonic functions (Y_{lm}) are defined by

$$Y_{lm}(\mu,\phi) = \gamma_{lm}\mathcal{P}_l^m(\mu)\cos m\phi \qquad \gamma_{lm} = \left(\frac{2l+1}{2\pi(1+\delta_{0m})}\frac{(l-m)!}{(l+m)!}\right)^{1/2} \tag{2.5}$$

where $\mathcal{P}_l^m(\mu)$ are associated Legendre functions. The spherical harmonic functions are orthogonal and normalized for integration over 4π steradians. In a two dimensional model the radiance is an even function of azimuth, so only cosine terms are needed in the expansion. This simplification halves the required number of spherical harmonic terms ($N_{lm} = (L+1)(M+1)$).

Recurrence relations were used to convert the streaming terms of the radiative transfer equation to the spherical harmonic basis. The z streaming term for the lmth spherical harmonic is

$$\left[\mu\frac{\partial I}{\partial z}\right]_{lm} = a_{lm}^{-}\frac{\partial I_{l-1,m}}{\partial z} + a_{lm}^{+}\frac{\partial I_{l+1,m}}{\partial z}, \tag{2.6}$$

where

$$a_{lm}^{-} = \left(\frac{(l-m)(l+m)}{(2l-1)(2l+1)}\right)^{1/2} \qquad a_{lm}^{+} = \left(\frac{(l-m+1)(l+m+1)}{(2l+1)(2l+3)}\right)^{1/2} \tag{2.7}$$

and the x streaming term is

$$\left[(1-\mu^2)^{1/2}\cos\phi\frac{\partial I}{\partial x}\right]_{lm} = b_{lm}^{--}\frac{\partial I_{l-1,m-1}}{\partial x} + b_{lm}^{+-}\frac{\partial I_{l+1,m-1}}{\partial x} + b_{lm}^{-+}\frac{\partial I_{l-1,m+1}}{\partial x} + b_{lm}^{++}\frac{\partial I_{l+1,m+1}}{\partial x}, \tag{2.8}$$

where

$$\begin{aligned} b_{lm}^{--} &= -\left(\frac{1+\delta_{1m}}{4}\frac{(l+m)(l+m-1)}{(2l-1)(2l+1)}\right)^{1/2} \\ b_{lm}^{+-} &= \left(\frac{1+\delta_{1m}}{4}\frac{(l-m+1)(l-m+2)}{(2l+1)(2l+3)}\right)^{1/2}, \end{aligned} \tag{2.9}$$

$$\begin{aligned} b_{lm}^{-+} &= \left(\frac{1+\delta_{0m}}{4}\frac{(l-m)(l-m-1)}{(2l-1)(2l+1)}\right)^{1/2} \\ b_{lm}^{++} &= -\left(\frac{1+\delta_{0m}}{4}\frac{(l+m+1)(l+m+2)}{(2l+1)(2l+3)}\right)^{1/2}. \end{aligned} \tag{2.10}$$

The coupling between the horizontal terms in the spherical harmonic expansion is limited to adjacent l and m terms in the series, resulting in a very sparse system of coupled linear equations. The terms involving $l > L+m$, $l < m$, $m > M$, and $m < 0$ are set to zero.

Since the phase function depends only on the scattering angle, it is expanded in a Legendre series in the scattering angle Θ

$$P(\cos\Theta) = \sum_{l=0}^{L+M} \chi_l \mathcal{P}_l(\cos\Theta). \tag{2.11}$$

The scattering integral can be expressed in a simple form in the spherical harmonic basis by using the addition theorem of associated Legendre function, integrating over angles (μ', ϕ'), and using the orthogonality relations of Y_{lm}. The scattering integral for the lmth term becomes

$$\left[\frac{1}{4\pi}\int_0^{2\pi}\int_{-1}^{1} P(\mu,\phi,\mu',\phi')I(\mu',\phi')d\mu' d\phi'\right]_{lm} = \frac{\chi_l}{2l+1} I_{lm}. \tag{2.12}$$

Note that if the phase function is only a function of scattering angle, the spherical harmonic terms are not coupled and the scattering integral is diagonal.

The delta-M method (Wiscombe, 1977) is used to improve the accuracy of the radiance calculations for highly asymmetric phase functions. In order to simplify the phase function, the method essentially considers the photons scattered into the strong forward peak as not being scattered at all. The method accomplishes this by approximating the forward peak of the phase function with a combination of a forward scattering delta function and a truncated Legendre series. The extinction, single scattering albedo and Legendre phase function coefficients are then rescaled to conserve energy. Since the spherical harmonic terms in the scattering integral are not coupled, the only term in the radiative transfer equation that is actually changed by the delta-M method is the solar pseudo-source term. The solar pseudo-source in the spherical harmonics basis is

$$S_{lm} = \frac{F_0}{\mu_0}\exp[-\tau_s(x,z)]Y_{lm}(\mu_0,\phi_0)\frac{k\tilde{\omega}\chi_l}{2l+1}. \tag{2.13}$$

τ_s is computed by integrating the extinction field from each grid point toward the sun to find the optical path. In the model the extinction field varies bilinearly inside each grid cell.

The thermal source term is isotropic and can be expressed using only the first term in the spherical harmonic expansion, that is,

$$S_{lm} = k(1-\tilde{\omega})B(T)(4\pi)^{1/2}\delta_{l0}\delta_{m0}. \tag{2.14}$$

2.1.2 Spatial grid discretization

The spatial variations in the radiance field and the optical properties in the model are represented by a uniformly spaced, rectangular grid. The x partial derivative is approximated by a three-point centered difference. The z partial derivative is approximated by a two-point trapezoidal difference because of difficulties in using a three-point scheme at the top and bottom boundaries. Although other spacing and finite differencing configurations are possible, this discretization was chosen for its relative simplicity.

The finite difference scheme is illustrated in the following example. In order to simplify the illustration, the radiative transfer equation is written in the form,

$$A\frac{\partial I}{\partial z} + B\frac{\partial I}{\partial z} + EI = S. \tag{2.15}$$

The finite difference form of the equation is

$$\frac{2A}{\Delta z}(I_{i+1,j} - I_{ij}) + \frac{B}{2\Delta x}(I_{i,j+1} + I_{i+1,j+1} - I_{i,j-1} - I_{i+1,j-1}) + E_{i+1,j}I_{i+1,j} + E_{ij}I_{ij} = S_{i+1,j} + S_{ij}, \tag{2.16}$$

where i is the z grid index, j is the x index, and Δz and Δx are the grid spacings.

The optical properties (extinction, single scattering albedo, and a Legendre series representation of the phase function) are read into the model from a file. The resolution of the grid in this optical property input file is independent of the resolution of the model's internal grid, and was always coarser than the model grid in the simulations. The optical properties are bilinearly interpolated onto the internal grid. (If the internal grid was coarser than the input grid then the input values would be averaged appropriately.) The resolution of the internal grid must be fine enough to approximate the spatial derivatives in the radiative transfer equation adequately. No well-defined mathematical criterion has been developed to determine what is an adequate resolution. Much of this work was done by trial and error and is discussed in more detail below. Furthermore, the introduction of gas absorption complicates this resolution as discussed later in Chapter 3.

2.1.3 Boundary conditions

The horizontal boundaries in the model are cyclic. As a result there are N_x grid points and N_x equations, and no boundary conditions in x are needed. The boundary conditions in z, however, are more problematic. The Marshak boundary condition method is used in the model to provide the additional information necessary to solve the radiative transfer equation. (See Evans (1993) for a more complete discussion of boundary conditions for the spherical harmonics method.) The method constrains the odd hemispheric moments of the radiance field at the boundaries of the model:

$$\int_0^1 [I(\mu) - \Gamma(\mu)]\, \mathcal{P}_l(\mu) d\mu = 0 \qquad l = 1, 3, ...L. \tag{2.17}$$

where Γ is the upward radiance at the lower boundary. The Marshak method was chosen since it can be readily generalized to multiple dimensions. By replacing the Legendre functions by Y_{lm}'s in eq(2.17) and integrating over the hemisphere, the Marshak boundary condition method can be generalized to:

$$\int_0^{2\pi} \int_0^1 [I(\mu, \phi) - \Gamma(\mu, \phi)]\, Y_{lm}(\mu, \phi)\, d\mu d\phi = 0, \qquad l - m \quad \text{odd}. \tag{2.18}$$

The parallelogram spherical harmonic truncation (see eq(2.4)) conveniently allows the number of constraint equations at each boundary to equal half the total number of terms.

Several simplifying assumptions were made in the boundary conditions, although additional complexity can be added. The boundary conditions for the 2D model are isotropic radiation (and the collimated solar beam) incident on the top of the domain and thermal emission or reflected direct solar radiation incident on the bottom of the domain. Only Lambertian reflection of the direct solar radiation is permitted at the lower boundary in order to avoid the complication of two collimated beams of radiation. Also, the boundary conditions are horizontally uniform except for variations in reflected direct solar radiation. For the lower boundary the upward radiance is

$$\Gamma_b(\mu, \phi) = \Gamma_e + \int_0^{2\pi} \int_{-1}^0 R(\mu, \phi, \mu', \phi') I(\mu', \phi')\, d\mu' d\phi', \tag{2.19}$$

where R is the surface reflection function, and Γ_e is the surface source of diffuse radiation (from emission or direct solar reflection). For a Lambertian surface with albedo α the reflection function is

$$R(\mu, \phi, \mu', \phi') = \frac{\alpha}{\pi}\mu'. \tag{2.20}$$

The boundary conditions can be expressed as a set of linear equations involving the spherical harmonic coefficients of the radiance field at each point on the boundaries. Because the radiance field is azimuthally symmetric, the equations involve a sum on the l index only,

$$\sum_{l'} U_{lm,l'} I_{l'm} = \Gamma_{lm} \qquad l - m \quad \text{odd} \tag{2.21}$$

The coefficients in the boundary conditions (U and Γ) are found by substituting eq. (2.19) into eq. (2.18) and integrating over azimuth. For the Lambertian surface U is

$$U_{lm,l'} = \pi(1+\delta_{0m}) \int_0^1 Y_{lm}(\mu, 0) \left[Y_{l'm}(\mu, 0) - 2\pi\delta_{m0} \int_{-1}^0 R(\mu, \mu') Y_{l'0}(\mu', 0) d\mu' \right] d\mu. \tag{2.22}$$

The right hand side of the boundary condition equation is

$$\Gamma_{lm} = 2\pi\delta_{m0} \int_0^1 \Gamma_e Y_{l0}(\mu, 0) d\mu. \tag{2.23}$$

Similarly, the boundary condition coefficients for the top boundary are

$$U_{lm,l'} = \pi(1 + \delta_{0m}) \int_{-1}^0 Y_{lm}(\mu, 0) Y_{l'm}(\mu, 0) d\mu$$

$$\Gamma_{lm} = 2\pi\delta_{m0} \int_{-1}^0 \Gamma_t Y_{l0}(\mu, 0) d\mu, \tag{2.24}$$

where Γ_t is the downward radiance at the top boundary. The integrals over μ in the above equations are solved using Gaussian quadrature integration.

2.1.4 Solution method

The coupled linear system resulting from the discretized radiative transfer equation and the boundary conditions provides a number of equations equal to the number of elements of the radiance vector so a unique solution can be found. The system of equations is solved to an arbitrary accuracy by the conjugate gradient method. This solution method iteratively reduces the residuals of the systems of equations to near zero so that the

radiative transfer equation and the boundary conditions are satisfied. Several variants of the conjugate gradient method were tested by Evans (1993), and the technique chosen for the SHSG method minimizes the RMS deviation of the conjugate gradient solution from the true solution.

Using matrix-vector notation, the discretized radiance field can be represented by the radiance vector $\mathbf{I}$. The residual equation is $\mathbf{r} = \mathbf{DI} - \mathbf{S}$, where $\mathbf{D}$ is a sparse matrix. In conjugate gradient methods, the residual vector must be multiplied by the transpose of $\mathbf{D}$. This operation can be derived from the residual equation. The steps involved in each conjugate gradient iteration (starting with the initial residual vector $\mathbf{r}_0$ and the initial step direction $\mathbf{p}_0 = -\mathbf{D}^T\mathbf{r}_0$ are shown below:

$$\begin{aligned} \lambda &= \frac{|\mathbf{r}_n|^2}{|\mathbf{p}_n|^2} \\ \mathbf{I}_{n+1} &= \mathbf{I}_n + \lambda \mathbf{p}_n \\ \mathbf{r}_{n+1} &= \mathbf{D}\mathbf{I}_{n+1} - \mathbf{S} \\ \gamma &= \frac{|\mathbf{r}_{n+1}|^2}{|\mathbf{r}_n|^2} \\ \mathbf{p}_{n+1} &= -\mathbf{D}^T\mathbf{r}_{n+1} + \gamma \mathbf{p}_n. \end{aligned} \tag{2.25}$$

The iterations are continued until the solution criterion, that is, the RMS of the residual divided by the RMS of the radiance vector, is less than a specified tolerance (usually 10^{-3}). Since the discretized radiative transfer equation itself is an approximation, there is usually no need to iterate beyond this level of accuracy.

The radiance field is initialized with the solution of the $L = 1, M = 0$ spherical harmonic truncation. This system has no horizontal coupling since $M = 0$ and is equivalent to a column wise two-stream model. A tridiagonal solver calculates the $l = 0$ and $l = 1$ terms and the rest of the terms are set to zero. The model can also be initialized from a previous SHSG solution with a different truncation or grid resolution.

2.1.5 Computing radiometric quantities

After the conjugate gradient calculations converge, several calculations are needed to convert the spherical harmonic radiance series into radiometric quantities. The hemispheric flux at each grid point is calculated by integrating (by Gaussian quadrature) the

cosine-weighted radiance over all angles. Thus, the upward flux is

$$F\uparrow = \sum_{l=0}^{L} I_{l0}\left[2\pi\int_0^1 \mu Y_{l0}(\mu,0)d\mu\right]. \tag{2.26}$$

and the downward flux is

$$F\downarrow = \sum_{l=0}^{L} I_{l0}\left[2\pi\int_{-1}^0 \mu Y_{l0}(\mu,0)d\mu\right]. \tag{2.27}$$

The net flux is simple to calculate in the spherical harmonic basis since it involves only one term:

$$\begin{aligned} F_x &= \int_{4\pi}\sin\theta\cos\phi I(\Omega)d\Omega \\ &= -\left(\frac{4\pi}{3}\right)^{1/2} I_{11} \\ F_z &= \int_{4\pi}\cos\phi I(\Omega)d\Omega \\ &= \left(\frac{4\pi}{3}\right)^{1/2} I_{10} \end{aligned} \tag{2.28}$$

The net flux convergence, related to the heating rate, is computed by integrating the right side of the radiative transfer equation over all angles to get

$$-\nabla\cdot\mathbf{F}_{\text{net}} = k(1-\tilde{\omega})\left[4\pi\overline{I} + \frac{F_0}{\mu_0}\exp(-\tau_s)\right], \qquad \text{solar source} \tag{2.29}$$

$$-\nabla\cdot\mathbf{F}_{\text{net}} = k(1-\tilde{\omega})4\pi[\overline{I} - B(T)], \qquad \text{thermal source} \tag{2.30}$$

where $\overline{I}$ is the mean intensity, which is proportional to the first spherical term ($\overline{I} = (4\pi)^{1/2}I_{00}$).

Radiances are more difficult to compute because the finite number of terms in the spherical harmonic series produces spurious oscillations in the radiance pattern if simple summation of series is used. Two different methods can be used to smooth the calculated radiances. The first method developed by Kourganoff (1952), goes through an extra step of integrating the radiative transfer equation in order to remove the oscillations. The spherical harmonic expansion of the radiance field is used to compute the scattering integral in the source function,

$$J_{\text{scat}}(\mu,\phi) = \frac{\tilde{\omega}}{4\pi}\int_0^{2\pi}\int_{-1}^1 P(\mu,\phi,\mu',\phi')I(\mu',\phi')d\mu'd\phi' = \sum_{m=0}^{M}\sum_{l=m}^{L+m}\frac{\tilde{\omega}\chi_l}{2l+1}I_{lm}Y_{lm}(\mu,\phi), \tag{2.31}$$

and is added to the thermal emission source or the solar pseudo-source to find the complete source function. The radiance emerging from the boundary of the model is calculated by integrating along a path s at the desired angle (μ, ϕ),

$$I(0) = \exp[-\tau(s)]I(s) + \int_0^s \exp\left[-\int_0^{s'} k(t)dt\right] J(s')k(s')ds', \tag{2.32}$$

where $I(s)$ is the radiance entering the opposite boundary. In the model, the integral is divided into segments for each grid cell where both the extinction and source function are approximated by bilinear interpolation of the four grid point boundaries.

The second method is presented in Dave and Armstrong (1974) and is called the Cesàro method. In this method the radiances are calculated using a smoothing function:

$$I(\mu, \phi) = \sum_{m=0}^{M} \sum_{l=m}^{L+m} \left(1 - \frac{l-m}{L+1}\right)\left(1 - \frac{m}{M+1}\right) I_{lm} Y_{lm}(\mu, \phi). \tag{2.33}$$

2.1.6 Independent pixel approximation

By removing the horizontal coupling in the model the SHSG method can be converted into a one dimensional model. The horizontal coupling is eliminated by setting the weights for the x finite differences to zero [*i.e.* the quantities in (2.9) and (2.10)]. The solar direct beam and radiance path integral calculations are also done on independent columns. This version of the model is called the "independent pixel approximation" (IPA) mode since the radiative transfer calculations become a series of one dimensional independent column calculations across the x domain. By comparing the results of the full two dimensional model and the IPA calculations, estimates of the effects of horizontal inhomogeneity can be directed calculated. This version of the model is helpful in quantifying the effects of macrophysics on radiative transfer in marine stratocumulus.

2.2 Phase Functions

As shown above, the phase functions in the simulations depend only on the scattering angle, and can be expressed in a Legendre series expansion in the scattering angle Θ

$$P(\cos\Theta) = \sum_{l=0}^{N} \chi_l \mathcal{P}_l(\cos\Theta). \tag{2.34}$$

The phase functions of the RAMS-derived droplet distributions were calculated using Lorenz-Mie theory. However, over one hundred Legendre terms would be required to accurately represent the Mie phase functions, and instead an approximate phase function form was used in the SHSG model. The phase functions in all of the radiative transfer calculations were approximated by a double Henyey-Greenstein (DHG) phase function. The DHG phase function is a weighted sum of two Henyey-Greenstein phase functions and is more accurate in representing the scattering function in the cloud than a single Henyey-Greenstein (HG) function. The DHG function is of the form

$$P_{dhg} = bP_{hg}(g1) + (1-b)P_{hg}(g2) \tag{2.35}$$

and the effective asymmetry factor of the DHG is defined as

$$g_{\text{eff}} = b \times g1 + (1-b) \times g2$$

where b is the weighting factor and $g1$ and $g2$ are the asymmetry parameters of the two Henyey-Greenstein phase functions.

Figure 2.1 compares the phase function derived from Lorenz-Mie calculations with those from the analytic forms of the single and double Henyey-Greenstein phase functions. The inability of the single or double Henyey-Greenstein function to accurately represent the forward scattering peak does affect the radiative transfer through the cloud, and consequently the retrieval of optical properties. King (1987) demonstrated the differences in the reflected radiance field from a cloud with a HG phase function compared to a cloud with a more realistic phase function.

By using asymptotic expressions for the reflection function of optically thick layers ($\tau \geq 9$), King computed the scaled optical thickness ($[1-g]\tau$) as a function of surface albedo and the difference between the reflection function of a semi-infinite atmosphere ($R_\infty(\mu, \mu_0, \phi)$) and the measured reflection function. The advantage of this method is the small number of terms required in the Fourier expansion of the reflection function of a semi-infinite atmosphere. Even optical depth retrievals for a Mie-derived phase function

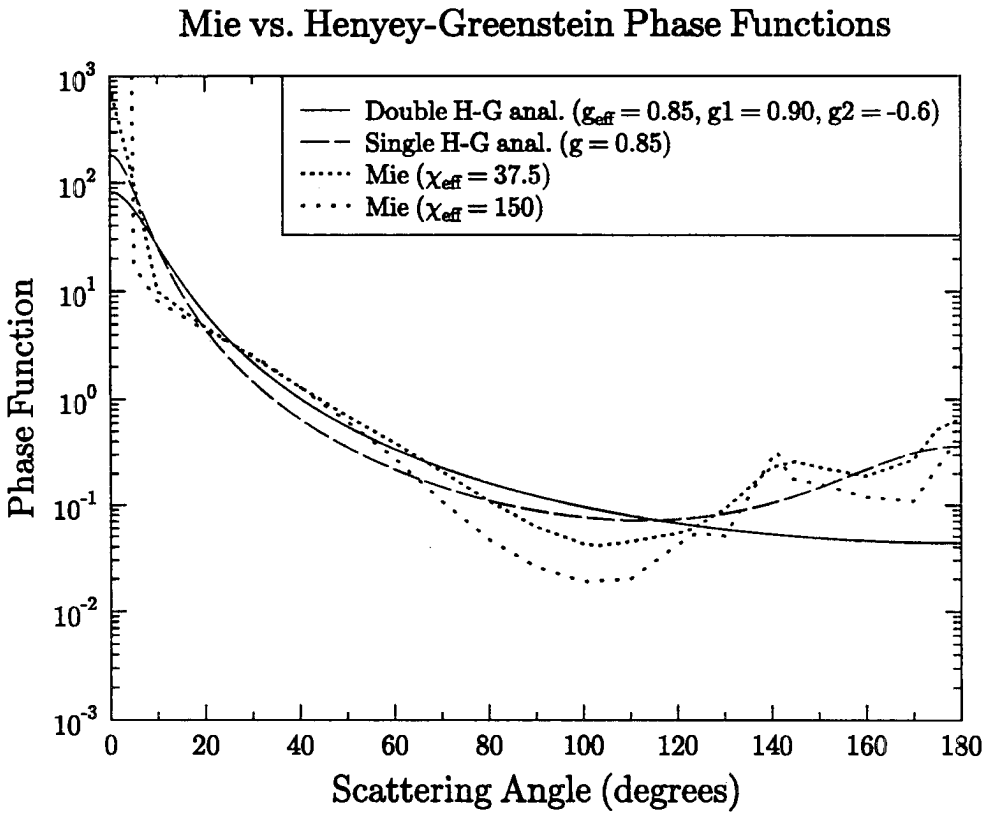

Figure 2.1: Comparison of analytic forms of Henyey-Greenstein and double HG phase functions with those derived from Mie theory.

can be efficiently computed since the number of Fourier terms is usually small. A comparison of the optical depth retrievals from an optically thick frontal cloud system over Oklahoma using the HG phase function and a Mie phase function of fair weather cumulus showed differences as large as 50 percent, even though the asymmetry factors of both phase functions were identical.

However, the exact shape of the phase function is not crucial in this dissertation since this study focuses on the differences in the IPA and 2D reflected radiance fields, rather than attempting to accurately reproduce observed radiance fields. In the model calculations, the phase functions are calculated by setting the asymmetry factor calculated from the Lorenz-Mie calculations equal to the effective asymmetry factor. The g1 parameter was defined as $g_{\text{eff}} + 0.05$ and g2 was set equal to -0.6 in all calculations. This set of parameters gave a reasonable approximation to the Mie phase functions, especially in the near backscattering angles. The two Mie phase functions shown roughly represent the range of the size parameters in the retrievals. The size parameters of the cloud droplets (7–13 microns) for 0.75 micron radiation range from 59 to 110, while the size parameters for $\lambda = 2.16\,\mu m$ range from 20 to 38.

Figure 2.2 shows the Legendre expansion of the DHG function for N=24 terms. The Legendre series cannot accurately represent the DHG function with less than at least 60 terms, and the delta-M method was necessary reduce the number of Legendre terms to an acceptable amount. Figure 2.3 shows the Legendre expansion of the phase function using the delta-M method for 24 terms. The expansion (24 terms) for effective asymmetry factors greater than 0.88 tend to become unstable, so the maximum value of the asymmetry factor allowed in the calculations was 0.88. In general, this value was only exceeded in the 2.16 micron calculations in the bottom of the model domain where the droplet distributions consisted of a few small drizzle droplets.

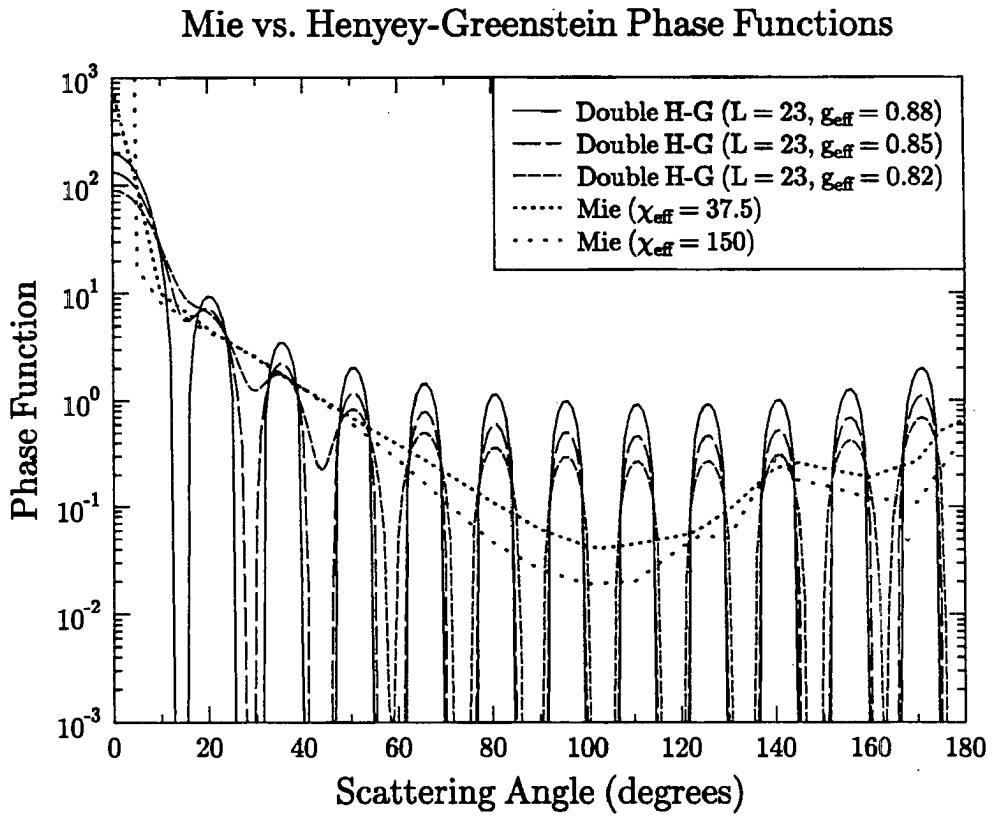

Figure 2.2: Legendre expansion of the DHG phase function for N=24 terms compared to Mie theory derived phase functions.

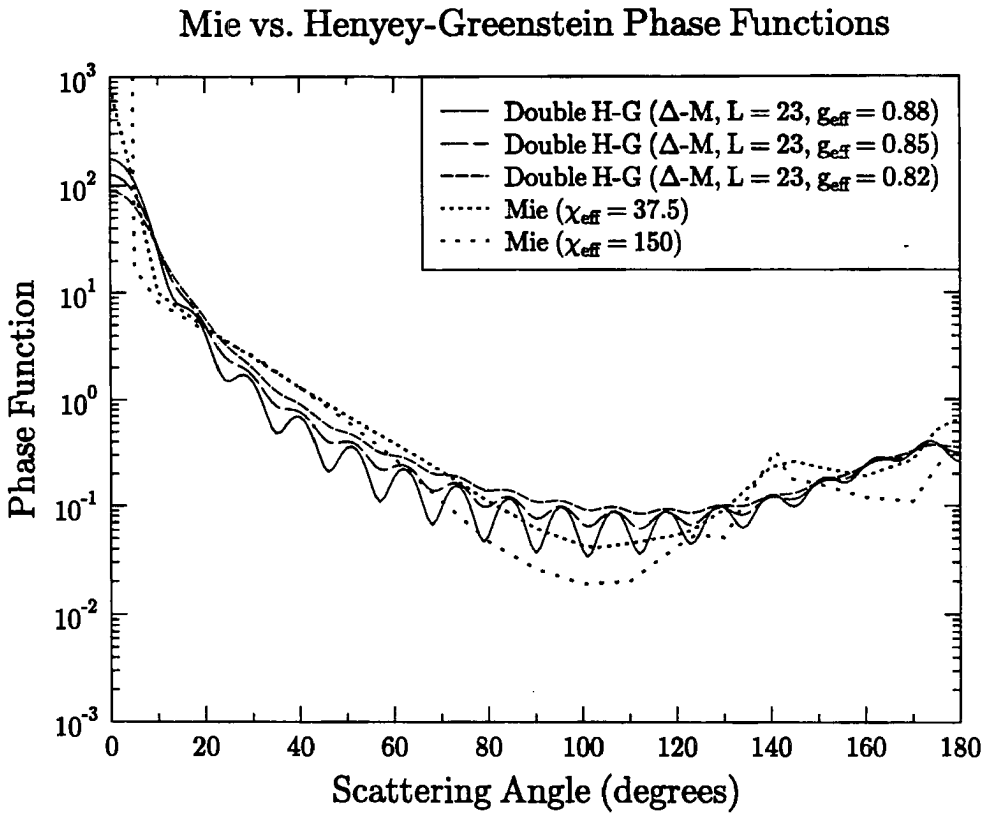

Figure 2.3: Same as Figure 2.2, but with the delta-M scaling for the DHG phase function. The scaling reduces the number of required Legendre terms.

2.3 Determination of Model Parameters

Evans (1993) includes some verification of the SHSG model by a comparison of results with other multi-dimensional models (primarily Monte Carlo models). The verification showed that the SHSG model calculations of fluxes and radiances in a highly variable cloud compared well with the Monte Carlo results when "modest grid sizes and angular resolutions" were used. The verification of the SHSG model was limited especially with respect to radiance calculations and a more complete check of the model was needed to assess its accuracy. As noted by Evans, the SHSG method should become more accurate as the level of approximation increases. However, the main computer memory requirements of the model are also proportional to the level of approximation. The main memory requirements for the computations come from the three vectors needed for the conjugate gradient calculation (radiance, residual, and step direction). Each of the three vectors has $N = N_x N_z N_{lm}$ floating point elements, where $N_x \times N_z$ is the internal grid size and $N_{lm} = (L+1) \times (M+1)$ is the number of spherical harmonic terms. The running time of the SHSG model was also found to be roughly proportional to the length of the radiance vector. A compromise between accuracy and computer resources was always necessary, and depended on the nature of the calculation.

The length of the radiance vector and thus the computational expense of the model depends both on the resolution of the internal grid (which affects the accuracy of the spatial derivatives in the radiative transfer equation) and the spherical harmonic truncation (which affects the angular accuracy of the radiances fields). In order to appreciate the computational requirements of the model, a calculation with an internal grid of size $N_x = 500$ by $N_z = 81$ and a spherical harmonic truncation of $L = 23$ and $M = 11$ would require over 144 megabytes of memory. Given the requirements in Evans (1993) that the maximum optical path per grid cell should of order one to give accurate results, the above conditions would be satisfied by a 12.5 km by 2 km cloud with a *maximum* extinction of 40 km^{-1}.

2.3.1 Grid resolution

The determination of an adequate grid resolution was done by trial and error. Since the grid resolution affects the accuracy of the spatial derivative in the radiative transfer equation, the appropriate resolution is a function of the extinction per grid cell. Obviously, finer resolutions are necessary as the solar zenith angle becomes larger and to some extent as the viewing angle moves from nadir. In this study the viewing angles were limited to a maximum of 45° from nadir to match the range of angles sampled by the aircraft radiometer used by Nakajima et al. (1991), and thus the effects of viewing angle are minimized. The maximum extinction and also the homogeneity of the extinction in the cloud field are also important factors that determine the necessary grid resolution. It is important to note that for a given maximum extinction, the grid resolution for a more homogeneous field must be finer than the grid resolution for less homogeneous field. The radiance gradients in the more homogeneous medium (near the extinction maximum) will tend to be larger because the grid cells surrounding the extinction maximum usually will be larger than in a less homogeneous cloud. As a result, it was found that the Evans (1993) extinction criterion was not adequate for thick, homogeneous clouds.

As noted above, the SHSG model can be initialized with a radiance field from a previous solution. Two methods of initialization were tested. The first method used the solutions from a series of runs using the same grid resolution as the final calculation, but a lower spherical harmonic truncations. For example, the first run would use a spherical harmonic truncation of $L = 7, M = 3$, the second a truncation of $L = 15, M = 7$ and the third $L = 23, M = 11$. The second method used the solution from a series of calculations using the same spherical harmonic truncation but coarser grid resolutions. The number of grid *cells* (in x and z) in each successive calculation had to be an integer multiple of the previous solution, so for example a series of calculations may have had internal grid sizes of $N_x = 50, N_z = 21$, $N_x = 100, N_z = 41$, and $N_x = 200, N_z = 81$. The second method was found to be substantially faster than the first method in speeding up the calculation of fine resolution grids, and was used exclusively in all of the following computations. It appears the second method was more effective in accelerating the calculations because the

level of spherical harmonic approximation affected the overall radiance field more than the level of spatial grid approximation. The radiance fields produced by the coarser grid resolutions more closely matched the final radiance field and the total number of conjugate gradient iterations resulting from the second method were much smaller than the number of iterations produced using the first method.

An adequate grid resolution was determined by using the second radiance field initialization method, and comparing the results of runs at various resolutions until the solutions appeared to converge. As a test, a microphysical field from the control run of the RAMS model simulation (see Chapter 4 for more details on the RAMS model and the simulations) was used as input for a set of calculations of varying resolutions. In order to create a greater range of satisfactory grid resolutions, the extinction coefficient at each grid point was halved. The various grid resolutions and corresponding maximum extinction per grid cell are shown in the table below:

Table 2.1: Grid resolutions used in spatial resolution test.

N_x, N_z	Max. extinction per grid cell
56,10	3.6
112,19	1.8
224,37	0.9
448,73	0.45

In the test the spherical harmonic truncation was set to $L = 23, M = 11$. The RMS difference in upward radiances along cloud top were calculated between the $N_x = 448, N_z = 73$ case and the coarser grid cases for a range of viewing angles from $\pm 45°$ from nadir. The range in RMS difference are shown for several solar zenith angles in the following table (Table 2.2).

The RMS differences in the downward radiances at cloud base tended to be smaller than the upward radiances at cloud top. As expected, the largest RMS differences for a given sun angle and grid resolution occurred for the viewing angles farthest from nadir. The RMS differences in the radiances between the $N_x = 224, N_z = 37$ case and the

Table 2.2: RMS difference in cloud top upward radiances from the $N_x = 448, N_z = 73$ case for a range of viewing angles from ±45°.

N_x, N_z	$\mu_0 = 10°$	$\mu_0 = 40°$	$\mu_0 = 60°$
56,10	0.0626 - 0.0797	0.0759 - 0.1031	0.1212 - 0.1556
112,19	0.0153 - 0.0170	0.0233 - 0.0277	0.0449 - 0.0557
224,37	0.0007 - 0.0012	0.0010 - 0.0015	0.0054 - 0.0084

$N_x = 448, N_z = 73$ case were less than one percent, even for the solar zenith angle of 60°, which confirms the criterion from Evans (1993) that the maximum extinction per grid cell in an highly variable medium must be equal to one or less. The maximum differences in upward radiance ranged from 12 to 34 percent for the $N_x = 56, N_z = 10$ case depending on solar zenith and viewing angle, while the maximum differences in the $N_x = 112, N_z = 19$ and $N_x = 224, N_z = 37$ cases ranged from 4 to 15 percent and 0.23 to 1.86 percent respectively.

Some other criteria were also checked to confirm that the SHSG model was converging toward a solution. Since the number of iterations required to meet the solution criterion of the conjugate gradient method is a measure of how close the initial radiance field is to the final radiance field, convergence could be expected when the number of iterations became small. For example, in the case where the solar zenith angle was 10°, the number of iterations in the runs dropped from 211 to 75 to 57 to 17 iterations as the grid resolution was increased.

Another useful criterion was a measure of the spatial gradient of radiance. The maximum difference in radiance (summed over the spherical harmonic terms) across each grid cell (in z) was calculated using the following formula:

$$\text{frac. diff.} = \left(2 \times \frac{\sum_{m=0}^{M} \sum_{l=m}^{L+m} [I_{lm}(x, z+1) - I_{lm}(x, z)]^2}{\sum_{m=0}^{M} \sum_{l=m}^{L+m} [I_{lm}(x, z+1)]^2 + [I_{lm}(x, z)]^2} \right)^{1/2} \tag{2.36}$$

This fractional difference in radiance across a grid equals zero when the radiance difference across a grid cell equals zero and reaches a maximum of two when the radiance drops from a non-zero value to zero across a grid cell. The maximum differences in z were always larger than the maximum differences in x. Experimentation suggests that when

the maximum fractional difference in radiance was less than one, the grid resolution was generally adequate.

For homogeneous clouds (such as those used the the bispectral grid calculations presented in Chapter 5), the grid resolution had to be increased greatly. Experimentation and the fractional difference calculations suggest that the maximum extinction per grid cell for thick, homogeneous clouds had to be much smaller than one (roughly 0.05) since the radiance gradients were very large.

The above discussion addresses the problem of grid resolution only from a numerical perspective and answers the question of what grid spacing is necessary to satisfy the spatial derivative approximation of the radiative transfer approximation. Another problem dealing with grid resolution results from the scale of interaction of radiation inside the cloud and our ability to measure cloud properties. For the test case above when $N_x = 448, N_z = 73$ the distance between grid points is only 6.25 m! It is obvious that present instruments cannot measure radiances to such a fine resolution. The resolution of aircraft radiometers are of the order of 100 m (Nakajima et al., 1991), and most satellite radiometers have a resolution of the order of 1 km. One unresolved question is at what spatial scale are measurements of cloud radiances necessary for an accurate assessment of clouds on radiative transfer. This problem is explored in detail in Stackhouse (1995), but will rarely be addressed here. In Chapter 6, some effects of the spatial scale on albedo measurements will be presented.

2.3.2 Spherical harmonic truncation

As evidenced by the slower convergence of the SHSG computations using an initial radiance field with a lower spherical harmonic truncation, the effects of the truncation is important in determining the accuracy of the model calculations. The level of truncation is less important for flux calculations than radiance calculations since the errors produced by the approximation are somewhat canceled by integration of the radiances over zenith and azimuth. Evans (1993) found that a truncation of $L = 7, M = 7$ produced RMS flux differences (from a higher order truncation run) of less than one percent, but expected the truncation for accurate radiance calculations would be much higher. Stackhouse

Table 2.2: RMS difference in cloud top upward radiances from the $N_x = 448, N_z = 73$ case for a range of viewing angles from ±45°.

N_x, N_z	$\mu_0 = 10°$	$\mu_0 = 40°$	$\mu_0 = 60°$
56,10	0.0626 - 0.0797	0.0759 - 0.1031	0.1212 - 0.1556
112,19	0.0153 - 0.0170	0.0233 - 0.0277	0.0449 - 0.0557
224,37	0.0007 - 0.0012	0.0010 - 0.0015	0.0054 - 0.0084

$N_x = 448, N_z = 73$ case were less than one percent, even for the solar zenith angle of 60°, which confirms the criterion from Evans (1993) that the maximum extinction per grid cell in an highly variable medium must be equal to one or less. The maximum differences in upward radiance ranged from 12 to 34 percent for the $N_x = 56, N_z = 10$ case depending on solar zenith and viewing angle, while the maximum differences in the $N_x = 112, N_z = 19$ and $N_x = 224, N_z = 37$ cases ranged from 4 to 15 percent and 0.23 to 1.86 percent respectively.

Some other criteria were also checked to confirm that the SHSG model was converging toward a solution. Since the number of iterations required to meet the solution criterion of the conjugate gradient method is a measure of how close the initial radiance field is to the final radiance field, convergence could be expected when the number of iterations became small. For example, in the case where the solar zenith angle was 10°, the number of iterations in the runs dropped from 211 to 75 to 57 to 17 iterations as the grid resolution was increased.

Another useful criterion was a measure of the spatial gradient of radiance. The maximum difference in radiance (summed over the spherical harmonic terms) across each grid cell (in z) was calculated using the following formula:

$$\text{frac. diff.} = \left(2 \times \frac{\sum_{m=0}^{M} \sum_{l=m}^{L+m} [I_{lm}(x, z+1) - I_{lm}(x, z)]^2}{\sum_{m=0}^{M} \sum_{l=m}^{L+m} [I_{lm}(x, z+1)]^2 + [I_{lm}(x, z)]^2} \right)^{1/2} \tag{2.36}$$

This fractional difference in radiance across a grid equals zero when the radiance difference across a grid cell equals zero and reaches a maximum of two when the radiance drops from a non-zero value to zero across a grid cell. The maximum differences in z were always larger than the maximum differences in x. Experimentation suggests that when

the maximum fractional difference in radiance was less than one, the grid resolution was generally adequate.

For homogeneous clouds (such as those used the the bispectral grid calculations presented in Chapter 5), the grid resolution had to be increased greatly. Experimentation and the fractional difference calculations suggest that the maximum extinction per grid cell for thick, homogeneous clouds had to be much smaller than one (roughly 0.05) since the radiance gradients were very large.

The above discussion addresses the problem of grid resolution only from a numerical perspective and answers the question of what grid spacing is necessary to satisfy the spatial derivative approximation of the radiative transfer approximation. Another problem dealing with grid resolution results from the scale of interaction of radiation inside the cloud and our ability to measure cloud properties. For the test case above when $N_x = 448, N_z = 73$ the distance between grid points is only 6.25 m! It is obvious that present instruments cannot measure radiances to such a fine resolution. The resolution of aircraft radiometers are of the order of 100 m (Nakajima et al., 1991), and most satellite radiometers have a resolution of the order of 1 km. One unresolved question is at what spatial scale are measurements of cloud radiances necessary for an accurate assessment of clouds on radiative transfer. This problem is explored in detail in Stackhouse (1995), but will rarely be addressed here. In Chapter 6, some effects of the spatial scale on albedo measurements will be presented.

2.3.2 Spherical harmonic truncation

As evidenced by the slower convergence of the SHSG computations using an initial radiance field with a lower spherical harmonic truncation, the effects of the truncation is important in determining the accuracy of the model calculations. The level of truncation is less important for flux calculations than radiance calculations since the errors produced by the approximation are somewhat canceled by integration of the radiances over zenith and azimuth. Evans (1993) found that a truncation of $L = 7, M = 7$ produced RMS flux differences (from a higher order truncation run) of less than one percent, but expected the truncation for accurate radiance calculations would be much higher. Stackhouse

and Stephens (1994) did an extensive comparison of radiance calculations between SHSG and Monte Carlo calculations and found that a truncation of $L = 23, M = 11$ produced accurate radiance calculations for a wide range of solar zenith and viewing angles. This truncation is used for all radiances calculations in this dissertation.

2.4 Summary

This chapter presents an overview of the monochromatic two dimensional radiative transfer model developed by Evans (1993). A discussion of the approximate phase functions used in the calculations is also presented. A determination of the grid resolution required for an accurate approximation of the spatial derivatives agrees with the statement in Evans (1993) that the maximum extinction per grid cell for highly variable clouds must be less than or equal to unity. However, in thick, homogeneous atmospheres this criterion must be more strict. The following chapter presents broadband version of the SHSG model and includes a discussion of the k-distribution method and the approximations used to limit the number of radiative transfer calculations needed in broadband computations.

Chapter 3

BROADBAND MODEL

While the SHSG method can make monochromatic calculations of a two dimensional medium, some modifications to the model are necessary for broadband calculations, since these are complicated by the rapid variability of gaseous absorption coefficient with wavenumber. Direct line-by-line calculations are barely practical for 1D radiative transfer (eg. Scott and Chedin, 1981) let alone in the context of the multi-dimensional SHSG method. In order to make broadband calculations with a 2D model, a band model must be used to reduce the number of radiative transfer computations from the several thousands needed in line-by-line calculations to a more reasonable number. Since the SHSG method is computationally intensive, the balance between speed and accuracy must be carefully considered. This chapter describes the band model implemented into SHSG, the k distribution band model, and the procedures used to reduce the total number of calculations while maintaining a proper level of accuracy. This leads to the large set of broadband radiative transfer simulations of multi-dimensional clouds described in the following chapters.

3.1 Gaseous Absorption

3.1.1 K distribution method

The k distribution method is used to compute broadband gaseous absorption in radiative transfer computations and is less empirically based than many other forms of broadband calculation. Since the gaseous absorption coefficient (k) is highly variable in some spectral regions, averaging k (or the transmittance function) over a frequency interval in a broadband model can sometimes be difficult. The k distribution method solves

this problem by transforming the highly irregular transmittance function in frequency space into a smooth probability distribution function in k space. Mathematically, the k distribution method converts the mean transmittance for a spectral band

$$\mathcal{T}(u) = \frac{1}{\Delta\nu}\int_{\Delta\nu} e^{-k_\nu u} d\nu \tag{3.1}$$

into k space

$$\mathcal{T}(u) = \int_0^\infty f(k) e^{-ku} dk \tag{3.2}$$

Figure 3.1 shows a schematic from Stephens (1984) that illustrates the method. Since the strongest and weakest absorption occur at the same frequency at all altitudes, the pressure effects on absorption can be explicitly represented in the value of k (ie., $f(k)$ is correlated to pressure). The ability of $f(k)$ to be calculated at a reference pressure (and also temperature) allows the k distribution method to also be very accurate. Chou, in a series of papers (including Chou and Arking (1980); Chou and Arking (1981); Chou and Peng (1983); Chou (1984)) has shown that the choice of a reference pressure in the upper troposphere can minimize gaseous optical path (and thus transmittance) errors at any point in the atmosphere as determined from the scaling approximation:

$$u = \left(\frac{\overline{p}}{p_{ref}}\right)^n \left(\frac{T_{ref}}{\overline{T}}\right)^m \frac{\overline{w}\Delta p}{g} \tag{3.3}$$

where $\overline{p}$ and $\overline{T}$ represent the mean pressure and temperature for a layer, p_{ref} and T_{ref} are the reference pressure and temperature at which k is defined and m and n are empirical scaling parameters. $\overline{w}$ is the mean mixing ratio of a gas in the layer of Δp thickness, and g is the acceleration due to gravity. Thus with one set of k distribution data computed at one pressure and temperature, the gaseous absorption throughout the atmosphere can be computed accurately. Both Chou (1986) and Lacis and Oinas (1991) claim that k distribution-based methods can calculate tropospheric, clear-sky heating rates to within 1% of those obtained by line-by-line calculations.

When equation (3.2) is discretized, the transmittance due to gaseous absorption can be expressed as:

$$\mathcal{T} \approx \sum_{i=1}^{n} w_i e^{-k_i u} \tag{3.4}$$

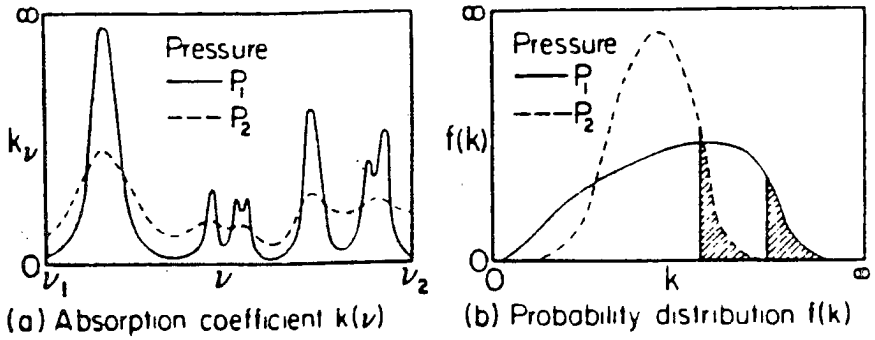

Figure 3.1: Schematic from Stephens (1984) that describes the k distribution method. The absorption coefficients (k) in figure (a) are transformed into a probability distribution function in k space.

where n is the total number of extinction coefficient values (k-values) in the band and w_i is the weight representing the fraction of the band with an extinction coefficient value of k.

The flux solutions for a particular band in the broadband model are found by summing the solutions from each individual k-value:

$$F^{\pm}_{\Delta\nu} = \sum_{i=1}^{n} w_i F^{\pm}_i(\tau_i), \tag{3.5}$$

where τ_i is the optical depth due to gas, cloud droplets and Rayleigh scattering for a particular k-value. For bands where two gases overlap, the transmittance for both gases is assumed to be:

$$\mathcal{T}_{12} \approx \left(\sum_{i=1}^{n_1} w_{1i} e^{-k_{1i}u}\right)\left(\sum_{j=1}^{n_2} w_{2j} e^{-k_{2j}u}\right) \approx \sum_{i=1}^{n_1}\sum_{j=1}^{n_2} w_{1i} w_{2j} e^{-u(k_{1i}+k_{2j})}, \tag{3.6}$$

and the resulting fluxes are:

$$F^{\pm}_{\Delta\nu} = \sum_{i=1}^{n_1}\sum_{j=1}^{n_2} w_{1i} w_{2j} F^{\pm}_{ij}(\tau_{ij}). \tag{3.7}$$

τ_{ij} is the sum of the optical depths due to both gases ($u(k_{1i} + k_{2j})$), cloud droplets and Rayleigh scattering.

The k distribution data used in the broadband model is derived from the original data used in a two-stream model developed by Stackhouse (1989). The data contains gaseous absorption data for three gases, H_2O, CO_2 and O_2. The bandwidths of the absorbing gases and the scaling parameters for the broadband model are presented in Table 3.1. The original k distribution data is discretized into 37 k-value weights and has a bandwidth resolution of 50 cm^{-1}.

Table 3.1: Bandwidths of absorbing gases and scaling parameters for the solar broadband model.

Gas	Bandwidths (cm^{-1})	P_{ref} (mb)	n	T_{ref} (K)	m
H_2O	2600 – 14450	300.00	0.800	240.00	0.000
CO_2	3300 – 4000, 4600 – 5300, 6000 – 7000	300.00	0.800	240.00	0.000
O_2	12850 – 13150, 14300 – 14550	300.00	0.800	240.00	0.000

3.2 Ozone UV cross section data

For gaseous absorption by ozone in visible and ultraviolet wavelengths, the cross section data developed by Stamnes and Tsay (1990) were used. These data use the continuum features of the ozone absorption coefficient in the ultraviolet wavelengths to calculate absorption accurately with only a few bands.

Since the ozone absorption coefficient in the visible and ultraviolet spectrum is a generally smooth function of wavenumber, the k-distribution method is unnecessary and a simpler averaging of the absorption coefficient across a spectral band can be used. Stamnes and Tsay used a solar flux weighted (or Chandrasekhar) mean value of the extinction coefficient across four bands from 0.175 microns to 0.700 microns:

$$k_{ave} = \frac{\sum_{\lambda_1}^{\lambda_2} k(\lambda) F_0(\lambda) d\lambda}{\sum_{\lambda_1}^{\lambda_2} F_0(\lambda) d\lambda} \tag{3.8}$$

where $F_0(\lambda)$ is the solar flux at the top of the atmosphere (TOA) for the wavelength λ. The four band model produced radiative heating rate errors of twenty percent or better

at any height in the atmosphere when compared with a one nanometer resolution model. Stackhouse used ten bands in the two-stream model that extended from only 0.28 microns to 0.687 microns, and produced more accurate results. Unlike the other gaseous absorption data, no pressure and temperature scaling is necessary for the cross section data. For the calculations in this dissertation, the downward solar fluxes computed at cloud top were used in the Chandrasekhar mean instead of the TOA fluxes. The cloud top fluxes were calculated from Stackhouse's two-stream model using a sounding profile obtained from the 7 July 1987 FIRE-I case study (Betts, 1989).

3.3 Particle and Molecular Extinction

Along with gaseous absorption, Rayleigh scattering in the atmosphere and the extinction by cloud particles must be incorporated in the definition of the basic optical properties used in the SHSG radiative transfer model. This section describes the parameterizations used to combine the different extinction processes in the model atmosphere into the optical depths, single scattering albedos and phase functions that make up the model's optical property files.

3.3.1 Optical depth

The total optical depth at each grid point in the model is a summation of the optical depths resulting from the separate radiative processes. For any spectral band,

$$\tau = \tau_{cloud} + \tau_{gas} + \tau_{Rayleigh}. \tag{3.9}$$

τ_{cloud} is determined from Lorenz/Mie theory, where

$$\tau_{cloud} = \sigma_{ext}\Delta z, \tag{3.10}$$

and σ_{ext} is the mean particle extinction coefficient (in units of km^{-1}) for a cloud layer of thickness Δz km. τ_{gas} for a particular gas is calculated from either the k distribution data or the ozone cross section data and can be expressed as:

$$\tau_{gas} = ku \tag{3.11}$$

k is the extinction coefficient (with units of $cm^2\ g^{-1}$) and is determined directly from the gaseous absorption data, while the optical path u is calculated from the scaling approximation (equation(3.3)) and is in units of $g\ cm^{-2}$. When two gases overlap, the optical depth due to both gases is:

$$\tau_{gas} = k_1 u_1 + k_2 u_2. \tag{3.12}$$

The optical depth due to Rayleigh scattering is computed using the empirical fit presented by Paltridge and Platt (1976). The fit calculates the optical depth for a path from the top of the atmosphere to a height H (in km) above the surface,

$$\tau_{Rayleigh} = 0.0088\lambda^{(-4.15+0.2\lambda)} e^{(-0.1188H-0.00116H^2)} \tag{3.13}$$

where λ is the wavelength in microns.

3.3.2 Scaling of the single scattering albedo and phase function

The single scattering albedo and the phase function of the cloud particles are determined from tabulated Mie solutions using the droplet distributions obtained from the RAMS model calculations discussed in the next chapter. A single scattering albedo incorporating the effects of both the cloud droplets and Rayleigh scattering is calculated by using an extinction weighted scaling (Liou and Sasamori, 1975; Slingo and Schrecker, 1982).

$$\tilde{\omega}_{Rayleigh+cloud} = \frac{\tau_{Rayleigh} + \tilde{\omega}_{cloud}\tau_{cloud}}{\tau_{cloud} + \tau_{gas} + \tau_{Rayleigh}} \tag{3.14}$$

In the broadband model, the phase function is computed by scaling the phase functions of the cloud particles and Rayleigh scattering with the method described by Liou and Sasamori (1975). The phase function for Rayleigh scattering is $\frac{3}{4}(1+\cos(\Theta)^2)$. The scaling of the phase function is accomplished in several steps. The DHG phase function (without delta-M scaling) is computed at each grid point for a specified number of Gaussian quadrature points (the number used in all calculations was 256 points). The Rayleigh phase function is also calculated at the quadrature points and scaled with the double HG phase function by the following formula:

$$P_{Rayleigh+cloud}(\Theta) = \frac{\tau_{Rayleigh}P_{Rayleigh}(\Theta) + \tilde{\omega}_{cloud}\tau_{cloud}P_{cloud}}{\tau_{Rayleigh} + \tilde{\omega}_{cloud}\tau_{cloud}} \tag{3.15}$$

where $P_{Rayleigh}$ and $\tau_{Rayleigh}$ are the Rayleigh phase function and optical depth, P_{cloud} and τ_{cloud} are the phase function and optical depth of the cloud, and $\tilde{\omega}_{cloud}$ is the cloud single scattering albedo.

The Legendre coefficients of the scaled phase function may be calculated from

$$\chi_l = \frac{(2l+1)}{2} \int_{-1}^{1} P_{Rayleigh+cloud}(\cos\Theta)\mathcal{P}_l(\cos\Theta)d(\cos\Theta), \tag{3.16}$$

where $\mathcal{P}_l(\cos\Theta)$ is a Legendre polynomial of order l. Gaussian quadrature is then used to numerically integrate the scaled phase function and obtain the coefficients in the Legendre expansion (King, 1983),

$$\chi_l \approx \frac{(2l+1)}{2} \sum_{j=1}^{J} P(\mu_j)\mathcal{P}_l(\mu)c_j, \tag{3.17}$$

where μ_j are the abscissas and c_j the weights for Gaussian quadrature from -1 to 1.

3.4 Reduction of Band Calculations

3.4.1 Reduction of the number of bands

In its original form, the solar broadband model contains 249 bands from 2600 cm^{-1} to 35710 cm^{-1} (0.28 microns to 3.8 microns). Although it provides detailed spectral information, it has a large computational cost. The treatment of gas overlap requires $k_1 \times k_2$ radiative transfer calculations for each overlap band, where k_1 and k_2 are the total number of non-zero weights for each overlapping gas. As a result, the original model requires over 12,400 radiative transfer calculations for the solar bandwidths.

Several methods were used to reduce the total number of required calculations while maintaining a reasonable level of accuracy. The first method was to average the k distribution data over wider bandwidths in order to reduce the total number of bands. The data in each spectral region where two gases overlapped were reduced to one band in order to keep the number of overlap band calculations to a minimum. The remaining spectral regions between overlap bands were also consolidated into single bands. In the visible and ultraviolet wavelengths, the bands were reduced to match the four band model in Stamnes and Tsay (1990). Since the solar radiation calculations only extend to 35710 cm^{-1}, only three of the four bands of ozone cross section data were used. The number of bands were

thus reduced from 249 to 14. Table 3.2 presents the fourteen bands and the absorbing gases in each band. The number of bands were not reduced further since additional consolidation would create bands where part of the band had two gases and other parts only one, and would make the treatment of gas overlap problematic. Also, as shown below, the rapid change in the cloud's single scattering albedo with respect to wavenumber made coarser bands too inaccurate for the purposes of the albedo calculations in Chapter 5.

Table 3.2: Bandwidths used in solar broadband model.

Band	Bandwidths (cm^{-1})	Absorbing gases in band
1	2600 – 3300	H_2O
2	3300 – 4000	H_2O, CO_2
3	4000 – 4600	H_2O
4	4600 – 5300	H_2O, CO_2
5	5300 – 6000	H_2O
6	6000 – 7000	H_2O, CO_2
7	7000 – 12850	H_2O
8	12850 – 13150	H_2O, O_2
9	13150 – 14300	H_2O
10	14300 – 14450	H_2O, O_2
11	14450 – 14550	O_2
12	14550 – 25000	O_3
13	25000 – 31746	O_3
14	31746 – 35710	O_3

The reduction of the number of spectral bands had little effect on the overall accuracy of the gaseous absorption calculations throughout most of the atmosphere. Figure 3.2 shows the clear sky solar heating rates (from 2600 to 35710 cm^{-1}) computed from Stackhouse's two-stream model for the FIRE-I atmospheric sounding. The discrete-ordinate backscattering approximation and a solar zenith angle of 10° were used in calculations with the full 249 bands and 14 bands. In the stratosphere the differences in heating rate reach up to twenty percent, due to the coarseness of the ozone absorbing bands in the ultraviolet wavelengths. At the top of the atmosphere and in the troposphere the differences are much less. Below 15 km, the differences are less than 0.1 K day^{-1}. In the domain of the SHSG model calculations presented in the following chapters (*ie.*, from the surface to

one kilometer), the clear sky heating rates are almost identical (less than 0.03 K day^{-1}). The difference in the net flux convergence in the lowest 14 km is only 0.2 W m^{-2} (163.2 W m^{-2} in the 249 band model versus 163.0 W m^{-2} in the 14 band model).

For cloudy skies, the accuracy of the reduced band model depends on the choice of the frequency used to represent the bands. The choice of frequency should be such that the optical properties of the cloud droplets calculated for that frequency match the means of the optical properties calculated for the entire band. Initially, the optical properties for each band were chosen by arithmetically averaging the refractive index of liquid water across each band and using the arithmetic mean of the band wavenumber as input for the Mie code. Figure 3.3a shows the heating rates for a typical marine stratocumulus cloud using this method to determine the optical properties for each band. The cloud modeled in Figure 3.3a is a composite of a cloud simulated in the RAMS 7 July 1987 control run. (See Chapter 4 for more details about the RAMS simulations.) The model cloud extends from 812 m to 362 m and is divided into 18 layers. The extinction for each layer was calculated from the mean extinction computed from a two dimensional cross section of the control run. The mean optical depth of the cloud is roughly 7.4.

The droplet distributions used in Figure 3.3 was a modified gamma distribution Flatau et al. (1989):

$$n(r)dr = \frac{N_t}{\Gamma(\alpha)} \left(\frac{r}{r_n}\right)^{\alpha-1} \exp\left(-\frac{r}{r_n}\right) d\left(\frac{r}{r_n}\right) \tag{3.18}$$

The size bins of the explicit microphysical model used in the RAMS simulations were each divided in half, and the resulting bins were used in the scattering calculations. This division produced fifty radius bins ranging from roughly 1.8 microns to 500 microns. The parameter α was determined from the average α determined from the droplet data from the RAMS control run and is a function of the mean radius and effective radius of the distribution (see Flatau et al. (1989) for details).

The values of the other variables in the modified gamma distribution (r, r_n, and N_t) were set such that the effective radius at each level in the cloud varied linearly from 13

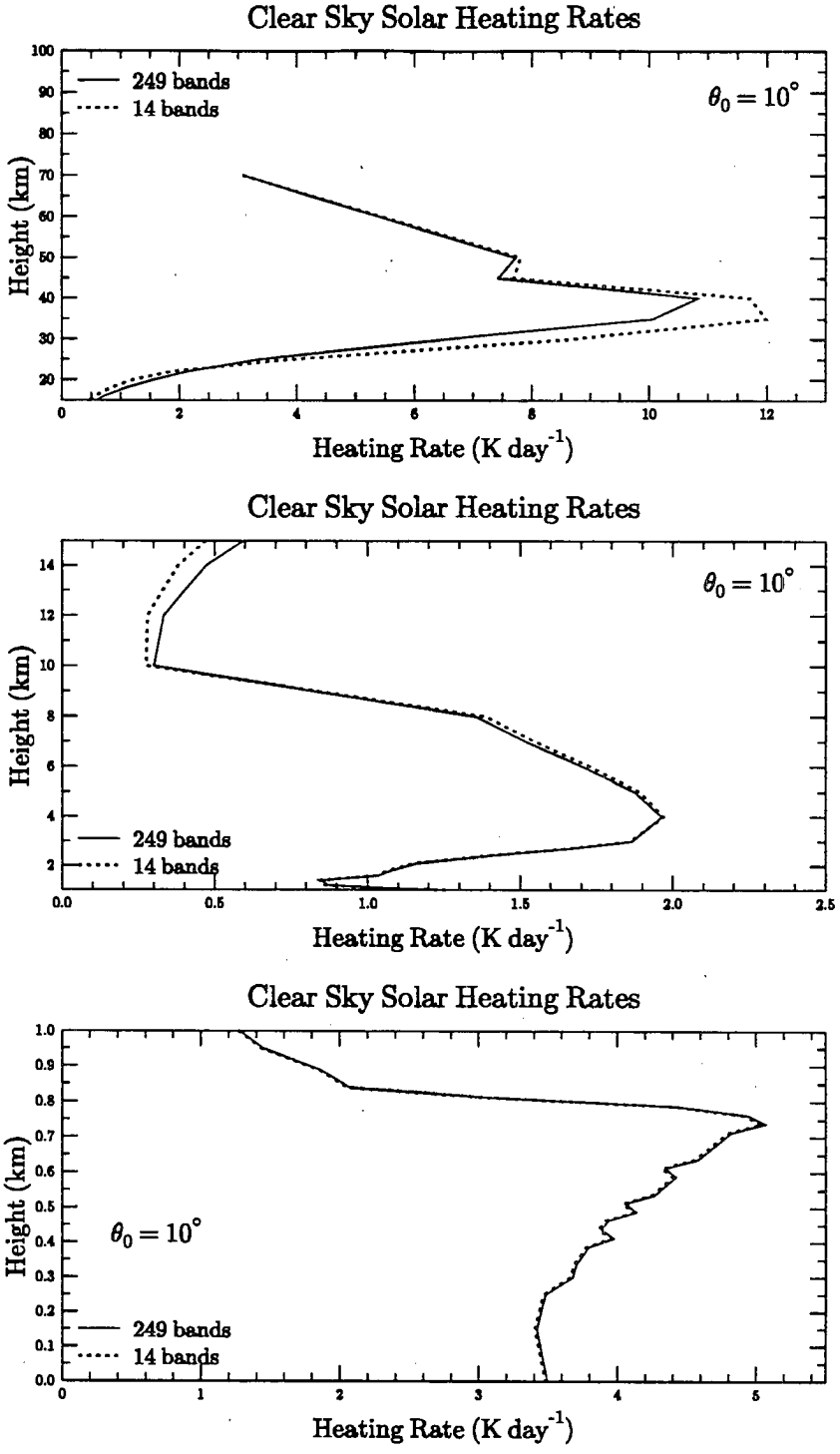

Figure 3.2: Clear sky solar heating rates computed from the 249 band and 14 band version of a two-stream broadband model. The solar zenith angle is 10 degrees.

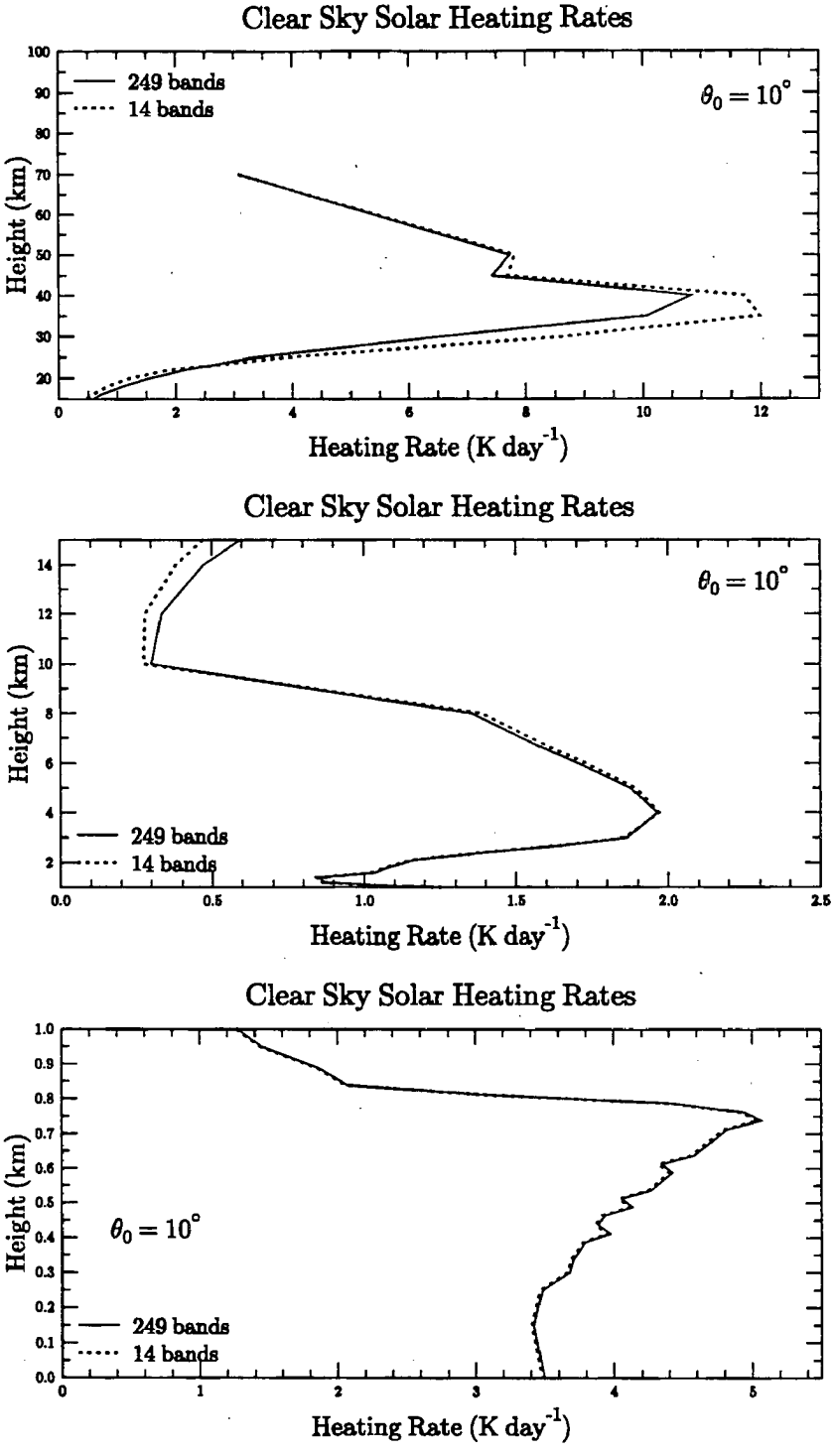

Figure 3.2: Clear sky solar heating rates computed from the 249 band and 14 band version of a two-stream broadband model. The solar zenith angle is 10 degrees.

one kilometer), the clear sky heating rates are almost identical (less than 0.03 K day^{-1}). The difference in the net flux convergence in the lowest 14 km is only 0.2 W m^{-2} (163.2 W m^{-2} in the 249 band model versus 163.0 W m^{-2} in the 14 band model).

For cloudy skies, the accuracy of the reduced band model depends on the choice of the frequency used to represent the bands. The choice of frequency should be such that the optical properties of the cloud droplets calculated for that frequency match the means of the optical properties calculated for the entire band. Initially, the optical properties for each band were chosen by arithmetically averaging the refractive index of liquid water across each band and using the arithmetic mean of the band wavenumber as input for the Mie code. Figure 3.3a shows the heating rates for a typical marine stratocumulus cloud using this method to determine the optical properties for each band. The cloud modeled in Figure 3.3a is a composite of a cloud simulated in the RAMS 7 July 1987 control run. (See Chapter 4 for more details about the RAMS simulations.) The model cloud extends from 812 m to 362 m and is divided into 18 layers. The extinction for each layer was calculated from the mean extinction computed from a two dimensional cross section of the control run. The mean optical depth of the cloud is roughly 7.4.

The droplet distributions used in Figure 3.3 was a modified gamma distribution Flatau et al. (1989):

$$n(r)dr = \frac{N_t}{\Gamma(\alpha)} \left(\frac{r}{r_n}\right)^{\alpha-1} \exp\left(-\frac{r}{r_n}\right) d\left(\frac{r}{r_n}\right) \tag{3.18}$$

The size bins of the explicit microphysical model used in the RAMS simulations were each divided in half, and the resulting bins were used in the scattering calculations. This division produced fifty radius bins ranging from roughly 1.8 microns to 500 microns. The parameter α was determined from the average α determined from the droplet data from the RAMS control run and is a function of the mean radius and effective radius of the distribution (see Flatau et al. (1989) for details).

The values of the other variables in the modified gamma distribution (r, r_n, and N_t) were set such that the effective radius at each level in the cloud varied linearly from 13

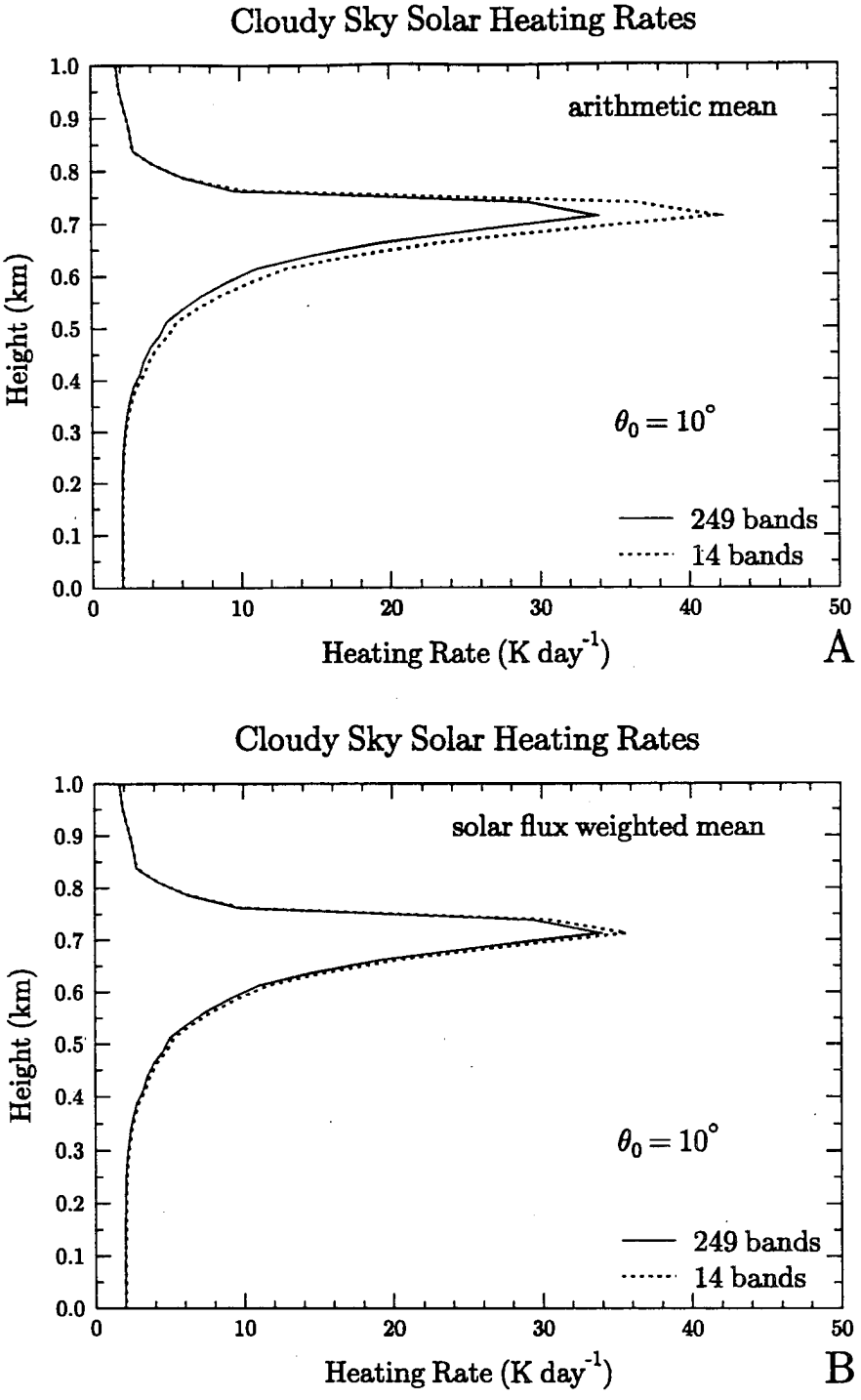

Figure 3.3: The top figure (A) computes the solar heating rates in a marine stratocumulus cloud using cloud optical properties derived from the each band's mean refractive index. The bottom figure (B) computes the solar heating rates using the cloud optical properties corresponding to the wavenumber within the band that most closely matches the solar flux weighted mean cloud optical properties of the band.

microns at cloud top to 4 microns at cloud base. This profile of effective radius roughly matches that found in the RAMS simulation. The total number concentration N_t was adjusted to match the computed extinction coefficient at each level.

The optical properties computed from the arithmetic mean refractive indices produced too much absorption in the cloud. The net flux convergence measured in the 14 band model was 19 percent larger than in the 249 band model. The method was not adequate since the optical properties of the cloud at a particular wavenumber are a function of more than just refractive index. The wavenumber itself and the effective radius of the droplet distribution also affect the cloud optical properties, making the single scattering albedo and asymmetry factor a rapidly varying function of wavenumber (Figure 3.4). The spectral distribution of the downward solar flux at the cloud top also helps to determine the amount of absorption and transmission inside the cloud for each band.

Instead of the arithmetic mean of the refractive index, another criterion was used to choose a representative frequency for each band. The downward flux at cloud top and the single scattering albedos for a set of modified gamma distributions with effective radii ranging from 4 μm to 13 μm were calculated for the each of the 249 bands. The solar flux and single scattering albedo data were then used to calculate a set of solar flux-weighted mean single scattering albedos for the 14 band model:

$$\tilde{\omega}_{ave} = \frac{\sum_{\nu_1}^{\nu_2} k(\nu)F(\nu)d\nu}{\sum_{\nu_1}^{\nu_2} F(\nu)d\nu} \tag{3.19}$$

These weighted single scattering albedos were then compared with the higher resolution single scattering albedo data to find the wavenumbers within each band where the single scattering albedo at that frequency match the weighted mean single scattering albedos. The wavenumbers and their corresponding refractive indices were then used to characterize each of the 14 bands. The heating rates computed using the new method are shown in Figure 3.3b. The differences in the cloud's maximum heating rate and its net flux convergence were reduced to 5.0 percent. Even this method produced some error since the changes in single scattering albedo are so rapid in the near infrared region, and no single

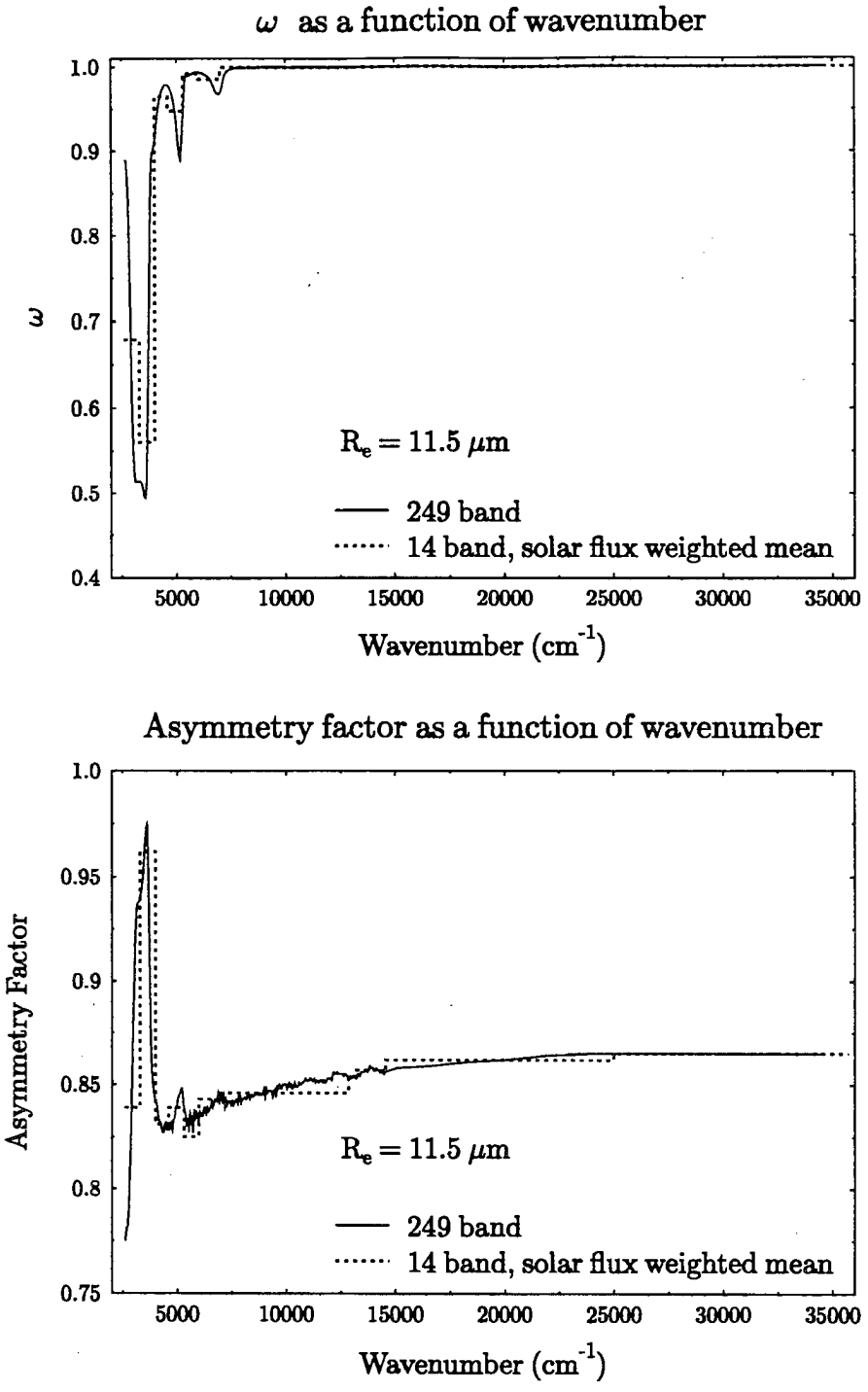

Figure 3.4: The single scattering albedo and asymmetry factor for a droplet distribution with an R_e of 11.5 μm as a function of wavenumber. The solid curve shows the values computed for the 249 band model, and the dashed curve shows the values computed for the 14 band model.

wavenumber for most bands could match both the solar flux averaged single scattering albedo and asymmetry factor.

The differences in the heating rates and cloud absorptivity are smaller for thinner clouds and larger for thicker clouds. The difference in the cloud's net flux convergence when the optical depth was reduced to 0.25 times its original value (1.85) was 1.9 percent, and the difference for a cloud with an optical depth four times larger (30) was 7.7 percent. The differences in heating rates were fairly insensitive to solar zenith angle and increased by only a couple percent compared to the $\theta_0 = 10°$ cases. However, given the sensitivity of the cloud's optical properties to wavenumber, it seems unlikely that the number of bands can be reduced any further for thick boundary layer clouds without sacrificing accuracy in the broadband solar heating rates. Since the changes in the heating rates computed in Chapter 5 resulting from changes in cloud microphysics are also on the order of 5 percent, the accuracy of the reduced band model with respect to heating rate calculations is barely adequate.

The cloud top solar albedos computed in the 14 band model were nearly identical to the 249 band model. The differences in albedo, measured as the ratio between the upward and downward fluxes at cloud top, changed less than 0.4 percent for all three optical depths for solar zenith angles ranging from 10 degrees to 75 degrees. Since the differences in cloud albedo produced by changes in the cloud's microphysics and macrophysics in Chapter 5 are on the order of 2 to 10 percent, further reduction of the number of bands was likely to make the accuracy of the albedo calculations too poor for the purpose of comparing these albedo differences.

The solar flux weighted mean method of determining the characteristic wavenumber for each band is tuned to this composite cloud, but it is likely that the results for the SHSG simulations will be similar. The wavenumbers that produced single scattering albedos to match the solar flux-weighted single scattering albedos generally did not change more than a few cm^{-1} across the range of droplet distribution sizes.

3.4.2 Reduction of k distribution weights

In order to reduce the total number of calculations further, the number of k-value weights were reduced by averaging the weights over the k domain. Chou (1986) reported that reducing the number of k's to ten produced differences in the clear sky heating rates of less than a few percent compared to line by line calculations.

The weights in the k distribution data were averaged uniformly across the k domain and 12, 9 and 7 weight data sets were produced. In a series of tests, the reduced k data sets were run in the 14 band two-stream model for the McClatchey et al. (1972) middle latitude clear sky profile and compared to the 37 weight model. The differences in the heating/cooling rates near the surface (0 - 10 km) from 37 weight model were roughly 0.3 K day^{-1} for the 7 weight model, 0.1 K day^{-1} for the 9 weight model and 0.02 K day^{-1} for the 12 weight model. Several different averagings of the weights across the k domain were also tested, but the uniform averaging provided the best overall results.

Figure 3.5 includes results of twelve weight, nine weight and seven weight data versus the original 37 weight data for a clear sky and a cloudy sky case. The clear sky case used the McClatchey et al. mid-latitude summer profile while the cloudy case used the same profile plus a one kilometer thick stratocumulus cloud (cloud base at one kilometer) based on data taken from the FIRE tethered balloon (Duda et al., 1991). The solar zenith angle was 45 degrees and the surface albedo was 0.20.

The maximum differences in the heating rates (in the lowest 25 kilometers) and downward solar radiation at the surface from the 37 weight case are shown in the table below:

Table 3.3: Maximum differences from the 37 weight case in the heating/cooling rates (K day^{-1}) and downward solar flux at the surface (W m^{-2}).

	CLEAR SKY		CLOUDY SKY	
	9 weight	12 weight	9 weight	12 weight
SW heating	0.10	0.028	0.12	0.07 (in cloud)
Flux at sfc.	2.59	0.99	0.19	0.15

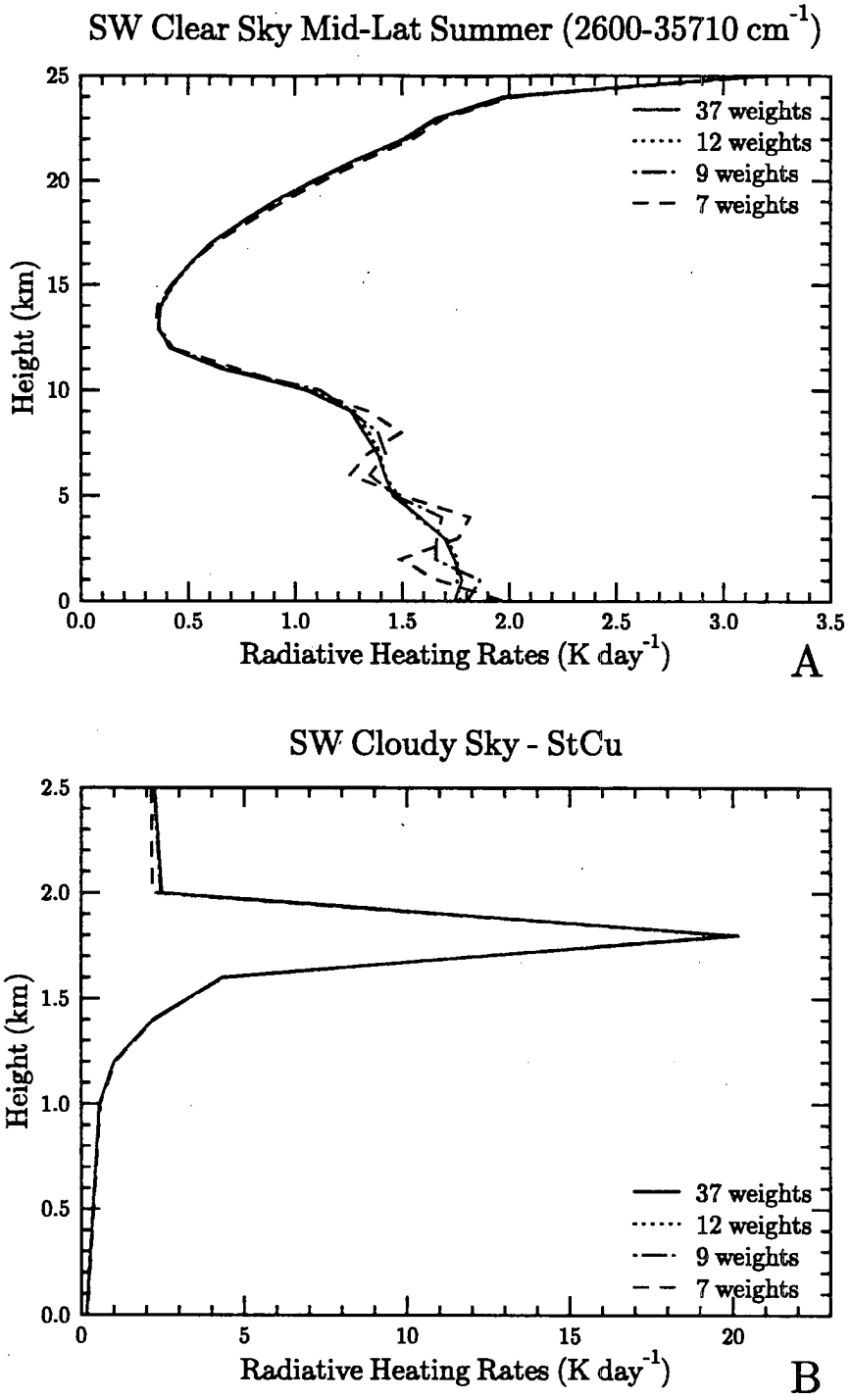

Figure 3.5: The top figure (A) shows the clear sky solar heating rates computed from the 14 band model using different numbers of k distribution weights. The bottom figure (B) shows a similar set of calculations of the heating rates in a marine stratocumulus cloud.

The downward solar flux at the surface in the clear sky case (37 weights) was 748.41 W m^{-2} and 135.02 W m^{-2} in the cloudy sky case. Note that in the cloudy sky case, the solar heating rates were nearly identical inside the cloud. Thus, averaging the weights across the k-value domain results in a large reduction in the total number of radiative transfer calculations without decreasing the accuracy of the model. The cloud top albedo computations are also nearly identical to the 37 weight model.

The nine weight model was chosen to be used in the SHSG broadband calculations since it had nearly identical results to the 37 weight model. In the domain of the SHSG model, tests of the two-stream model in a typical marine stratocumulus cloud show that the model produced relative errors in the broadband solar heating rates of less than ten percent for a wide range of solar zenith angles and optical depths. For solar albedo calculations, the absolute differences between the full 249 band, 37 weight model and the 14 band, 9 weight model were less than 0.5 percent. This reduced band and weight model thus provides adequate accuracy for the calculation of albedo differences in the RAMS model clouds presented in Chapter 5, with a substantial reduction in the required number of radiative transfer computations.

3.5 Implementation of SHSG into broadband model

Once the final form of the k distribution and ozone cross section data was determined and the scaled broadband optical properties were computed, the SHSG model (or any other monochromatic radiative transfer code) could be easily placed into the framework of the broadband model. However, some complications resulting from the incorporation of the 2D model into the k distribution method had to be eliminated before broadband calculations could be started.

In the k distribution method some of the radiative transfer calculations involve large k-values. Under these conditions, gas absorption dominates the radiative transfer. The optical depth of the gas becomes extremely large, and the extinction coefficients in the model can reach the order of 1.0E+05 km^{-1}. Since the single scattering albedo of the medium is calculated as an optical depth-weighted average of the albedos of the cloud

droplets, Rayleigh scattering and the gases, for large k-values the single scattering albedo of the medium approaches zero. Both the large extinction and the low single scattering albedo create problems for the SHSG method. In areas of the model grid where the single scattering albedo is very small, the approximations produced by the model's spatial discretization become magnified as the flux in the medium approaches zero. As a result, negative fluxes may be calculated.

Even in a relatively conservatively scattering atmosphere, the large extinction associated with large k-values slows the computation of the radiative fluxes. In order to accurately compute the spatial derivatives in radiative transfer equation, the optical depth per grid cell should be no more than unity (Evans, 1993). As the k-value increases, the number of grid cells necessary for accurate calculations can quickly become extremely large, and the calculations become extremely slow. For the largest k-values, the calculations become impossibly large for the computer to solve.

Fortunately, the problems at large k-values are compensated by several factors. The weights corresponding to the k-values are small, even for the strongest absorbing bands. Also, the horizontal inhomogeneity of the clouds becomes overwhelmed by the homogeneous nature of the gas. At sufficiently large k-values the radiative transfer essentially becomes plane parallel and one dimensional models can be used. In fact, since the gaseous absorption becomes so strong at high k-values, the radiative transfer can be adequately approximated by the Beer-Bouget-Lambert law. Finally, and perhaps most importantly for calculations in the lower atmosphere, in many of the calculations with the largest k-values all of the downward flux is absorbed in the upper atmosphere before reaching cloud top. This eliminates many of the troublesome k-value calculations in the case of low lying marine stratocumulus.

A series of two-stream calculations were run in order to determine under what conditions the direct beam solution may be accurate. For the calculations a vertically homogeneous, ten layer cloud was used. The model was run for a range of total optical depths (τ) from 0.001 to 1000 and for single scattering albedos ($\tilde{\omega}$) from 0.001 to 1. Five cases were run using different values for surface albedo, asymmetry factor (g) and solar zenith angle (θ_0). Table 3.4 shows the values used in each run.

Table 3.4: Values of optical variables used in two-stream direct beam test.

Case	asymmetry factor	surface albedo	solar zenith angle
1	0.85	0.20	45°
2	0.70	0.20	45°
3	0.85	0.05	45°
4	0.85	0.20	10°
5	0.85	0.20	75°

For each radiative transfer calculation, the downward diffuse flux at each level in the model was compared with the total downward flux at the same level. The maximum value of the diffuse downward flux relative to the total downward flux is plotted in Figure 3.6 as a function of τ and $\tilde{\omega}$ for Case 1. As τ increases, more of the downward flux becomes diffuse. Only at very small values of $\tilde{\omega}$ does the fraction of diffuse flux reach an asymptotic limit. However, when τ is large, the total downward flux also becomes small inside the cloud and the direct beam solution may still be sufficiently accurate even though all of transmitted flux is diffuse. A better way to compare the direct beam solution to the full solution is to compare the downward diffuse (and upward) fluxes with the incident flux at the top of the model. Figures 3.7 and 3.8 show the maximum diffuse downward flux and maximum upward flux in the model as a fraction of the total incident downward flux, respectively, as a function of τ and $\tilde{\omega}$.

From Figure 3.7, when $\tilde{\omega} \ll 1$ or τ is very small or very large, the downward diffuse flux tends to be small (for small τ almost all of the flux is directly transmitted and for large τ it is absorbed) compared to the incident flux. The downward diffuse flux is usually largest relative to the incident flux at moderate optical depths, when $1 \leq \tau \leq 10$. (One exception is when τ is large and $\tilde{\omega}$ approaches 1.) From Figure 3.7, the maximum downward diffuse flux is 5% of the incident flux at moderate τ's when $\tilde{\omega} \approx 0.15$. Considering the magnitude of the weights associated with the large k-values (less than 10 percent), the errors introduced by the direct beam solution when $\tilde{\omega}$ is smaller than 0.15 will be negligible in the broadband calculations.

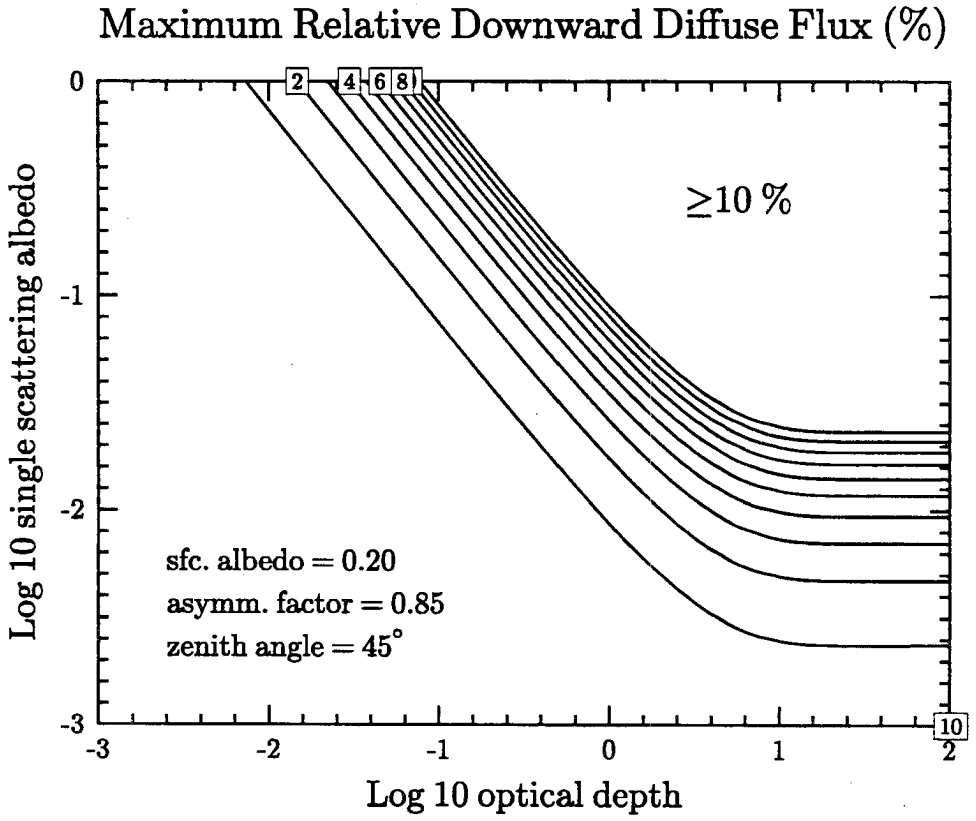

Figure 3.6: The maximum value of the downward diffuse flux as compared the the total downward flux at any level of a cloud layer as a function of the cloud's τ and $\tilde{\omega}$. The surface albedo was 0.20, the asymmetry factor was 0.85 and the solar zenith angle was 45°.

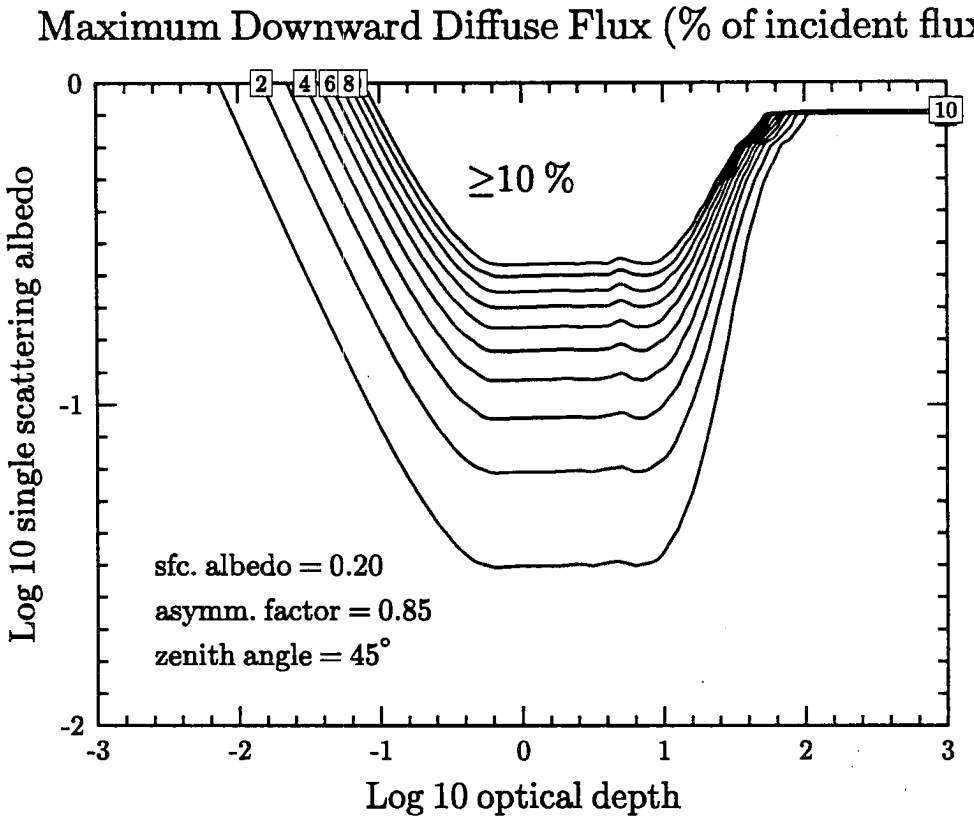

Figure 3.7: The maximum value of the downward diffuse flux in a cloud compared to the incident downward flux as a function of cloud τ and $\tilde{\omega}$. The surface albedo was 0.20, the asymmetry factor was 0.85 and the solar zenith angle was 45°.

Figure 3.8 shows that when the optical depth is small ($\tau < .1$), the maximum upward diffuse flux relative to the incident flux asymptotes toward the surface albedo value (in this case twenty percent). When the optical depth is large ($\tau > 5$) and $\tilde{\omega} \ll 1$, the upward flux in the model becomes small compared to the incident flux. In Figure 3.8, the maximum upward flux at large τ's is 5% of the incident flux when $\tilde{\omega} \approx 0.63$.

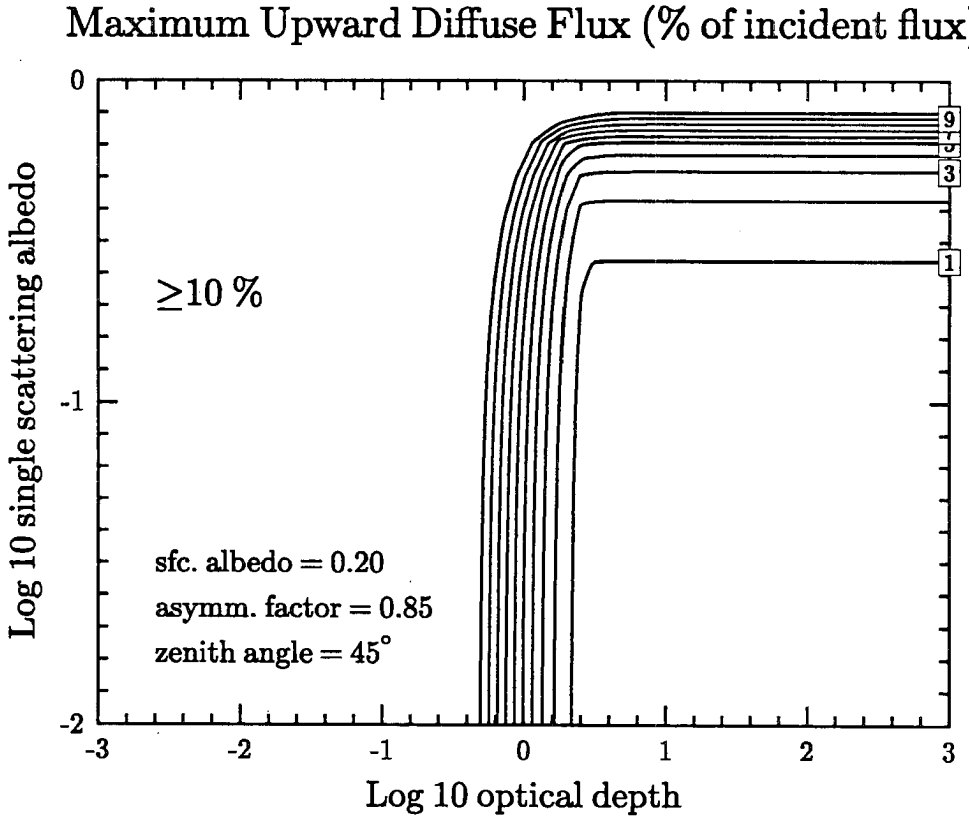

Figure 3.8: The maximum value of the upward diffuse flux in a cloud compared to the incident downward flux as a function of cloud τ and $\tilde{\omega}$. The surface albedo was 0.20, the asymmetry factor was 0.85 and the solar zenith angle was 45°.

Figures 3.7 and 3.8 show results for Case 1. The values plotted in Figure 3.7 are insensitive to changes in asymmetry factor and surface albedo, but are sensitive to changes in solar zenith angle. In Case 5, when $\theta_0 = 75°$, the maximum downward diffuse flux is

5% of the incident flux when $\tilde{\omega} \approx 0.105$. The values in Figure 3.8 are sensitive to changes in surface albedo when τ is small, but they are insensitive when τ becomes large. The values in Figure 3.8 are also sensitive to changes in asymmetry factor and solar zenith angle. At large values of optical depth, the 5% line in Case 3 (when g = 0.70) occurs at $\tilde{\omega} \approx 0.47$ and in Case 5 (when $\theta_0 = 75°$) it occurs at $\tilde{\omega} \approx 0.35$.

Most of the radiative transfer calculations in the following chapters are done in atmospheres with moderate optical depths, that is, when $1 \leq \tau \leq 10$. The results from the two-stream tests suggest a threshold of $\tilde{\omega} = 0.1$ is needed to keep the flux errors from the direct beam solution to less than 5 percent. This is a conservative estimate since for all radiative transfer computations involving large k-values the associated weight is generally very small (much less than 10 percent). Also the bands that contain the largest k-values contain only a small fraction of the total downward flux at cloud top. This is fortunate since the combination of large optical depths and low single scattering albedos requires the resolution of the SHSG internal grid to be so fine that the memory capacity of the largest available computer (roughly 120 megabytes) was exceeded when the optical depths were greater than 100 and the single scattering albedo was less than 0.50. In another test using the two-stream model, all of the radiative transfer computations where the full 2D model could not be used were not made, and the results were compared to the regular two-stream model with all k-value computations. The differences in the fluxes throughout the cloud were negligible, and the differences in the heating rates at any point in the cloud were less than 0.01 percent. This allowed a substantial number of computations to be eliminated, and as a result only 92 monochromatic calculations were necessary to simulate broadband solar fluxes.

3.6 Summary

This chapter describes the SHSG broadband model and modifications used to reduce the total number of radiative transfer calculations. By reducing the number of bands and k distribution weights, the number of radiative transfer computations necessary for broadband solar flux and heating rate calculations was reduced from over 12,400 to almost

200 while maintaining adequate accuracy (0.5 percent) for the computation of solar albedo. Of the remaining computations, several can be approximated by the direct beam solution (or for low altitude marine stratus they can be neglected) without any decrease in accuracy, since most of the radiation in the strongest absorbing bands has already been absorbed before reaching the top of the cloud. As a result, broadband solar computations can be accurately completed in a fairly reasonable amount of time.

Chapter 4

RAMS-DERIVED MICROPHYSICAL DATA

The two previous chapters describe the radiative transfer model used to make monochromatic radiance and broadband flux calculations in a two dimensional atmosphere. In order to simulate the radiative transfer in a marine stratocumulus cloud or any other atmospheric medium, a source of optical property data for the entire two dimensional domain must be used. This chapter describes the three dimensional dynamical model used to generate the optical property data in this dissertation. A series of model runs designed to study the impact of cloud condensation nuclei (CCN) concentrations on the cloud optical properties is also presented and discussed.

4.1 Description of LES-EM model

Near simultaneous observations of the physical properties of an entire cloud system are difficult to collect and presently can only be obtained by remote sensing techniques (*ie.*, from radar data). Alternatively, microphysical data from a marine stratus cloud can be simulated by using a detailed numerical model. The microphysical data used in this study were provided by the second method. Although the simulations from even the most sophisticated model are only approximations of actual clouds, one advantage of numerical models over radar data is the ability to control the external conditions in the boundary layer. A relevant example for this study is that numerical models allow for an investigation into the effects of CCN concentration on boundary layer clouds independent of other effects.

4.1.1 RAMS dynamical model

The Regional Atmospheric Modeling System (RAMS) developed at Colorado State University was used to provide the microphysical data in this research. RAMS is a multi-purpose modeling system and was set up as a fully compressible large eddy simulation (LES) model. The horizontal grid resolution in the model is 55 meters and the vertical resolution is 25 meters. This fine-scale grid spacing allows the model to resolve the major energy-containing eddies explicitly, and provides a sophisticated numerical simulation of a stratocumulus cloud. Since Pielke et al. (1992) describe RAMS in detail and Stevens et al. (1994) present the coupled LES/explicit microphysics version of the model, only a brief overview of the LES model is presented in this dissertation. Since RAMS is represented spatially on a discrete grid, the results from the dynamical model can be easily incorporated into the SHSG model.

RAMS is an Eulerian model that contains prognostic equations for several variables. They include the momentum equation for a rotating fluid under the Boussinesq approximation for the three velocity components (u, v, w), and equations for liquid water potential temperature (θ_l), perturbation Exner function π, and total water mixing ratio r_t (the sum of vapor and liquid water mixing ratios). The version of RAMS used to generate the microphysical data includes an explicit cloud microphysics model (Tzivion et al., 1987) in order to model the effects of changing CCN concentrations. Unlike the bulk microphysics scheme used in previous versions of RAMS, the explicit microphysics (EM) model predicts the condensate in the cloud using a twenty five size bin spectrum and diagnoses the liquid water mixing ratio r_l as the sum of the mixing ratios in each bin. Prognostic equations are also required for each of these bins for both droplet mass and number mixing ratio. More details of the explicit microphysics model are presented below.

The water vapor mixing ratio r_v is diagnosed as the difference between the total mixing rate r_t and the liquid water mixing ratio r_l. Temperature T is diagnosed from the prognostic variables θ_l and r_l, while the cloud supersaturation S is calculated from:

$$S = \frac{r_v}{r_s(T)} - 1 = \frac{r_t - r_l}{r_s(T)} - 1, \tag{4.1}$$

where $r_s(T)$ is the saturation mixing ratio calculated from the diagnosed temperature T. The supersaturation calculation, a necessary input for the explicit microphysics model, was found to be numerically stable for a model time step of two seconds (Cotton et al., 1992).

The advection of microphysical variables in RAMS was also modified from previous versions of the model. Various time differencing schemes were used depending on the nature of the advected variable. Vector quantities (u, v, w) are advected using a fourth order leap-frog method, while liquid water substances and other scalar quantities are advected using a positive definite, sixth order forward differencing scheme. A flux corrected transport (FCT) method with peak preservers was used to eliminate false oscillations in the prognostic variables (such as supersaturation) when they are advected across sharp gradients, especially at cloud top. (See Stevens et al. (1994) for a description of the time differencing methods.) Due to the large mean winds in the simulations, the domain was subjected to a Galilean transform to maintain numerical stability.

An error was recently found in the dynamical model which affected the results of the simulations presented in this chapter (Stevens, personal communication). The subsidence imposed on the boundary layer was found to not be in balance with the dynamics of the model, resulting in an evacuation of mass throughout the boundary layer. The loss of mass was manifested in the model as an additional cooling term which slowly cooled the entire boundary layer, increased the temperature gradient between the ocean and the lowest model levels, and increased the strength of the circulation and the moisture fluxes in the boundary layer. The clouds produced by the model are therefore slightly thicker and more heterogeneous than expected. Despite this shortcoming, the model clouds presented are still very similar to those measured during FIRE and the utility of the model data was deemed to be unaffected by this problem.

The model includes the radiation parameterization developed by Chen and Cotton (1983) to compute longwave and shortwave radiative flux divergence, and the dynamical model includes explicit feedback of bulk cloud properties on radiative heating and cooling. Sub-grid scale diffusion is parameterized using a stability-modified Smagorinsky diffusional

scheme. Since the grid scale of the model was chosen to fall in the inertial range, the model is fairly insensitive to the details of the sub-grid parameterization. The lower boundary condition is based on the Louis (1979) surface layer parameterization. The top boundary is a rigid lid with Rayleigh friction in the upper seven model layers. Lateral boundary conditions in the dynamical model are cyclic, like in the SHSG model.

4.1.2 Explicit microphysics (EM) model

The explicit microphysical model used in RAMS is an accurate moment-conserving scheme developed by the Tel-Aviv University Cloud Physics Group. The model uses a two-moment solution of the stochastic collection equation (SCE) to compute the evolution of a droplet spectrum. Closure in the SCE is achieved with the aid of a dimensionless parameter connecting neighboring moments. The two-moment solution conserves both liquid water content and number concentration. Tzivion et al. (1987) have demonstrated that the model is as accurate as models that predict only mass concentration in each bin, but requires two to three times fewer bins. For the simulations of stratocumulus, the droplet spectrum is divided into twenty-five bins ranging from 1.56 to 504 microns in radius, with mass doubling between adjacent bins (Table 4.1).

Table 4.1: RAMS explicit microphysics model bin number, droplet radius, and mass.

Bin number	Radius (μm)	Mass (μg)	Bin number	Radius (μm)	Mass (μg)
0	1.56	1.6×10^{-5}	13	31.50	0.13
1	1.97	3.2×10^{-5}	14	39.69	0.26
2	2.48	6.4×10^{-5}	15	50.01	0.52
3	3.13	1.3×10^{-4}	16	63.00	1.05
4	3.94	2.6×10^{-4}	17	79.38	2.09
5	4.96	5.1×10^{-4}	18	100.01	4.19
6	6.25	1.0×10^{-3}	19	126.00	8.38
7	7.88	2.0×10^{-3}	20	158.75	16.76
8	9.92	4.1×10^{-3}	21	200.02	33.52
9	12.50	8.2×10^{-3}	22	252.00	67.03
10	15.75	1.6×10^{-2}	23	317.50	134.07
11	19.85	3.3×10^{-2}	24	400.03	268.13
12	25.00	6.5×10^{-2}	25	504.00	536.27

The microphysical processes affecting the droplet spectrum are droplet activation from CCN, condensation/evaporation, collision/coalescence, and sedimentation. Since the clouds simulated in the model produce only light amounts of drizzle, the size ranges specified in Table 4.1 should be adequate to model the droplet distributions in the cloud, and drop breakup is not considered.

A droplet activation scheme was developed in order to couple the explicit microphysics model with the dynamical model. The CCN were divided into six bins based on their observed activation supersaturation (see Table 4.2). An advantage of this supersaturation space representation of the CCN spectrum is that no assumptions about the aerosol composition of the initial CCN spectrum need to be made if it is initialized from observations.

Table 4.2: Activation characteristics of the CCN distribution. For $S > S_k$ all the CCN in bins $j > k$ will be activated. Parameters match observational data of Hudson and Frisbee (1991), and $C_0 = 121$ cm^{-3}.

k	S_k (%)	S_{k+1} (%)	$\overline{C}_k(t_0)/C_0$
1	1.00	2.00	0.1072
2	0.60	1.00	0.1274
3	0.30	0.60	0.2049
4	0.10	0.30	0.3083
5	0.02	0.10	0.2654
6	0.00	0.02	0.0940

The nucleation scheme is a generalized version of the Twomey (1959) formula ($N_a = CS^\kappa$):

$$N_a = \overline{C}_j f(S) + \sum_{k=j+1}^{6} \overline{C}_k; \tag{4.2}$$

where

$$f(S) = \frac{\exp(\kappa \ln(S)) - \exp(\kappa \ln(S_j))}{\exp(\kappa \ln(S_{j+1})) - \exp(\kappa \ln(S_j))}. \tag{4.3}$$

which defines a fractional activation of droplets out of bin j. N_a is the number concentration mixing ratio of activated aerosol, and j is the bin which satisfies $S_j \leq S \leq S_{j+1}$. $\overline{C}_k$ is the number concentration mixing ratio of CCN in bin k. The CCN mixing ratios are

initialized by the formula:

$$\overline{C}_k(t=0) = C_0(\exp(\kappa \ln(S_{k+1})) - (\exp(\kappa \ln(S_k))), \tag{4.4}$$

where C_0 is the number of CCN that activate at 1% supersaturation. The empirical constant κ was represented as a function of S to better match the observed activation spectra in which κ changes with supersaturation. In the simulations κ is represented as:

$$\kappa(S) = a + b\ln(S); a = 0.2158, b = 0.0992. \tag{4.5}$$

to match the observations of Hudson and Frisbie (1991) for the spectra observed on 29 June 1987.

Since most of the CCN activate at radii below the smallest droplet radius, these aerosol are assumed to grow quickly enough to be placed in the first droplet bin by the end of the first time step (two seconds). This assumption is not unreasonable since such aerosol are well described by equilibrium theory and grow rapidly. For larger aerosol which activate directly into the droplet bin structure assumptions about aerosol composition are necessary. These aerosol are not likely to be in equilibrium with the ambient vapor pressure and their activation sizes are difficult to parameterize (Stevens et al., 1994). In the model, large CCN are assumed to be NaCl and are mapped to the droplet bins based on their 95% relative humidity equilibrium sizes. Simulations using a two dimensional version of RAMS did not show a sensitivity to this mapping. Aerosol regeneration (by evaporation of droplets) is parameterized statistically such that the aerosol distribution is returned toward its initial state and total aerosol number. However, the aerosol are also assumed to grow large enough that upon evaporation they are never returned to the first (smallest size) aerosol bin. Although this parameterization is crude, the favored regeneration of the largest CCN categories is consistent with observations.

4.2 CCN Concentration Effects on Cloud Properties

In the following sections, three simulations from RAMS are presented. In each simulation, the model configurations are identical except for the prescribed initial CCN field.

The first simulation, the control run, is modeled as representative of a typical marine cloud. The following simulations contain an additional source of CCN which is allowed to be entrained into the cloud layer. The second simulation contains a layer of enhanced CCN above cloud top, while the third simulation contains a layer near the surface.

4.2.1 Control run

Model configuration

The first model scenario was a control run that simulated the marine stratus measured during the FIRE-I experiment near San Nicholas Island on 7 July 1987. The setup of the model is as follows:

- The dynamical model was initialized using a composite atmospheric sounding derived from aircraft data measured near the island (Betts and Boers, 1990). The model fields (including θ_l, π, and r_t) were initially horizontally homogeneous with random perturbations of surface temperature not exceeding 0.1 K. Sea surface temperatures were set to 0.3 K greater than the initial air temperature at the lowest model level (289.3 K).

- The initial CCN field was horizontally homogeneous and matched to the measurements of Hudson and Frisbie (1991) taken in the FIRE observational area on 29 June 1987. Approximately 120 cm^{-3} nuclei activate at 1 % supersaturation.

- The model domain is 58 $\times$ 58 $\times$ 36 points in x, y, and z respectively. Due to the sixth order advection scheme six grid points in each horizontal direction are redundant. With cyclic boundary conditions this leads to a horizontal domain of 52 $\times$ 52.

- The horizontal grid spacing is 55 meters, while the vertical grid spacing is 25 meters below 900 m with vertical grid stretching of 10 to 20 % to the model top at 2250 m.

- The model start time is 15:30 local time on 7 July 1987.

The "spin up" of the model takes 60 minutes (of model time). During spin up, a more simple version of the model is used, including a four second time step, second order advection, the implicit bulk microphysics parameterization and radiation calculations every five minutes. The model then uses a two second time step, the more sophisticated fourth and sixth order advection schemes, the explicit microphysics model and radiation calculations every 60 seconds for the following 140 minutes of the simulation. As noted earlier, the model configuration in all three simulations was the same except for the initial CCN field.

Model fields

A three dimensional simulation is necessary for a proper representation of the turbulent eddies in the dynamical model. However, the radiative transfer calculations are too computationally intensive to produce an accurate three dimensional radiance field across the model domain. Instead, 2-D "slices" of the cloud field were used as input into the SHSG model. Figure 4.1 shows the liquid water path (LWP) field in the control run after 7260 seconds of simulation. Two cross sections through the cloud were sampled for radiative transfer calculations. The first cross section, labelled 1a, is an east-west section that passes through one of the liquid water path maxima. The second cross section (1b) runs north-south and passes through the edges of two LWP maxima and a region of low liquid water path. These cross sections were chosen for their relative heterogeneity and to emphasize the effects of cloud geometry in the radiative transfer simulations.

Figure 4.2 presents the liquid water content fields for both cross sections. For computational purposes, the vertical domain in the radiative transfer calculations the vertical domain was limited to the region from 812.5 m to 362.5 m above the ocean. This area contains most of the model cloud in all of the simulations. The general structure of both liquid water content fields is similar, with a minima in the middle of the domain surrounded by two maxima. The largest liquid water contents and the greatest horizontal variability appear in cross section 1b. Although both plots show horizontal variability throughout the model domain, it is important to note that both cross sections would be considered to be 100% overcast from current satellite cloud cover algorithms. Figure

4.3 shows the corresponding total droplet concentrations. The maximum droplet concentrations in both cross sections nearly match the initial CCN concentration of 120 cm^{-3}. The total droplet concentration is generally uniform throughout the depth of the cloud, although the concentrations are roughly 20 percent lower in the low LWP regions of the cloud.

Figure 4.4 shows the effective radius profile through the cross sections. Effective radius increases with height throughout the entire cloud, with values near 6 μm near cloud base and 11 μm near cloud top. The vertical velocity fields are shown in Figure 4.5. The regions of downdrafts appear to correlate well with areas of reduced liquid water contents, although the strongest updraft regions do not always match the areas with largest liquid water contents. Since the cross sections only provide a two dimensional snapshot of an evolving three dimensional medium, it is unlikely that the two fields would be exactly correlated.

Two additional cross sections from the control run are presented in Figures 4.6 through 4.9. The cross sections for Cases 1c and 1d were taken from the same location in the model domain as Cases 1a and 1b, respectively, but at a model time of 9000 seconds. The microphysical properties in these cross sections are similar to those in Cases 1a and 1b, although the depth of the clouds and the overall macrophysical structure of the clouds are different. The mean LWP in Cases 1a and 1b are 54.1 g m^{-2} and 70.2 g m^{-2} respectively, while the liquid water paths in Cases 1c and 1d are 44.8 g m^{-2} and 47.5 g m^{-2}. The standard deviation in LWP are also larger in the first two cross sections in the control runs. The standard deviations in Cases 1a and 1b are 39 g m^{-2} and 42 g m^{-2}, while in Cases 1c and 1d the standard deviations are only 24 g m^{-2} and 30 g m^{-2} respectively.

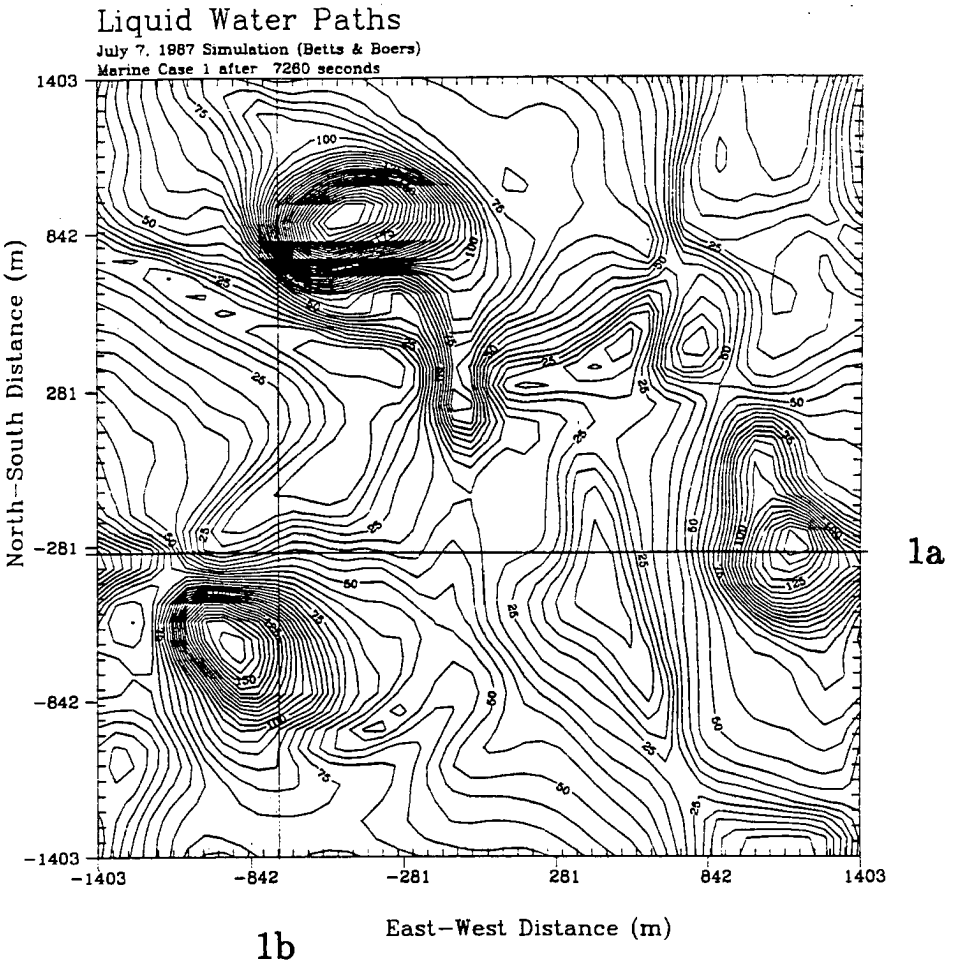

Figure 4.1: The liquid water path field for the RAMS control run after 7260 seconds. The east-west cross section is labeled 1a, and the north-south cross section is labeled 1b.

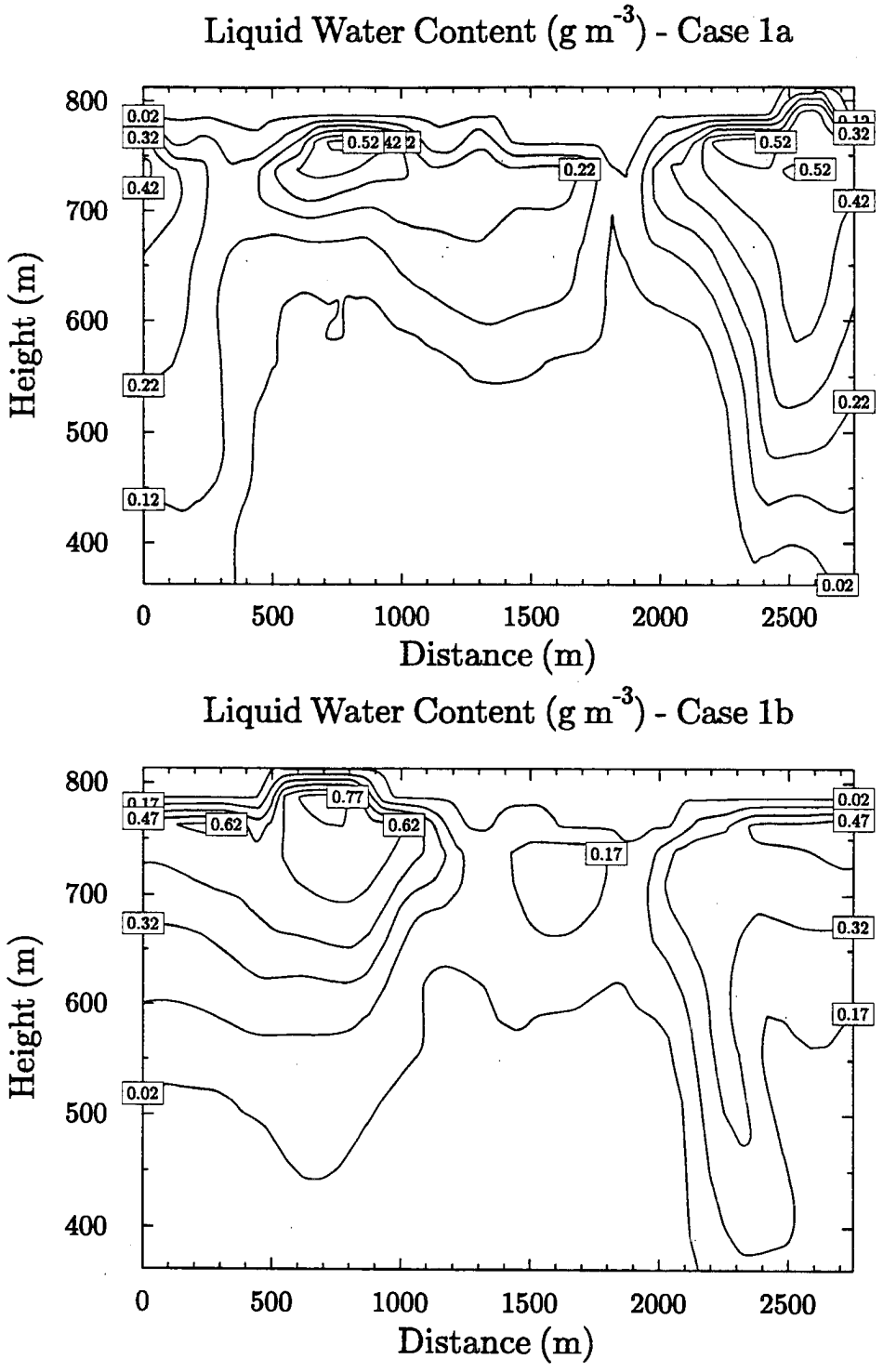

Figure 4.2: The liquid water content fields computed for cross sections 1a and 1b.

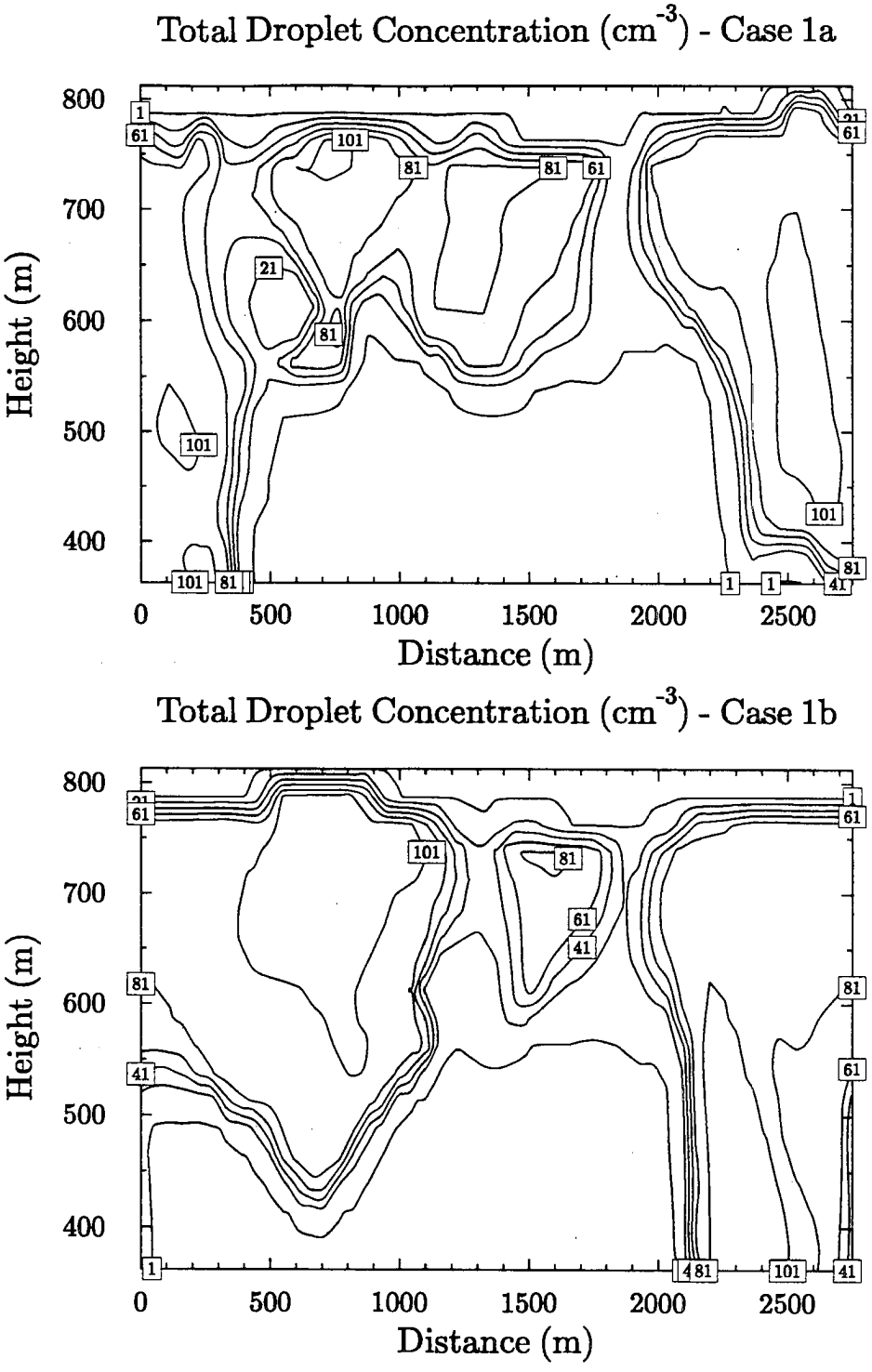

Figure 4.3: The total droplet concentration fields computed for cross sections 1a and 1b.

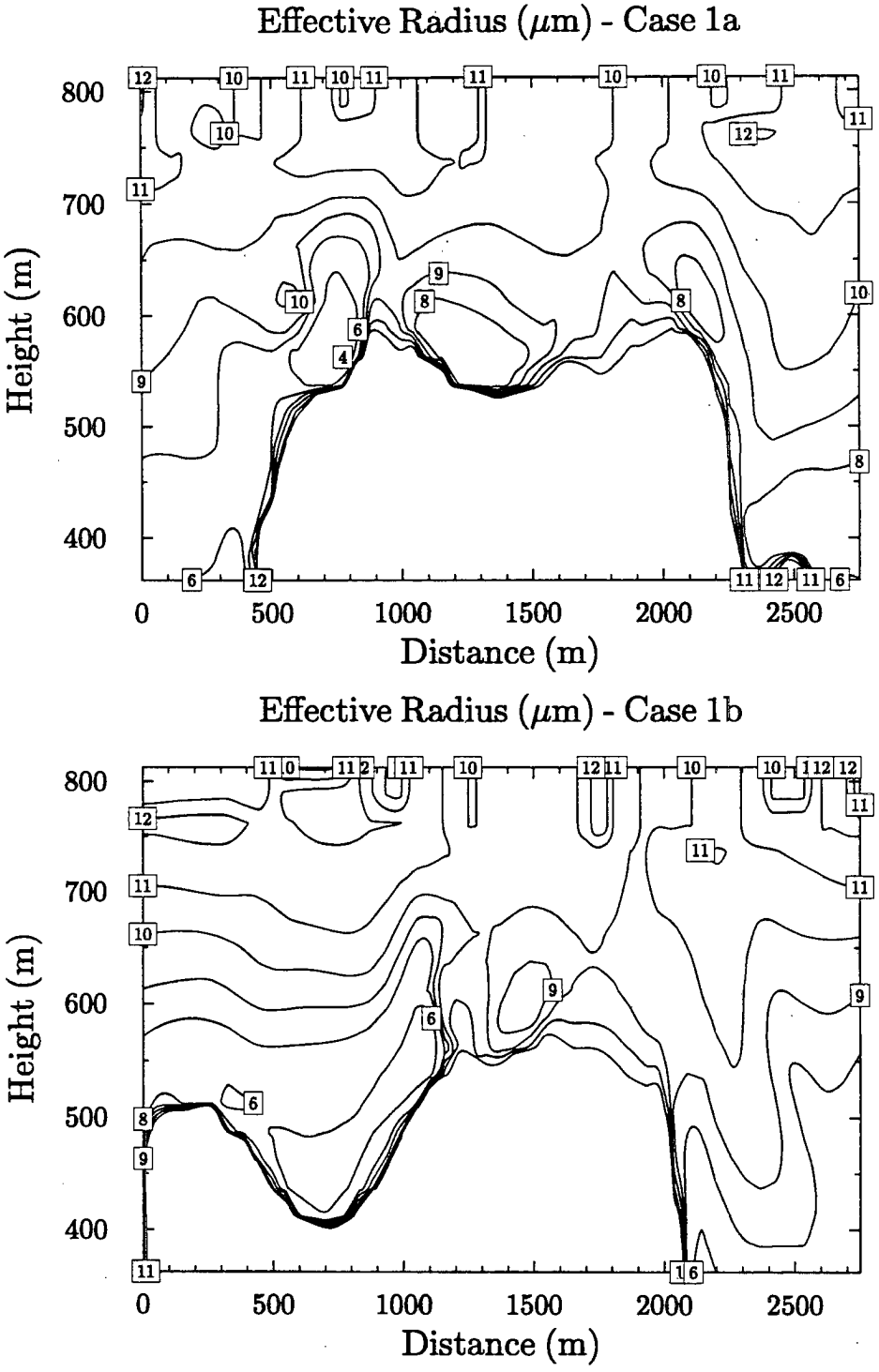

Figure 4.4: The effective radius fields computed for cross sections 1a and 1b.

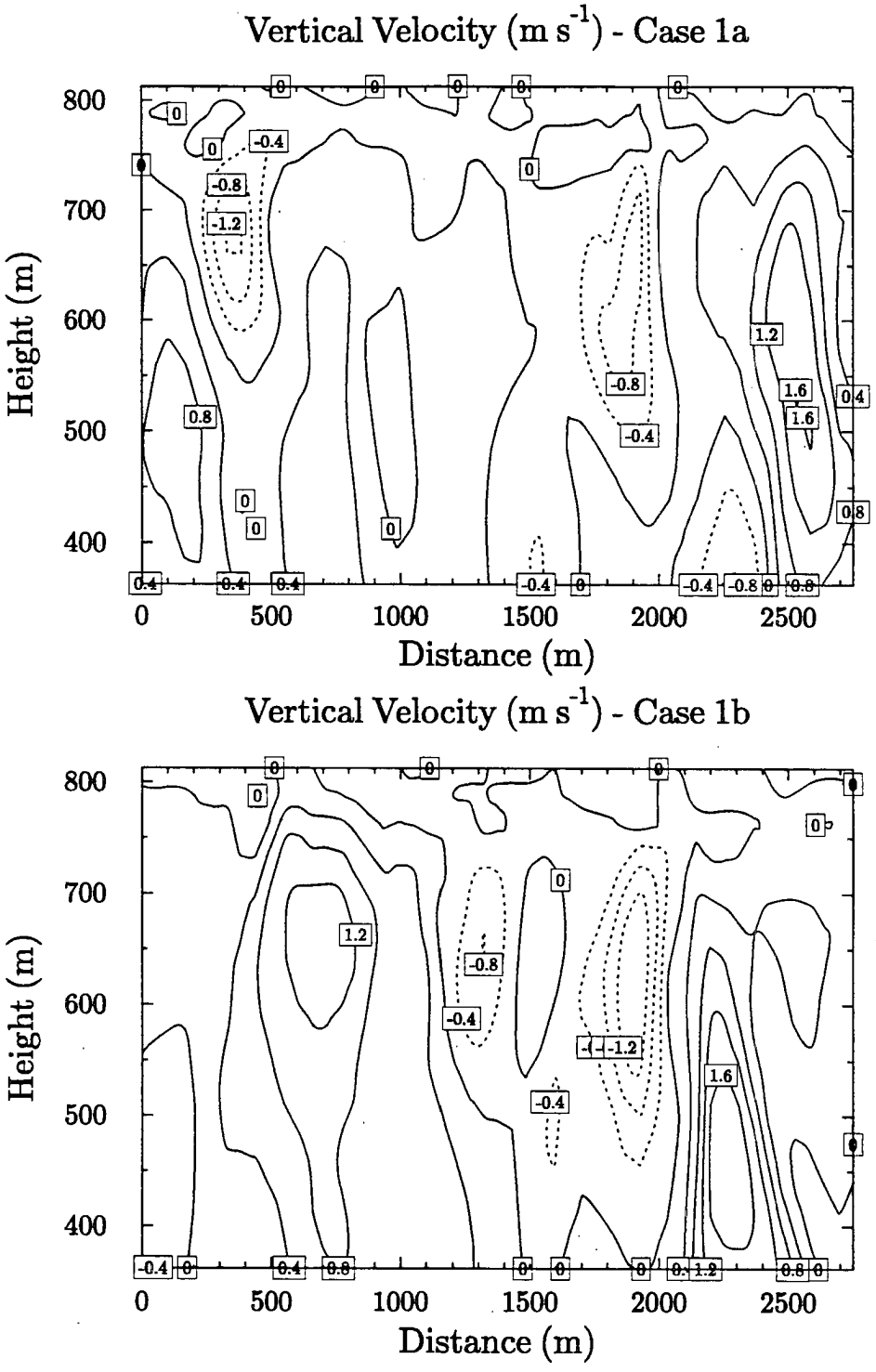

Figure 4.5: The vertical velocity fields computed for cross sections 1a and 1b.

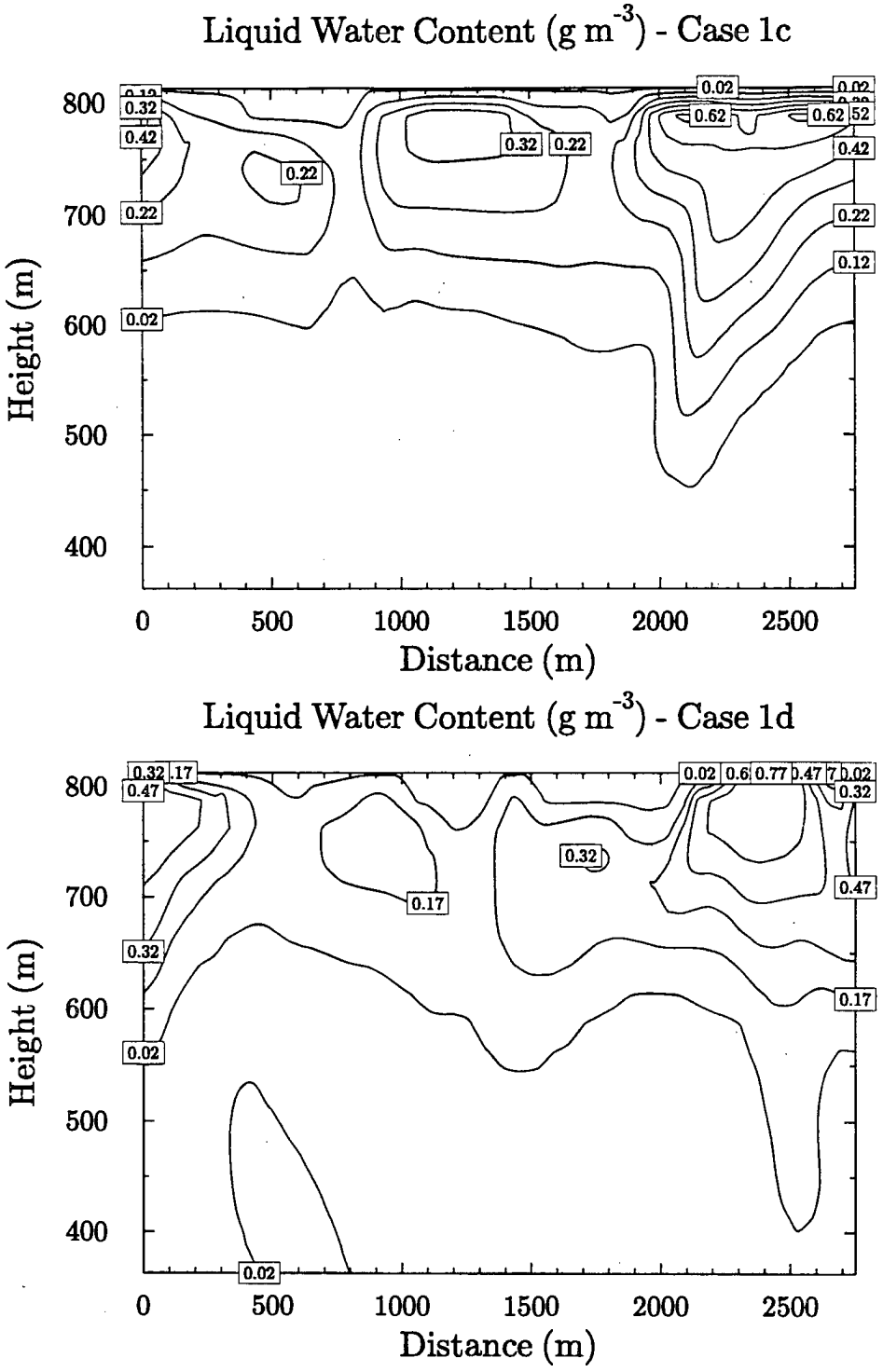

Figure 4.6: The liquid water content fields computed for cross sections 1c and 1d. These cross sections are at the same locations as cross sections 1a and 1b respectively, but at a model time of 9000 s.

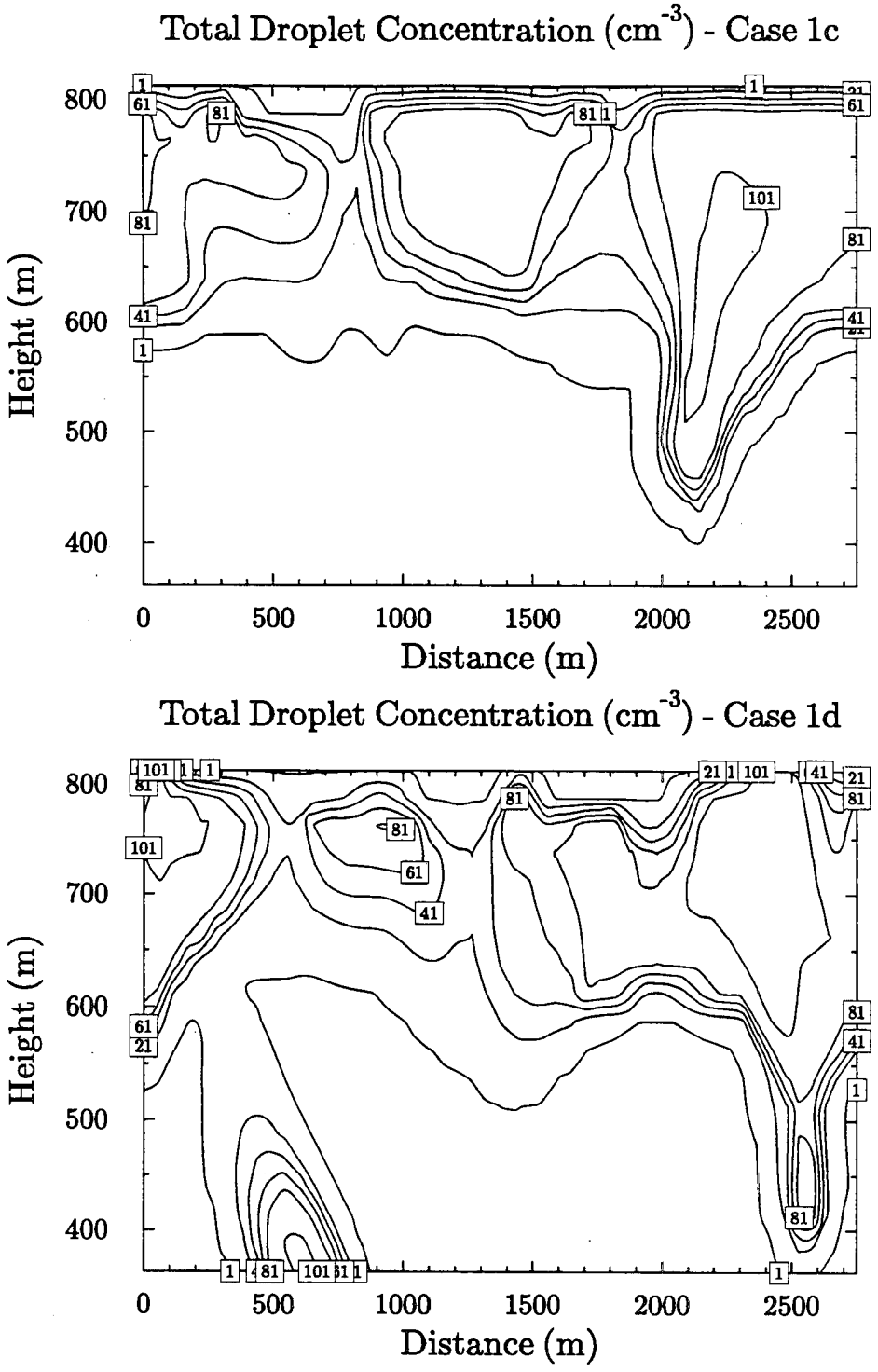

Figure 4.7: The same as Figure 4.6, but for the total droplet concentration fields.

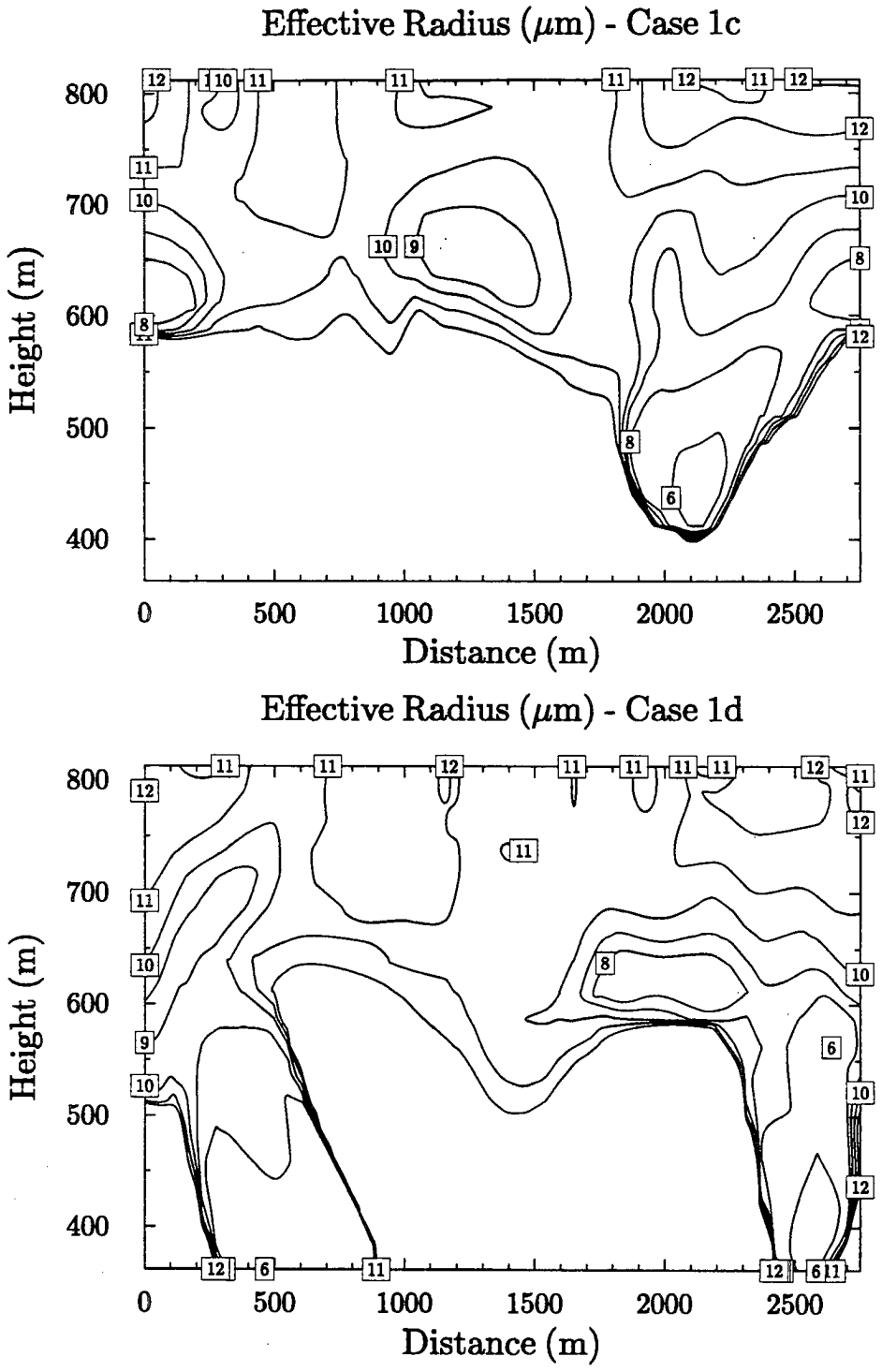

Figure 4.8: The same as Figure 4.6, but for the effective radius fields.

4.2.2 Enhanced CCN above cloud top

The second cloud simulation investigated the effects of enhanced CCN concentrations that are entrained from above the cloud layer. Enhanced concentrations of aerosol above cloud top have been observed in marine stratus off the coast of California (Hegg et al., 1990) and during ASTEX (Martin et al., 1994), and this experiment examines their possible impact on the cloud layer. The dynamical model was initialized identically to the control run, except that above the 296 K θ level (from approximately 900 m to the model top) the initial CCN concentrations were increased to six times the level in the control run. The CCN concentrations below this level were the same as in the control run. The model was run identically to the control run, and by 9000 seconds microphysical changes resulting from the inclusion of the additional aerosol could be noticed throughout the entire cloud layer. Two cross sections at the same locations as Cases 1a and 1b were taken at a model time of 9000 seconds and are presented in Figures 4.10 through 4.13. The dynamics of the boundary layer were virtually unaffected by the inclusion of the extra aerosol, since the vertical velocity fields in Figures 4.9 and 4.13 are almost identical. Since neither simulation produced any significant amounts of drizzle, the CCN concentration/drizzle feedback mechanism proposed by Albrecht (1989) to increase LWP or alter the boundary layer thermodynamic structure was not evident. A comparison between the control run (Cases 1c and 1d) and the first enhanced CCN sensitivity run (Cases 2c and 2d) show that the statistics of the LWP fields are almost the same. The mean LWP in Cases 2c and 2d are 43.8 g m^{-2} and 45.8 g m^{-2} respectively, while the corresponding standard deviations are 24 g m^{-2} and 28 g m^{-2}. These values are within a few percent of those for Cases 1c and 1d shown above. As expected, the structure of the liquid water content fields in Figures 4.6 and 4.10 are very similar.

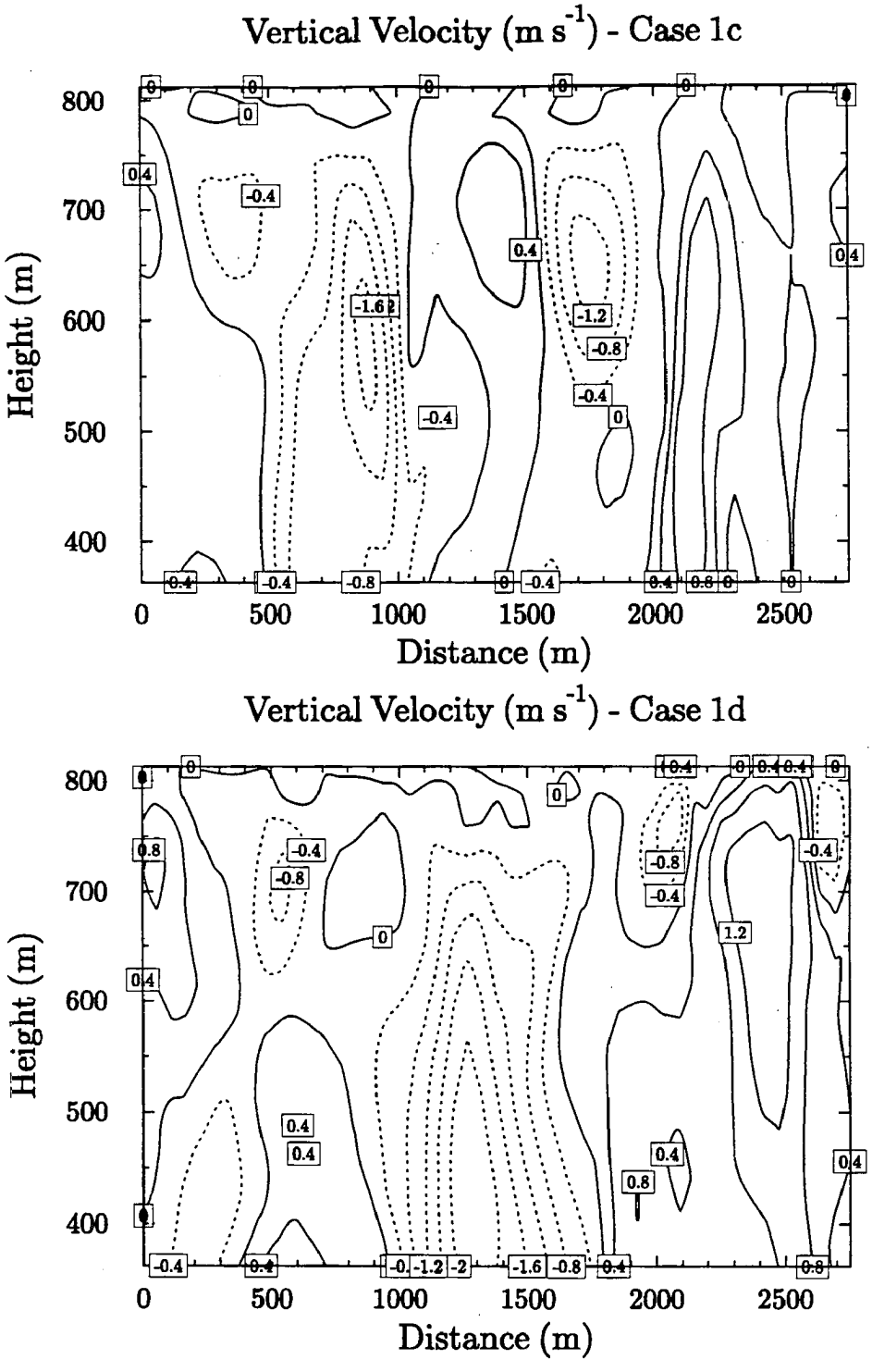

Figure 4.9: The same as Figure 4.6, but for the vertical velocity fields.

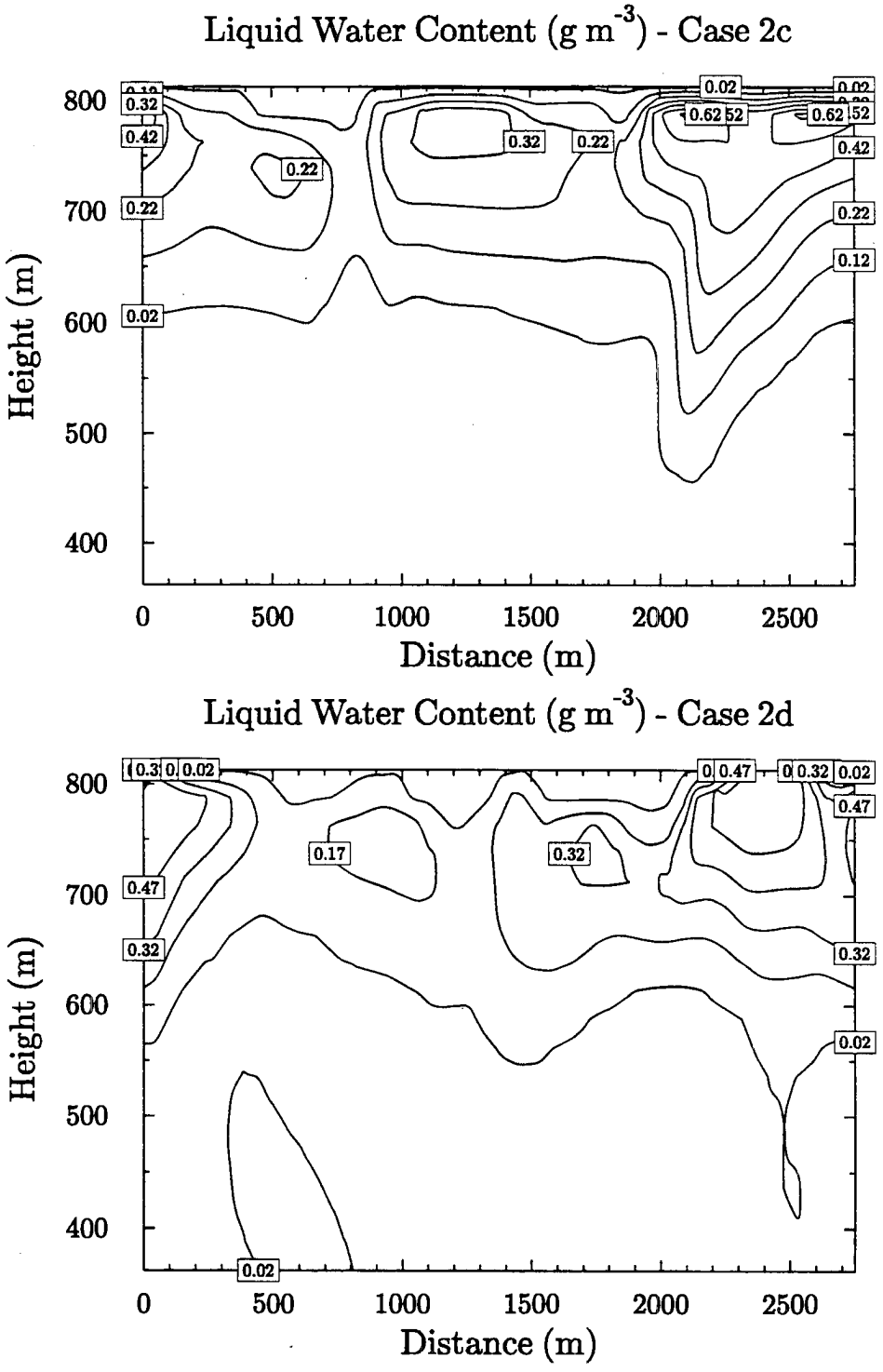

Figure 4.10: The same as Figure 4.6, but for the first sensitivity run.

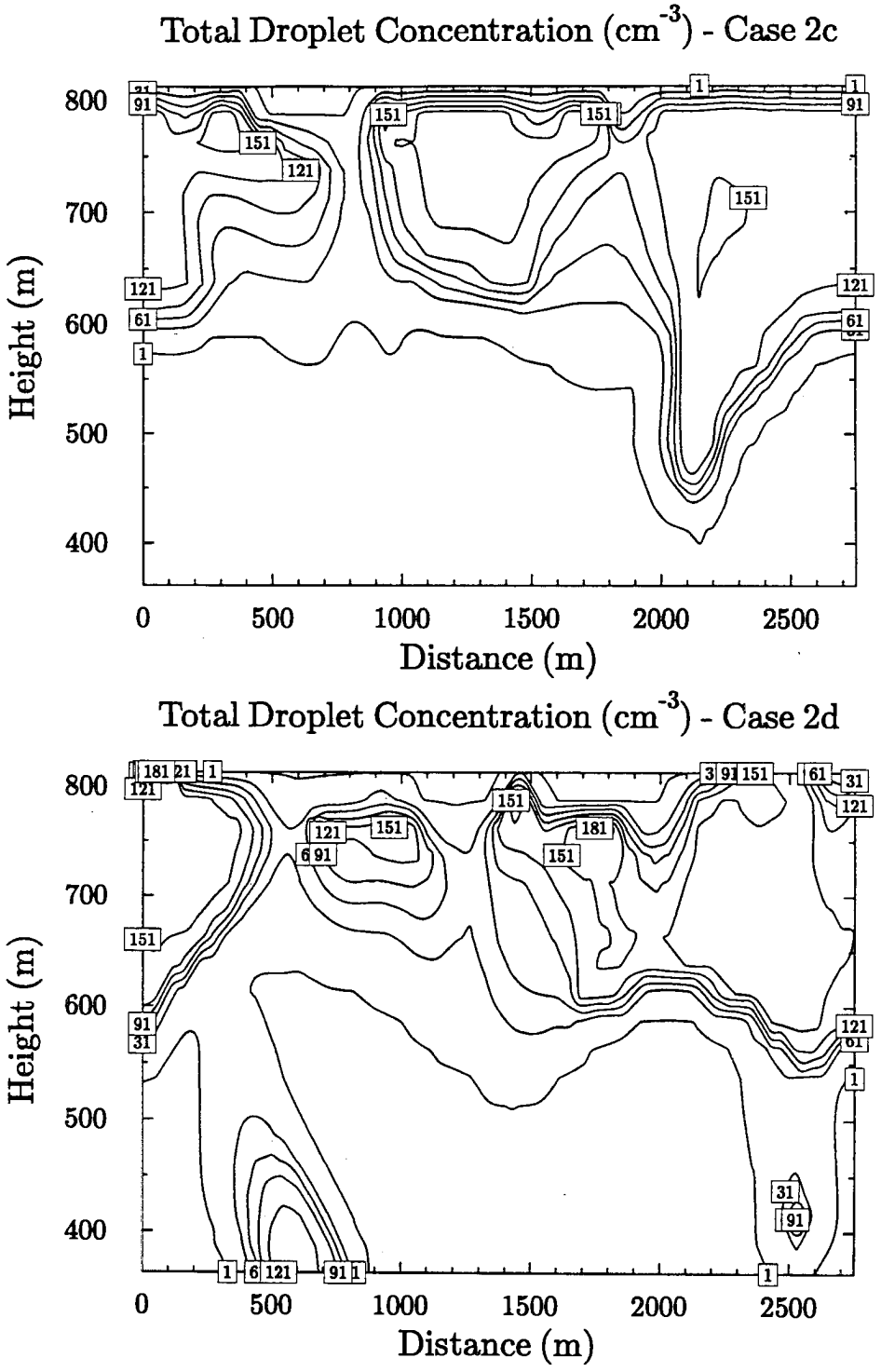

Figure 4.11: The same as Figure 4.7, but for the first sensitivity run.

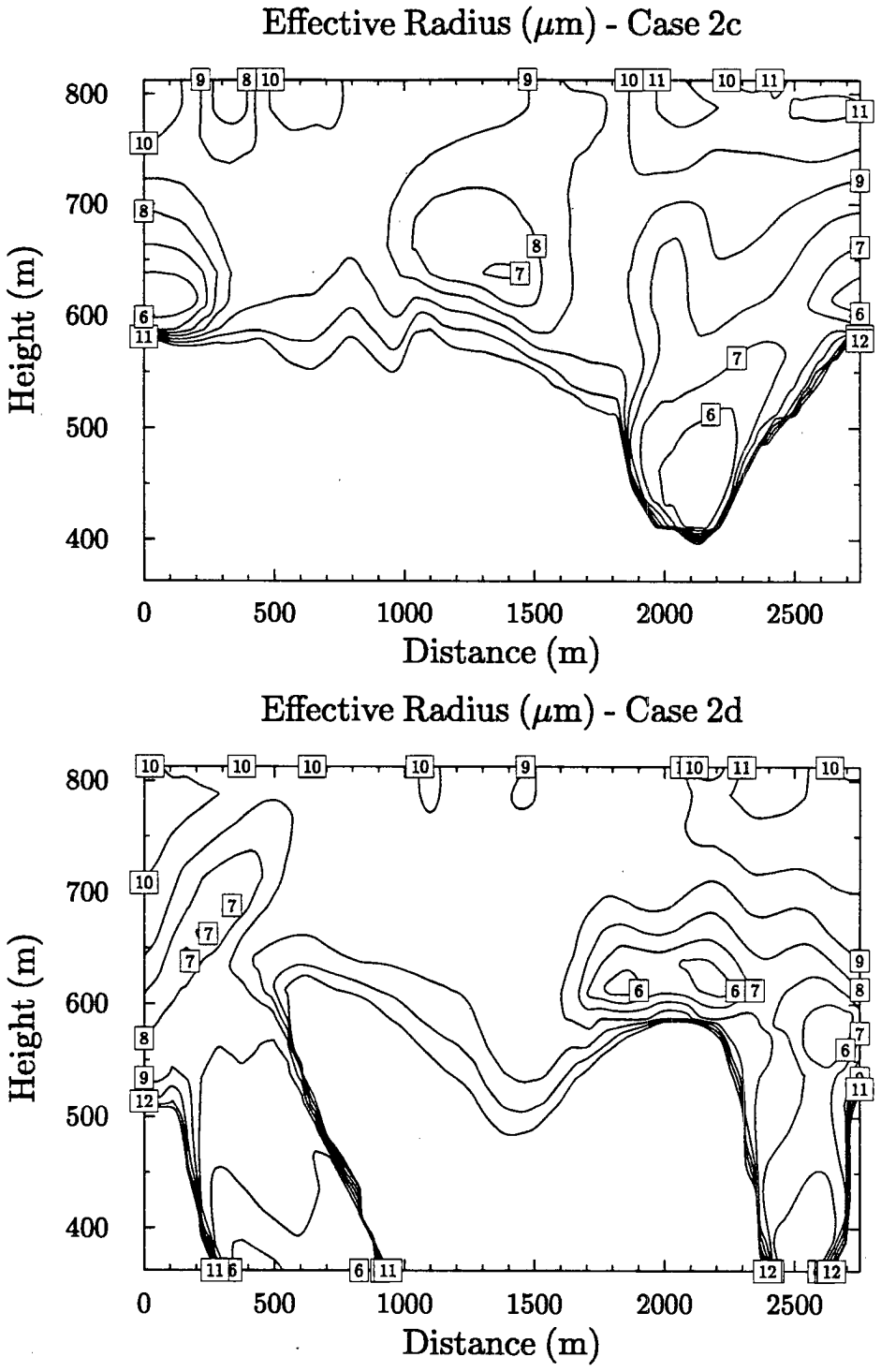

Figure 4.12: The same as Figure 4.8, but for the first sensitivity run.

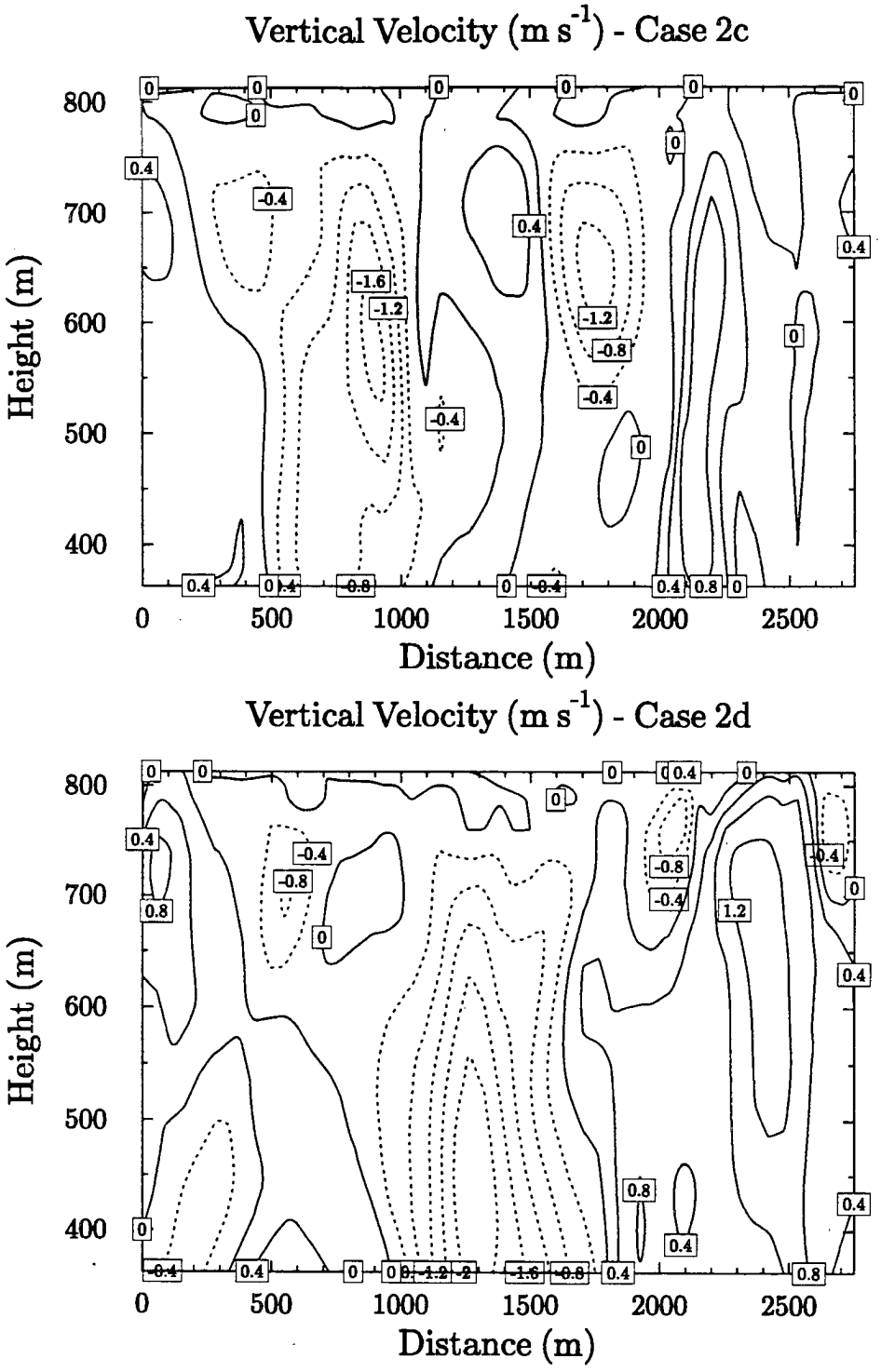

Figure 4.13: The same as Figure 4.9, but for the first sensitivity run.

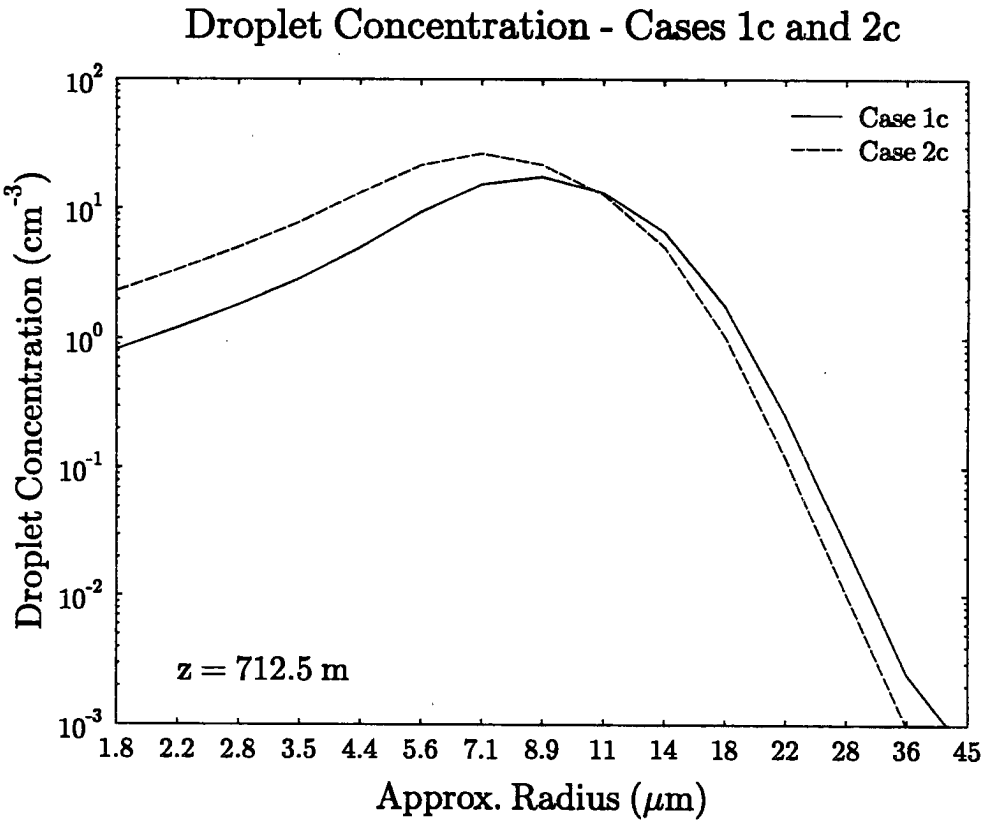

Figure 4.14: The layer averaged droplet concentration distributions computed at $z = 712.5m$ for Cases 1c and 2c.

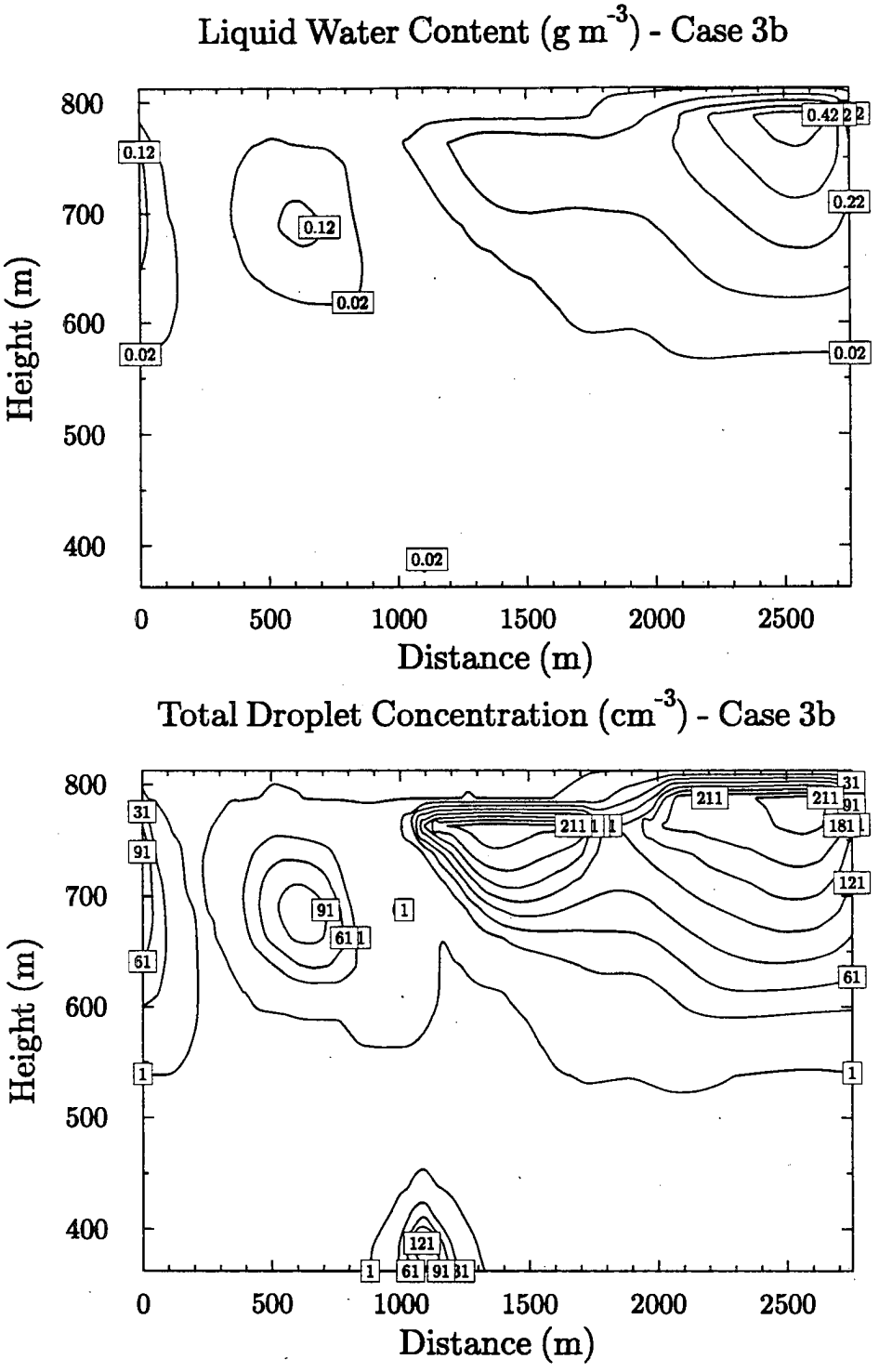

Figure 4.15: The liquid content field and total droplet concentration field computed for a cross section from the second sensitivity run (Case 3b).

Although clouds in Cases 2c and 2d look identical to those in Cases 1c and 1d, the additional aerosol in the second model run makes the clouds different microphysically. Figures 4.7 and 4.11 illustrate the impact of enhanced CCN concentrations on total droplet concentrations. The droplet concentrations in the second set of cross sections are roughly 50 to 100 % larger than those in the control run. Consequently, the effective radii in the sensitivity run decreased by 1.5 to 2 microns (See Figure 4.14). These microphysical changes have a significant effect on the cloud optical properties, which are presented in Chapter 5.

4.2.3 Enhanced CCN below cloud base

A final RAMS simulation was conducted with the purpose of studying the impact of extra aerosol introduced into the subcloud layer on the radiative properties of the cloud. Increased amounts of CCN have been observed below continental stratus in which the subcloud layer is temporarily decoupled from the cloud layer (Martin et al., 1994). In a layer from below the 288K θ surface to the ocean (roughly 400 m deep), the initial CCN concentration was increased to six times the concentration in the control run. The second sensitivity run was otherwise identical to the control run, except the sub-grid scale diffusion was inadvertently set at a higher (more diffusive) level. The result of the change in the diffusion setting was to change the boundary layer dynamics slightly and produce a thicker cloud deck.

The liquid water content and total droplet concentration fields for Case 3b are shown in Figure 4.15. Although the cloud as a whole was thicker, this cross section contains a thinner, more broken cloud. The mean LWP in cross section 3b was only 20.5 g m^{-2} and the standard deviation was almost as large (18 g m^{-2}) as the mean, reflecting the more broken nature of the cloud field. The increase in the inhomogeneity of the cloud in the second sensitivity run is likely the result of the slightly stronger circulation produced by the different diffusion setting. The changes in microphysics in the second sensitivity run are even more pronounced than in the first sensitivity run. The microphysical changes are more a result of the location of the extra aerosol than the cloud's dynamics since they were greater even at the beginning of the model run, when the dynamics were more

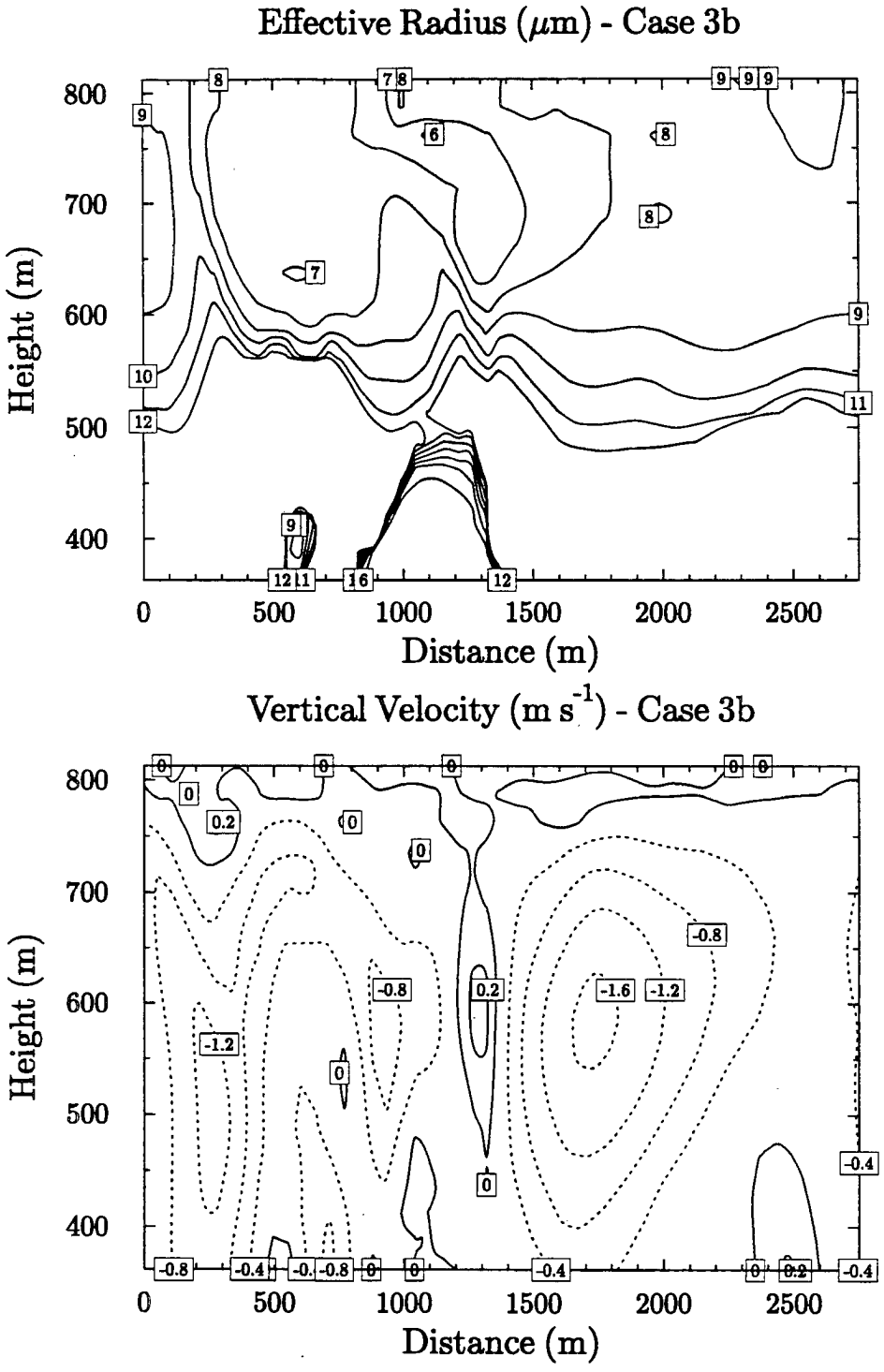

Figure 4.16: The same as Figure 4.15, but for the effective radius and vertical velocity fields.

similar to those in the first sensitivity run. The total droplet concentrations are over 200 cm^{-3} near cloud top and tend to increase from cloud base to cloud top, unlike the more uniform profiles in the other simulations. The effective radii in Case 3b (shown in Figure 4.16) are over 3 microns smaller than in the control run and more uniform throughout the cloud layer. The data from Case 3b allow us to investigate the combined effects of cloud microphysical and macrophysical changes on radiative transfer. Since the cloud in Case 3b appears to be the most broken of all model simulations, it is expected the effects of horizontal inhomogeneity will be most noticeable in this cross section.

4.3 Summary

A brief description of the LES-EM (large eddy simulation-explicit microphysics) model used to produce realistic two dimensional cloud physics data for the radiative transfer simulations is presented in this chapter. RAMS is a sophisticated numerical model that can explicitly simulate the important dynamical and microphysical processes in a marine boundary layer. A series of model runs based on observations taken during the FIRE-I experiment were done to simulate a typical marine stratus cloud deck and to quantify the effects of introducing enhanced concentrations of CCN from above and below the cloud layer.

Two dimensional cross sections taken from the simulation provide a set of cloud physics data that can be used to investigate both the microphysical changes between the control run and the sensitivity runs, and the macrophysical changes between the different cross sections in each run. The addition of aerosol above the cloud in the first sensitivity run increased the total droplet concentrations 50 to 100 percent, while the cloud top effective radii in the cloud decreased from over 11 microns to less than 10 microns. Enhanced concentrations of aerosol below the cloud appeared to have a greater impact on the cloud microphysics, as the total droplet concentrations in the cloud increased up to 110 percent and the cloud top effective radii decreased to 8.5 microns.

Chapter 5

BROADBAND RADIATIVE TRANSFER

With the modeling tools described in the previous chapters, an investigation into the effects of the microphysics and macrophysics of clouds on radiative transfer can be made. This study will consist of two parts. The first part, described in this chapter, examines the impact of enhanced CCN concentrations and cloud inhomogeneity on cloud optical properties and the subsequent effects on solar broadband albedo and heating rates. The second part focuses on the impact of horizontal inhomogeneity on the retrieval of cloud physical properties from spectral reflectance calculations. These calculations and a discussion of two dimensional radiative effects on remote sensing will be presented in Chapter 6.

5.1 Relationships between CCN, cloud droplets and cloud optical properties

Twomey (1977) hypothesized that for most clouds an increase of pollution in the atmosphere would increase their albedo, and thus increase the albedo of the entire planet. Other researchers have postulated that sources of natural CCN could also affect cloud droplet size and cloud albedo, and have hypothesized a temperature related CCN/albedo feedback that may partially counteract the effects of global warming by greenhouse gases (Charlson et al., 1987). The relationship between CCN concentrations and cloud albedo is believed to be an important issue in global climate change, but is not fully understood. Due to the simplifications of the plane parallel models used in the study of this relationship in the past, knowledge about the effects of horizontal inhomogeneity on cloud albedo are still unknown. Also, despite the considerable amount of airborne cloud physics data collected during the past several decades, detailed observations of a stratus deck at a single moment in time are rare and difficult to obtain. Such simultaneous cloud physics

data is necessary for accurate multi-dimensional radiative transfer computations. With the models described above, these difficulties can be overcome and a more accurate study of the CCN/albedo relationship can be accomplished.

The enhanced CCN concentrations resulting from increasing pollution or increases in natural sources of aerosol like dimethyl sulfide (DMS) are believed to be able to change the optical properties of a cloud in several ways. Twomey (1977) noted that an increase in droplet concentration at constant liquid water content would increase the optical depth of the cloud. Also, since the resulting water droplets would generally be smaller, the asymmetry factor would decrease slightly. Both of these effects would tend to increase cloud albedo. Twomey also assumed that the increasing pollution would tend to lower the single scattering albedo of the entire cloud layer and for thick enough clouds would result in a decrease in the cloud albedo. The effect of moderately absorbing aerosol on cloud albedo, though, is very small for optical depths less than thirty (see Twomey (1977) Figure 3) and no direct attempt was made to model the effects of interstitial aerosol. However, when the optical depth in the SHSG model domain approaches zero, the efficiency of the conjugate gradient method is reduced and the number of iterations necessary for a model calculation increase significantly (Evans, 1993). In order to speed up the radiative transfer calculations, a lower threshold of particle extinction was set to define cloud-free regions. For the radiance calculations the threshold was set at 0.05 km^{-1}, while the threshold was set at 0.5 km^{-1} for the more computationally intensive broadband calculations. Since the depth of the cloud-free region in any of the simulations was less than 300 meters, the maximum increase in the optical depth was less than 0.015 in the radiance calculations and 0.15 in the broadband calculations. Since global average measurements of aerosol optical depths in the lowest kilometer of the atmosphere are about 0.04 (Toon and Pollack, 1976), the aerosol extinction coefficients in a marine atmosphere are of the order of a few hundredths per kilometer. It should be noted that for most solar wavelengths, the single scattering albedos in the cloud-free regions were similar to values for most aerosol near the surface (Toon and Pollack, 1976). Thus, the overall effect of the model threshold is probably greater than, but relatively close to, the effects of interstitial aerosol on the

optical properties of the entire layer. Also, the impact of the extinction threshold on the albedos is small, especially since all of the cloud-free regions occur in the lower half of the model domain. Figure 5.1 shows the visible (0.28 – 0.7 μm) albedo computed from the SHSG broadband model for two of the RAMS model cross sections. The solid lines were computed using an extinction threshold of 0.5 km^{-1}, while the dashed lines were calculated with a lower threshold of 0.05 km^{-1}. The differences were within a couple tenths of a percent at all points along the horizontal domain.

Another effect of enhanced CCN concentrations on cloud albedo not explicitly stated in Twomey (1977) is the increase in the overall droplet single scattering albedo as a result of smaller droplet sizes. This effect will counteract the single scatter albedo-lowering effects of the aerosol and strengthen the overall impact of increased CCN on cloud albedo. As a result, it is expected that increasing the overall CCN concentration in a marine stratus-capped boundary layer will likely increase the cloud albedo, regardless of cloud optical depth.

Figures 5.2 and 5.3 show how the introduction of CCN above the top of the cloud layer influence the droplet distributions in the cloud by the end of the model simulations (9000 s). Figure 5.2 presents the domain-averaged relative difference in droplet concentration between Case 2c and Case 1c for several levels included in the model domain of the radiative transfer computations. The concentrations of small droplets increased in Case 2c at almost every level in the vertical domain (362.5 m to 812.5 m), and the magnitude of the increase is progressively larger with height. The one exception is the moderate increases at 812.5 m, which contains a mixture of cloudy air and clear air at cloud top. Near cloud top the increases in the smallest droplet sizes are almost 200 percent. For drops larger than bin 10 (12.5 – 15.75 μm radius), however, the concentrations are lower in the enhanced CCN case than in the control case. The depression in larger drops is greatest in the upper levels of the cloud and demonstrates that the addition of additional CCN at cloud top creates many more smaller droplets at the expense of larger droplets, with the greatest effects near the top of the cloud. Figure 5.3 shows the droplet concentration

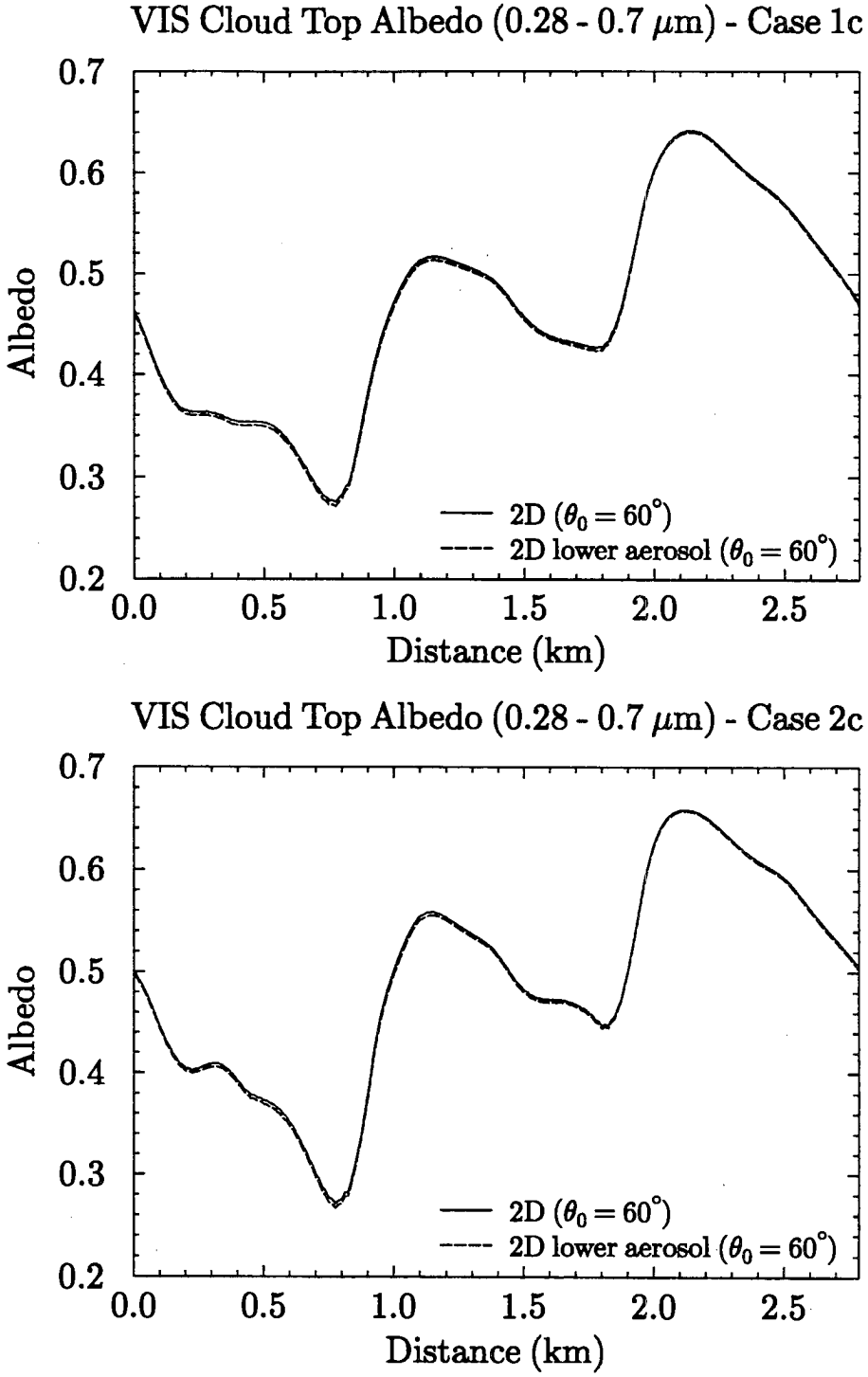

Figure 5.1: The visible (0.28 – 0.7 μm) albedo computed from the 2D SHSG broadband model for Case 1c as a function of horizontal distance in the cross section. The solid line shows the albedo computed using an extinction threshold of 0.5 km^{-1}, while the dashed line shows the albedo computed using a threshold of 0.05 km^{-1}.

differences between Case 2d and Case 1d. The concentration changes in these cross sections are different than the changes shown in Figure 5.2. While in the upper 200 m of the model domain the increase in small droplet concentration increases with height, in the bottom half of the domain the concentration changes in small droplets are often negative and reach a minimum in the 512.5 m and 562.5 m levels. Much of the bottom half of the model consists of cloud-free atmosphere (see Figure 5.9).

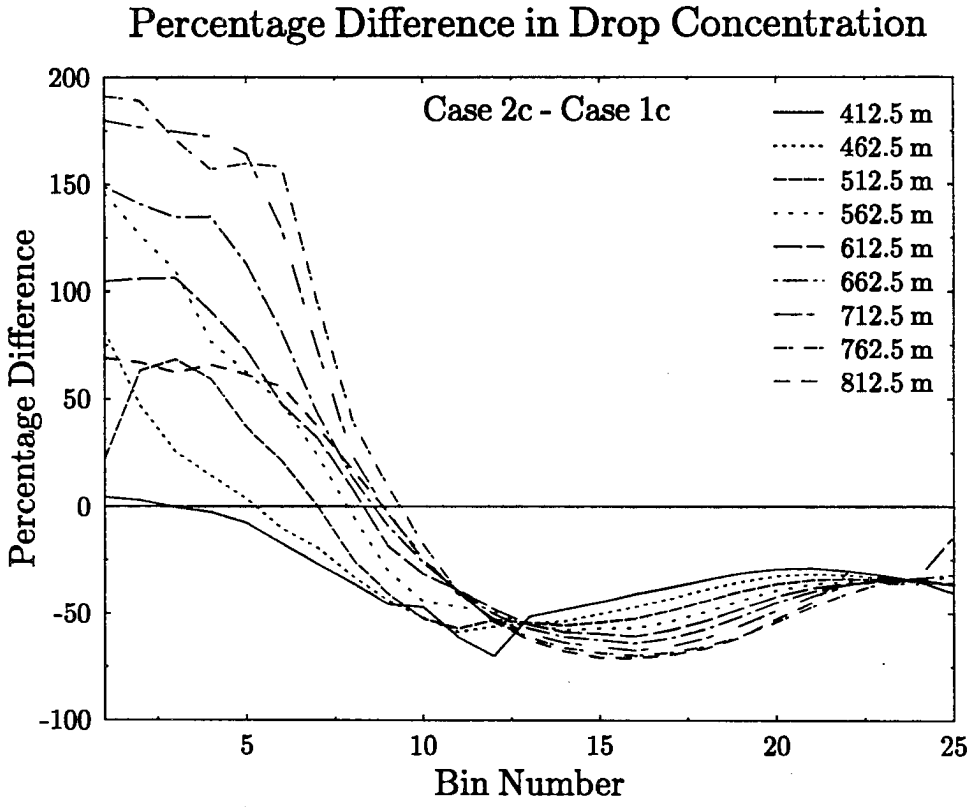

Figure 5.2: The level averaged relative differences in droplet concentration between Cases 1c and 2c as a function of bin number.

This difference in the small droplet concentration changes in the lower part of the model cross sections may be due to a less complete mixing of the extra CCN throughout the domain in Case 2d compared to Case 2c. Case 2d was crudely sampled by vertical velocity

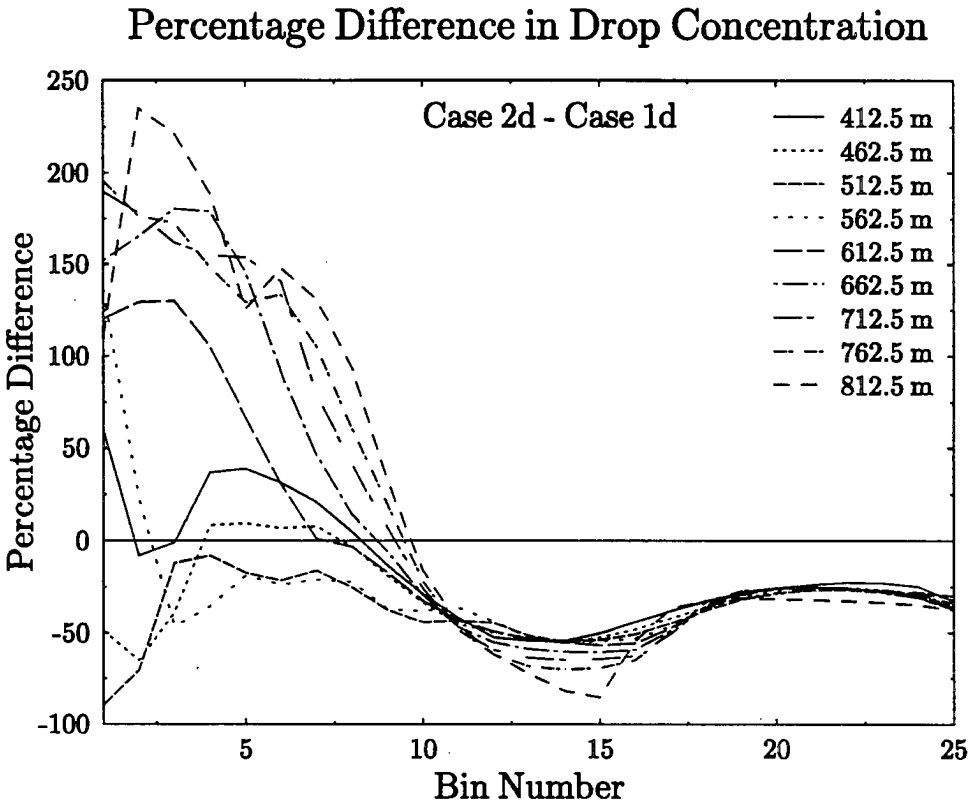

Figure 5.3: The same as Figure 5.2, but for Cases 1d and 2d.

into three sections as shown in Figure 5.4b. In Figure 5.5, the droplet concentration differences for each region is presented. Region A extends across the first kilometer of the horizontal domain and has weak and localized updrafts and downdrafts. Like the graph for the entire horizontal domain, in Region A the droplet concentration changes at the smaller bin sizes reach a minimum at 562.5 m, but the small droplet concentrations show an increase instead of a decrease. The region between 1000 m and 1600 m (Region B) is dominated by a strong downdraft and nearly the entire region has vertical velocities of -0.4 m s^{-1} or less. This region shows a smooth increase in the small droplet concentrations with height similar to the droplet concentration differences shown between Cases 2c and 1c. As shown in Figure 5.4a, the vertical velocity field in Case 2c is dominated by two strong downdrafts and show generally weaker and more narrow updrafts than Case 2d. The strong downdrafts in Region B and Case 2c help transport the extra CCN at cloud top throughout the cloud layer. The final region (Region C) contains a broad region of strong updraft. Region C shows the dichotomy in droplet concentration differences between the upper and lower levels of the cloud that was evident in the above graph of the entire domain. The droplet concentration changes are reflected in changes in the domain average effective radius that was calculated for regions in the model with an extinction coefficient greater that 1 km^{-1}. The domain average effective radius decreased by thirteen percent from Case 1c to 2c (from 10.01 to 8.72 μm) and decreased by 11.6 percent from Case 1d to 2d (from 9.88 to 8.74 μm). In the cloudy regions below 587.5 m the relative effective radius decreases between Cases 1c and 2c (from 7.56 to 6.70 μm – 11 percent) are noticeably larger than those between Cases 1d and 2d (from 7.77 to 7.21 μm – 7 percent).

The transfer from larger droplets to smaller droplets is also shown in the changes in the mass spectrum between the control cases and enhanced CCN cases. Figure 5.6 presents the change in the layer averaged liquid water mass in each bin (between Cases 2c and 1c) as a percentage of the layer averaged total liquid water mass (for Case 1c). The total liquid water mass in each layer of the enhanced CCN case is *less* than those in the control case, especially in the lowest layers of the domain where the increases in the number of small droplets are small. Toward cloud top the differences in the total mass

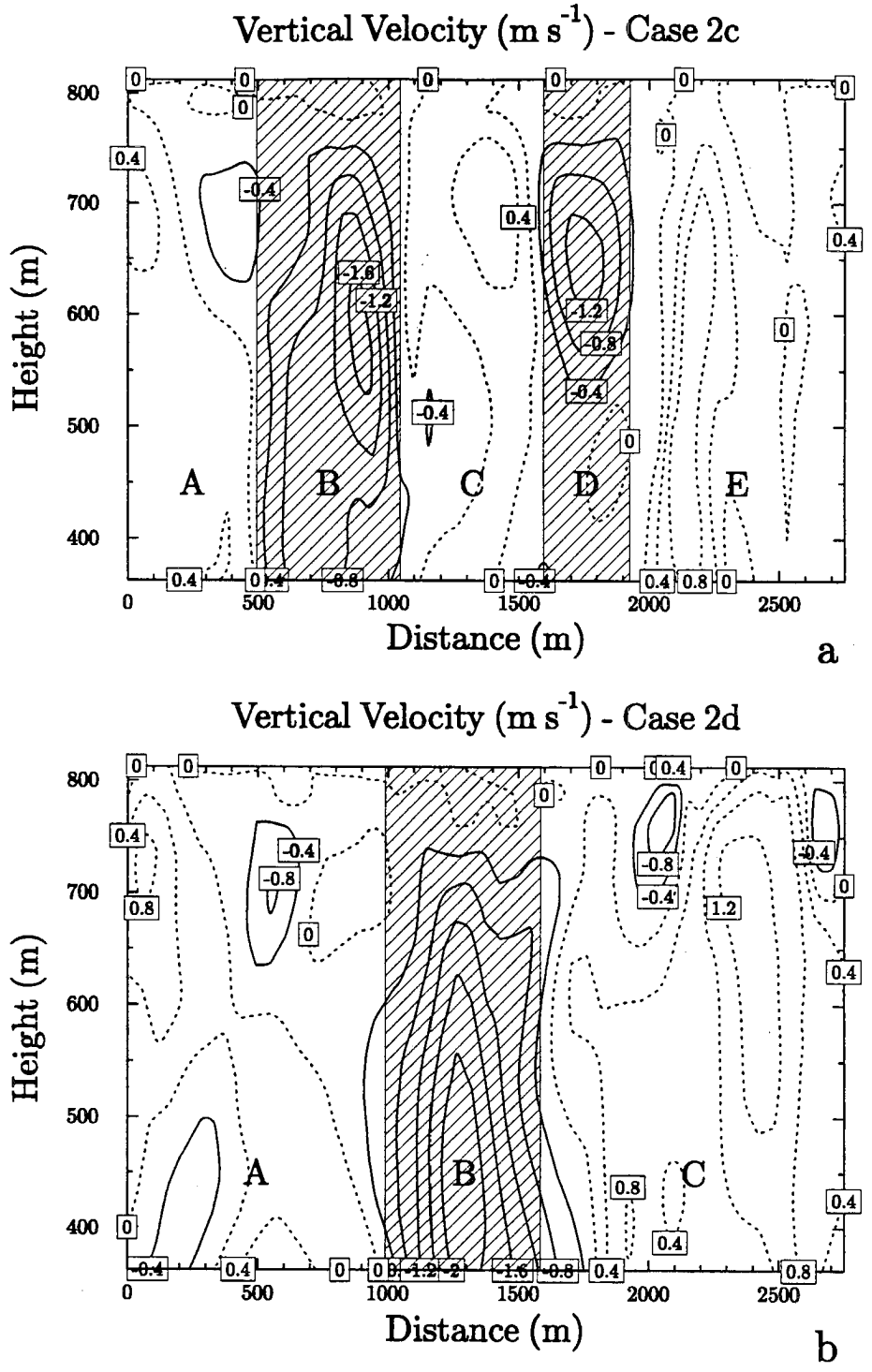

Figure 5.4: The vertical velocity fields for Cases 2c and 2d. The cross sections are divided according to large regions of updrafts or downdrafts.

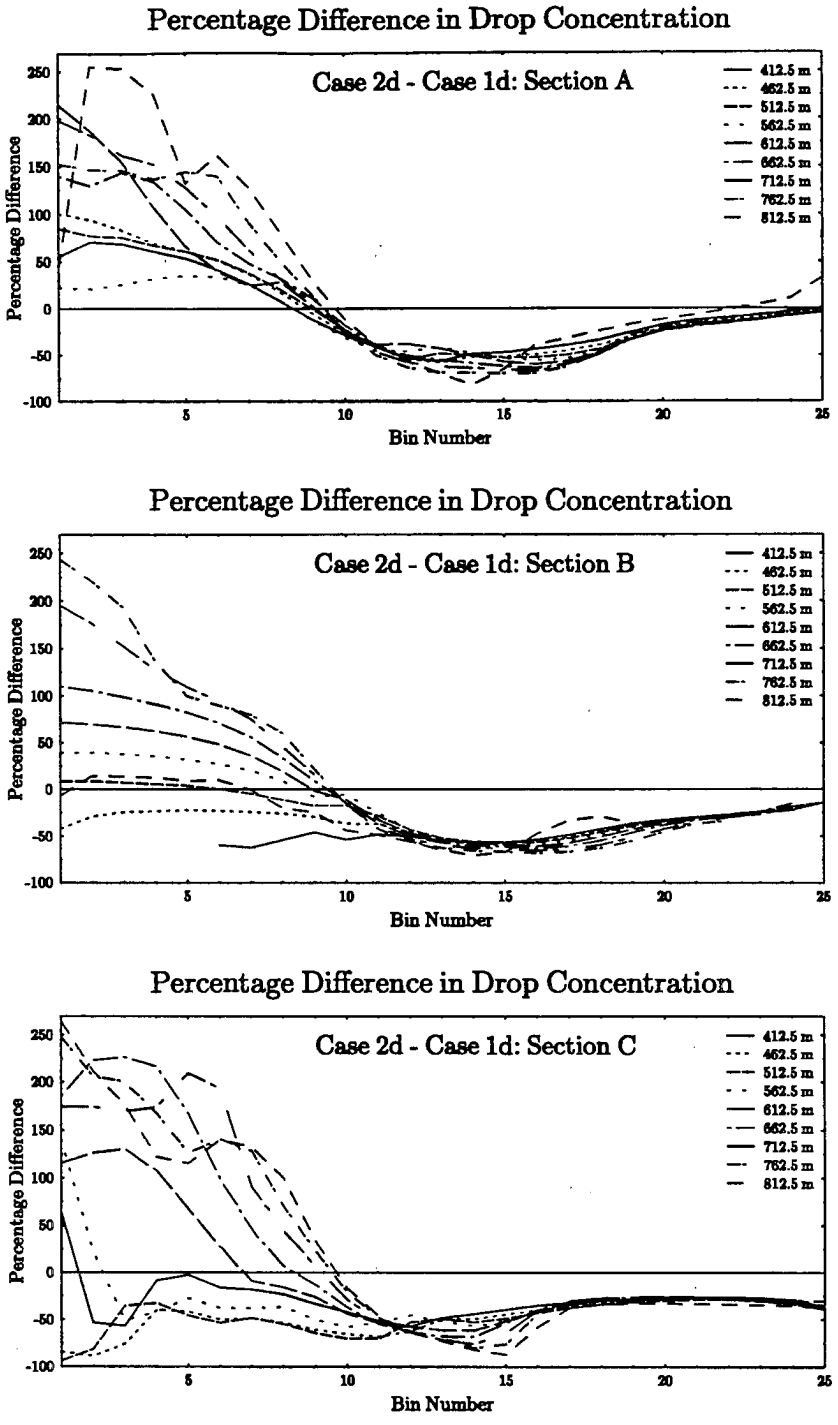

Figure 5.5: The same as Figures 5.3, for the regions of updrafts or downdrafts shown in Figure 5.4.

between Cases 2c and 1c are smaller while the shift in mass from larger to smaller droplets is more clear and larger in magnitude. Figure 5.6 shows that most of the mass shifts from droplets in bins 9 – 11 (radius 9.92 – 19.85 μm) to those in bins 6 – 8 (radius 4.96 – 9.92 μm). Between Cases 2d and 1d, the transfer of mass is broken into two regimes (see Figure 5.7). In the bottom half of the domain the mass is generally larger in Case 1d for bins 5 through 12 (radius 3.94 – 31.50 μm). One exception is the larger mass in Case 2d for bins 4 through 7 at 412.5 m. In the upper half of the domain the transfer of mass is from higher bins to lower bins, similar to the differences between Cases 2c and 1c. Near cloud top, both the maxima and minima in mass difference tend toward larger bins and become more narrow.

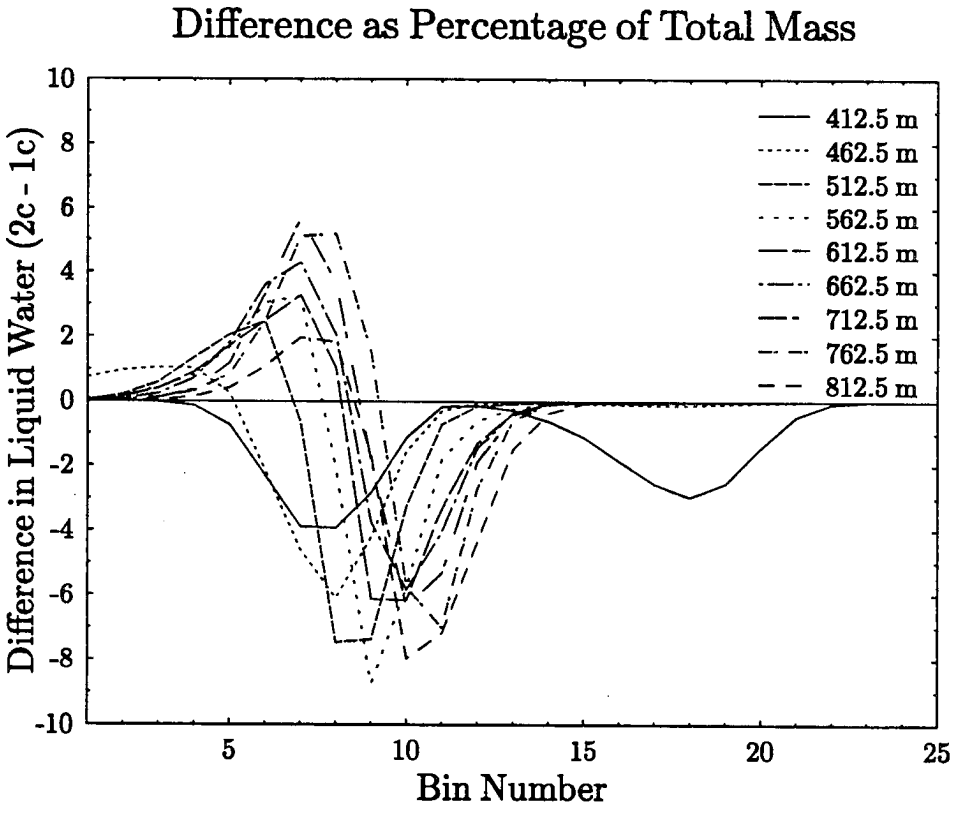

Figure 5.6: The level averaged differences in liquid water mass (as a percentage of the total mass at each level) between Cases 1c and 2c as a function of bin number.

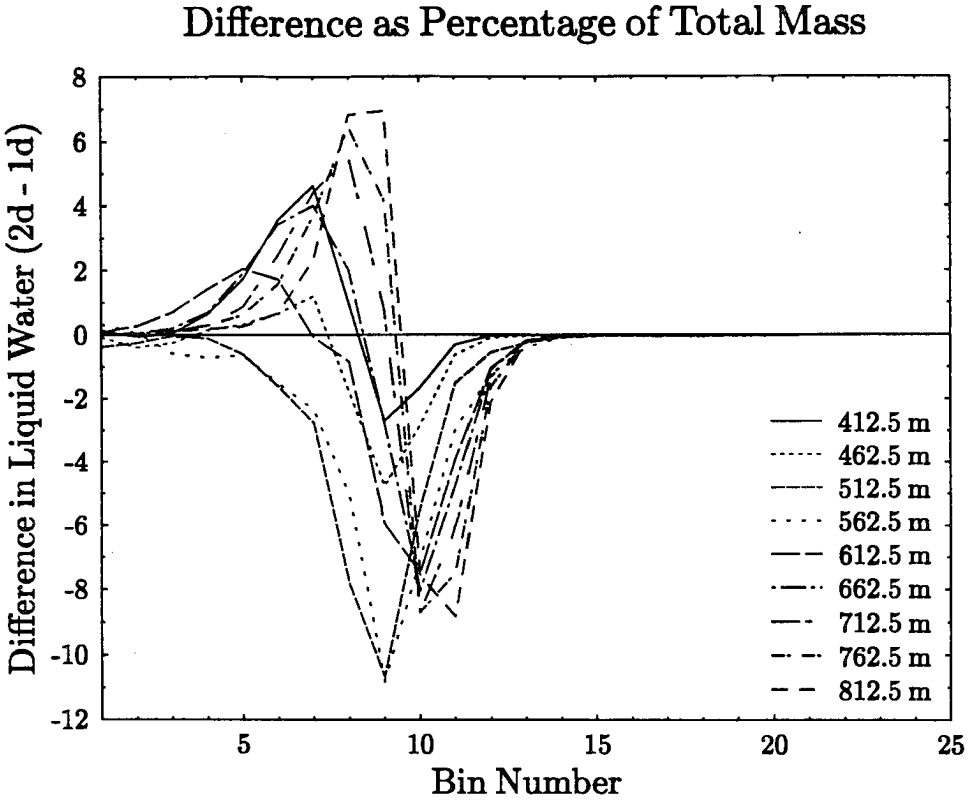

Figure 5.7: The same as Figure 5.6, but for Cases 1d and 2d.

As mentioned above, the creation of larger numbers of smaller droplets at the expense of larger droplets produces several changes in the cloud optical properties. The conversion of the cloud's liquid water into greater numbers of smaller droplets increases the total cross sectional area of the cloud particles. As a result, the clouds in the enhanced CCN case can scatter light more efficiently and the enhanced CCN case should result in an increase in optical depth (or equivalently extinction coefficient). The scattering function of the smaller droplets also has a smaller forward peak, and thus the asymmetry factor decreases in the cloud with the enhanced concentration of CCN. Finally, for near infrared wavelengths the smaller droplet sizes produce larger single scattering albedos, especially at more absorbing wavelengths.

Figures 5.8 – 5.16 and Tables 5.1 – 5.2 illustrate the cloud optical property changes resulting from the introduction of additional CCN in the RAMS aerosol sensitivity tests. For all of the figures and tables the cloud properties are shown for the third band in the broadband model, which corresponds to the wavenumbers from 4000 cm^{-1} to 4600 cm^{-1} and includes the 2.16 μm channel used in the radiance calculations in Chapter 6. Figures 5.8 through 5.10 show the extinction coefficient field for five of the model simulations. The fields match the corresponding liquid water content fields shown in Chapter 4, and have peak values near 80 km^{-1}. The mean optical depth in Case 1c is 6.9, while it is 7.0 for Case 1d. In the sensitivity tests the enhanced CCN concentrations led to an increase in the optical depth (as expected) and the average optical depth in both Cases 2c and 2d is 7.9. The increase in optical depth between the control cases (1c and 1d) and the enhanced CCN cases (2c and 2d) is thirteen percent, and is due almost entirely to changes in microphysics.

Figures 5.11 – 5.13 present the single scattering albedos for the same cases shown in Figures 5.8 – 5.10. The figures are based on Mie scattering calculations from the droplet distributions and the single scattering values in the cloud-free areas are not shown for clarity. The cloud-free regions contain lower values (roughly 0.830 in Case 1c) of single scattering albedos and reflect the scattering properties of the few large droplets that appear in these areas. The mean single scattering albedos of the cloudy regions in Cases 1c and 1d were 0.9697 and 0.9702 respectively. The "cloudy" regions in these figures are regions with an extinction coefficient of 1.0 km^{-1}. This corresponds roughly to a liquid water content slightly less than 0.02 g m^{-3} and matches the lowest valued contour in Figures 5.8 through 5.10. The enhanced CCN in Cases 2c, 2d and 3b resulted in an increase in single scattering albedo, as the mean single scattering albedos in those cases were 0.9736, 0.9737 and 0.9756 respectively. The increase resulted from the decrease in the overall size of the cloud droplets and demonstrates the close correlation between single scattering albedo and effective radius that was utilized in the droplet size retrievals presented in Chapter 6.

The asymmetry factor fields for the five simulations are shown in Figures 5.14, 5.15 and 5.16. The effect of the increased cloud droplet concentrations on g are small but still

noticeable. The mean asymmetry factor in the cloudy regions of Cases 1c and 1d were 0.828 and 0.829 respectively, while the corresponding values in Cases 2c, 2d and 3b were 0.822, 0.822 and 0.825.

The differences in optical depth, single scattering albedo and asymmetry factor between Cases 1c and 1d compared to Cases 2c, 2d and 3b all work to increase the overall cloud albedo. Figure 5.17 shows the net difference in cloud extinction coefficient between Cases 1c and 2c and between Cases 1d and 2d. The increases in extinction coefficient were largest in the top of the cloud, but the increases do not coincide exactly with the regions of largest liquid water content. Tables 5.1 and 5.2 present the layer-averaged differences in optical properties for Case 2c versus Case 1c and Case 2d versus Case 1d respectively. In the cloud layer, the increase in single scattering albedo and the decrease in asymmetry factor are fairly uniform with height although the differences are more variable in the sub-cloud layer. The differences between Case 1b and 3b are not shown since the dynamics in both models are not the same, but the second sensitivity run has higher single scattering albedos and lower asymmetry factors than Case 1b. Note that despite the slightly more thorough CCN mixing in the lower half of the model in Case 2c compared to Case 2d, the differences don't appear to affect the magnitude of the optical property changes in these cross sections. The magnitude of the relative optical property changes between Cases 2c and 1c are almost the same as the changes between Cases 2d and 1d.

5.2 Broadband Albedos

In the next two sections of this chapter three sets of radiative transfer calculations will be compared. The first set are broadband flux calculations from the SHSG model, and they represent the radiative transfer through the two dimensional media obtained from the RAMS simulations. These calculations will be denoted as 2D calculations. The second set of calculations are calculations at closely spaced points across the horizontal domain of the media, and the atmosphere at each point is assumed to be horizontally homogeneous (or equivalently no net horizontal transport of energy is computed). This type of calculation is called the independent pixel approximation (IPA) (see Cahalan

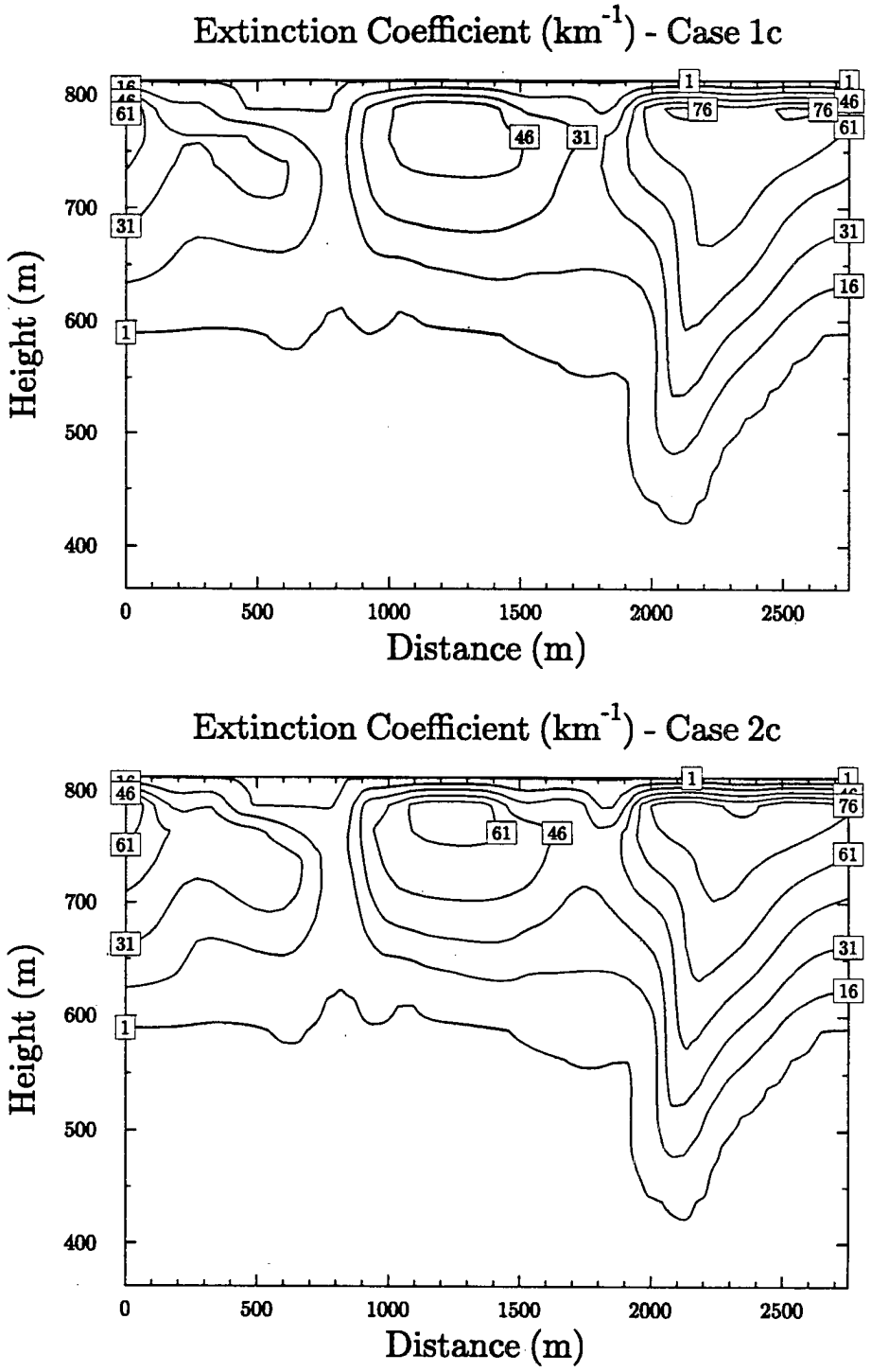

Figure 5.8: The extinction coefficient fields for Cases 1c and 2c.

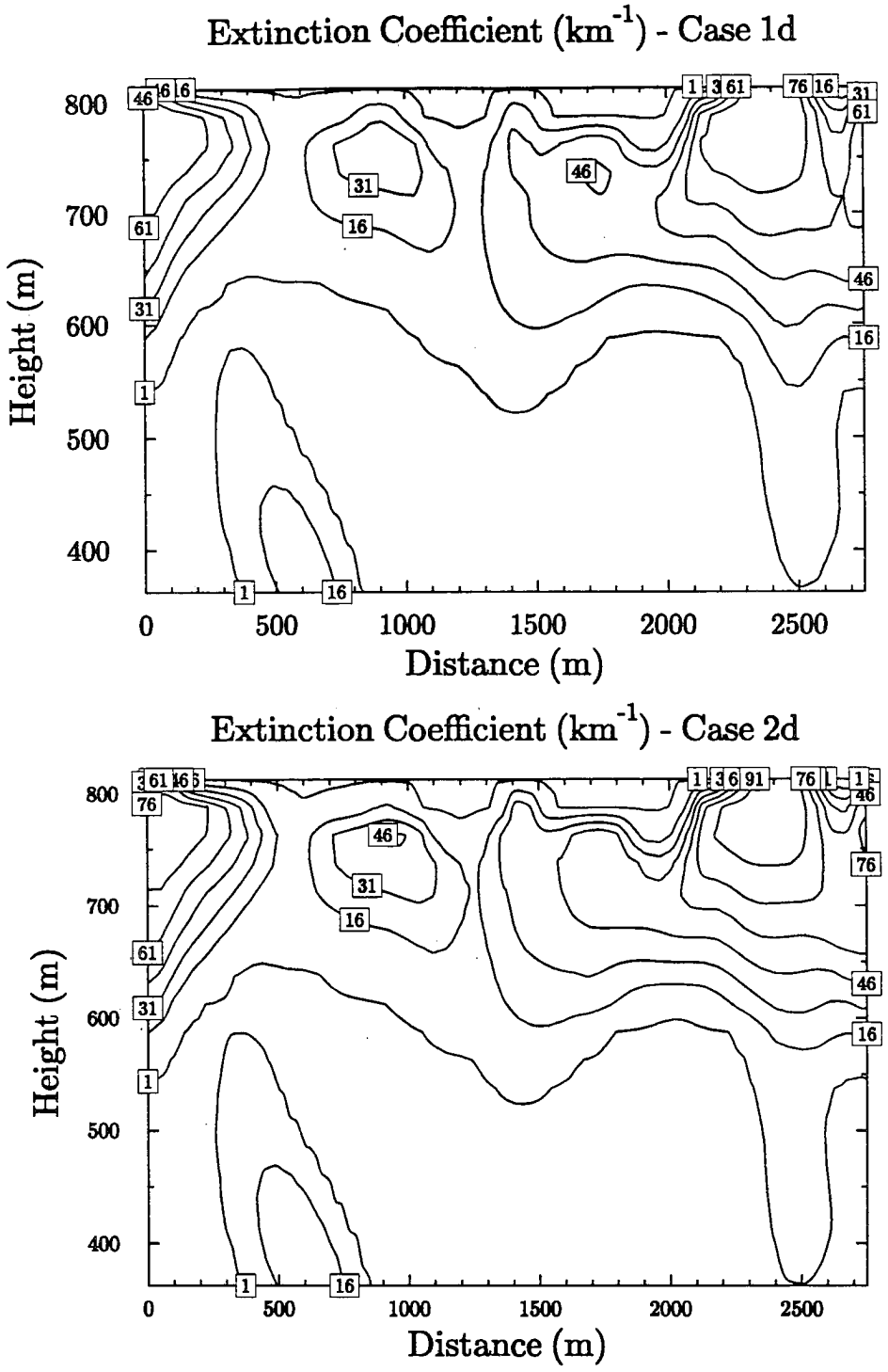

Figure 5.9: The extinction coefficient fields for Cases 1d and 2d.

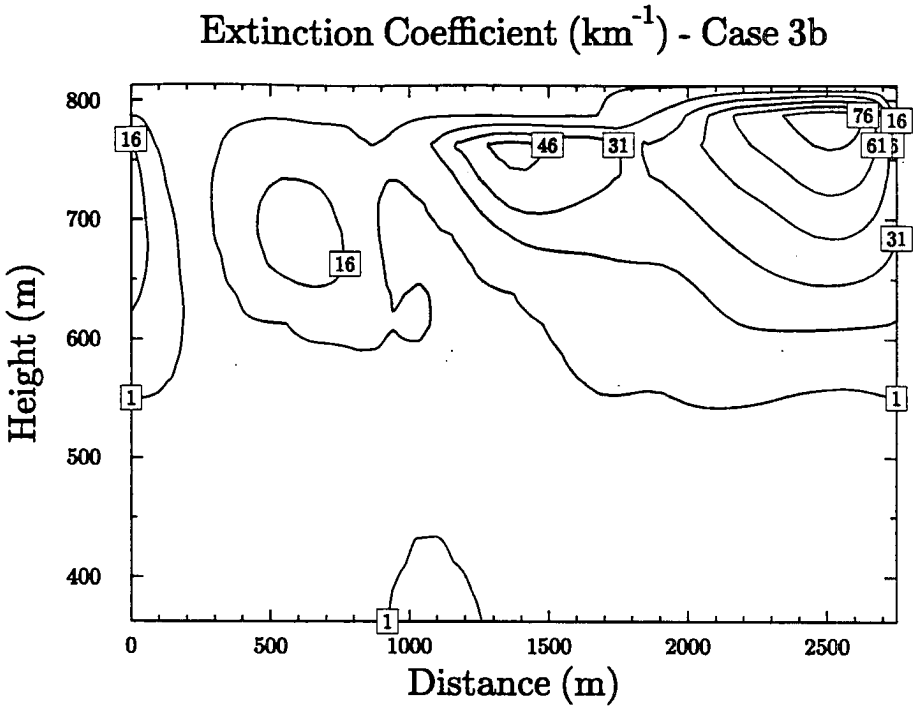

Figure 5.10: The extinction coefficient field for Case 3b.

et al., 1994), and is used to approximate the horizontal variability of a medium with a plane parallel model. The final form of radiative transfer calculation is the plane parallel approximation (PPA). This method uses a single horizontally homogeneous cloud with domain averaged optical properties to approximate the radiative transfer throughout the model domain. The plane parallel approximation has been used almost exclusively by researchers to estimate mean fluxes throughout the atmosphere. In this section, the three sets of calculations will be compared by examining the broadband albedos derived from each method. The broadband albedo is simply:

$$a = \frac{F^{\uparrow}}{F^{\downarrow}}, \tag{5.1}$$

and is defined for horizontally homogeneous calculations. In the next section the solar heating rates and net flux convergence computed by each method will be compared.

5.2.1 Visible (0.28 μm – 0.7 μm)

Figures 5.18 through 5.22 show a series of broadband visible albedos for the five cases described in the previous section. Figures 5.18 and 5.19 show the albedos for Cases 1c

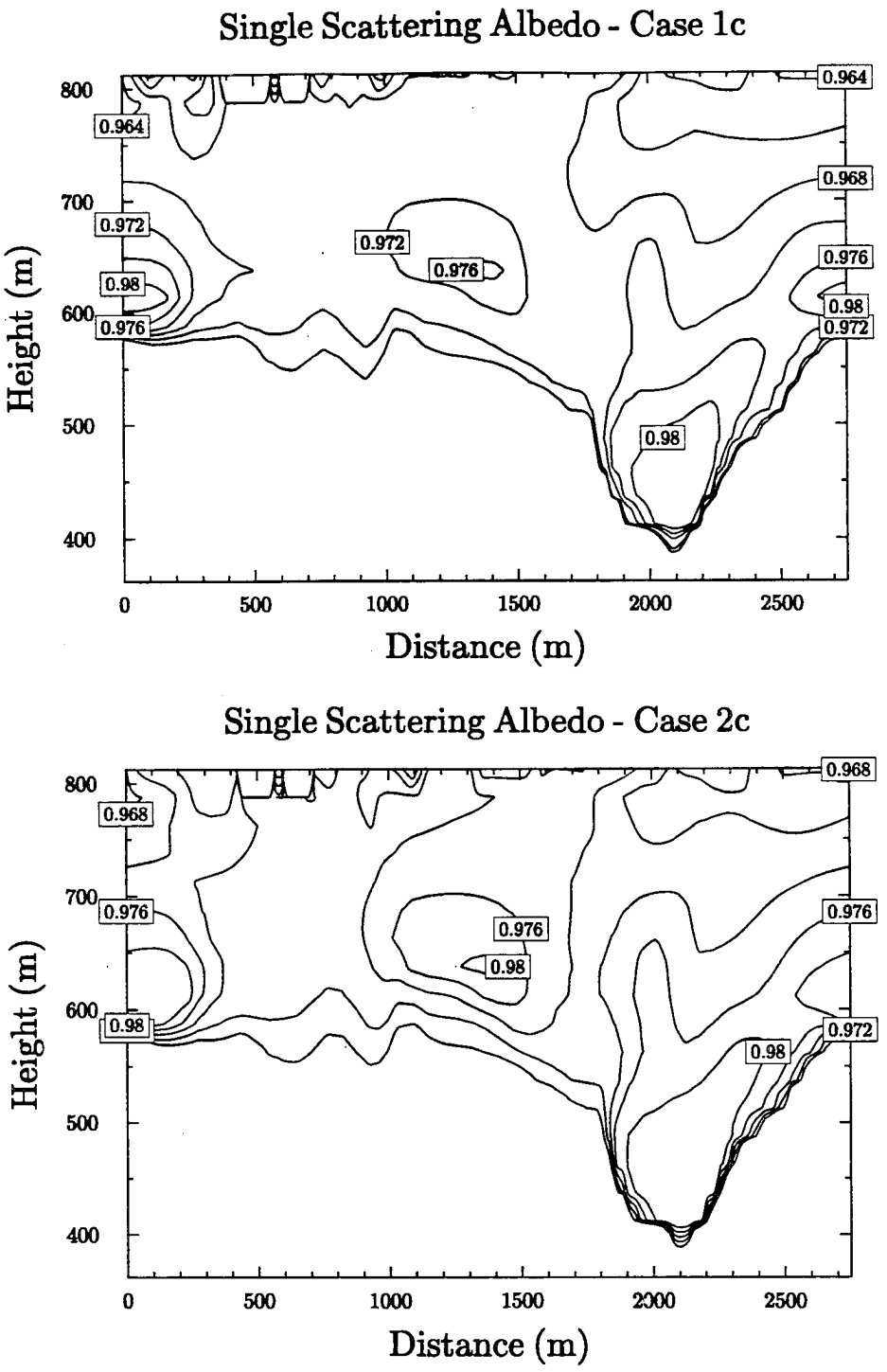

Figure 5.11: The single scattering albedo fields for Cases 1c and 2c. The values below cloud base are not shown for clarity.

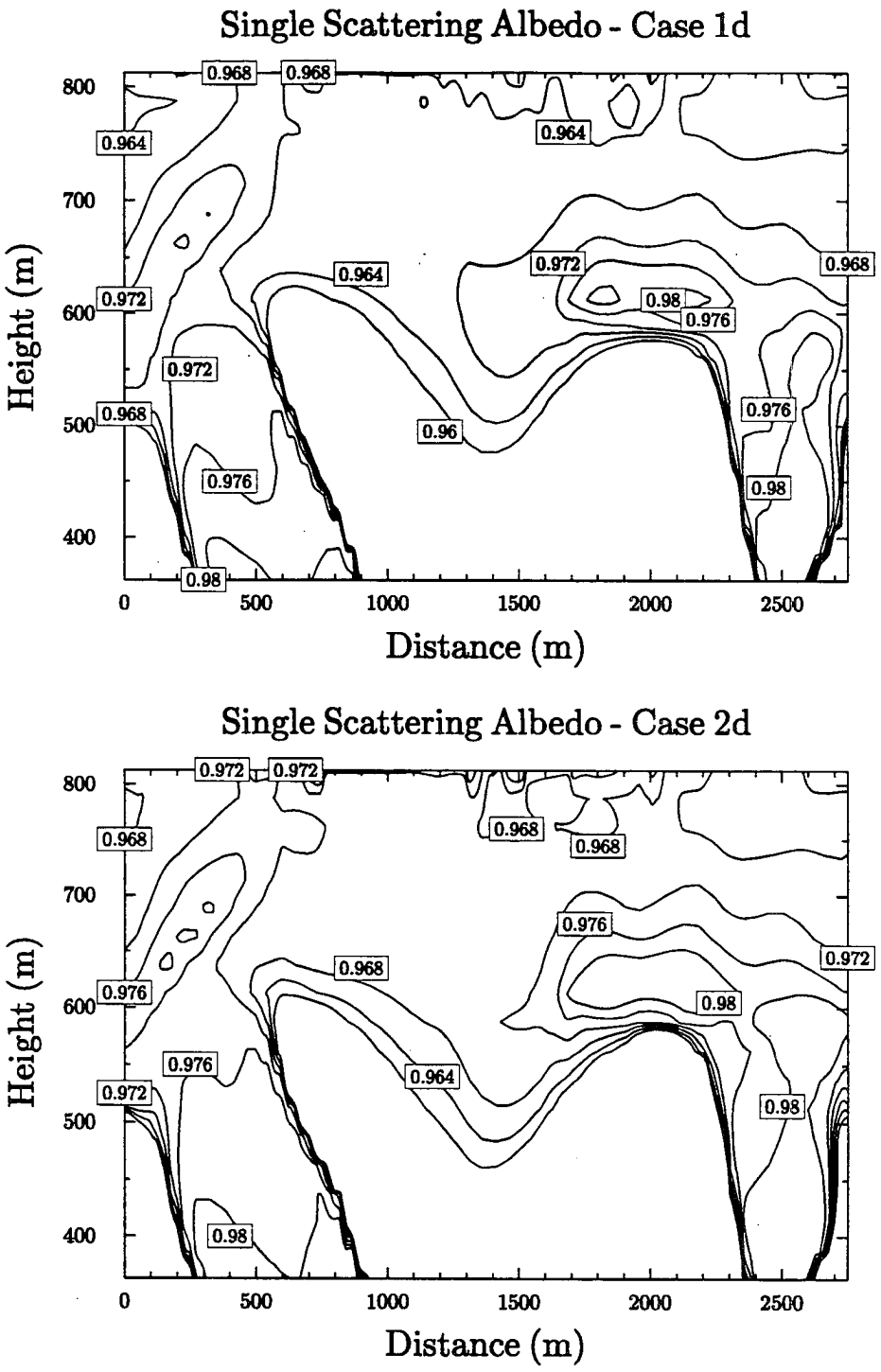

Figure 5.12: The single scattering albedo fields for Cases 1d and 2d. The values below cloud base are not shown for clarity.

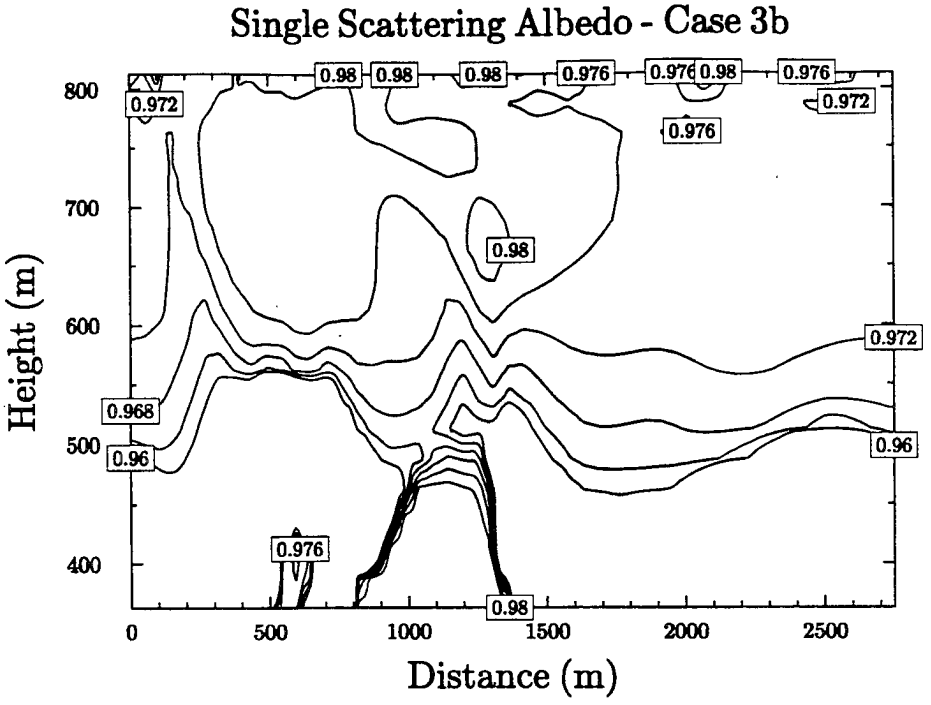

Figure 5.13: The single scattering albedo fields for Case 3b. The values below cloud base are not shown for clarity.

and 2c at solar zenith angles of 10° and 60° for the 2D calculations and the corresponding IPA and PPA calculations. Generally, the effect of the horizontal dimension in the 2D radiative transfer is to smooth out the albedo field compared to the IPA runs, especially when the solar zenith angle is 10°. When $\theta_0 = 60°$, the effects of horizontal inhomogeneity in the 2D calculations are more noticeable. A three or four percent (absolute) difference between the 2D and IPA albedos appears from 0 km to 0.6 km, in the "shadow" of a large extinction maxima near the left border of the model domain. Near 2.1 km in the horizontal domain the 2D albedo is 3 or 4 percent larger percent larger than the corresponding IPA albedo, and is located on the sunlit side of a large extinction maxima near cloud top. The horizontal size of this region is on the order of 250 meters. Although at each horizontal grid point the albedo calculated by the independent pixel approximation usually differed from the 2D calculation, the domain averaged albedo for both calculations was nearly identical. The domain average albedo in the 2D run for Case 1c and a solar zenith angle of 10° was 33.06 percent and the corresponding value for the IPA run was 33.10 percent. Similar

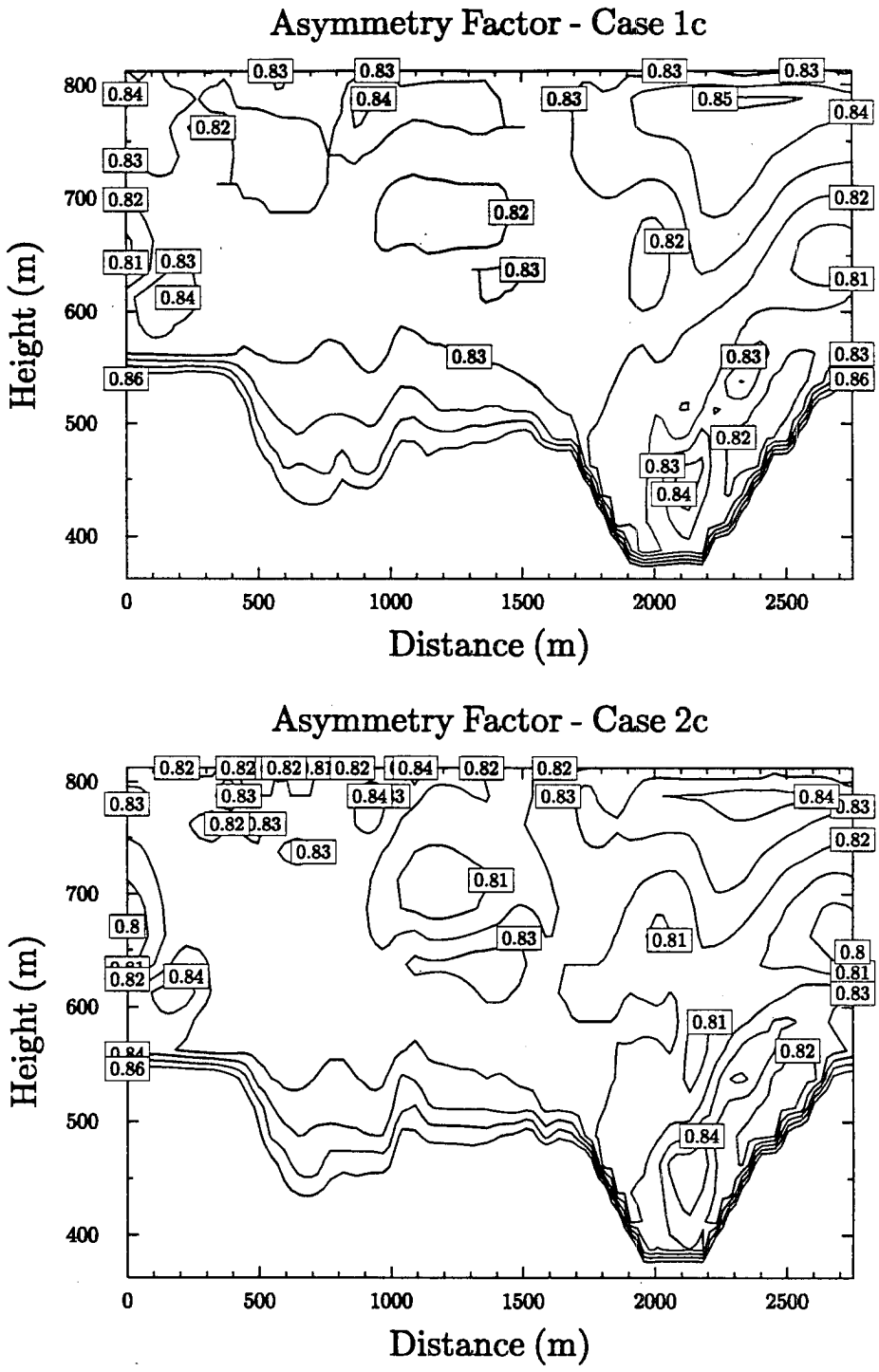

Figure 5.14: The same as Figure 5.11, but for asymmetry factor.

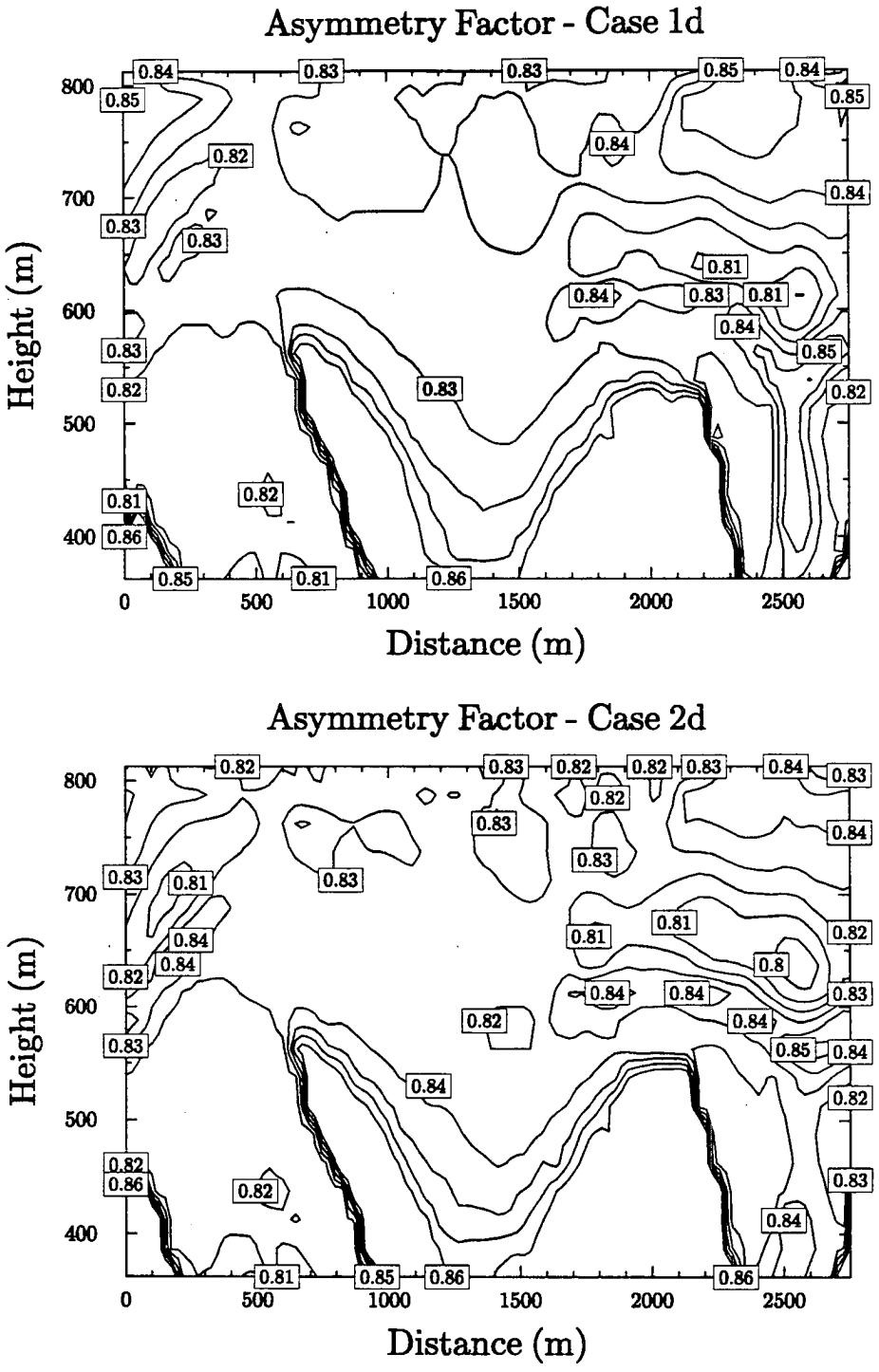

Figure 5.15: The same as Figure 5.12, but for asymmetry factor.

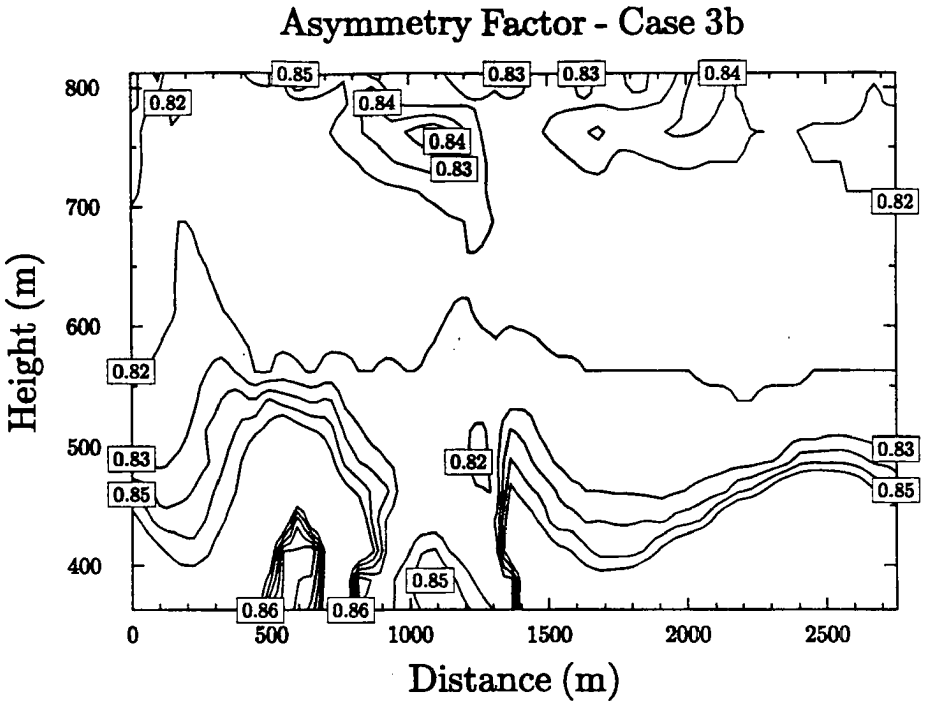

Figure 5.16: The same as Figure 5.13, but for asymmetry factor.

results were obtained for all five cases and for near infrared (0.7 – 2.5 μm) calculations. The small differences in the domain average values suggest that in an unbroken, horizontally stratified cloud like marine stratus, the effects of horizontal transfer of radiation on solar albedos tend to cancel out over large areas. This result was also found by Cahalan et al. (1994) in a comparison between monochromatic IPA calculations and 3D Monte Carlo calculations, and suggest that IPA calculations with spacing of the order of roughly 100 m or less are adequate for accurately computing area-averaged solar albedos in marine stratus.

Figures 5.18 and 5.19 also show the visible albedos computed using PPA compared to the domain average values from the 2D and IPA methods. The albedos computed from PPA were larger that computed from IPA due to the nonlinear relation of albedo to optical depth (Cahalan et al., 1994). Since the decrease in albedo at points with an optical depth below the mean optical depth by a given amount are always larger than the increase in albedo at those points with an optical depth above the mean optical depth by the same

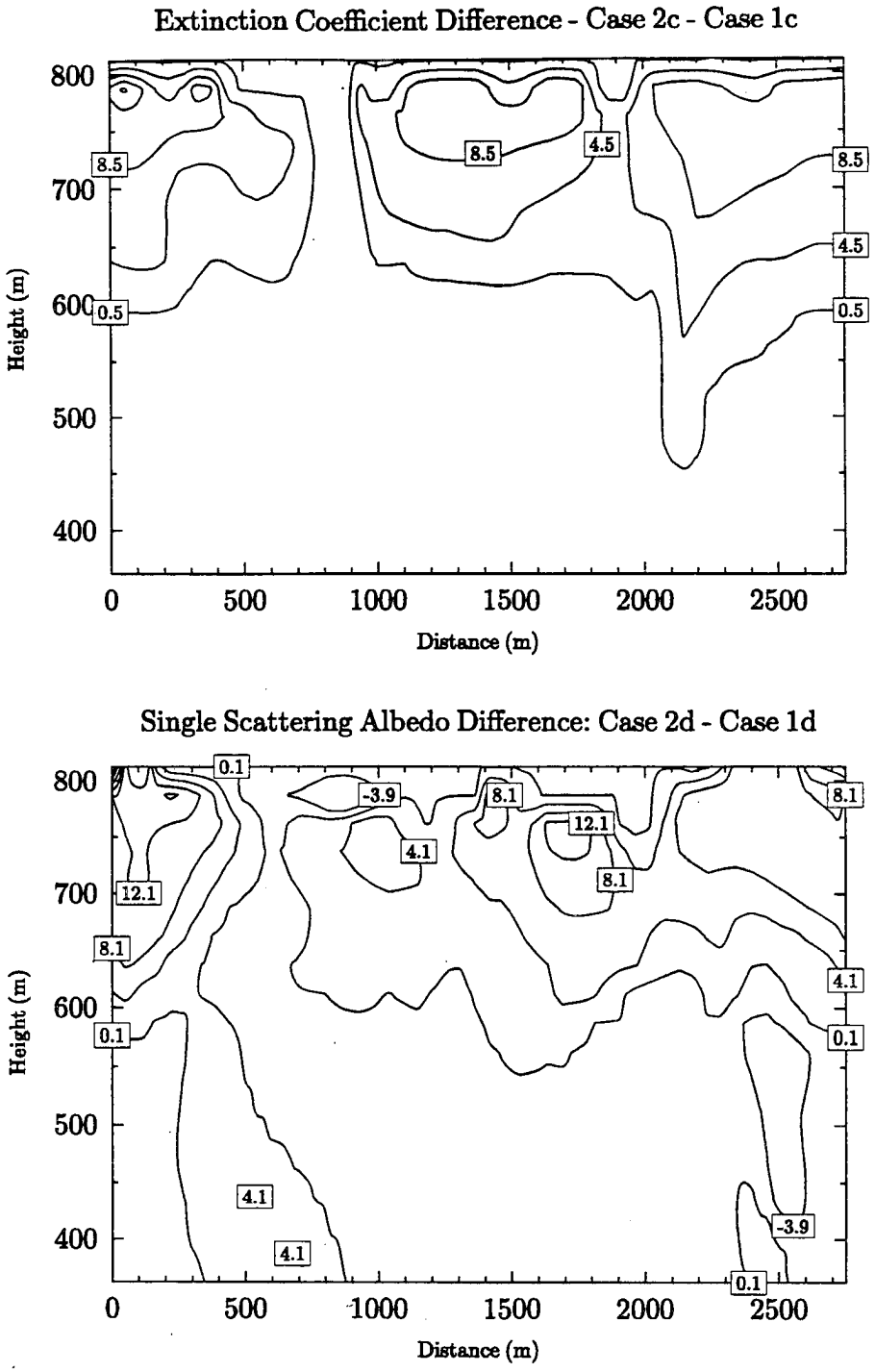

Figure 5.17: The net difference in cloud extinction coefficient between Cases 1c and 2c and between Cases 1d and 2d.

Table 5.1: Layer average difference in cloud optical properties between Cases 2c and 1c.

Layer Height (m)	Ext. Coeff. Diff. (km^{-1})	Alb. Diff.	Asy. Fac.
812.5	-0.010	0.011587	-0.0706
787.5	7.175	0.004450	-0.0071
762.5	8.212	0.004663	-0.0084
737.5	7.359	0.004516	-0.0090
712.5	6.082	0.004231	-0.0093
687.5	4.865	0.003957	-0.0077
662.5	3.650	0.003765	-0.0047
637.5	2.372	0.003652	-0.0022
612.5	1.091	0.003459	-0.0007
587.5	0.414	0.003463	-0.0007
562.5	0.259	0.003613	-0.0012
537.5	0.072	0.001630	-0.0003
512.5	0.014	0.000225	-0.0004
487.5	0.021	-0.004048	0.0021
462.5	0.003	-0.004370	0.0047
437.5	-0.021	-0.003617	0.0040
412.5	-0.002	-0.003219	0.0042
387.5	0	-0.003383	0.0033
362.5	0	-0.001818	0.0003

Table 5.2: Layer average difference in cloud optical properties between Cases 2d and 1d.

Layer Height (m)	Ext. Coeff. Diff. (km^{-1})	Alb. Diff.	Asy. Fac.
812.5	1.854	0.004436	-0.0061
787.5	3.623	0.004010	-0.0073
762.5	7.164	0.004362	-0.0058
737.5	7.258	0.004337	-0.0069
712.5	6.215	0.004117	-0.0082
687.5	4.911	0.003926	-0.0082
662.5	3.489	0.003823	-0.0064
637.5	2.253	0.003891	-0.0021
612.5	0.671	0.003945	0.0006
587.5	-0.149	0.004390	0.0011
562.5	-0.800	0.002863	-0.0020
537.5	-0.627	0.000535	-0.0004
512.5	-0.368	0.002287	-0.0023
487.5	-0.262	0.002419	-0.0015
462.5	-0.143	0.000645	-0.0034
437.5	0.069	0.000536	0.0014
412.5	0.362	0.002149	0.0010
387.5	0.519	-0.001058	0.0006
362.5	0.426	0.002242	0.0015

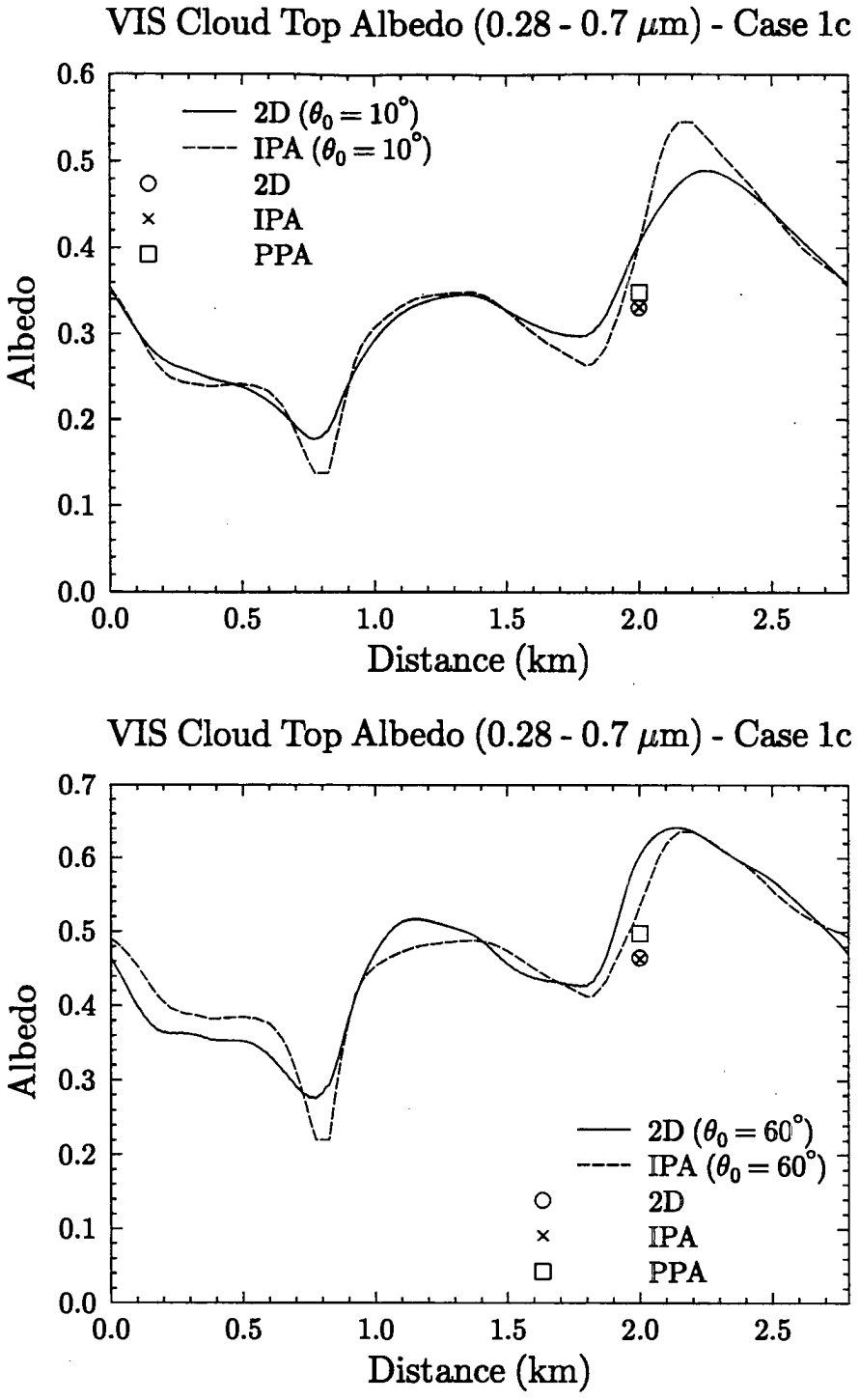

Figure 5.18: The visible (0.28 – 0.7 μm) cloud top albedo computed as a function of horizontal distance in cross section 1c from the 2D and IPA version of the SHSG broadband model for solar zenith angles 10° and 60°. The symbols show the domain average cloud albedo computed from the 2D, IPA and PPA models.

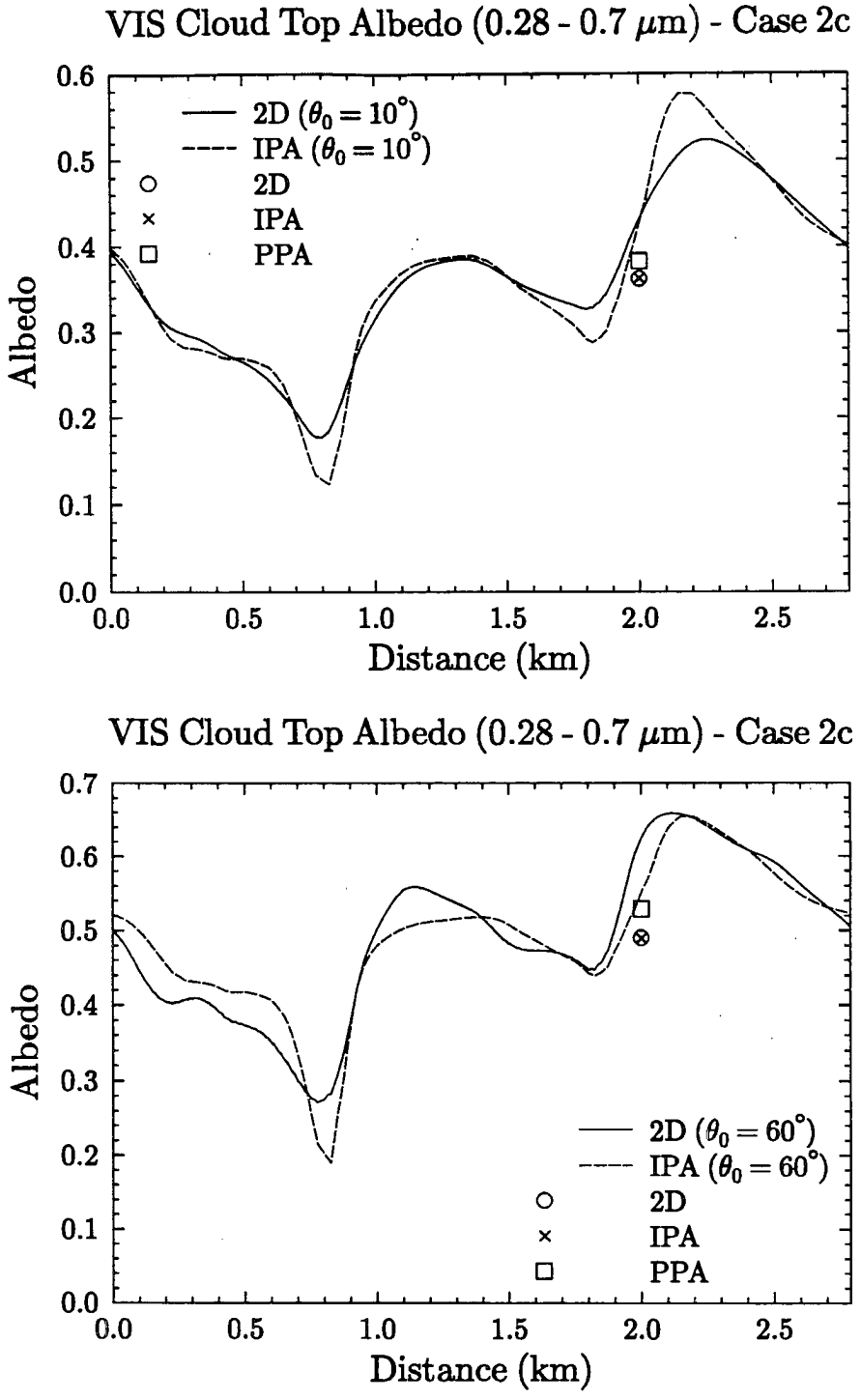

Figure 5.19: The same as Figure 5.18, but for Case 2c.

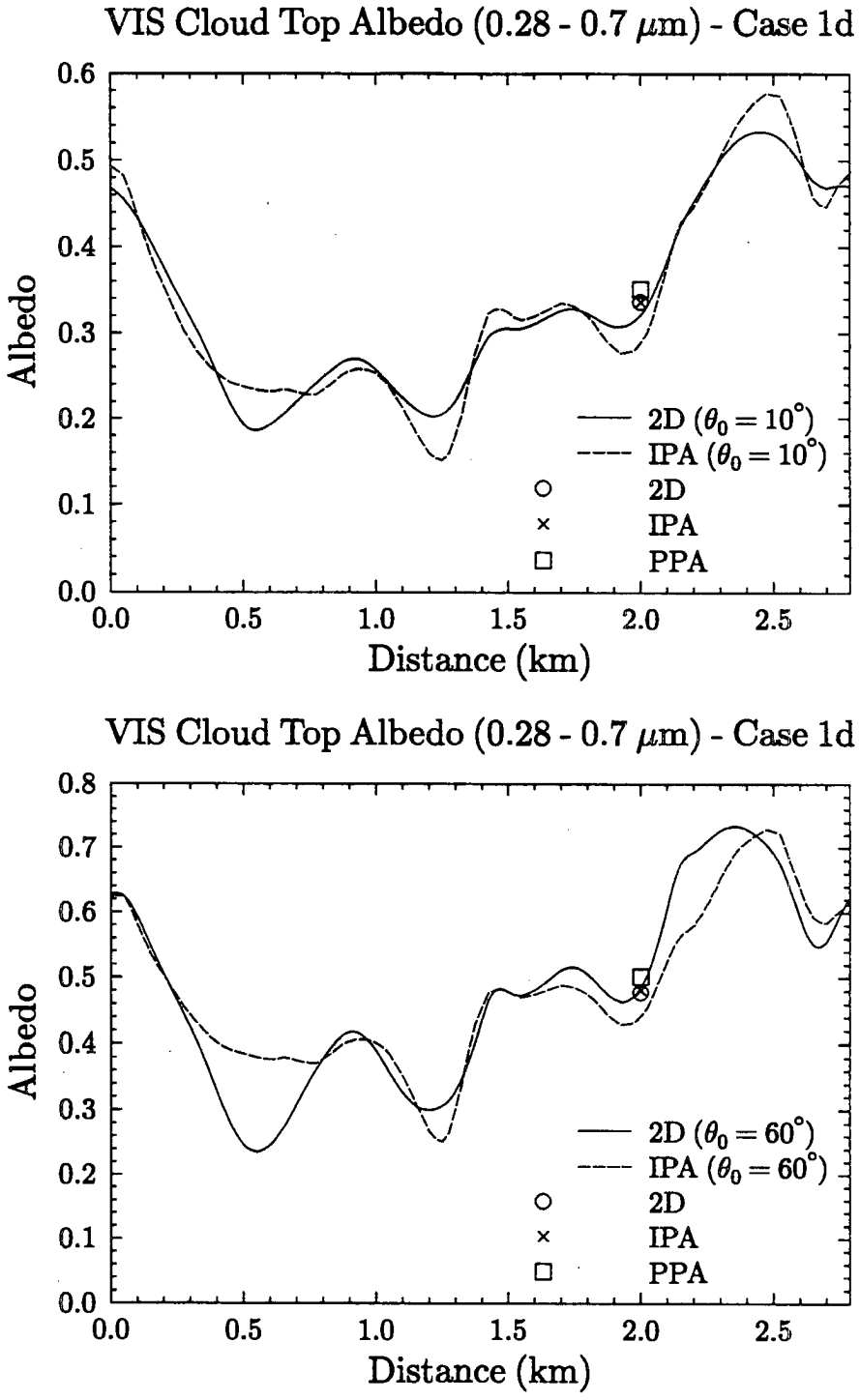

Figure 5.20: The same as Figure 5.18, but for Case 1d.

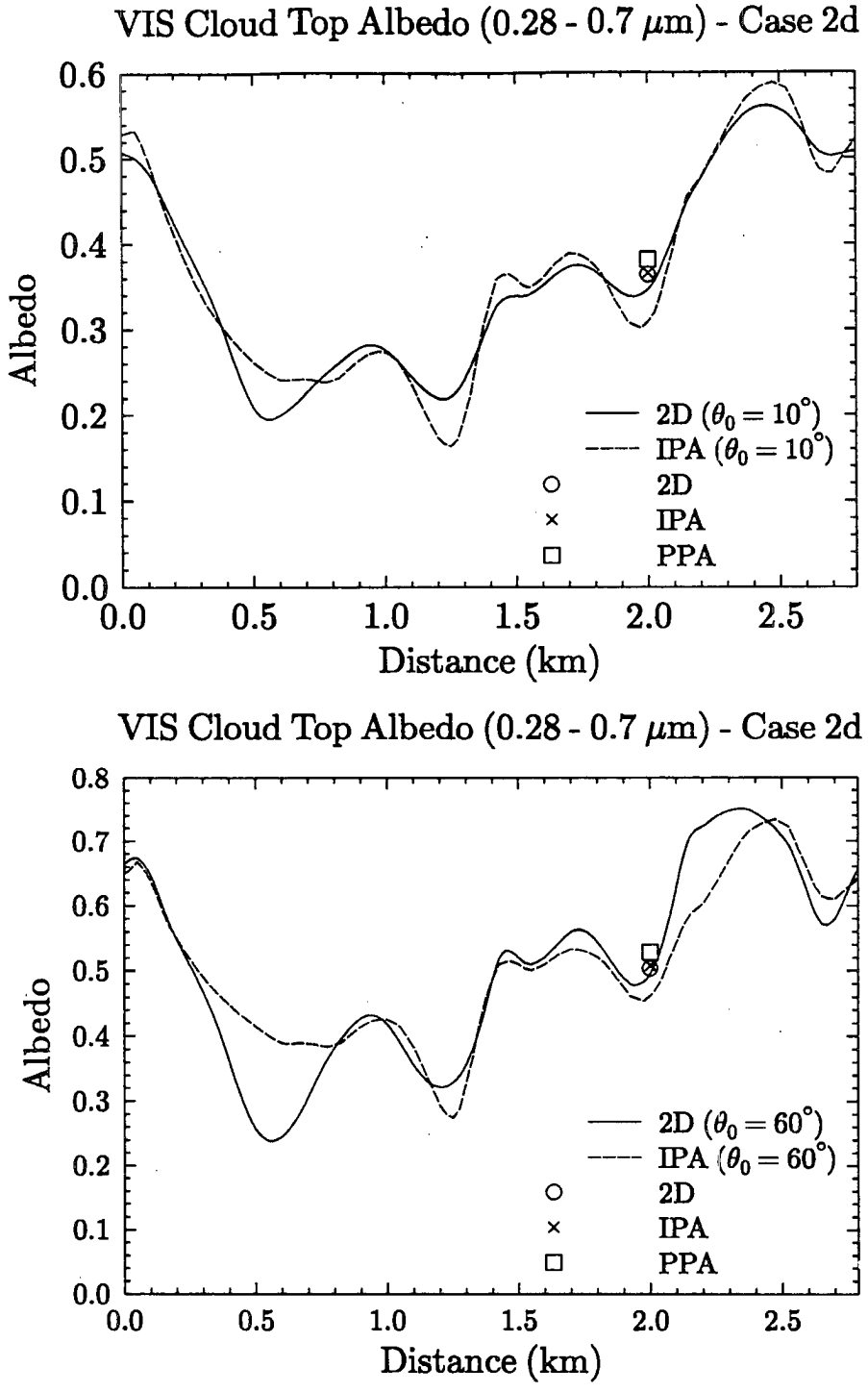

Figure 5.21: The same as Figure 5.18, but for Case 2d.

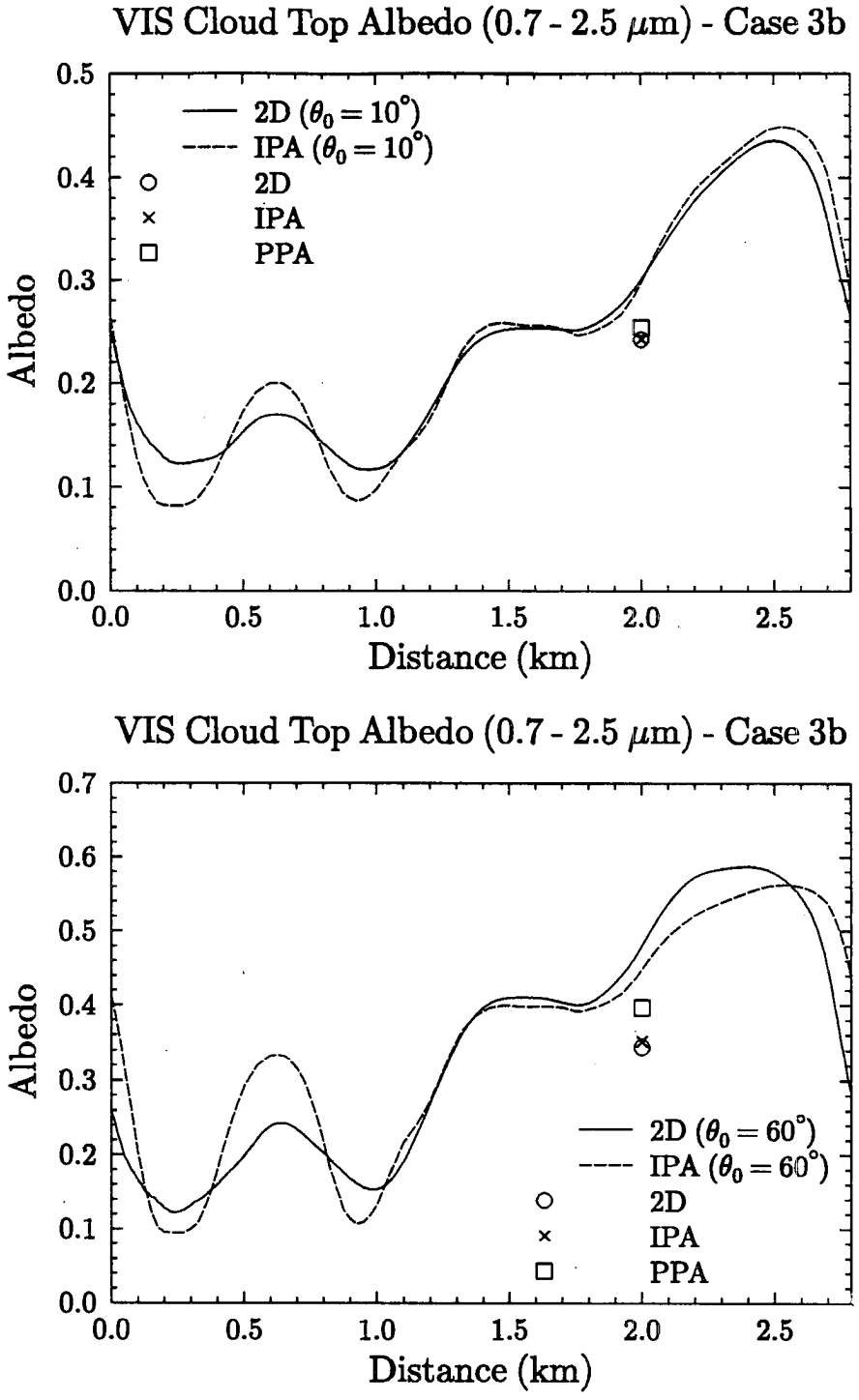

Figure 5.22: The same as Figure 5.18, but for Case 3b.

amount, the PPA albedo will always be larger than the IPA albedo (and the 2D albedo). This difference is even greater in the 60° case since the IPA albedo/optical depth curve was even more convex at this solar zenith angle (see, for example Figure 5.26).

The visible albedos computed for Cases 1d and 2d are shown in Figures 5.20 and 5.21. The results are similar to those from Figures 5.18 and 5.19. Although the point by point differences in these figures were sometimes larger than those in Figures 5.18 and 5.19, the domain averaged values of the 2D and IPA derived albedos were nearly identical. One noticeable difference is the relatively small difference between the PPA and the domain averaged 2D and IPA albedos in Cases 1d and 2d. The relative difference between the domain average 2D and the PPA albedo at $\theta_0 = 60°$ in Cases 1c and 2c were 7.0 and 7.8 percent respectively, while the differences in Cases 1d and 2d were 5.0 and 4.9 percent. Finally, the visible albedos for Case 3b are shown in Figure 5.22. Unlike the other cases, Case 3b was not completely overcast. Assuming that the minimum cloud optical depth necessary for satellite detection using the reference reflectance threshold of Wielicki and Parker (1992) (ie., $R_{clr} + 0.015$) is 0.25, the cloud fraction in Case 3b was roughly 95 percent. The plane parallel approximation in this cross section was therefore computed using a length weighted average of the cloudy and clear sky albedos. The results from the $\theta_0 = 60°$ simulation were the most striking. Case 3b contains two small "holes" centered at 0.23 and 0.90 kilometers. The 2D albedo in the cloudy area between the holes was significantly smaller than the IPA albedo, while the 2D albedos in the "holes" did not completely compensate this difference. Case 3b thus shows the largest discrepancy between the 2D and IPA domain averaged albedos, although the relative difference was still only two percent. The differences between the PPA and domain average 2D and IPA albedos were much larger than in the other cross sections, with a relative difference of over 15 percent. In contrast, the relative PPA/2D albedo difference in the $\theta_0 = 10°$ case was only 4.6 percent.

2D domain average versus PPA albedos - Macrophysics

Several observations about the role of cloud inhomogeneity on cloud albedo can be made from the plots of visible albedo shown above. As previously mentioned, on the size

scale of at least a few kilometers, the effects of the horizontal transport of visible light tend to cancel out in the calculation of the domain average albedo. At small solar zenith angles some solar radiation is transported away from the thicker parts of the cloud toward thinner parts and the overall albedo field is smoothed compared to the IPA calculated field. At larger solar zenith angles the horizontal transport exhibits shadowing effects near extinction maxima, with a decrease in the albedo on the shadow side of the extinction peak and an increase on the illuminated side of the peak. The mean albedo computed in the 2D medium, however, is nearly identical to that computed using the independent pixel approximation.

When the domain average 2D albedo is compared to the PPA, larger discrepancies occur than between the domain averaged 2D and IPA albedos. In Cahalan et al. (1994), the positive bias in the PPA albedo compared to the IPA albedo was explained by the nonlinear relationship between cloud reflectivity and optical depth. The magnitude of the plane parallel albedo bias in a simple fractal model of marine stratocumulus was found to be related to the fractal parameter f, which in turn is related to the standard deviation of the logarithm of vertically integrated liquid water path (W). Since the fractal model assumes a constant effective radius, the liquid water path is linearly related to optical depth. In more realistic clouds like those simulated in the RAMS model, effective radius is not constant in the cloud. A better quantity to estimate a quantity like f in a model of more realistic marine stratus would be the standard deviation of the optical depth. Figures 5.23 – 5.25 show normalized probability distributions of the logarithm of optical depth for each cross section at three different bands. The distributions for Cases 1c, 1d, 2c and 2d were all similar and have similar values of the standard deviation of $\log(\overline{\tau})$ (0.237, 0.249, 0.249, and 0.246 respectively). The standard deviation values showed very little sensitivity to wavelength, and none of the three bands showed any tendency to have consistently larger or smaller values than the other bands. These values are considerably smaller than the value presented in Cahalan et al. (1994) as typical of the marine stratocumulus measured during the FIRE-I experiment in July 1987 (0.39). This explains why the PPA biases measured in the RAMS clouds were so much smaller than those in Cahalan et al. (1994).

Estimating from Figure 3 of Cahalan et al. (1994), the standard deviation in $\log \tau$ from the RAMS cross sections would produce relative biases of the range from 6 to 8 percent. This compares well with the relative biases computed for Cases 1c and 2c (from 5 to 8 percent) but is slightly higher than the biases computed for Cases 1d and 2d (4 to 5 percent). In Case 3b the distribution of $\log \tau$ is much wider than the other distributions, and the standard deviation is nearly twice as large, 0.468. This value is even larger than that measured during the FIRE-I experiment and would produce a PPA bias around 26 percent. However, that figure is based on a cloud with a much larger mean optical depth than that in Case 3b (15 versus 4). For thinner clouds the PPA bias is smaller since the relationship between albedo and optical depth is more linear.

The slightly smaller PPA bias in Cases 1d and 2d can also be explained by the relationship between albedo and optical depth. Figures 5.26 through 5.30 present graphs of the visible albedo calculations versus optical depth (Band 12) for each of the five cross sections. In all five cases, the IPA albedos closely followed a curve, while the 2D albedos tended to be more variable and fall above and below the IPA curve and the PPA albedos usually appeared at a single point along the IPA curve. Figure 5.30 shows that the deviations in the 2D albedos from the IPA albedo curves correspond to the illuminated and shaded parts of the cloud. This correlation is especially evident in Figure 5.30b, where illuminated parts of the cloud turrets between 1.8 and 2.575 km are above the IPA curve and shaded parts of the cloud between 2.575 and 2.8 km, and in the first 0.15 km of the horizontal domain, are below the albedo curve. Although the variability of the 2D albedos as a function of optical depth increased in the $\theta_0 = 60°$ calculations and increased slightly in the enhanced CCN cases, as shown above the domain average 2D albedos were nearly identical to the IPA albedos. Note that the IPA albedo curves in the $\theta_0 = 10°$ calculations tend to be straighter than those in the $\theta_0 = 60°$ calculations, and this explains the lower PPA biases at the smaller solar zenith angle. The difference in the curves is most clearly seen in Figure 5.26 which has the same vertical and horizontal scales for both graphs. While the IPA albedo curves in Cases 1c and 2c generally show a

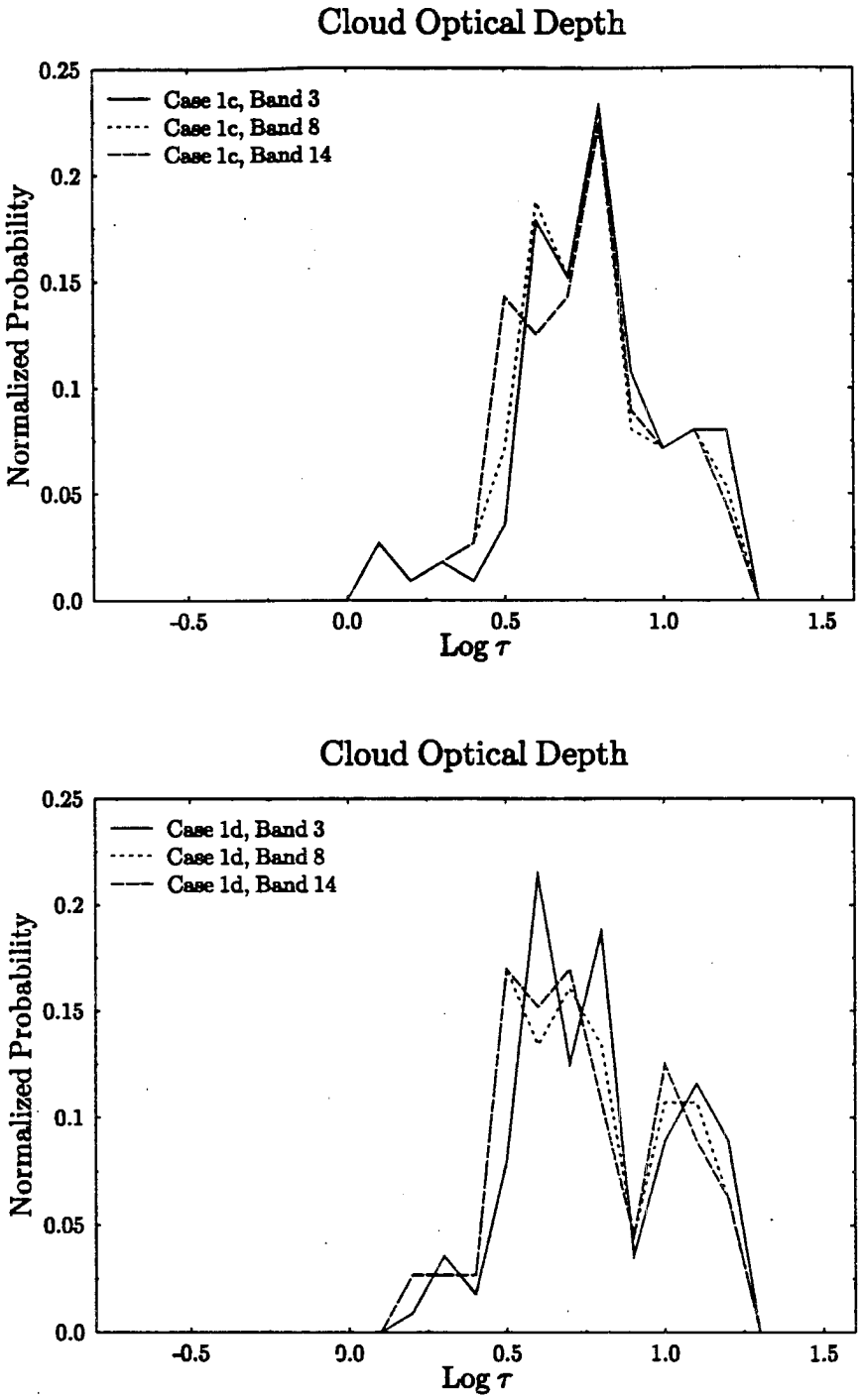

Figure 5.23: The normalized probability distributions of $\log \tau$ for Cases 1c and 1d at three different model bands.

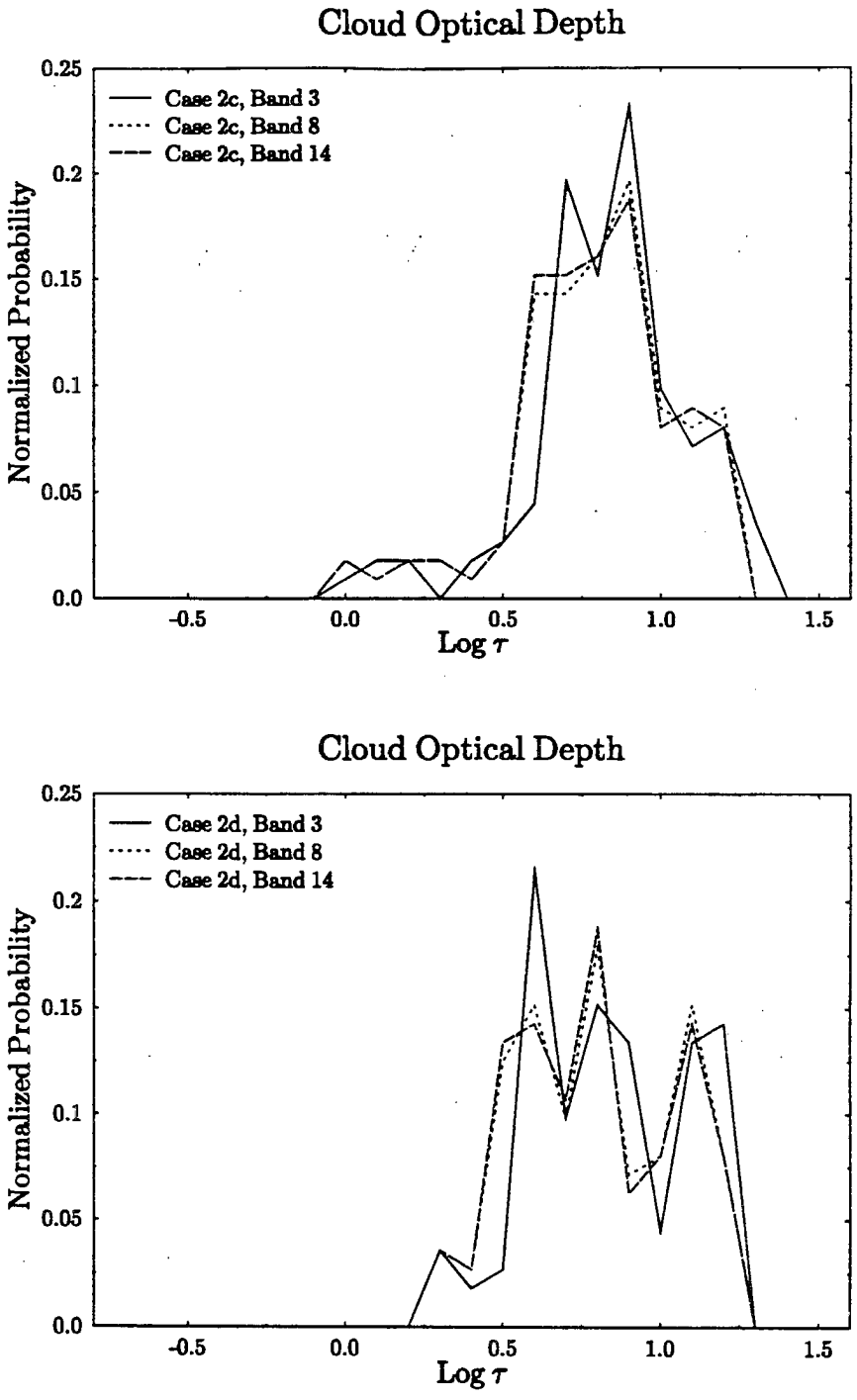

Figure 5.24: The same as Figure 5.23, but for Cases 2c and 2d.

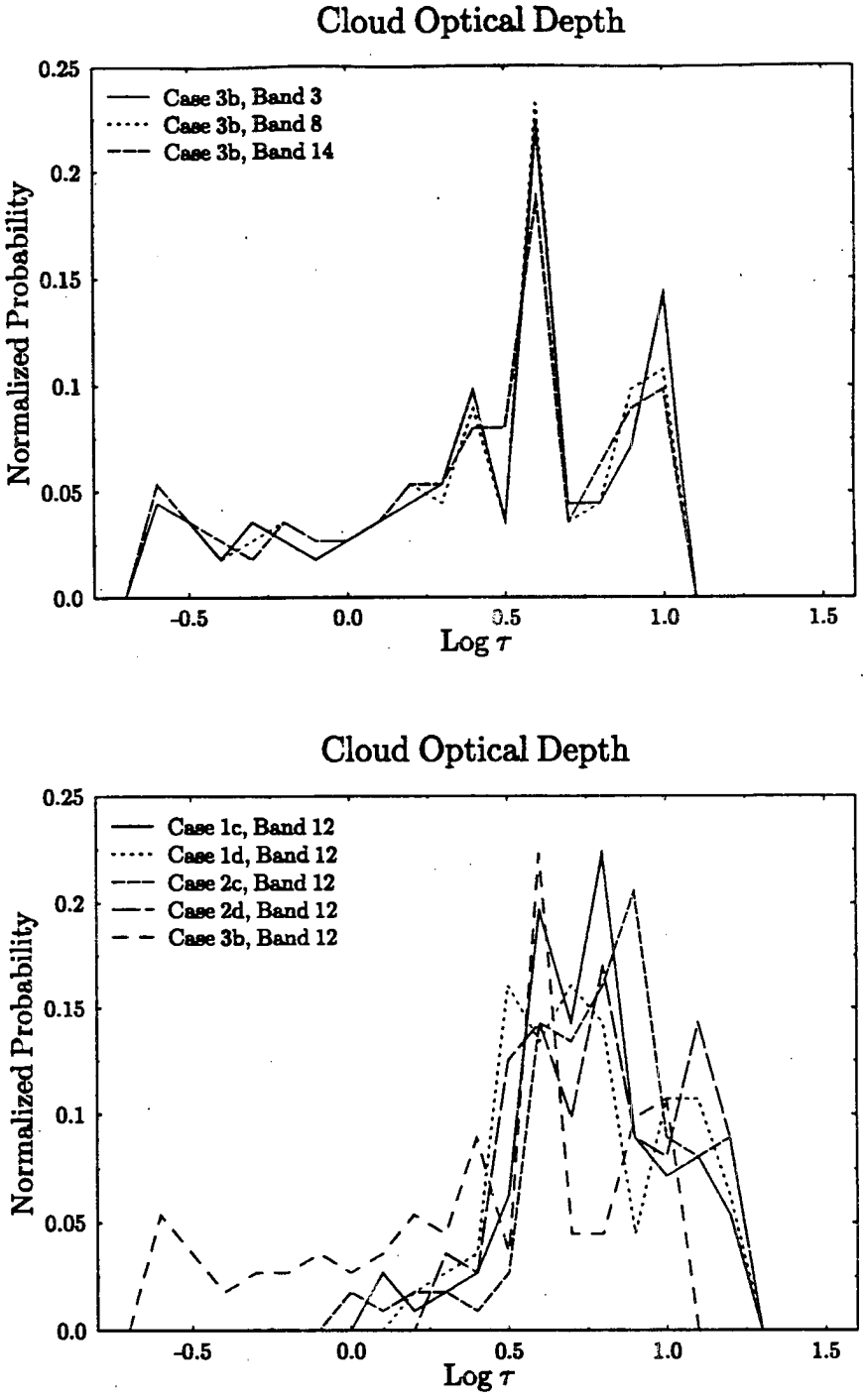

Figure 5.25: The normalized probability distributions of $\log \tau$ for Cases 3b at three different model bands, and the distributions for five RAMS cross sections at Band 12 (14550 – 25000 cm^{-1}.)

convex shape throughout the entire range of optical depths, the curves in Cases 1d and 2d deviate from this curvature. For the solar zenith angle of 10 degrees, the albedo curves become nearly linear for optical depths greater than 5. In the $\theta_0 = 60°$ calculations, the curve becomes concave at the largest optical depths. The concavity of the albedo/optical depth relationship reduces the PPA bias in these cases.

When the arithmetic mean of the effective radius in each cloud cross section is plotted versus optical depth, the reason for the shape of the albedo/optical depth curves becomes apparent. Figure 5.31 shows the relationship between mean effective radius and optical depth for all five cross sections. Cases 1c, 1d, 2c and 2d have a downward trend in effective radius as optical depth increases with a secondary maximum around an optical depth of 10 – 12. Since for a given optical depth clouds with smaller droplets are more reflective than clouds with larger droplets, the effective radius/optical depth relationship can change the shape of the IPA albedo curves. In Cases 1d and 2d the secondary peak is much more pronounced and results in the concavity of the albedo/optical depth relation at optical depths greater than 12. It is noted that when the liquid water path is held constant, the optical depth will be inversely proportional to effective radius since for solar wavelengths optical depth can be approximated by

$$\tau = \frac{3}{2}\frac{W}{\rho_\ell R_e}, \tag{5.2}$$

where W is the liquid water path in g m^{-2}, ρ_ℓ is the density of liquid water in g cm^{-3} and R_e is effective radius in microns. A roughly inverse relationship between optical depth and effective radius was also observed in marine stratocumulus clouds during FIRE (Nakajima et al., 1991). However, the trend in Case 3b is toward increasing effective radius with increasing optical depth which helps to increase the magnitude of the PPA bias. When the entire RAMS domain was sampled (Figure 5.32) no clear relationship between optical depth and effective radius was found since the effective radius is directly proportional to liquid water path (Figure 5.33). Therefore, for an entire RAMS model cloud the overall effect of the effective radius variations on the PPA albedo bias would be diminished by

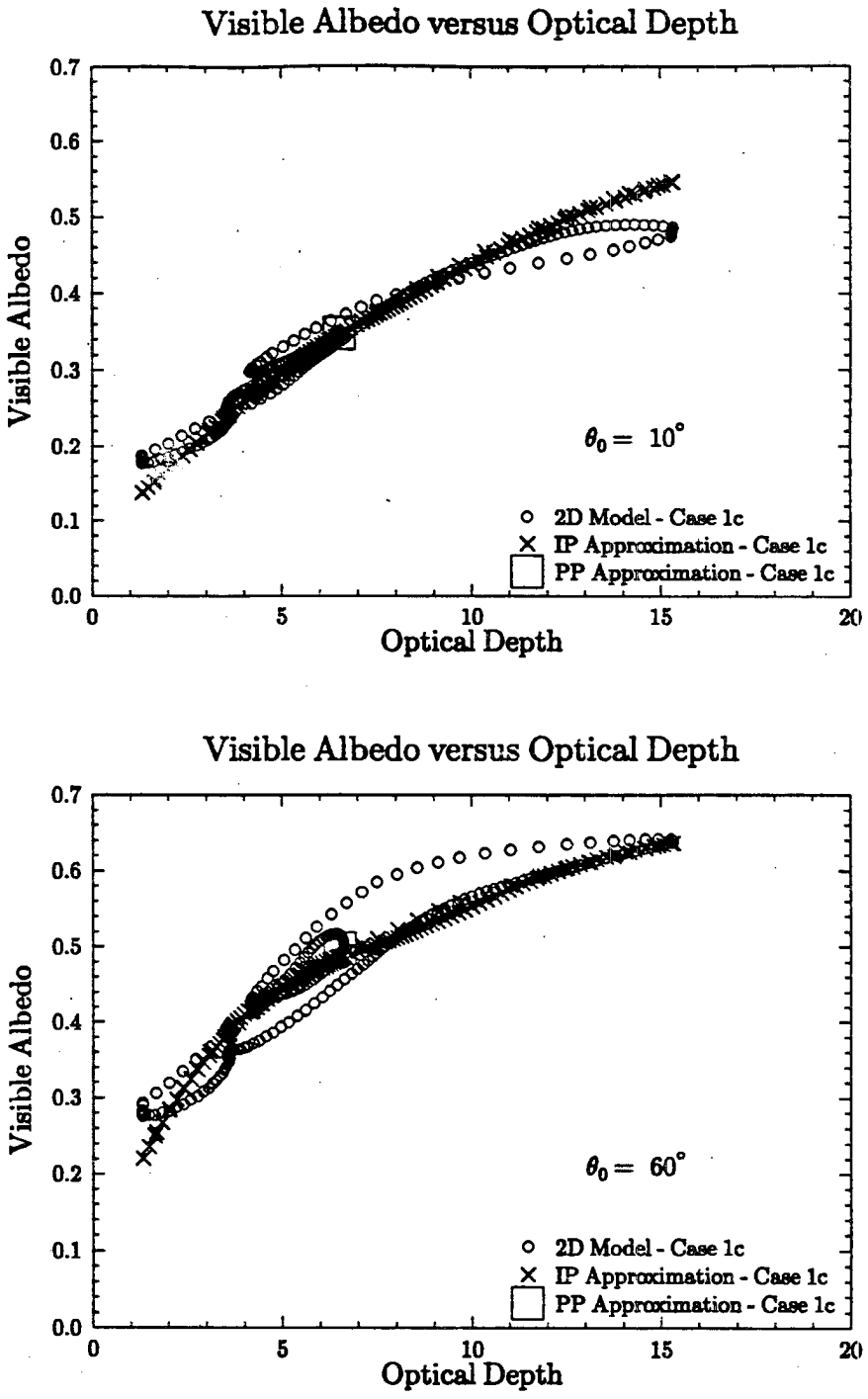

Figure 5.26: The visible albedos compu i for Case 1c at $\theta_0 = 10°$ and $\theta_0 = 60°$ as a function of cloud optical depth in Band 12 for the 2D, IPA and PPA models.

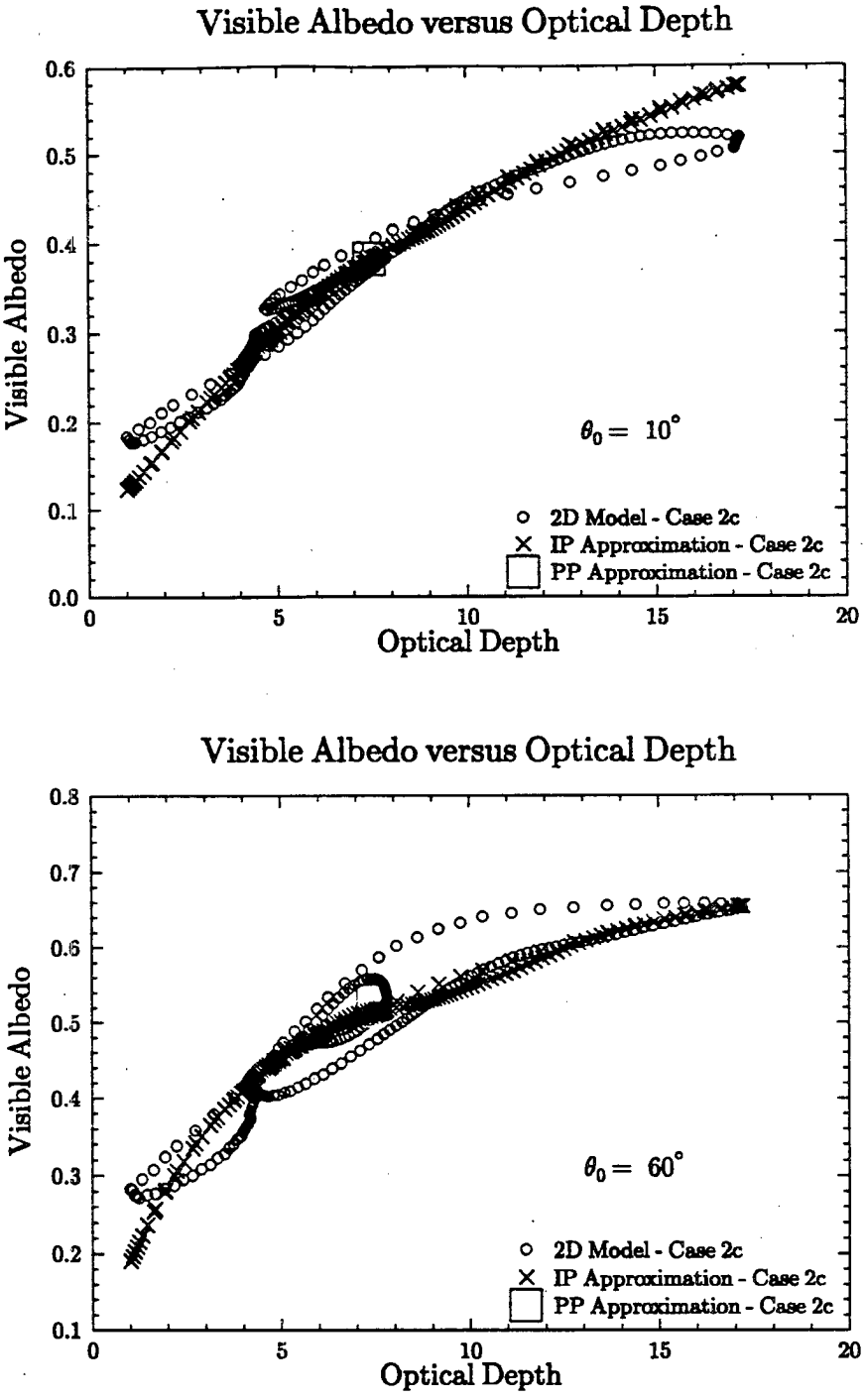

Figure 5.27: The same as Figure 5.26, but for Case 2c.

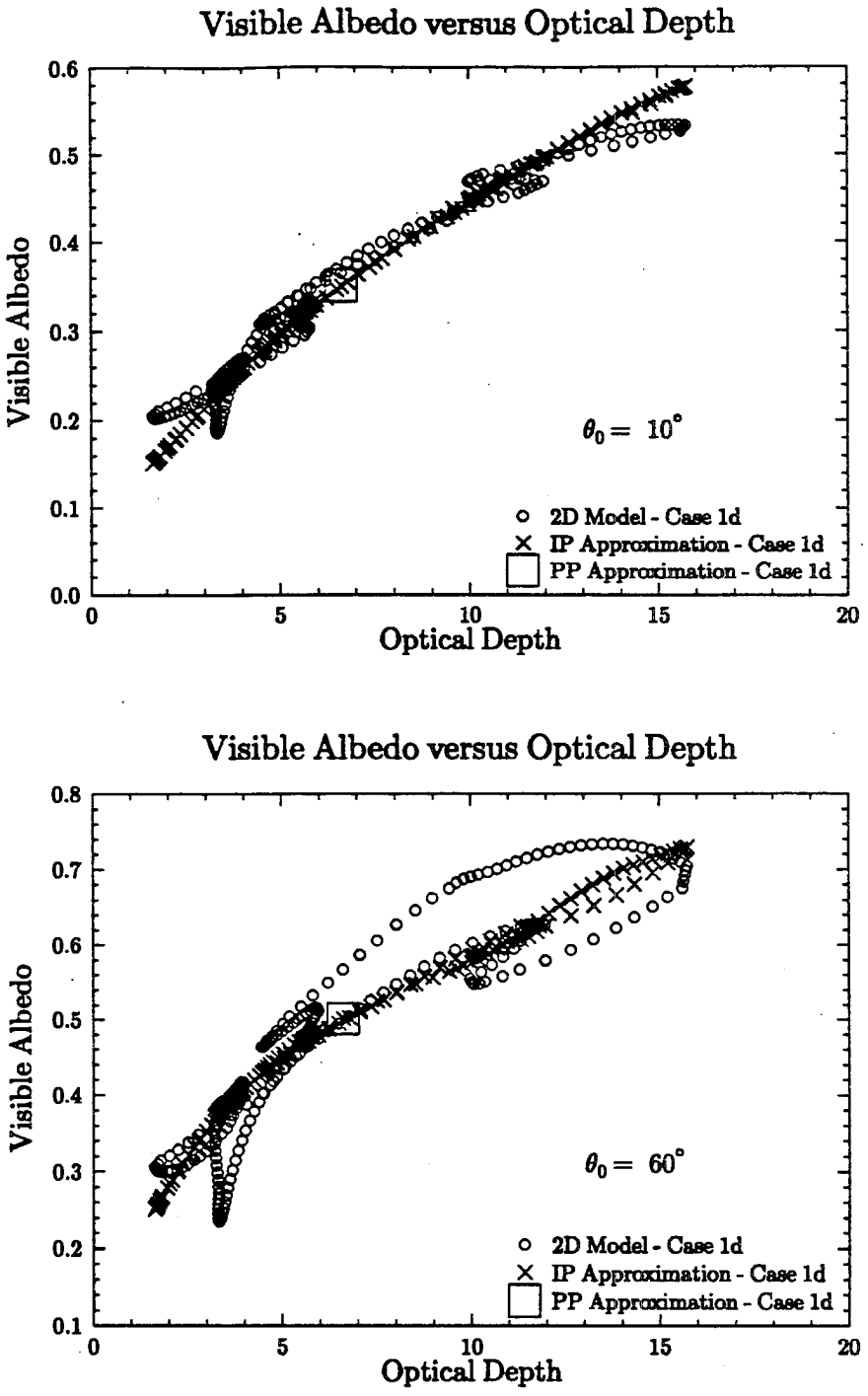

Figure 5.28: The same as Figure 5.26, but for Case 1d.

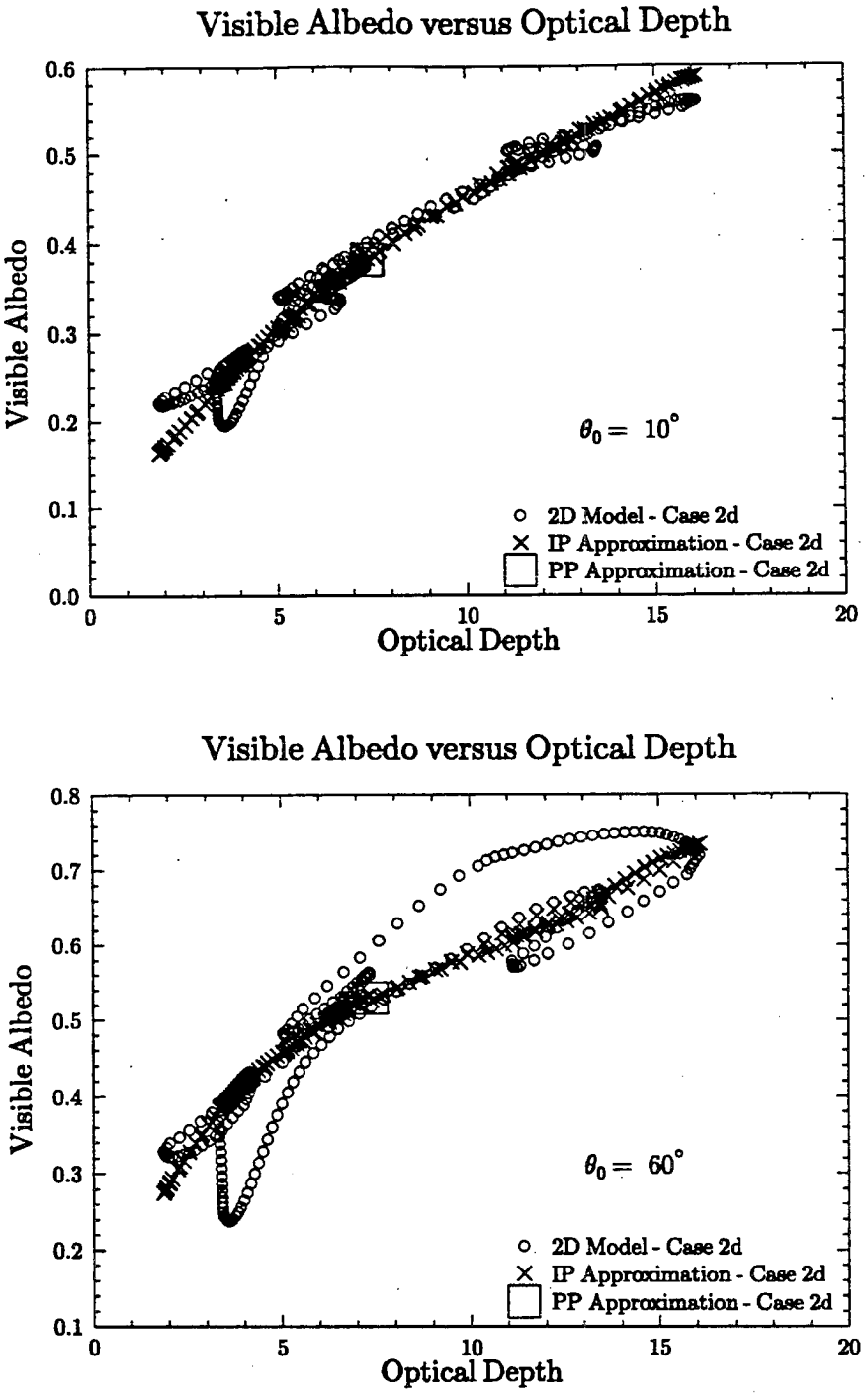

Figure 5.29: The same as Figure 5.26, but for Case 2d.

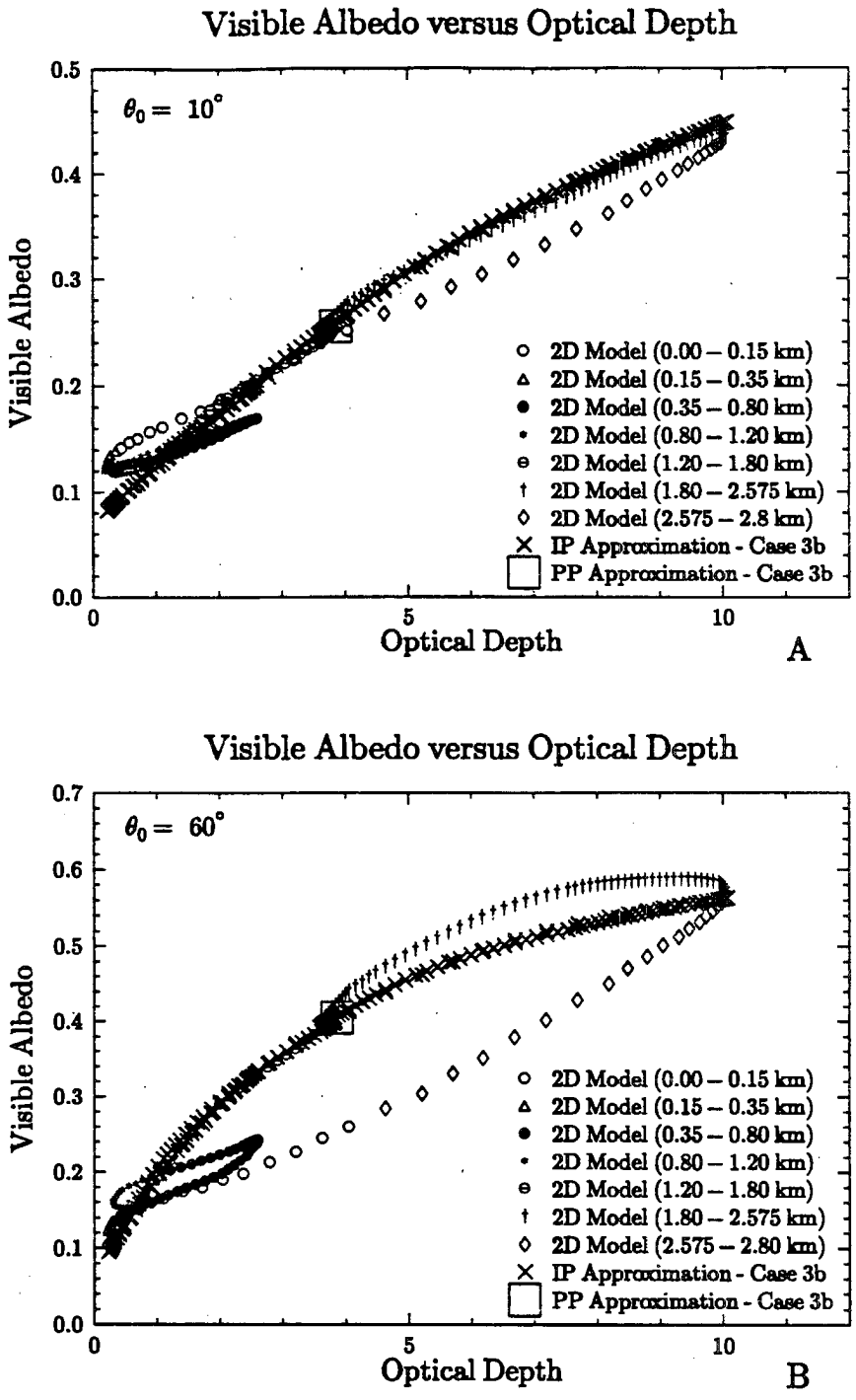

Figure 5.30: The same as Figure 5.26, but for Case 3b. The 2D model results are shown at different segments of the model domain in order to highlight the local effects of shading on cloud albedo.

the lack of correlation between effective radius and optical depth. (In Figures 5.32 and 5.33, the effective radius was computed by weighting the effective radius in a column by its liquid water path:

$$R_e = \frac{\sum_{i=1}^{N} W_i R_{e_i}}{W} \tag{5.3}$$

where N is the total number of vertical layers in a column where the mean liquid water content is greater than 0.005 g m^{-3}, W_i is the liquid water path in layer i in g m^{-2}, R_{e_i} is the arithmetic mean of the effective radius in layer i, and W is the total liquid water path in the column.)

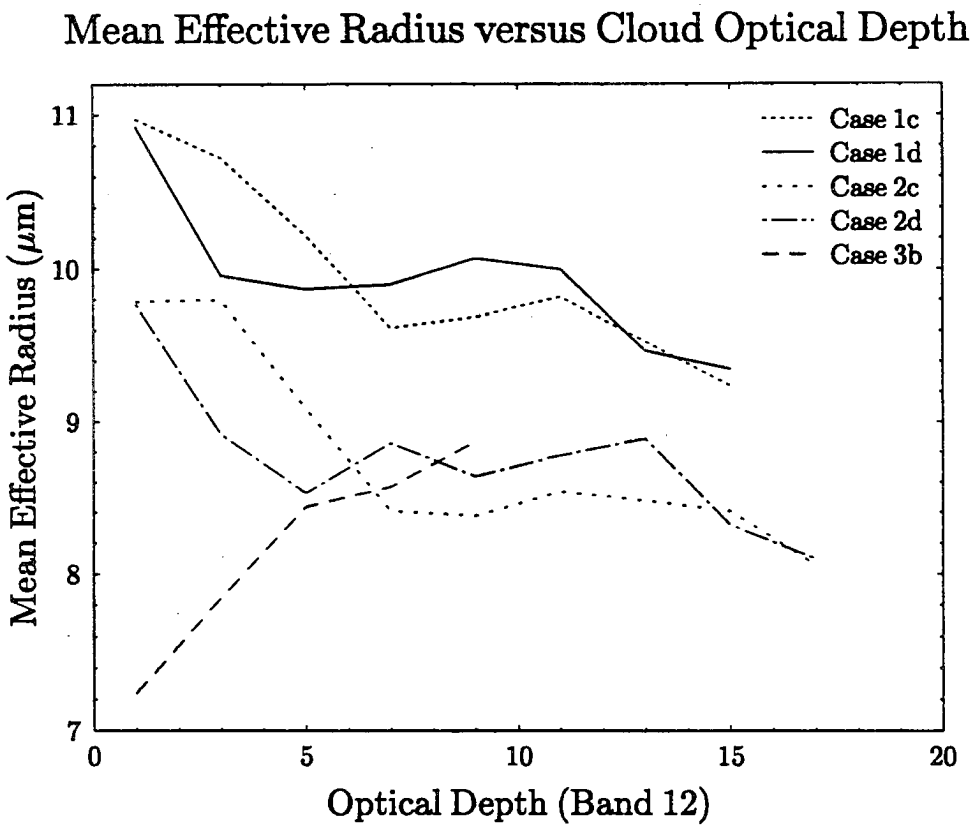

Figure 5.31: The arithmetic mean of effective radius in the cloud as a function of the optical depth (at Band 12) in the column. The effective radius values were binned into 0.5 wide ranges of optical depth from 0 to 17. The lines show the relationships for five RAMS cross sections.

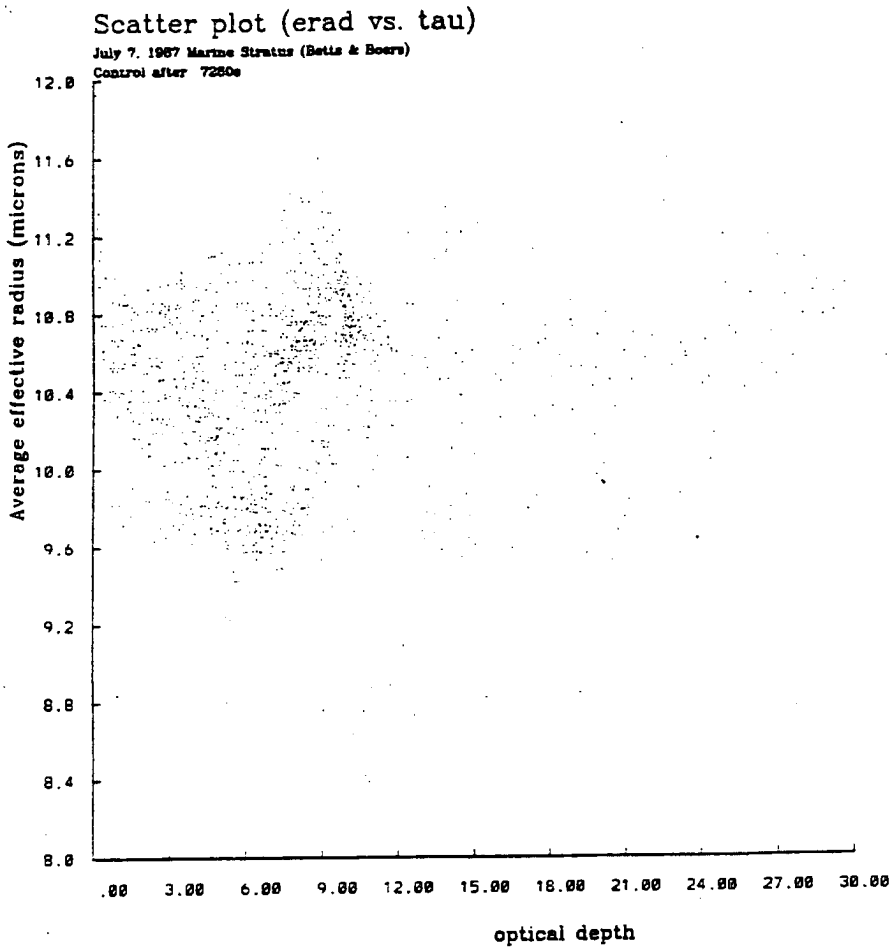

Figure 5.32: The mean effective radius as a function of optical depth for the entire model domain in the control run at 7260 seconds.

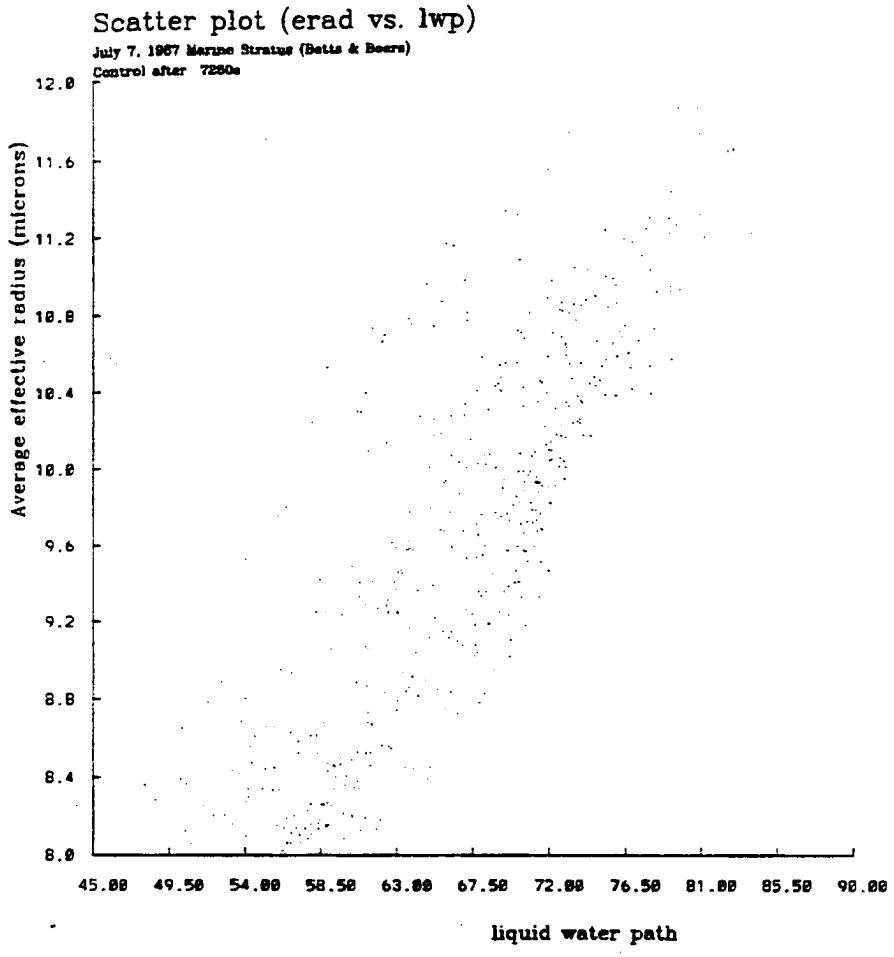

Figure 5.33: The mean effective radius as a function of liquid water path for the entire model domain in the control run at 7260 seconds.

Control CCN case albedos versus enhanced CCN case albedos - Microphysics

Table 5.3 presents the absolute and relative differences in the domain averaged visible albedos between Cases 2c and 1c and between Cases 2d and 1d for all three radiative transfer computations. The albedos in the enhanced CCN cases are approximately 3 percent larger (absolute difference) than those in the control CCN cases, and result from the changes in the microphysical and radiative properties of the individual droplets described above.

Table 5.3: Absolute and relative differences (in percent) in the domain averaged visible (0.28 – 0.7 μm) albedos between the enhanced CCN cross sections and the control CCN cross sections.

Case	θ_0 (degrees) angle	RTM	Absolute difference	Relative difference
2c - 1c	10	2D	3.12 %	9.4 %
		IPA	3.11 %	9.4 %
		PPA	3.42 %	9.8 %
	60	2D	2.53 %	5.4 %
		IPA	2.59 %	5.6 %
		PPA	3.10 %	6.2 %
2d - 1d	10	2D	2.80 %	8.3 %
		IPA	2.95 %	8.8 %
		PPA	3.14 %	9.0 %
	60	2D	2.66 %	5.6 %
		IPA	2.75 %	5.7 %
		PPA	2.75 %	5.5 %

The differences between Cases 2c and 1c are slightly larger than those between Cases 2d and 1d when the solar zenith angle was 10 degrees. This may reflect the slightly larger microphysical and optical property differences between the former pair of cross sections. The optical property differences will be most noticeable at the smaller solar zenith angles since the radiative transfer will include less multiple scattering than at larger solar zenith angles. For example, the slight difference in the increase in optical depth between Case 2c and 1c compared the corresponding increase between Case 2d and 1d will have the greatest impact when the sun is overhead. When the sun is low, multiple scattering will

tend to minimize the effects of the small differences in optical depth. Multiple scattering effects also explain why the relative differences in albedo are nearly twice as large in the $\theta_0 = 10°$ cases compared to the $\theta_0 = 60°$ cases.

5.2.2 Near infrared (0.7 μm – 2.5 μm)

Figures 5.34 through 5.38 show a series of broadband near infrared (0.7 – 2.5 μm) albedo calculations for the five cross sections. The relationship between the 2D and IPA albedos were the same as those for the 2D and IPA visible albedos shown in Figures 5.18 – 5.22. Once again the shadowing effects of the extinction maxima were evident in the $\theta_0 = 60°$ cases, and the domain averaged values of 2D and IPA albedos were nearly identical.

Macrophysics – Part 2

A comparison of the 2D and IPA domain averaged near infrared albedos with the PPA albedos show that the PPA biases in the near infrared are slightly different than the visible counterparts. In particular, the PPA biases in Cases 1d and 2d are larger. The changes in Cases 1c and 2c are mixed, with larger near infrared PPA biases at $\theta_0 = 10°$ and relatively smaller biases at $\theta_0 = 60°$. Inspection of the near infrared albedo versus optical depth curves in Figures 5.39 – 5.43 show that some differences in the PPA biases between the visible and the near infrared can be explained by differences in the respective IPA albedo/optical depth relationships. For example, the IPA curves for near infrared albedo in Cases 1d and 2d at a solar zenith angle of 10 degrees are more concave than the corresponding visible albedo curves. A plot of the mean effective radius with the near infrared optical depth (Band 6) in Figure 5.44 was nearly the same as the the R_e/visible optical depth plot in Figure 5.31. Overall, it appears that absorption at near infrared wavelengths may reduce the influence of effective radius changes on the PPA bias. The range of the relative PPA bias in Cases 1c, 1d, 2c and 2d in the visible albedos was from 4.3 percent to 7.8 percent, while the range in the near infrared PPA albedo bias was from 5.4 percent to 6.9 percent.

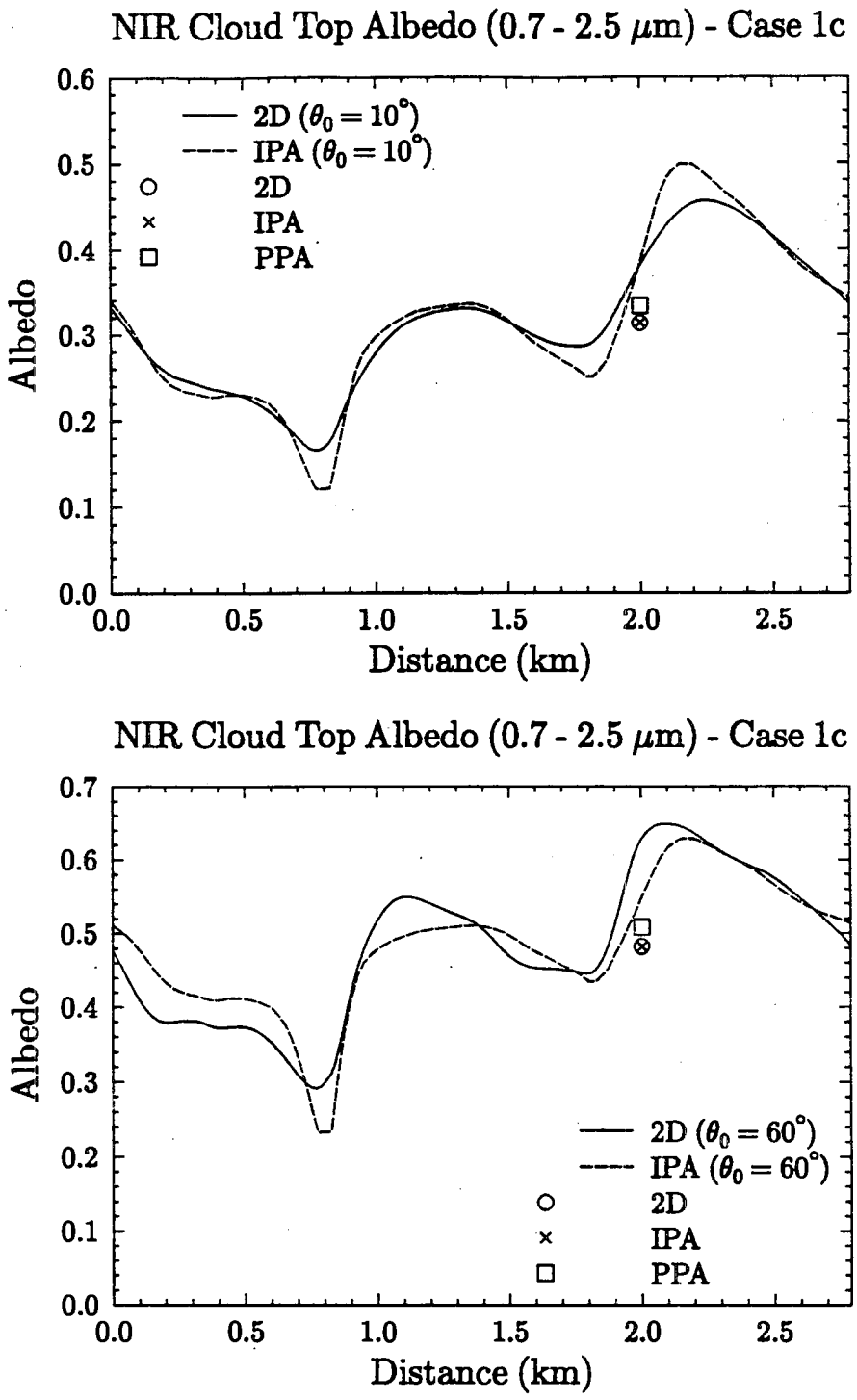

Figure 5.34: The same as Figure 5.18, but for near infrared albedo (0.7 – 2.5 μm).

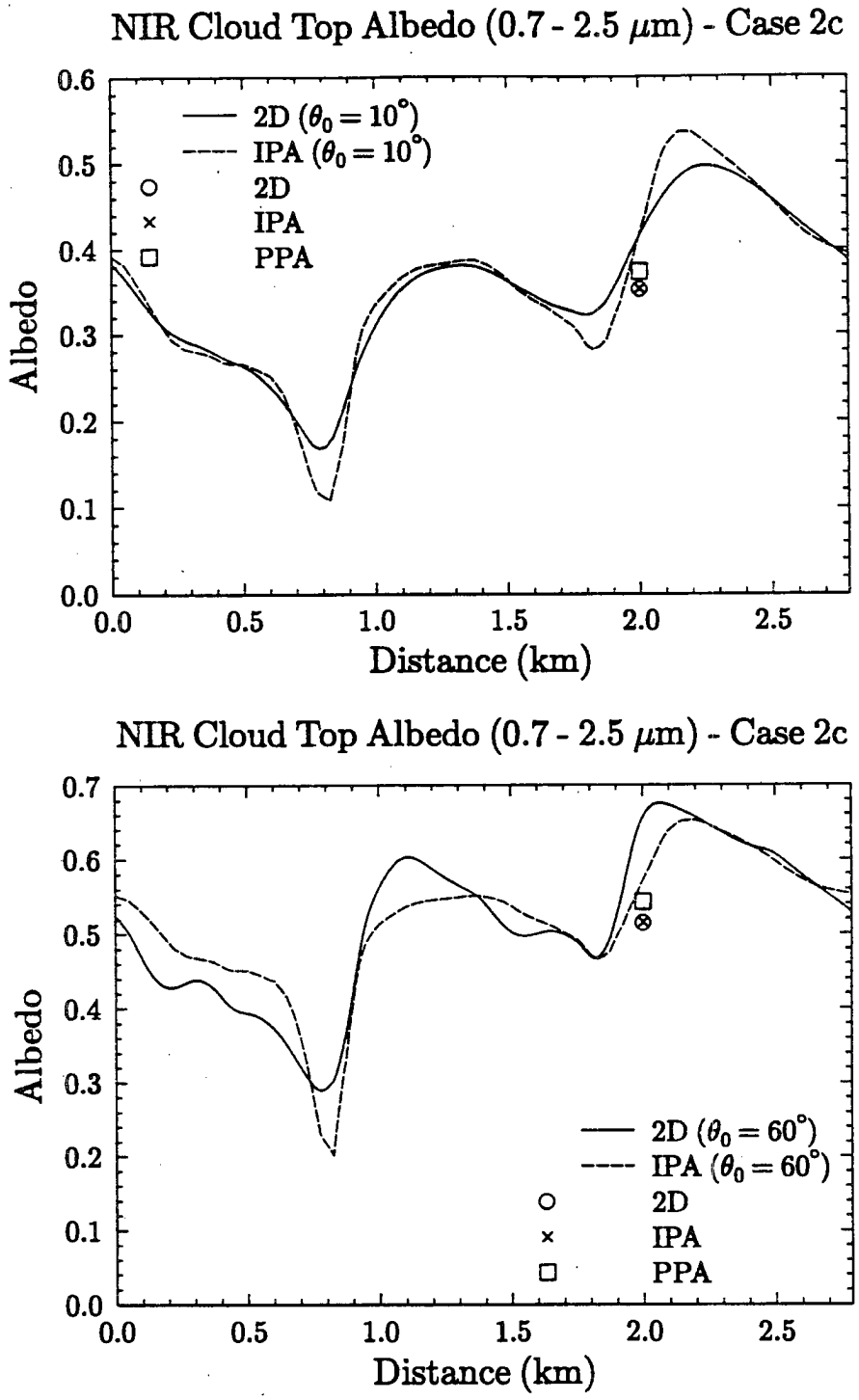

Figure 5.35: The same as Figure 5.34, but for Case 2c.

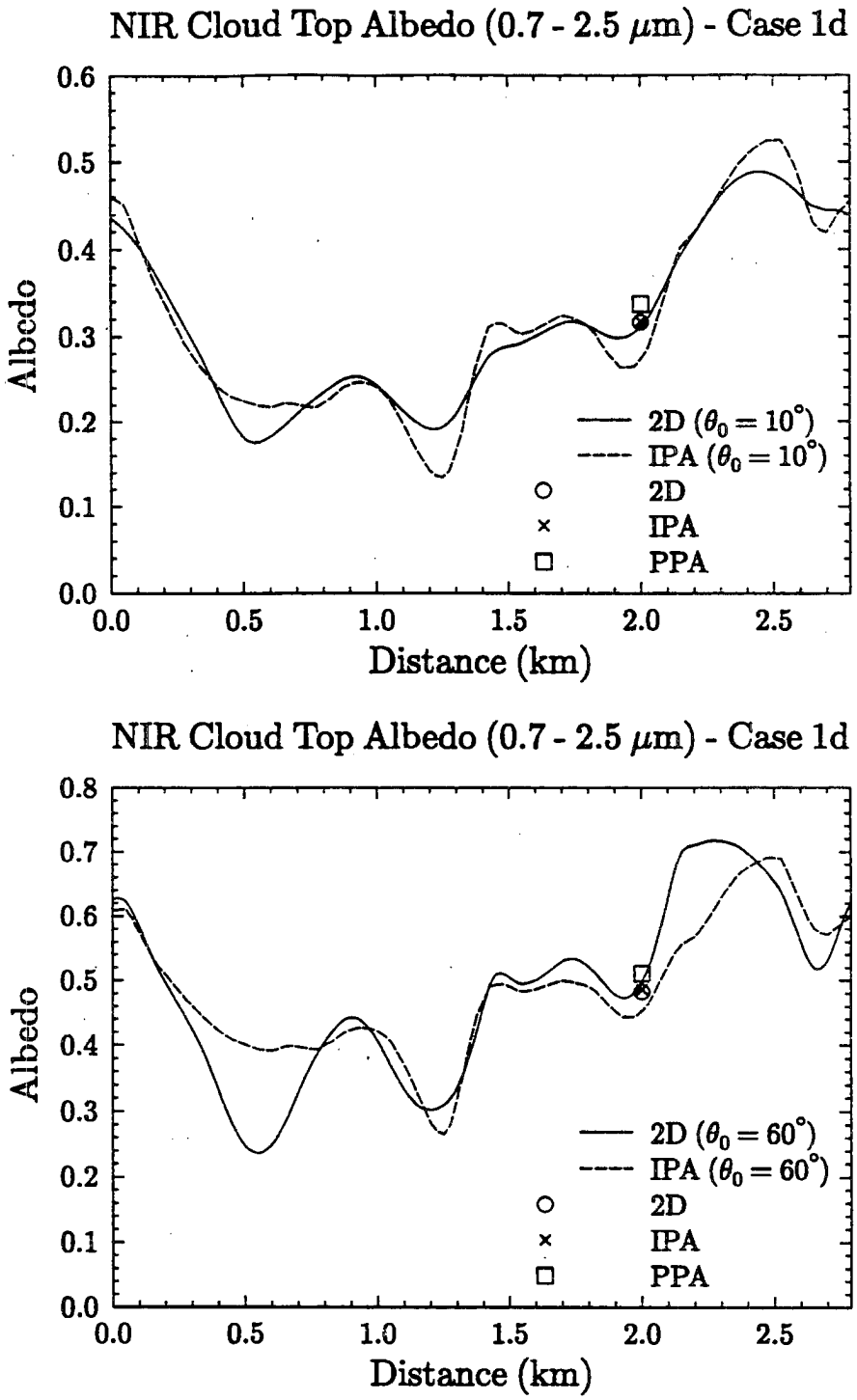

Figure 5.36: The same as Figure 5.34, but for Case 1d.

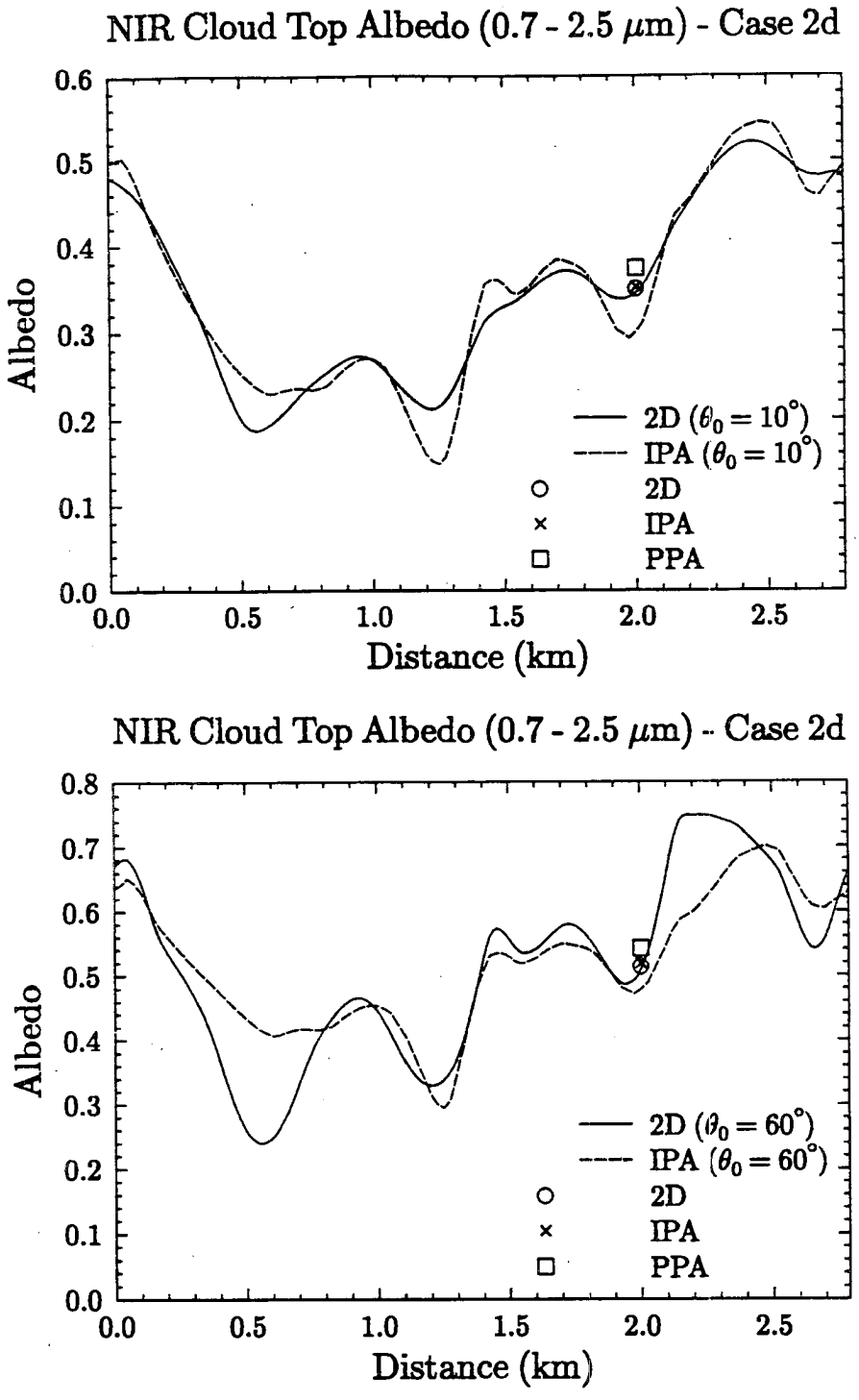

Figure 5.37: The same as Figure 5.34, but for Case 2d.

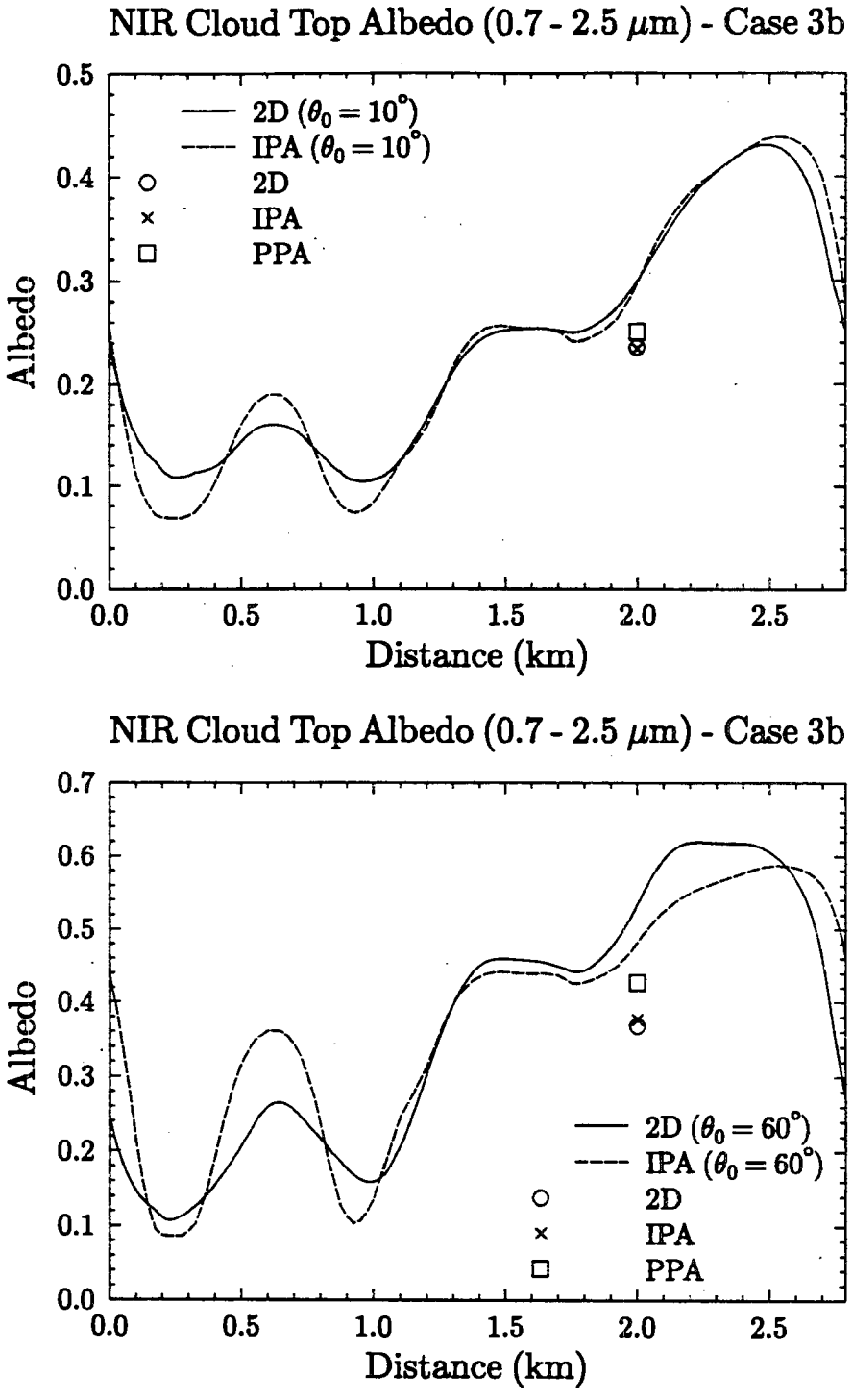

Figure 5.38: The same as Figure 5.34, but for Case 3b.

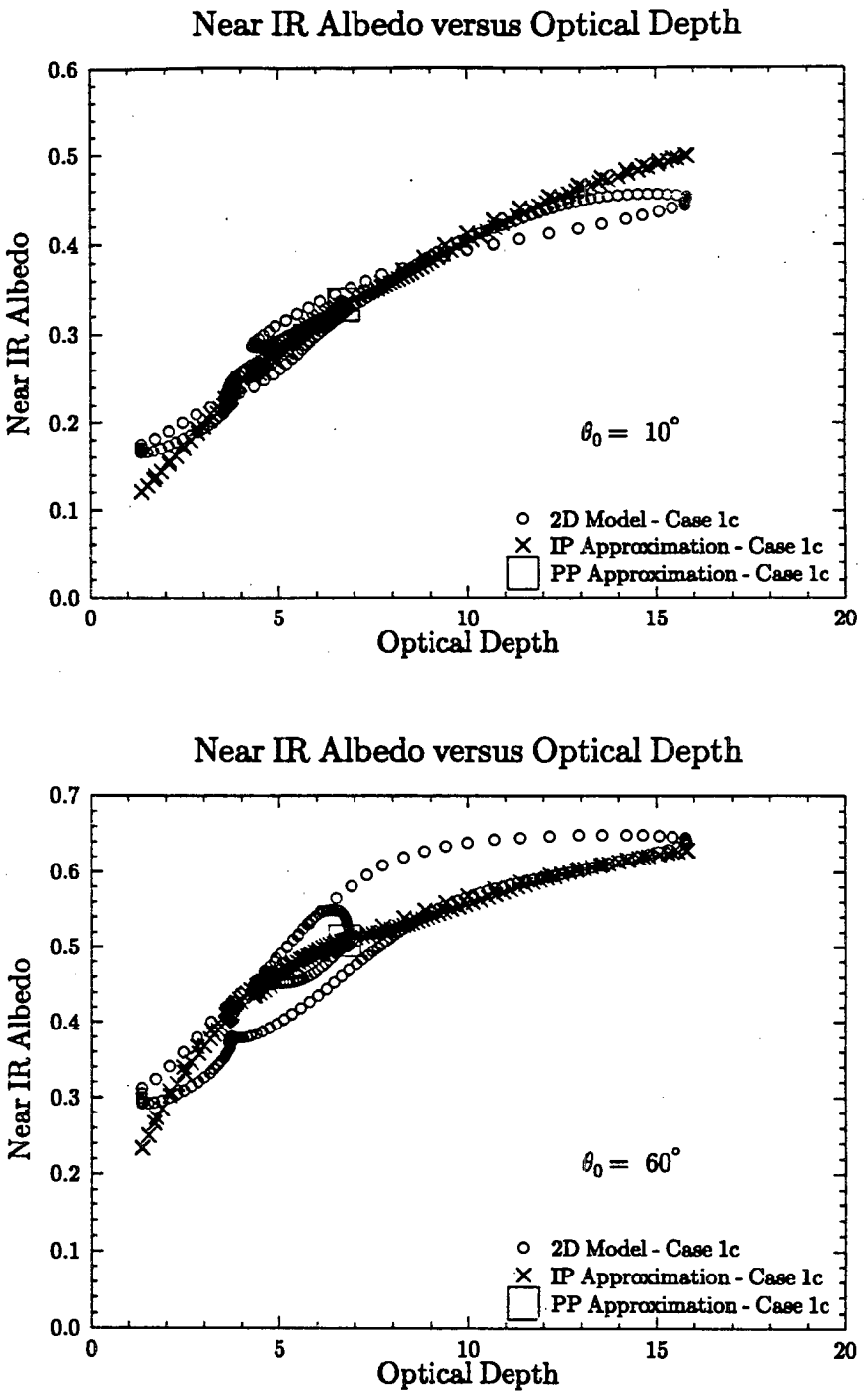

Figure 5.39: The same as Figure 5.26, but for near infrared albedo (0.7 – 2.5 μm) and optical depths at Band 6.

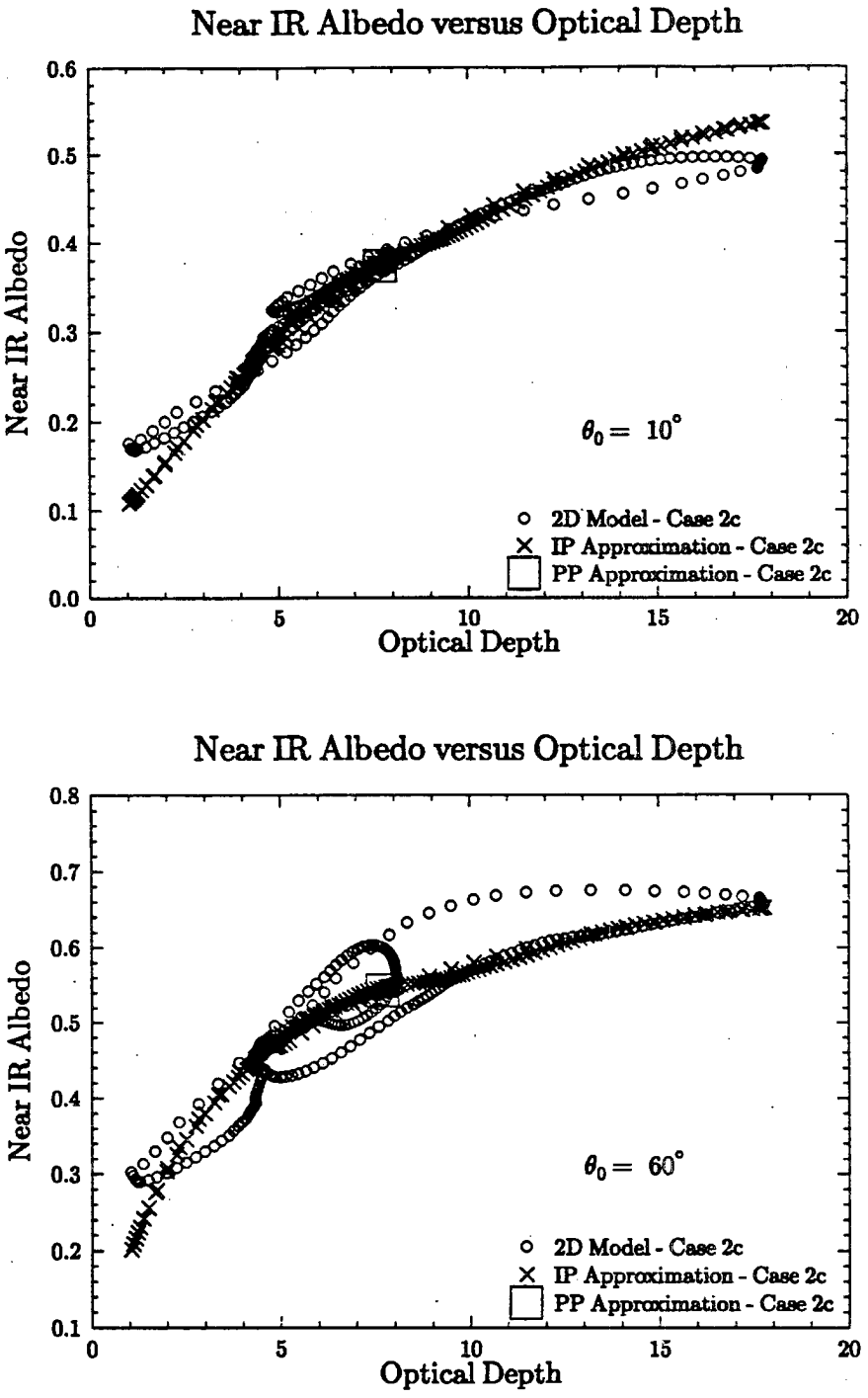

Figure 5.40: The same as Figure 5.39, but for Case 2c.

Microphysics – Part 2

Table 5.4 presents the absolute and relative differences in the domain averaged near infrared albedos between Cases 2c and 1c and between Cases 2d and 1d for the 2D, IPA and PPA calculations. The absolute differences in the near infrared albedos are roughly 3 to 4 percent, and are systematically larger than the visible albedo changes. The larger differences in the near infrared albedos between the enhanced CCN cases and the control CCN cases are the result of the relatively larger increases in optical depth and single scattering albedo compared to the visible wavelengths.

Table 5.4: Absolute and relative differences (in percent) in the domain averaged near infrared (0.7 – 2.5 μm) albedos between the enhanced CCN cross sections and the control CCN cross sections.

Case	θ_0 (degrees) angle	RTM	Absolute difference	Relative difference
2c - 1c	10	2D	3.89 %	12.4 %
		IPA	3.91 %	12.5 %
		PPA	4.01 %	12.0 %
	60	2D	3.27 %	6.8 %
		IPA	3.35 %	7.0 %
		PPA	3.52 %	6.9 %
2d - 1d	10	2D	3.33 %	10.5 %
		IPA	3.47 %	11.0 %
		PPA	3.68 %	10.9 %
	60	2D	3.12 %	6.5 %
		IPA	3.24 %	6.7 %
		PPA	3.14 %	6.1 %

5.2.3 Total solar (0.28 μm – 2.5 μm)

The contributions from the visible and near infrared albedos were added together to find the total impact of cloud microphysics and macrophysics on the solar broadband albedos. The domain average total solar albedos for Cases 1c, 1d, 2c, 2d, and 3b are presented in Table 5.5 for the three radiative transfer models.

A comparison between Cases 1c and 2c and Cases 1d and 2d in Table 5.5 show that the relative increase in the total solar albedo due to microphysical changes was near 10

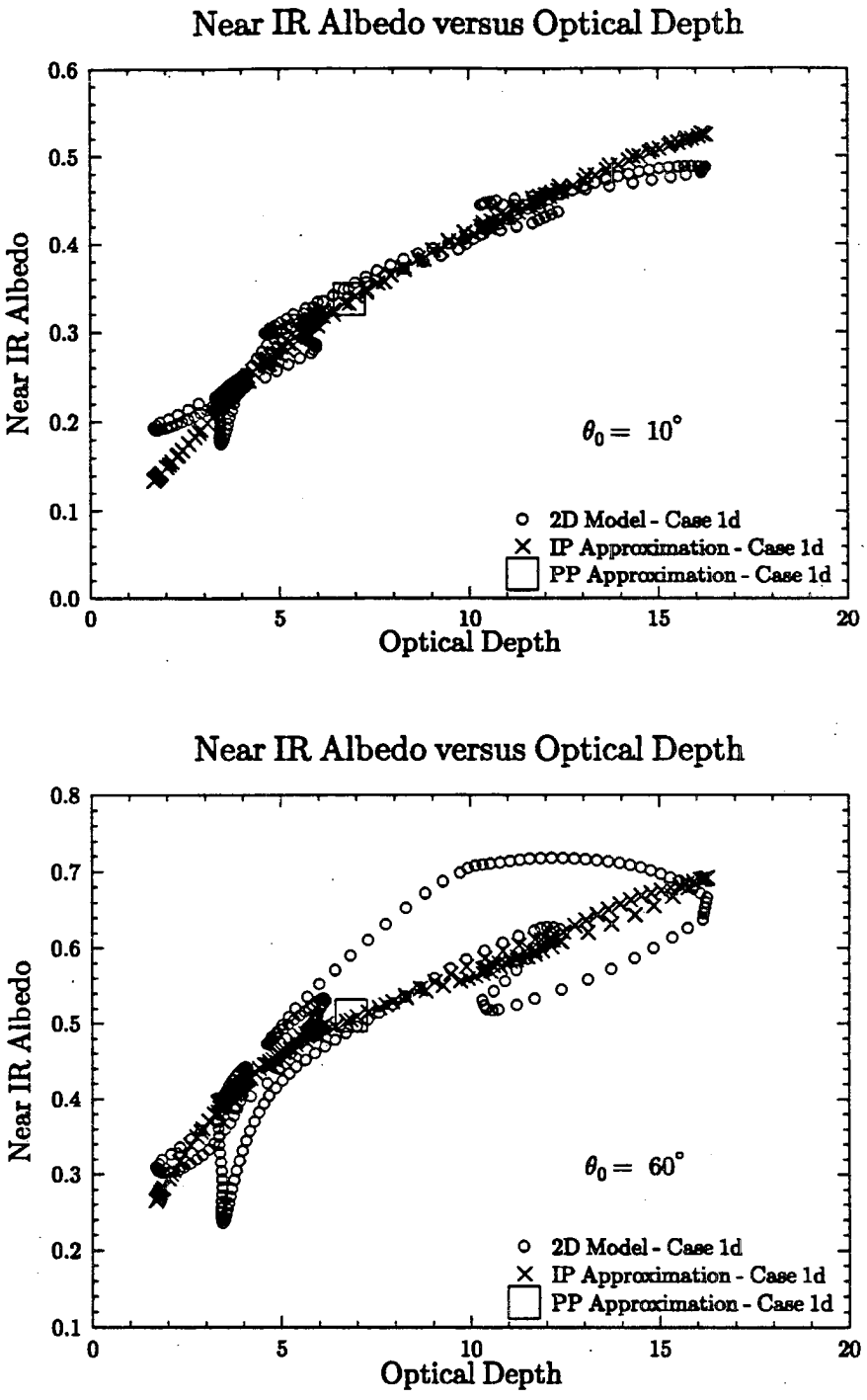

Figure 5.41: The same as Figure 5.39, but for Case 1d.

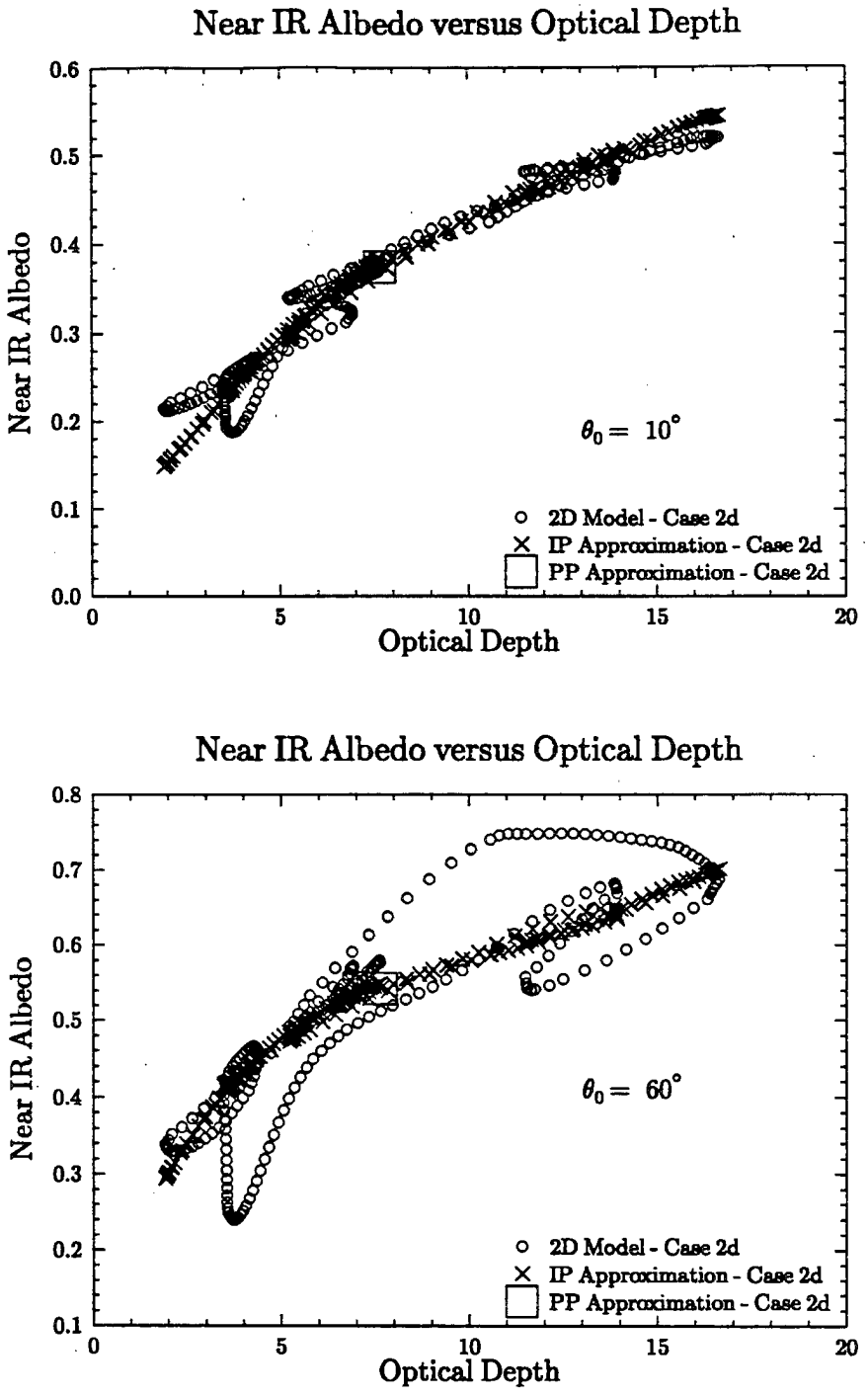

Figure 5.42: The same as Figure 5.39, but for Case 2d.

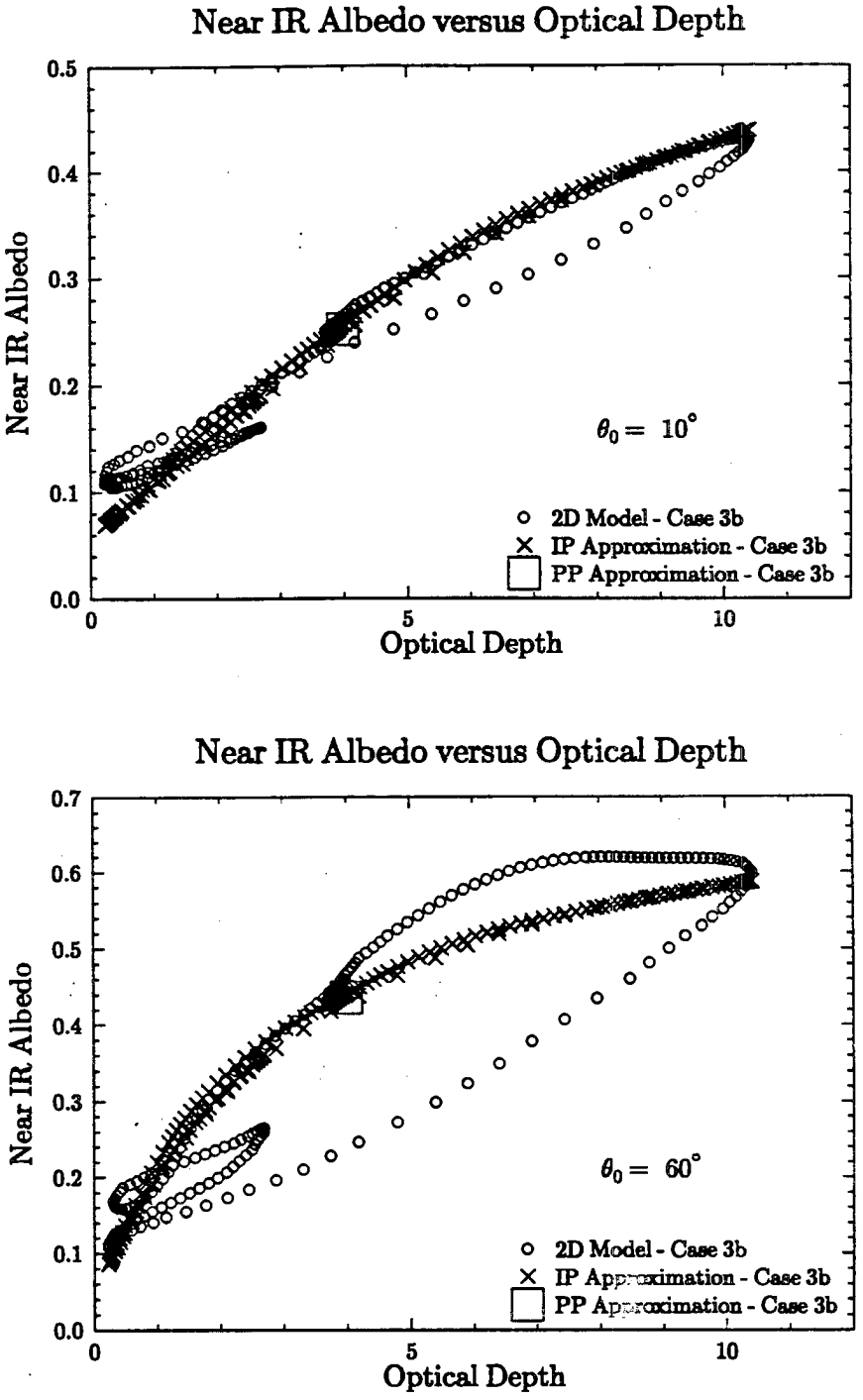

Figure 5.43: The same as Figure 5.39, but for Case 3b.

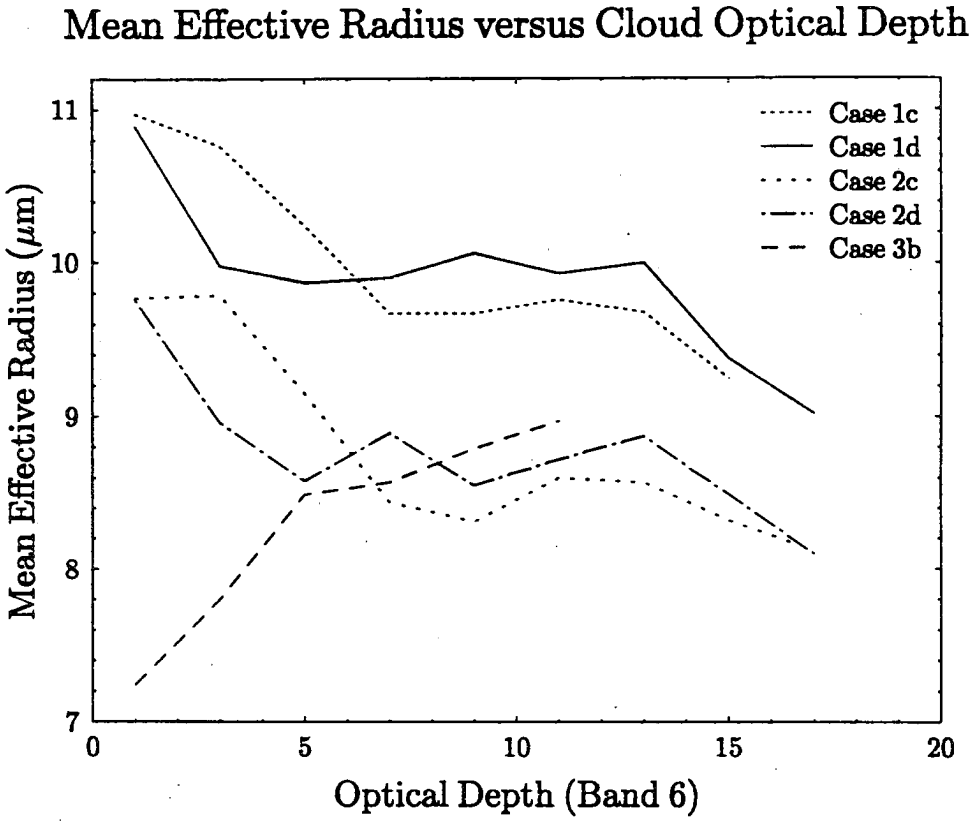

Figure 5.44: The same as Figure 5.31, but for optical depths at Band 6.

Table 5.5: Domain averaged total solar (0.28 – 2.5 μm) albedos for the five RAMS cross sections computed from the 2D, IPA and PPA radiative transfer models for solar zenith angles of 10° and 60°. The relative difference from the 2D model is also presented.

Case	θ_0 (degrees) angle	RTM	Albedo	Relative difference
1c	10	2D	32.25	— %
		IPA	32.28	0.1 %
		PPA	34.10	5.7 %
	60	2D	47.32	— %
		IPA	47.23	-0.2 %
		PPA	50.27	6.2 %
1d	10	2D	32.68	— %
		IPA	32.70	0.1 %
		PPA	34.41	5.3 %
	60	2D	48.01	— %
		IPA	48.32	0.6 %
		PPA	50.62	5.4 %
2c	10	2D	35.73	— %
		IPA	35.77	0.1 %
		PPA	37.79	5.8 %
	60	2D	50.21	— %
		IPA	50.19	< 0.1 %
		PPA	53.57	6.7 %
2d	10	2D	35.74	— %
		IPA	35.89	0.4 %
		PPA	37.81	5.8 %
	60	2D	50.89	— %
		IPA	51.31	0.8 %
		PPA	53.56	5.2 %
3b	10	2D	23.89	— %
		IPA	23.83	-0.3 %
		PPA	25.12	5.1 %
	60	2D	35.59	— %
		IPA	36.36	2.2 %
		PPA	40.98	15.1 %

percent when the solar zenith angle was 10 degrees, and 6 percent when the solar zenith angle was 60 degrees. The PPA bias compared to the 2D calculations is between 5 to 7 percent for all cases and solar zenith angles except for the $\theta_0 = 60°$ calculation for Case 3b, when the bias is 15 percent. Also, except for the low sun Case 3b simulation, the differences between the 2D and IPA domain averaged albedos were less than one percent. The agreement between the 2D and IPA albedos for the $\theta_0 = 10°$ runs was even better, as the largest difference was only 0.4 percent. Gabriel and Evans (1994) have shown that at large solar zenith angles (greater than say 45 degrees) in broken clouds (with cloud fractions significantly less than 100 percent), the IPA computed domain average albedos may become inaccurate since the IPA model is not capable of accounting for the illumination of cloud sides and the effects of horizontal inhomogeneity on the "pseudo-source" term of radiative transfer. However, since the cloud fractions in all cases were near unity and the clouds were relatively horizontally homogeneous, the 2D/IPA differences in these simulations were never greater than 2 percent.

Since the domain average albedos computed from the 2D model are approximated very well by the albedos calculated from the IPA method, an assessment of the effects of cloud microphysics and cloud macrophysics on the entire three dimensional RAMS model domain is possible using the IPA method to compute the domain average broadband albedo of the entire model domain. This method should be most accurate at small solar zenith angles. In this assessment, several individual factors that influence cloud albedo can be examined. These include:

1. Changes in cloud structure (specifically, changes in horizontal inhomogeneity)
2. Changes in cloud microphysics
3. Location of enhanced CCN concentrations (Will the albedo changes be greatest when the additional aerosol is introduced from above or below the cloud layer?)

In order to separate the different factors mentioned above, several cloud fields from different times during each model run were examined and statistics of optical depth and effective radius were compared. The cloud fields from all three runs were examined at

roughly 5 minute intervals from 7260 seconds to 9000 seconds model time. Each cloud field was divided into four quadrants (26×26 grid points each) in order to increase the total number of cloud field samples and to decrease the total computational time involved in the IPA calculations. The optical depth and column average effective radius for each grid point in a quadrant were computed using equations (5.2) and (5.3) respectively. The optical depth and effective radius statistics computed from selected cloud field quadrants are presented in Table 5.6.

Table 5.6: Optical depth and effective radius statistics computed for selected cloud field quadrants from the RAMS model runs. The quadrants are identified by the model run, model time and quadrant number. The effective radius statistics are in units of microns.

Quadrant name	Model run	Model time	Quadrant number	$\overline{\tau}$	$\overline{R_e}$	st. dev. ($\log \tau$)	st. dev. (R_e)
A1	control	7560 s	1	6.87	10.33	0.335	0.668
B1	control	7560 s	2	7.97	10.70	0.313	0.674
C1	control	8460 s	2	7.99	10.60	0.500	0.591
D1	control	9000 s	3	6.96	10.34	0.578	0.855
A2	sens. 1	7560 s	1	7.50	9.51	0.347	0.666
B2	sens. 1	7560 s	2	8.49	9.95	0.316	0.674
C2	sens. 1	8460 s	2	8.75	9.60	0.547	0.768
D2	sens. 1	9000 s	3	7.80	9.10	0.631	0.899
E3	sens. 2	8160 s	1	11.86	7.82	0.516	0.561
F3	sens. 2	8160 s	3	7.21	8.14	0.352	0.684

By examining the cloud optical depth and effective radius statistics from Table 5.6, it is apparent that the effects of cloud macrophysics and cloud microphysics on the cloud albedo may be separated by comparing the albedos of different quadrants. The effects of cloud macrophysical changes on cloud albedo may be estimated when quadrants with similar mean statistics but difference variance statistics are compared. Since the domain average optical depth and effective radius in quadrants B1 and C1 are very similar, any differences in domain average albedo are almost entirely due to changes in the horizontal homogeneity of the cloud fields. Quadrants A1 and D1 also have similar means but different standard deviations of optical depth and effective radius.

Similarly, the effects of cloud microphysical changes on cloud albedo may be computed from the quadrant pairs A1/A2, B1/B2, C1/C2, and D1/D2, which have similar cloud geometries and similar variance statistics (especially the A1/A2 and B1/B2 pairs). The pairs A2/D2 and B2/C2 could also be used to examine the macrophysical impact on cloud albedo, but the means of the optical depth and effective radius between the pairs do not match as well as those from the control run. A comparison of the standard deviations of $\log \tau$ and R_e between the control run quadrants and the first sensitivity run quadrants (where enhanced CCN concentrations were added above the cloud layer) show some increases in the variance of the cloud optical properties. An increase was also noted in the entire domain statistics of the second sensitivity run. For example, at 9000 seconds in the control run the standard deviation of $\log \tau$ for the entire domain was 0.450 and the standard deviation of R_e was 0.764 μm. In the first sensitivity run at 9000 seconds the corresponding standard deviations were 0.482 and 0.807 μm. The standard deviations of $\log \tau$ and R_e in the second sensitivity run were 0.588 and 1.46 μm, respectively. The circulation in the second sensitivity run was especially vigorous at 9000 seconds and may account for some of the increase in the variability of the cloud properties in this run.

Finally, the differences between the two sensitivity runs and the effect of adding aerosol from above or below the cloud layer may be estimated by comparing the albedo differences between quadrants A1/F3 with the differences between quadrants A1/A2. Both pairs of cloud fields have similar variances in the optical depth and effective radius, and comparable domain average optical depths. As an extreme test of the effects of cloud microphysical changes in the clouds, a comparison between the albedos in quadrants C1 and E3 are used. Quadrant E3 has a substantially larger mean optical depth (11.86 versus 7.99) and smaller mean effective radius (7.82 μm versus 10.60 μm) than quadrant C1.

Macrophysics – Part 3

The domain average albedos for the ten quadrants shown above were computed at solar zenith angles of 10 degrees and 40 degrees and are presented in Table 5.7. These solar zenith angles are expected to produce IPA domain average albedos that would most closely match those from multi-dimensional RTMs. The domain average albedos were computed

from the 14 band, 37 k-value version of the Stackhouse (1989) two-stream model using the Betts and Boers (1990) sounding for levels above the RAMS model domain.

Table 5.7: Domain averaged solar albedos computed from IPA calculations of selected cloud field quadrants from the RAMS model runs. The 14 band, 37 k-value version of Stackhouse (1989) was used to compute the broadband fluxes from 0.28 to 2.8 microns at solar zenith angles of 10° and 40°.

Quadrant name	Albedo ($\theta_0 = 10°$)	Albedo ($\theta_0 = 40°$)
A1	38.59	40.62
B1	41.59	43.58
C1	40.34	42.21
D1	36.75	38.73
A2	41.27	43.30
B2	43.96	45.95
C2	42.98	44.82
D2	40.08	42.03
E3	46.66	48.55
F3	42.31	44.35

The relative differences in the domain averaged albedos between quadrants A1/D1 and quadrants B1/C1 at $\theta_0 = 10°$ were 4.8 percent and 3.0 percent respectively. Similar differences were found for a solar zenith angle of 40°. As expected, the quadrants with the larger standard deviation in $\log \tau$ (producing the larger PPA bias) had the lower albedo. The larger albedo differences between quadrants A1 and D1 reflect the larger differences in the variance of the optical depth distribution, and possibly of the effective radius distribution. The relative differences in the albedos between quadrants A2/D2 and quadrants B2/C2 at $\theta_0 = 10°$ were 2.9 % and 2.2 % respectively. The differences in the first sensitivity runs were smaller than in the control run since the quadrants with larger variances in $\log \tau$ also had larger mean τ.

Microphysics – Part 3

The relative differences in the domain averaged albedos (for $\theta_0 = 10°$) between the corresponding quadrants from the control run and the first sensitivity run (A1/A2, B1/B2, C1/C2, and D1/D2) were 6.9%, 5.7%, 6.5%, and 9.1% respectively. The larger differences

between quadrants D1 and D2 were the result of the larger microphysical changes between the control run and the first sensitivity run at the end of the model run compared to earlier times. A comparison between the albedo differences between quadrants A1/A2 and A1/F3 show that the microphysically induced albedo changes are larger in the second sensitivity run (6.9% versus 9.6% when $\theta_0 = 10°$) and are due to the larger decrease in effective radius when the enhanced CCN concentrations are added below the cloud layer. The differences between the albedos in quadrants C1 and E3 are 15.7% at $\theta_0 = 10°$, and represent the most extreme impact of cloud microphysics in the albedo calculations. Some of the differences are due to the stronger dynamics and deeper cloud depths in the second sensitivity run, especially near the end of the simulation (8160 seconds). Unless cloud microphysical changes can feedback and produce stronger circulations in marine stratus, such large increases in cloud albedo due to enhanced CCN concentrations alone are not expected.

5.3 Broadband Heating Rates and Net Flux Convergence

In this section the near infrared heating rates inside the five RAMS model cross sections are presented for the 2D, IPA and PPA calculations. The magnitude and vertical distribution of solar heating inside stratocumulus clouds can have a profound influence on the radiative energy budget of the cloud and its thermodynamic stability. Therefore, horizontal inhomogeneity may possibly influence the radiative energy budget of the cloud through changes in the mean vertical distribution of solar heating.

5.3.1 Near infrared heating rates

Figures 5.45 and 5.46 show cross sections of the near infrared (0.7 – 2.5 μm) heating rates in K hr^{-1} for Cases 2d and 3b. The results for the other three cases are similar. The independent pixel approximation heating rates appear to match the heating rates computed in the two dimensional medium well, especially for the solar zenith angle of 10 degrees. In the $\theta_0 = 60°$ computations, some differences are apparent. The most noticeable is the two corridors of net flux convergence in the lower half of Case 3b that coincide with the broken areas in the cloud field. The differences between the 2D and

IPA heating rate fields for both cross sections are presented in Figure 5.47. Figure 5.47 confirms that the largest local differences in heating rate occur in the lower sun cases. Especially in the $\theta_0 = 60°$ case, the horizontal transport of radiation leads to more flux convergence on the sunny side of cloud top extinction maxima, and less flux convergence on the shadow side of the extinction peak. The relative differences in heating rate can be quite large. For example, near 2.15 km in Case 2d ($\theta_0 = 60°$) the increase in the solar heating rate is over 0.4 K hr^{-1} which is a relative difference of over 20 percent. In Case 3b at the 60 degree solar zenith angle, the two corridors of heating are apparent, and produce heating rate differences up to 0.08 K hr^{-1}.

Like the results from broadband albedo, the local differences in heating rate between the 2D and IPA calculations tend to cancel out in the domain average. Figures 5.48 through 5.52 present the domain average vertical profiles of heating rate for each cross sections. Figures 5.48 – 5.50 show the 2D, IPA and PPA calculations at a solar zenith angle of 10 degrees. The 2D and IPA profiles are nearly identical at this sun angle, while the PPA profile tend to show slightly larger heating rates throughout most of the vertical domain. In Case 3b, two PPA profiles are shown, one accounting for cloud fraction while the second assumes a completely overcast layer. The PPA profiles are identical. In the heating rate profiles for $\theta_0 = 60°$, the 2D and IPA results are still very close though some small differences appear. The agreement between the 2D and PPA heating rates becomes better at the larger solar zenith angle.

5.3.2 Total net flux convergence

The total mean net flux convergence in each cross section is presented in Table 5.8 for all three radiative transfer methods. The table shows that the net flux convergence in the 2D and IPA calculations at a solar zenith angle of 10 degrees are nearly identical, while the PPA computed net flux convergences are 2.5 percent to 5.0 percent larger. At $\theta_0 = 60°$, all three methods calculate nearly the same net flux convergence, and in Case 2c and 3b the 2D values are larger than the corresponding PPA values.

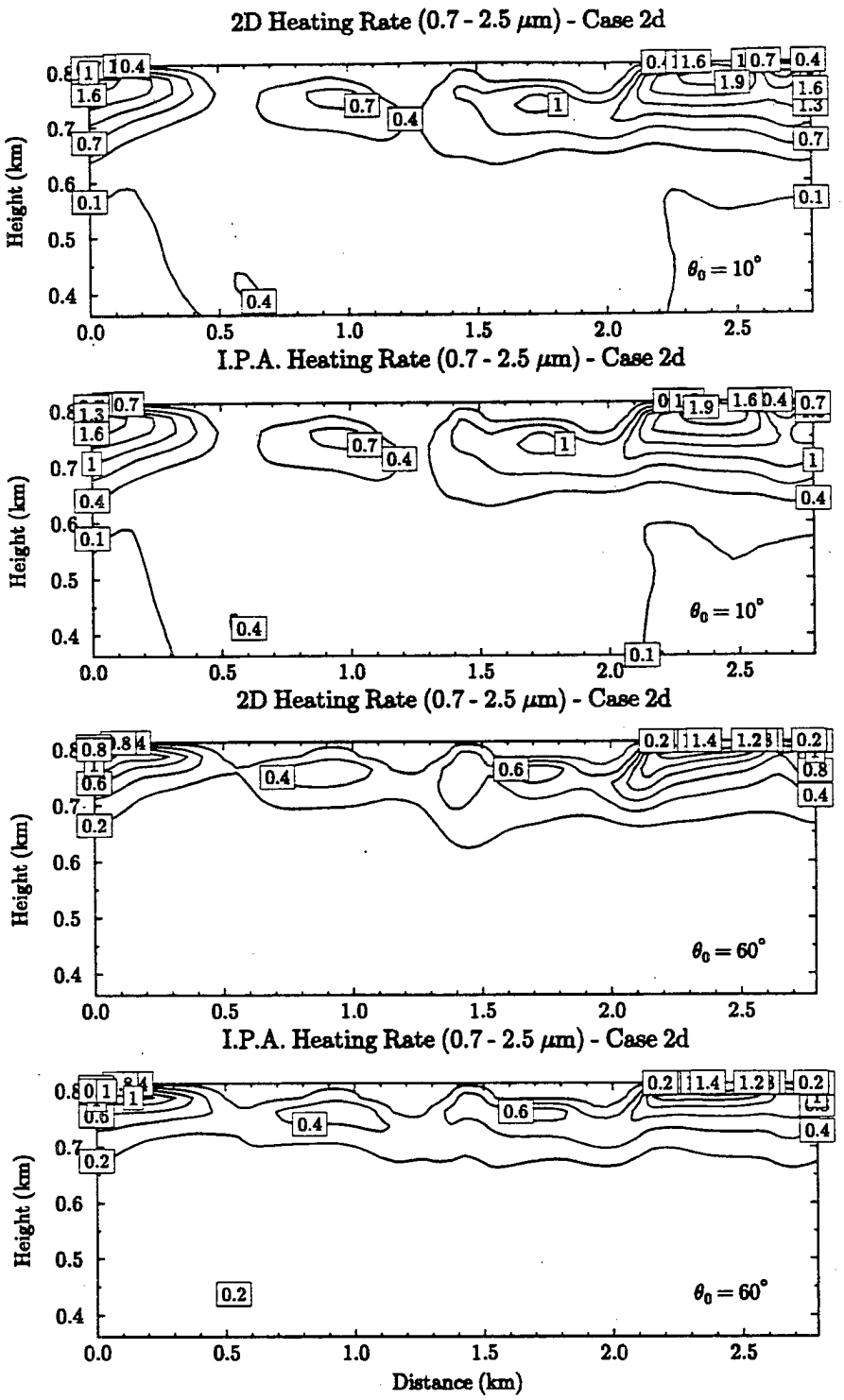

Figure 5.45: The solar heating rate fields in K hr^{-1} in Case 2d at solar zenith angles of 10° and 60° computed from the 2D and IPA models.

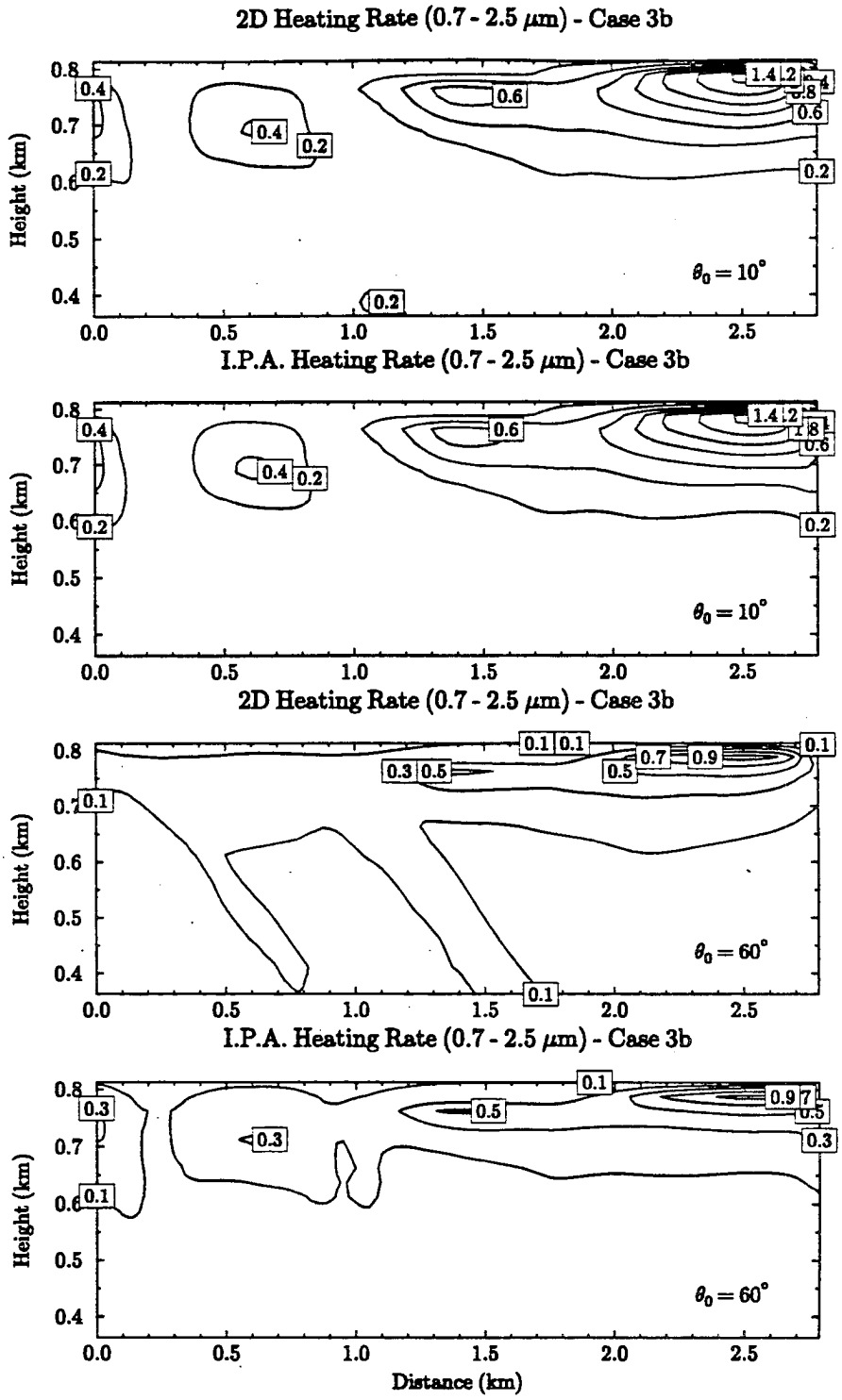

Figure 5.46: The same as Figure 5.45, but for Case 3b.

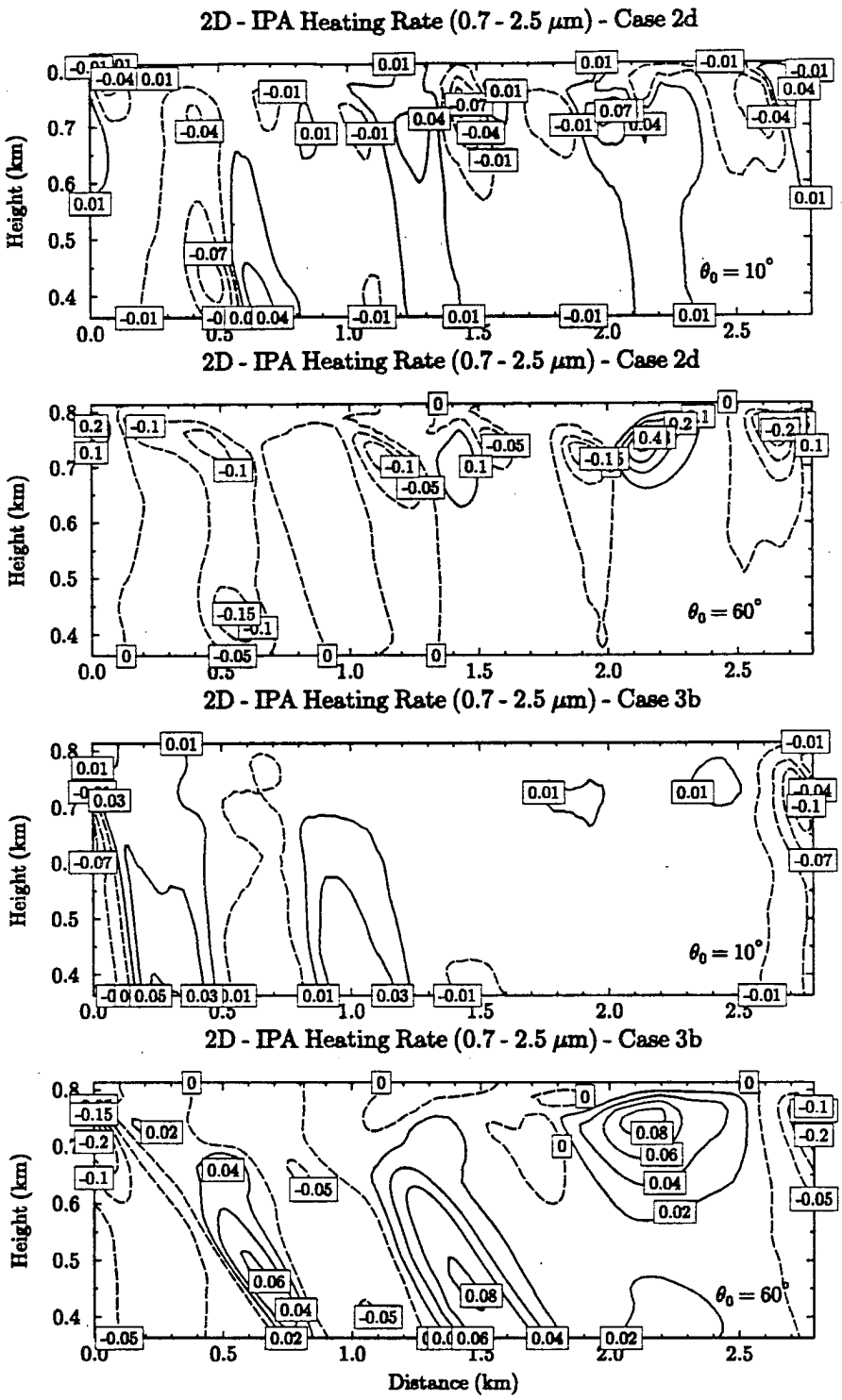

Figure 5.47: The difference between the 2D and IPA computed heating rate fields in K hr^{-1} in Cases 2d and 3b for solar zenith angles 10° and 60°.

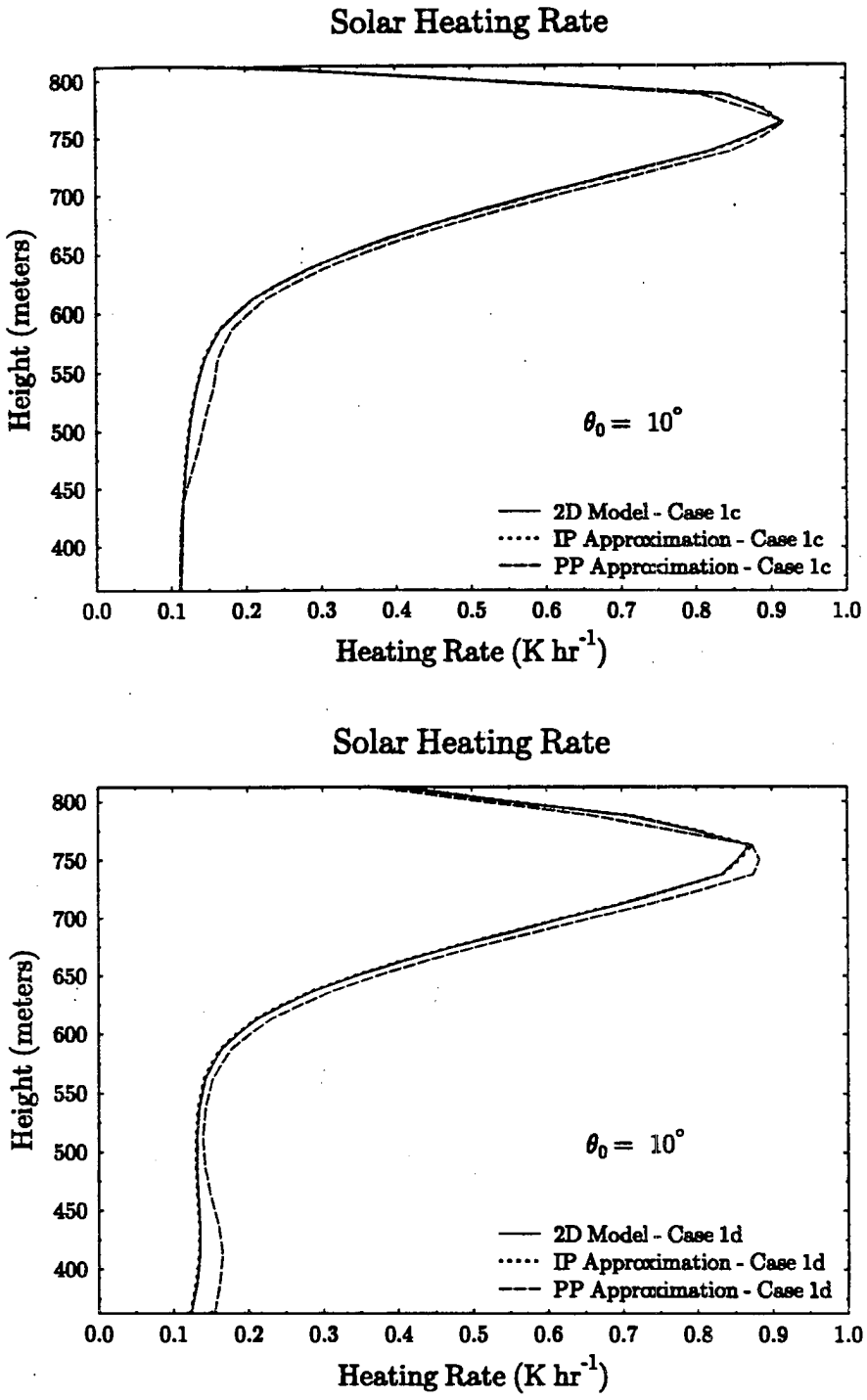

Figure 5.48: Vertical profiles of domain averaged solar heating rates computed at $\theta_0 = 10°$ for Cases 1c and 1d using the 2D, IPA and PPA models.

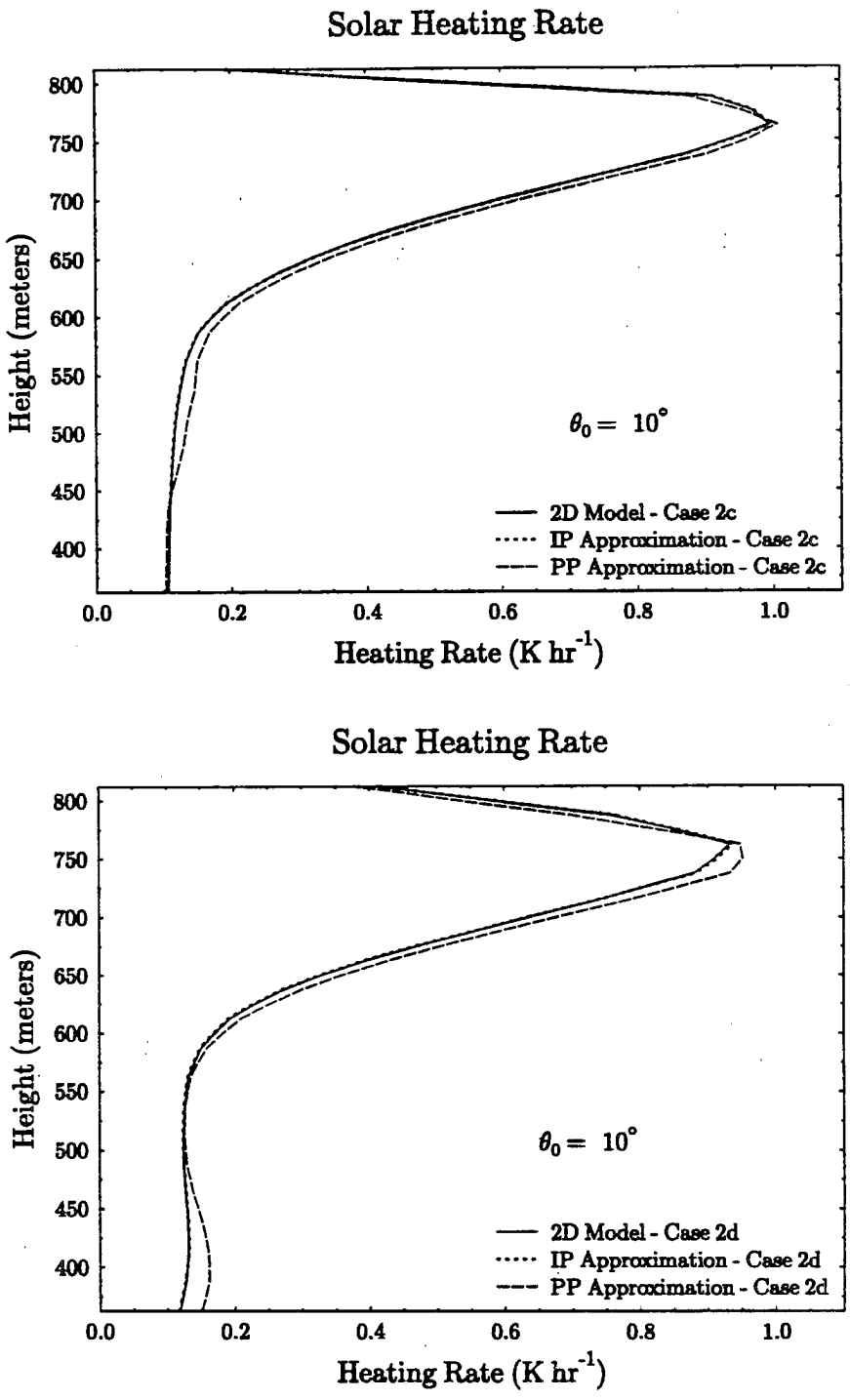

Figure 5.49: The same as Figure 5.48, but for Cases 2c and 2d.

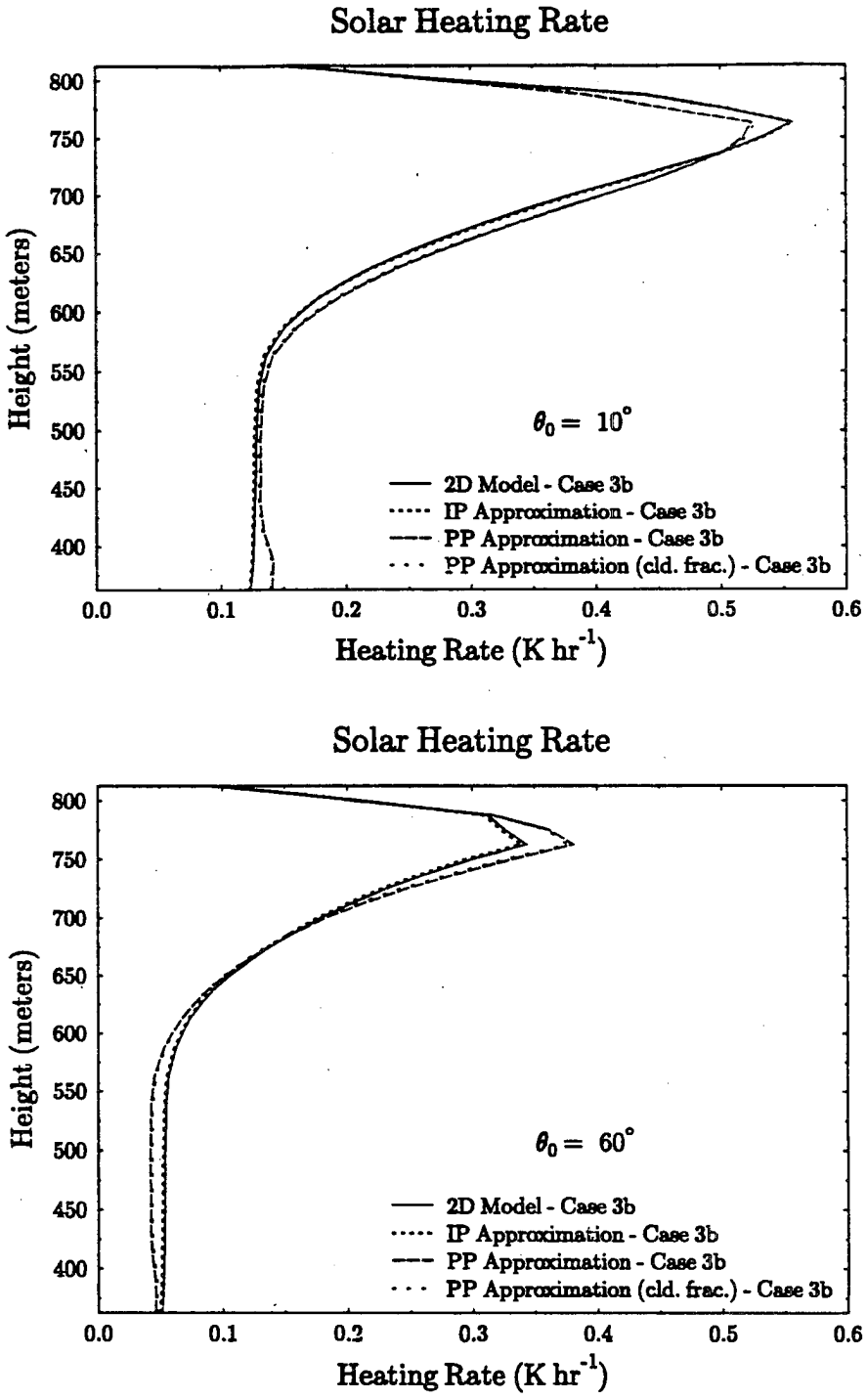

Figure 5.50: Vertical profiles of domain averaged solar heating rates computed at $\theta_0 = 10°$ and $\theta_0 = 60°$ for Case 3b using the 2D, IPA and PPA models.

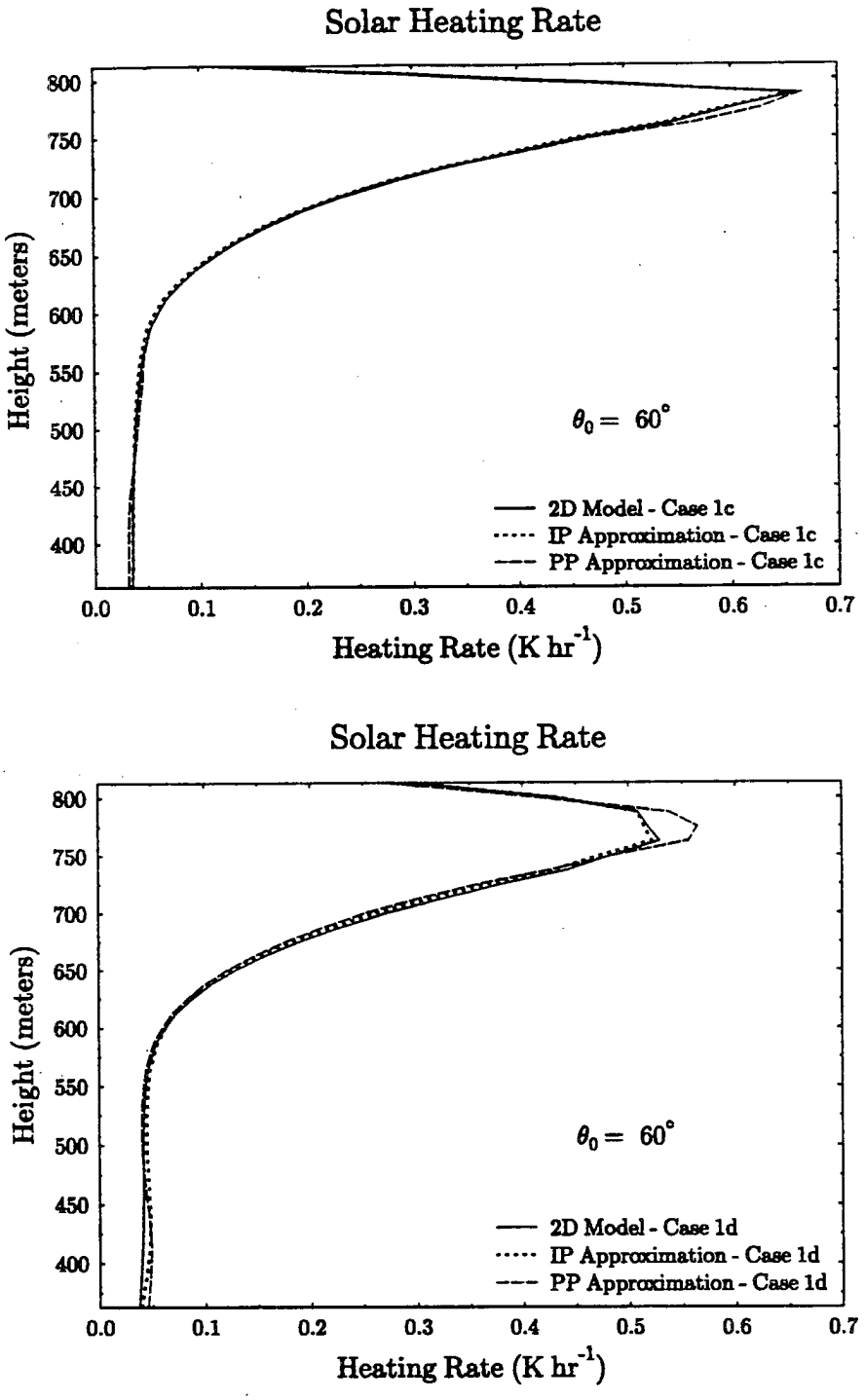

Figure 5.51: The same as Figure 5.48, but for a solar zenith angle of 60°.

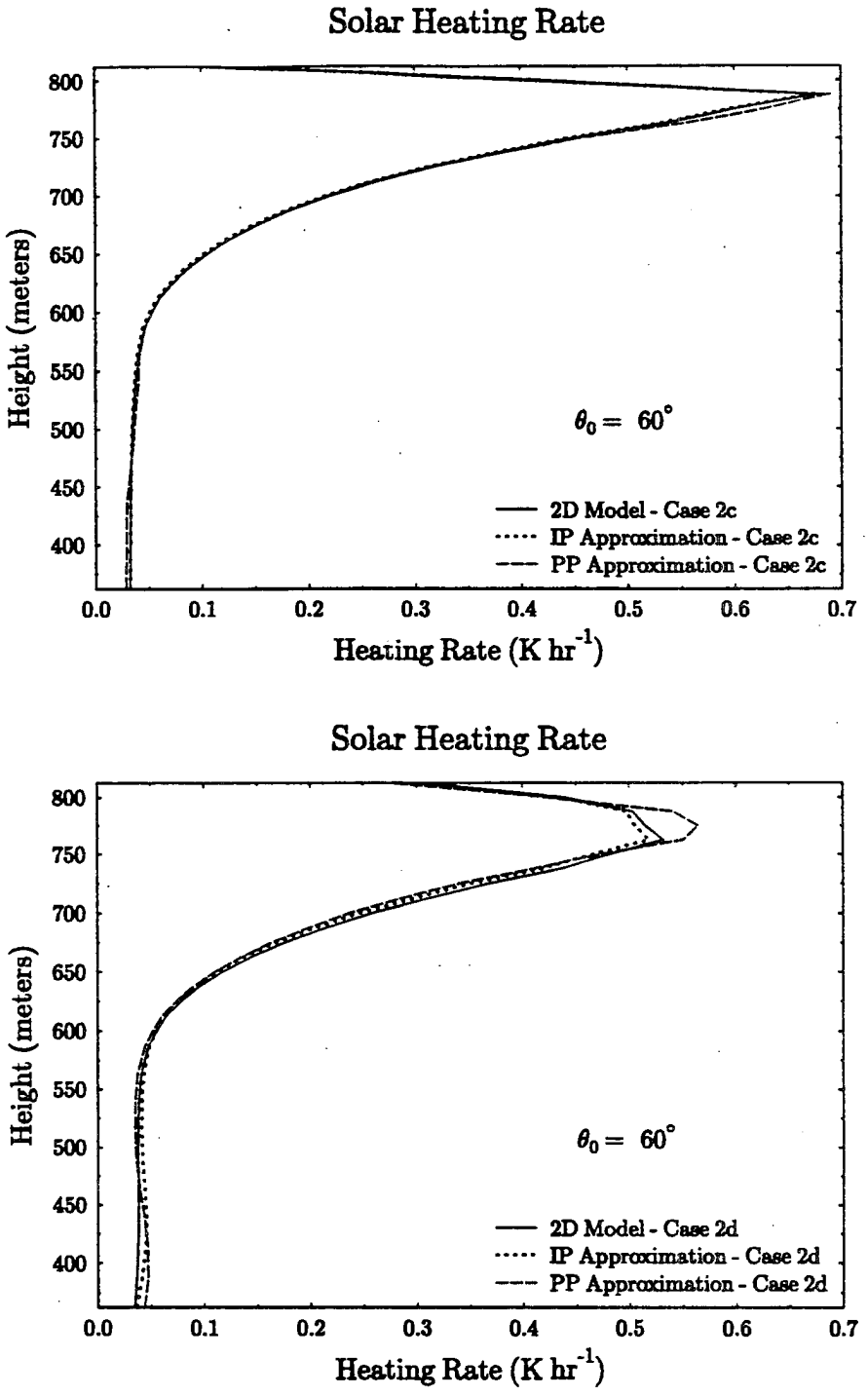

Figure 5.52: The same as Figure 5.49, but for a solar zenith angle of 60°.

Table 5.8: Domain average net flux convergence (0.7 – 2.5 μm) in W m^{-2} computed by the 2D, IPA and PPA radiative transfer methods for five RAMS cross sections.

Case	θ_0 (degrees)	PPA	2D	IPA	(PPA - 2D)/2D
1c	10	48.914	47.133	47.199	3.6 %
	60	22.385	22.285	21.950	0.4 %
1d	10	50.684	48.255	48.156	5.0 %
	60	23.065	23.179	23.052	0.5 %
2c	10	49.842	47.956	47.980	3.9 %
	60	21.565	21.424	21.131	0.7 %
2d	10	51.122	48.835	48.782	4.7 %
	60	22.145	23.403	22.124	-1.1 %
3b	10	34.844	33.982	33.981	2.5 %
	60	16.668	16.942	16.671	-1.6 %

The positive bias in the PPA net flux convergence at the small solar zenith angle, and the general lack of a bias at the larger solar zenith angle, when compared to the IPA net flux convergence can be explained by the relationship between net flux convergence and optical depth (Band 6). An examination of the IPA net flux convergence curves in Figures 5.53 through 5.55 shows that for $\theta_0 = 10°$, the curves are slightly convex in shape. At $\theta_0 = 60°$, the relationships are more confused but the IPA plots have a more linear or concave shape.

The domain averaged heating rate and net flux convergence differences between the RAMS control case and the enhanced CCN cases are very small, and suggest the overall impact of the microphysical changes on solar heating are negligible. The relative differences in net flux convergence between Cases 1c and 2c or Cases 1d and 2d are generally less than 2 percent.

5.4 Summary

This chapter presents the results of three types of radiative transfer calculation derived from the SHSG broadband model. A comparison of the point by point 2D and IPA albedos showed significant differences locally in the broadband solar albedo, but the overall effects of the horizontal transport of broadband solar radiation on the domain averaged albedo

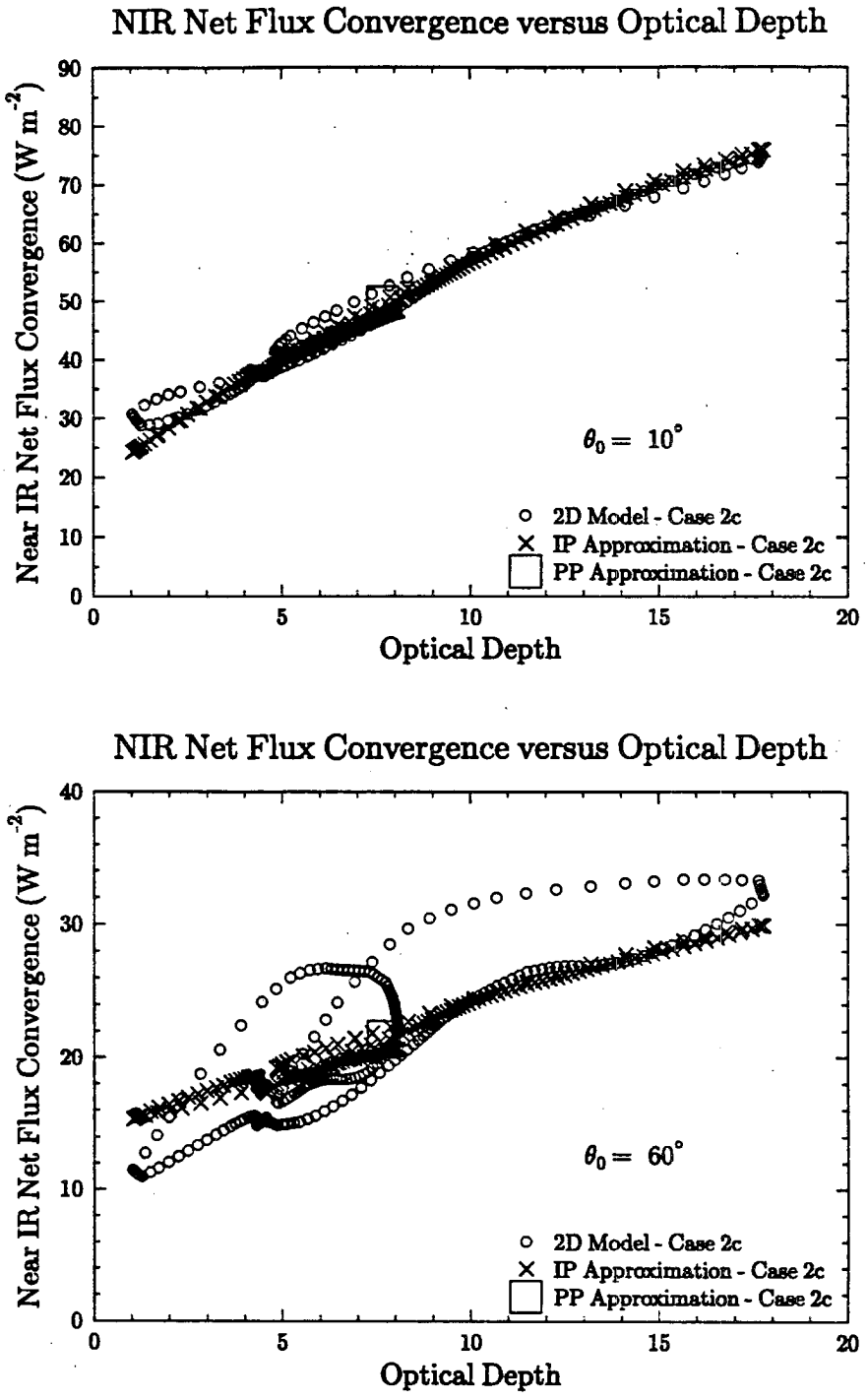

Figure 5.53: The net near infrared flux convergence computed for Case 2c at $\theta_0 = 10°$ and $\theta_0 = 60°$ as a function of cloud optical depth at Band 6 for the 2D, IPA and PPA models.

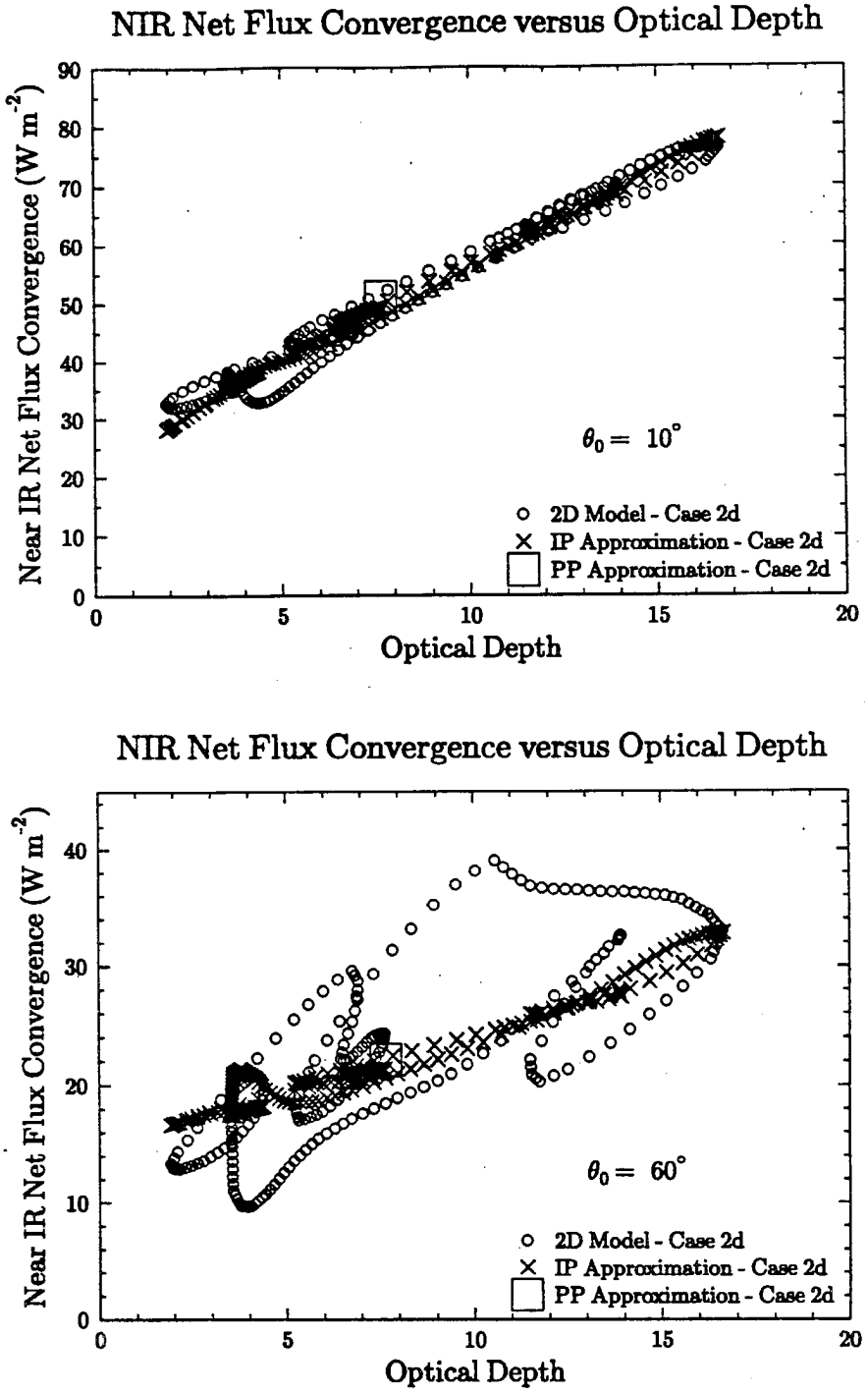

Figure 5.54: The same as Figure 5.53, but for Case 2d.

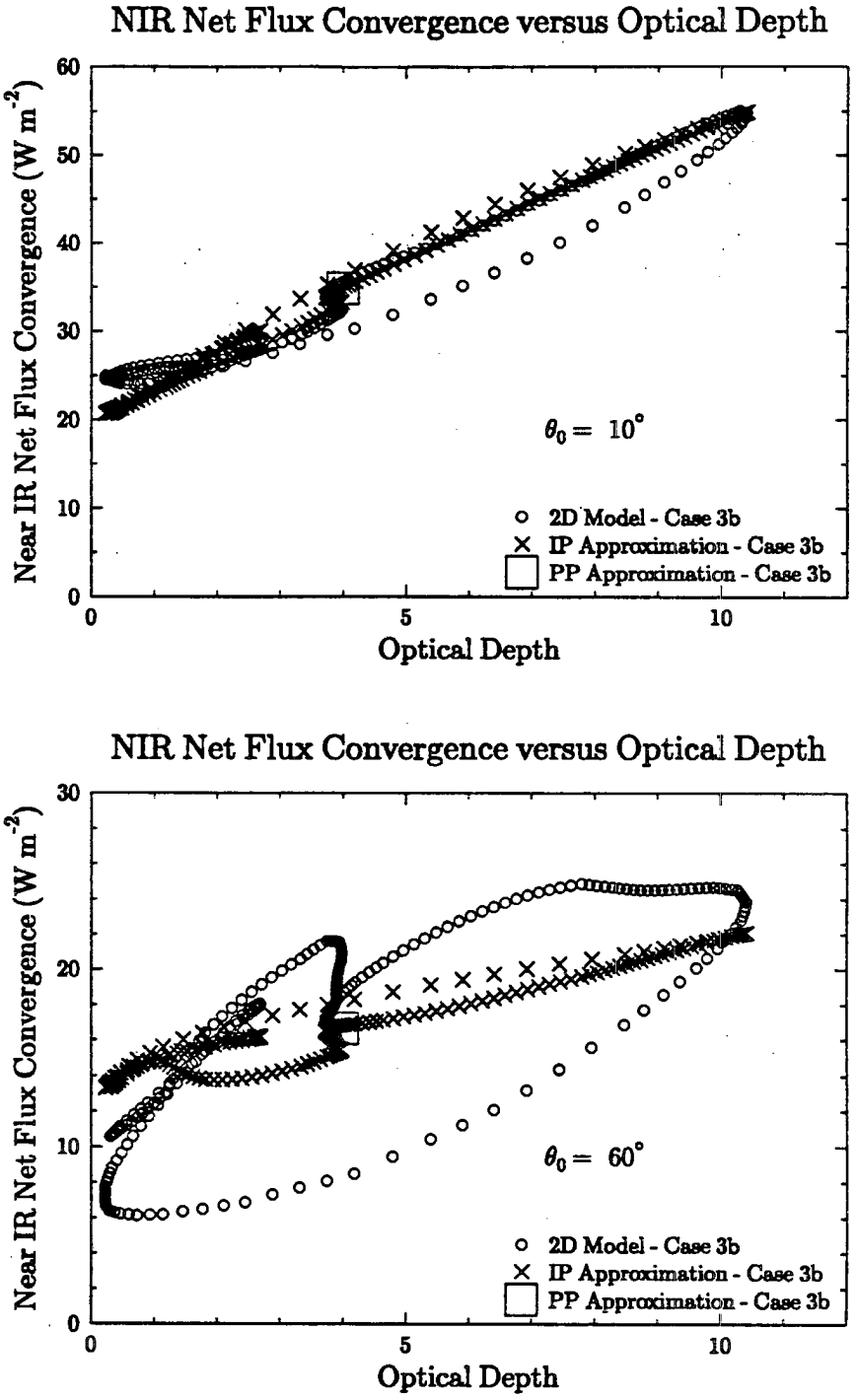

Figure 5.55: The same as Figure 5.53, but for Case 3b.

were negligible in unbroken stratus. The albedos calculated in Case 3b suggest that broken cloud cover may result in small differences between the multi-dimensional and IPA domain average albedos at large solar zenith angles.

Calculations of the PPA broadband albedo bias were generally consistent with the monochromatic results of Cahalan et al. (1994). The impact of macrophysics on the mean broadband solar albedo in marine stratus therefore comes mainly from the horizontal variability of optical depth and the nonlinear relationship between albedo and optical depth rather than effects due to the horizontal transport of solar radiation. At visible wavelengths, changes in mean effective radius with optical depth were found to influence the albedo/optical depth relationship, and consequently the PPA bias. The effects of effective radius differences on the PPA bias at near infrared wavelengths appeared to be smaller as the range in the PPA bias between all cases was 5.4 percent to 6.9 percent in the near infrared wavelengths compared to 4.3 percent to 7.8 percent in the visible wavelengths.

Given the good agreement between the domain averaged albedos computed by the IPA and multi-dimensional RTMs in this study and Cahalan et al. (1994), computations of the mean albedo computed over the three dimensional RAMS domain were made for parts of all three RAMS simulations using IPA calculations from a two-stream model. Comparisons of the total solar albedos computed by this method between clouds with similar mean microphysics and different macrophysics show the relative difference in cloud albedo resulting from typical macrophysical differences in marine stratus were between three to five percent. The relative differences in cloud albedo due to microphysical changes resulting from the sixfold increase of CCN concentrations above cloud top ranged from six to nine percent. When the same increase in CCN concentration was introduced below the cloud layer, the increase in cloud albedo ranged from ten to fifteen percent, although some of the increase was due to cloud dynamical changes not associated with the effects of the additional CCN. The impact of microphysics on the cloud was greatest for small solar zenith angles.

Like the broadband albedos, local differences in the 2D and IPA computed heating rates were significant but the domain averages were very similar. The effects of PPA

bias on the net flux convergence in the cloud were as large as 5 percent in the $\theta_0 = 10°$ simulations, but very small at $\theta_0 = 60°$. The effects of the microphysical changes on the mean net flux convergence were less than 2 percent.

Chapter 6

REMOTE SENSING

During the past several years many methods have been developed to estimate cloud physical properties from satellite radiance measurements. For example, measurements of cloud optical depth and mean effective radius have been inferred from the reflected radiances measured by aircraft and satellites (Curran and Wu, 1982; Twomey and Cocks, 1982; Foot, 1988; Twomey and Cocks, 1989; Nakajima et al., 1991; Nakajima and Nakajima, 1994; Han et al., 1994). These methods have shown some agreement with simultaneous *in situ* measurements, but are somewhat limited since they are based on one dimensional RTM calculations. The development of multi-dimensional radiative transfer models like SHSG now allow us to examine to what extent horizontal inhomogeneity affects the retrieval of cloud physical properties.

Accurate satellite retrievals of cloud optical depth and effective radius would provide a valuable source of data. The determination of cloud optical properties over large areas is essential for climate change studies because of the strong impact of clouds on climate. According to the results of the last chapter, accurate determinations of optical depth and effective radius distributions over a cloud system are also needed to estimate the effects of both cloud microphysics and cloud macrophysics on observed solar broadband albedos.

6.1 Retrieval method

The essence of these retrieval techniques is the principle that the reflection from a cloud at non-absorbing channels in the visible wavelength region is mostly a function of cloud optical thickness, while the reflection at a channel where liquid water absorbs is mostly a function of effective radius. The non-absorbing channel used in this dissertation

was 0.75 microns, and the absorbing channels were 2.16 and 3.70 microns. Similar frequencies have been used by other researchers to retrieve cloud optical properties (Nakajima et al., 1991; Nakajima and Nakajima, 1994). In order to retrieve the cloud properties from airborne or satellite measurements, the measured radiances at both wavelengths are compared to plane parallel radiative transfer calculations of clouds with a wide variety of effective radii and optical depths. Since this dissertation focuses only on the effects of cloud geometry on retrievals, the method was simplified by comparing the reflected solar radiances at cloud top. The effects of the atmosphere above and below the cloud and any relevant gas absorption on the reflected radiances must be considered in a true satellite retrieval, but the neglect of radiative transfer in the atmosphere outside the cloud will not alter the results and conclusions of this research. For the effective radius retrievals at 3.70 microns, the impact of thermal radiation must be removed, and a description of such a retrieval is presented in Nakajima and Nakajima (1994). In practice, an accurate treatment of the undesirable thermal radiation depends on the accuracy of the radiative transfer model and the specified properties of the atmosphere (Rossow, 1989), but many of these concerns are addressed in Nakajima and Nakajima (1994). In this study the retrieval at 3.70 μm is further simplified by only computing the solar portion of the radiance at this wavelength, and assuming the necessary treatment of the thermal radiation would be completely accurate. This allows for a clear determination of the cloud geometry effects on solar radiances and the retrieval of cloud properties.

Several simulations were run on the RAMS cloud cross sections 1a, 1b, 1c and 2c using the 0.75/2.16 micron and the 0.75/3.70 micron retrievals at three solar zenith angles $(10°, 40°, 60°)$. Several viewing directions were chosen to view the cloud top reflected radiances. These viewing angles are presented in Table 6.1.

Both the solar zenith angle (μ_0) and the viewing angle (μ) are measured from the zenith. The azimuthal angle (ϕ) of the viewer is 0° for radiances directed opposite the sun (toward the right hand side of the domain) and 180° for radiances in the direction toward the sun (toward the left hand side of the domain). Since the radiances are azimuthally symmetric, the azimuthal angle of 90 degrees could be considered to be either the direction into the paper or out of the paper.

Table 6.1: Viewing angles selected in case studies.

μ (degrees)	ϕ (degrees)
0	0
15	0, 45, 90, 135, 180
30	0, 45, 90, 135, 180
45	0, 45, 90, 135, 180

A bispectral retrieval grid was created for each RAMS model cross section to facilitate the retrieval process. The retrieval grids consist of SHSG independent pixel approximation calculations of normalized reflectances $R_\lambda = \frac{\pi I_\lambda}{\mu_0 F_0}$ (see Nakajima and King, 1990) from a wide range of plane parallel, vertically homogeneous clouds with effective radii ranging from 4 microns to 62 microns, and optical depths ranging from 1 to 30. In all of the radiance calculations the spherical harmonic truncations were set to L=23, M=11. In order to distinguish these baseline calculations from the other radiance calculations mentioned below, they will be referred to as the bispectral grid (BG) calculations. The normalized reflectances computed from the 2D SHSG radiance calculations of the RAMS cross sections are compared to the bispectral grid in order to retrieve effective radius and optical depth. The optical properties used in the retrieval grids were the mean single scattering albedo and mean asymmetry factor measured from Mie scattering calculations of all the droplet distributions from each cross section. For each effective radius in the grid, the droplet distributions were adjusted to the required effective radius by adjusting the size of the droplets in each of the twenty five size bins according to the following formula:

$$D_i = D_{eff} \left(\frac{M_i}{N_i}\right)^{1/3} \left(\frac{\sum_{i=1}^{25} N_i^{1/3} M_i^{2/3}}{\sum_{i=1}^{25} M_i}\right), \tag{6.1}$$

where D_{eff} is the required effective diameter, M_i is the total mass in bin i, and N_i is the total number concentration in bin i. This formula was used since the adjusted droplet distributions could easily be computed from droplet mass and number data produced by the RAMS model. The adjusted distributions also retained the same number concentrations and roughly similar shapes compared to the original droplet distributions.

Examples of the retrieval grids are shown in Figures 6.1 and 6.2. Note that the shape and size of the grid (in reflection function space) are a function of the sun/viewer geometry. Unlike Figure 2 in Nakajima and King (1990), the reflection function at 0.75 microns is slightly more dependent on effective radius since the surface albedo is nonzero (six percent). Also, for effective radii less than 6 microns, the reflectance function at 2.16 μm begins to decrease with decreasing effective radius and some combinations of reflectance functions lead to non unique estimates of optical properties (Nakajima and King, 1990). The larger imaginary index of refraction for liquid water at 3.70 μm eliminates some of this non-uniqueness permitting retrievals of effective radii as small as 4 microns (see Figures 6.3 and 6.4). However, no efforts were made to distinguish between the different solutions at small effective radii since in all of the RAMS simulations the effective radii throughout the clouds were almost always greater than 6 microns. Those sections of the cloud with radii below 6 microns were rare and generally confined to the base of the clouds, so they were not expected to influence the retrievals significantly (Nakajima and King, 1990).

The accuracy and precision requirements of the bispectral grids were strict. An examination of the grids in Figures 6.1 and 6.2 show that at small optical depths (between 3 and 4) the relative difference in the reflectance function at 2.16 μm for each one micron difference in effective radius was as small as 1 or 2 percent. These small reflectance differences present at least two problems for the retrieval grids. Firstly, the resolution of the spatial grid must be very fine for homogeneous clouds in order to accurately approximate the spatial derivatives in the radiative transfer equation and provide accurate results (see Chapter 2). (The optical depth per grid cell was set to 0.05 in the retrieval grid calculations.) Secondly, the SHSG solution method is numerical and must be solved to an arbitrarily small error. The solution criterion in SHSG is a global criterion, and more than one approximate solution may satisfy it. When bispectral grids were created using a solution criterion of 1.0×10^{-3}, discontinuities in the grid would sometimes appear as a result of the approximate nature of the solution method. When the solution criterion was lowered to 1.0×10^{-4}, the discontinuities in the bispectral grids were eliminated. The calculations, however, were extremely computationally expensive. The IPA version

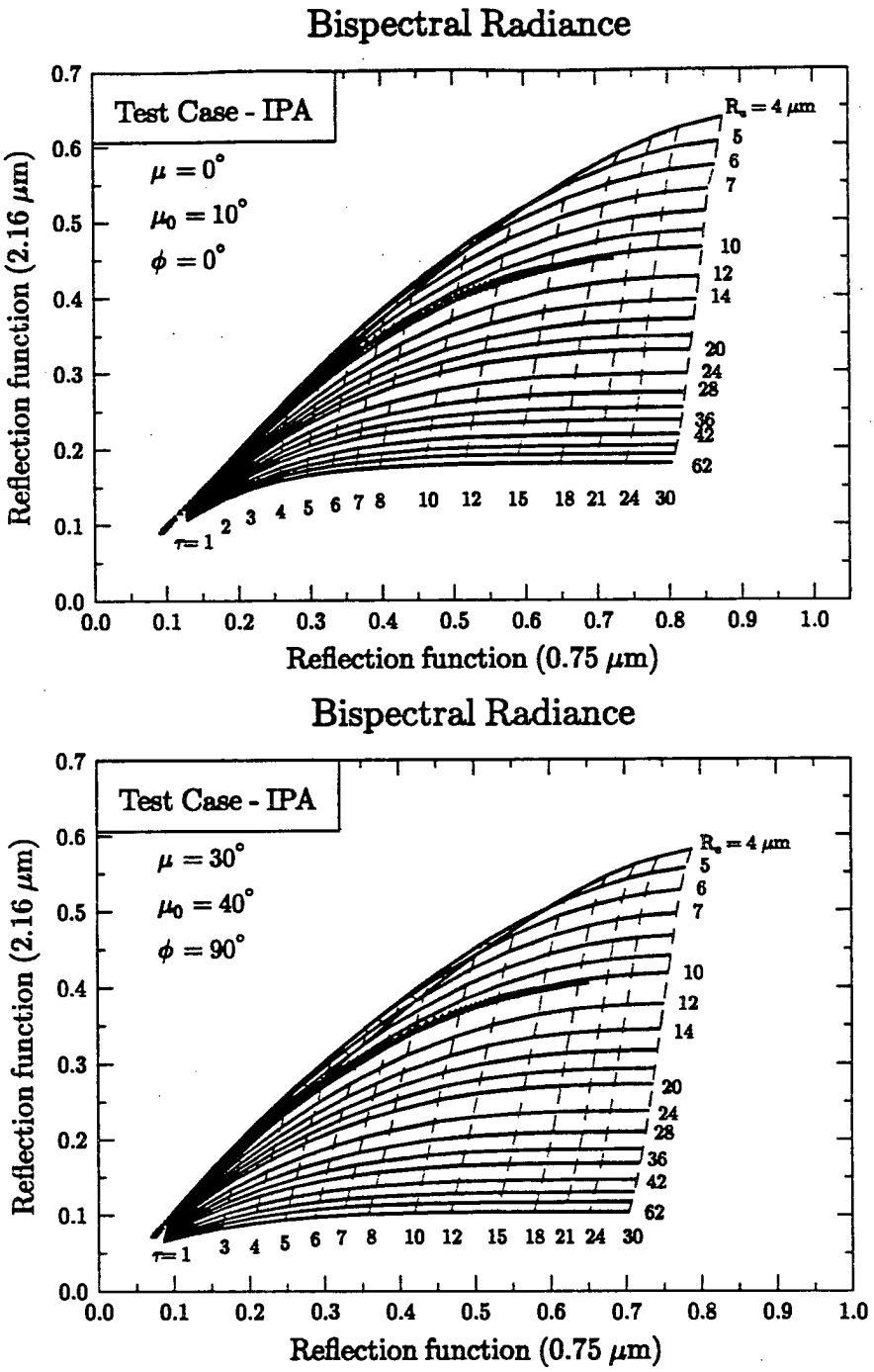

Figure 6.1: Bispectral retrieval grids based on PPA calculations of the reflectance function at 0.75 μm and 2.16 μm for $\mu = 0°, \mu_0 = 10°$, and $\phi = 0°$ and for $\mu = 30°, \mu_0 = 40°$, and $\phi = 90°$. The symbols show the point by point IPA calculated reflectance functions from the test case.

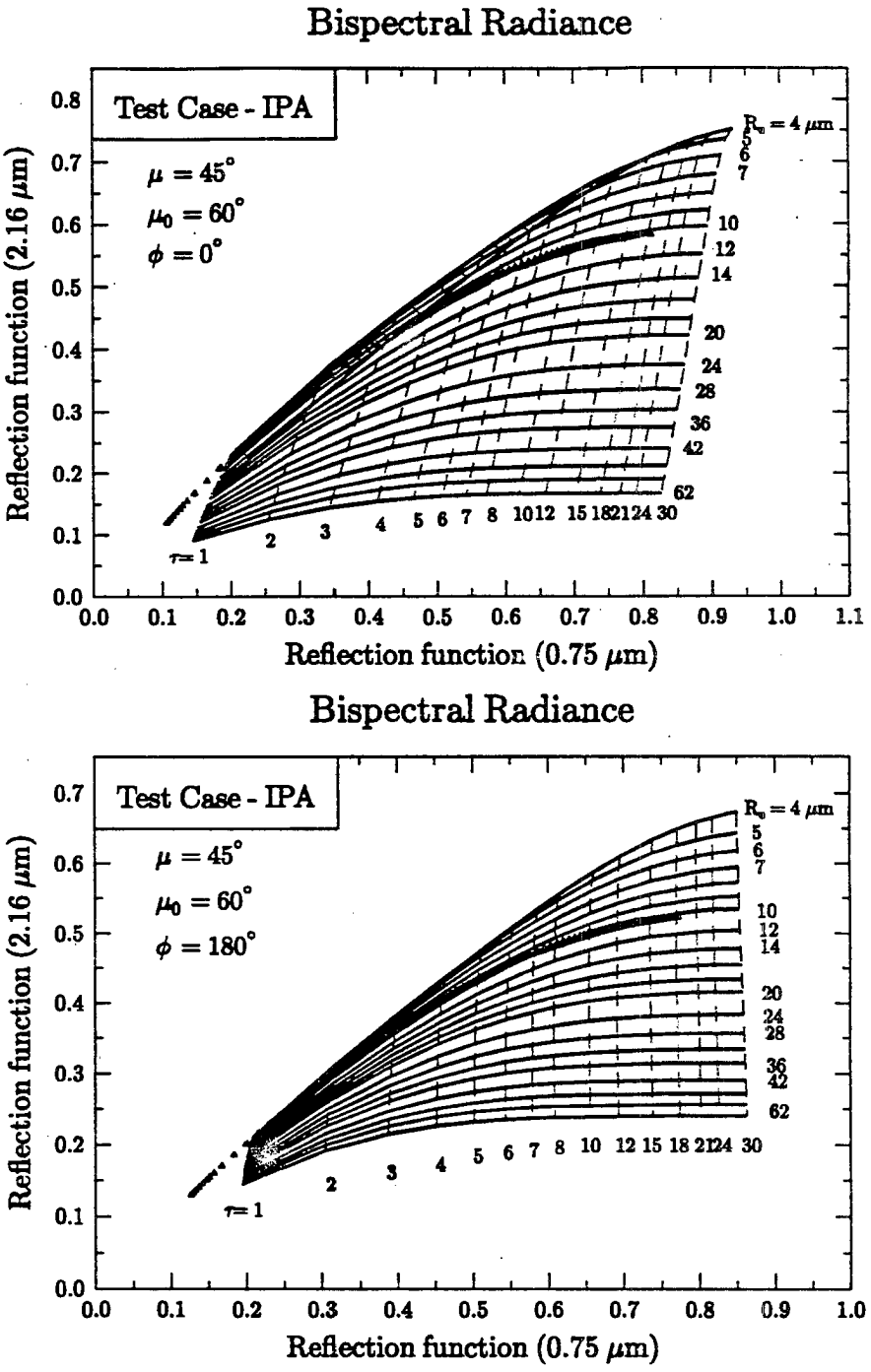

Figure 6.2: The same as Figure 6.1, but for $\mu = 45°, \mu_0 = 60°$, and $\phi = 0°$ and for $\mu = 45°, \mu_0 = 60°$, and $\phi = 180°$.

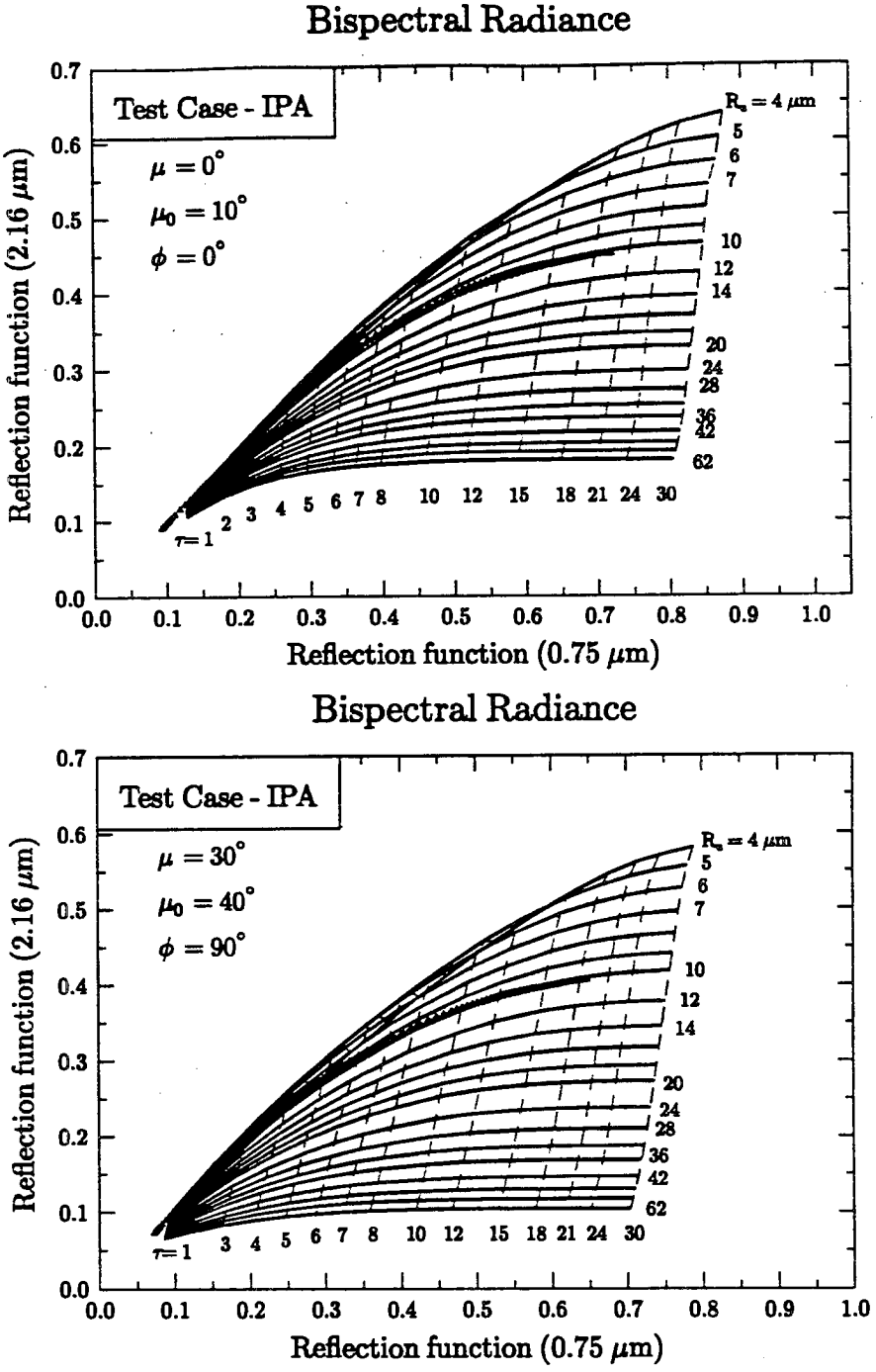

Figure 6.1: Bispectral retrieval grids based on PPA calculations of the reflectance function at 0.75 μm and 2.16 μm for $\mu = 0°, \mu_0 = 10°$, and $\phi = 0°$ and for $\mu = 30°, \mu_0 = 40°$, and $\phi = 90°$. The symbols show the point by point IPA calculated reflectance functions from the test case.

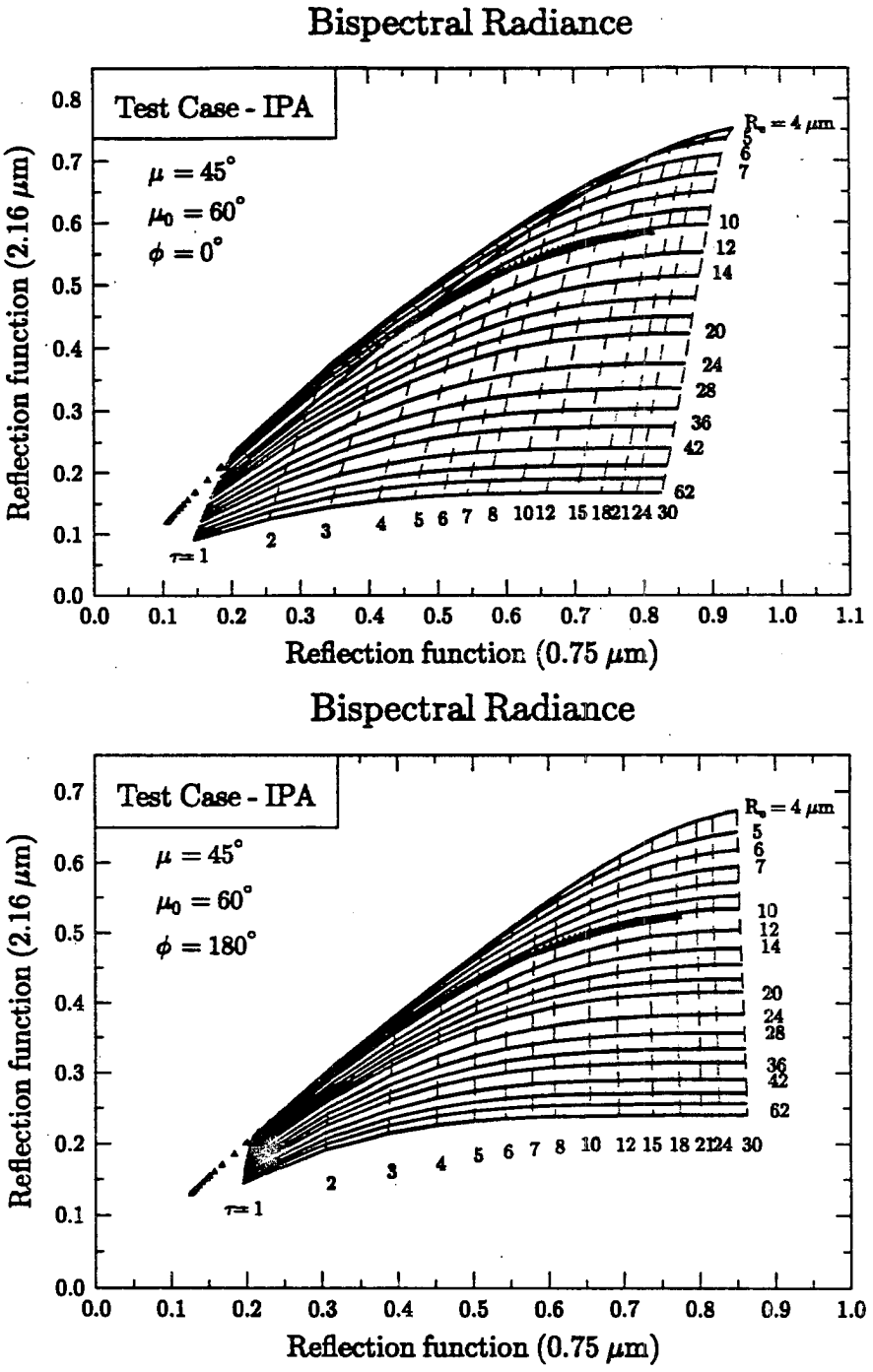

Figure 6.2: The same as Figure 6.1, but for $\mu = 45°, \mu_0 = 60°$, and $\phi = 0°$ and for $\mu = 45°, \mu_0 = 60°$, and $\phi = 180°$.

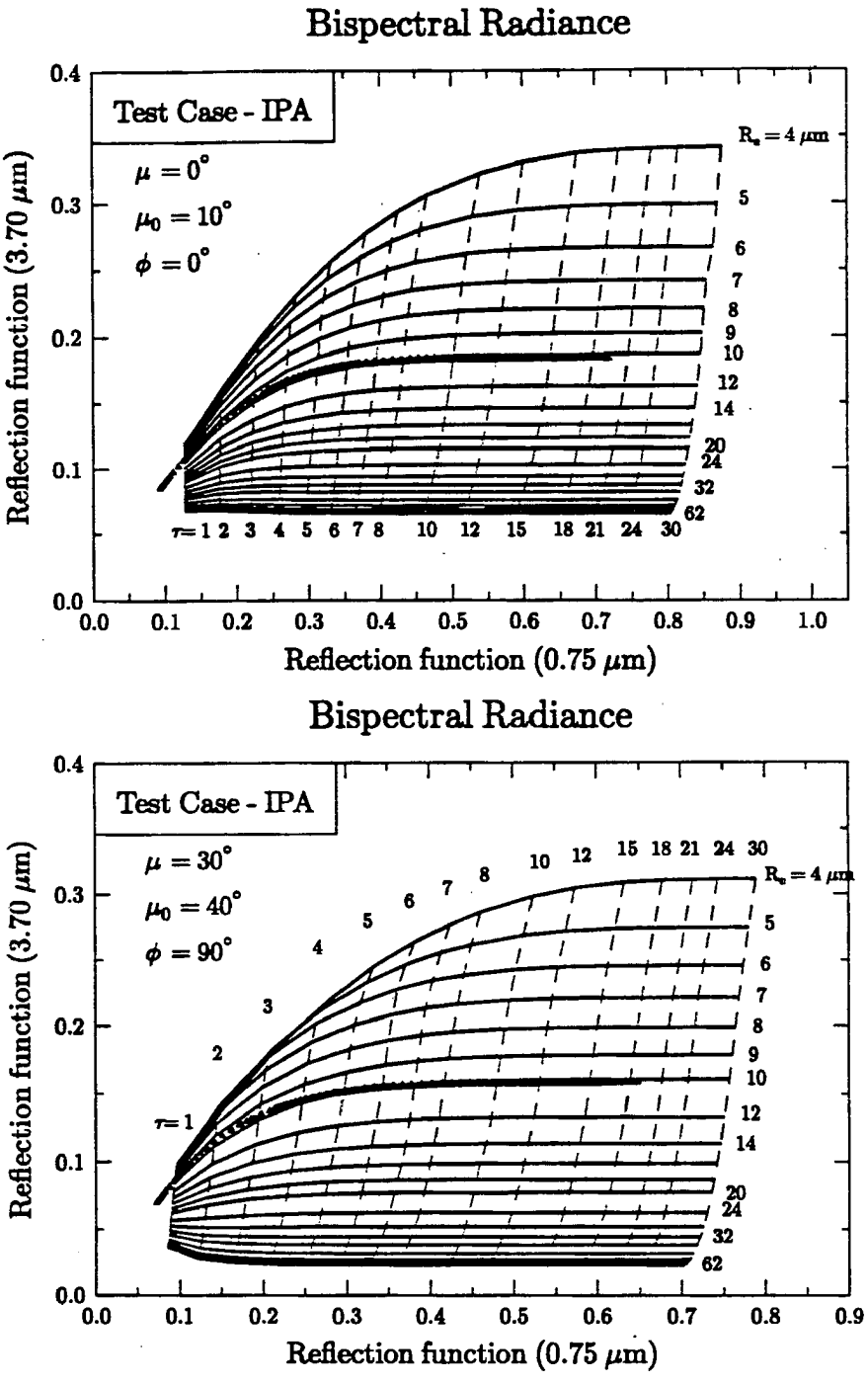

Figure 6.3: The same as Figure 6.1, but for the 0.75 μm and 3.70 μm retrieval grids.

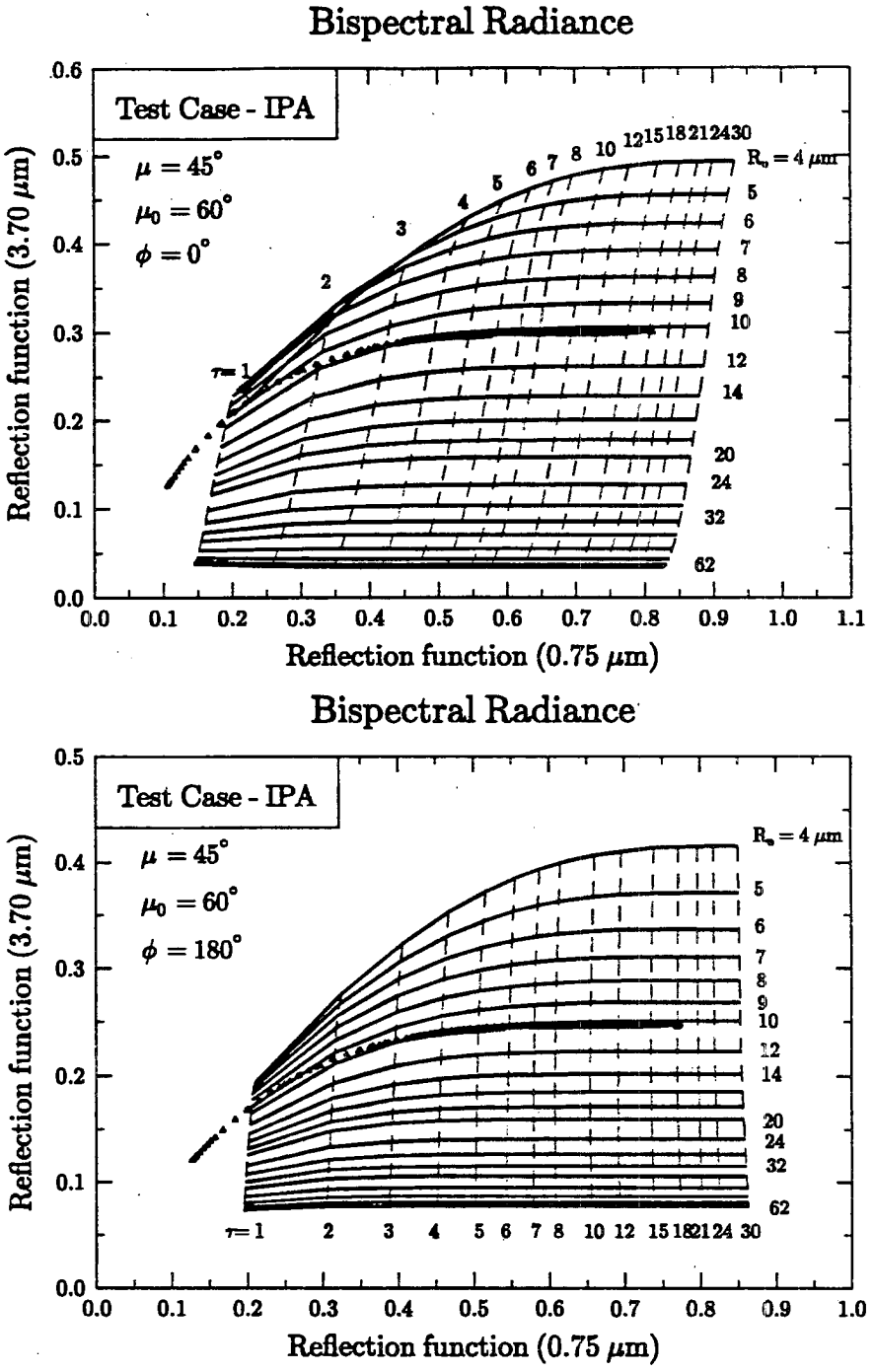

Figure 6.4: The same as Figure 6.2, but for the 0.75 μm and 3.70 μm retrieval grids.

of the SHSG model was chosen to create the bispectral grids since it is computationally consistent with the 2D model. More simple plane parallel models could be used to make the grids once they are compared with the results of the IPA model. In both the BG and RAMS cross section radiance calculations the Kourganoff integration technique was used to derive radiances so that errors introduced by the radiance computation method were eliminated. Stackhouse and Stephens (1994) have recently shown through comparisons with Monte Carlo calculations that the Cesàro filtering technique is more accurate overall in computing radiances, especially at the backscattering angle. However, the computational expense of creating new bispectral grids prevented the use of this averaging method. When the Cesàro method was used in the RAMS cross section radiance calculations and compared to the Kourganoff computed radiances, the differences in the domain average retrievals of effective radius were generally only a few tenths of a micron except near the back scattering direction where the differences were up to 0.8 of a micron. The differences in the domain average retrievals of optical depth were usually only a few tenths, except in the backscattering sun/viewing geometries where the differences were as large as 0.7.

6.2 Test case

Since the grid resolution and solution criterion requirements of the retrieval grid were more strict than those computationally feasible for RAMS radiance calculations, a test case was run to assess the impact of the different computational standards. The test case used the extinction coefficient data from Case 1a of the RAMS simulations, and the mean single scattering albedo and asymmetry factor from the droplet distributions adjusted to the 10 micron effective radius. Rather than using the full SHSG model to compute radiances, the IPA mode of the model was used. The results of the test case are presented in Figures 6.1 and 6.2 for a range of solar zenith and viewing angles. Ideally, the results from these IPA test calculations should fall exactly on the 10 micron retrieval grid curve since the same model is used to compute radiances in virtually the same cloud. The effects of the vertical inhomogeneity in extinction in each column are practically unimportant since the vertical coordinate in the model computations is converted to optical depth. However, as a result

of the coarser grids in the test case, the accuracy of the finite difference approximations across each grid cell in the cloud can be slightly different. These differences and the effects of the larger solution criterion (8×10^{-4}) result in the computed reflectance functions in the IPA test case not exactly following the retrieval grid. At larger optical depths the test case does follow the curve well, but as the optical depth decreases the curve approaches the smaller effective radii curves. The minimum retrieved effective radius value is near 8 microns at an optical depth of 3. Another result of the different computational standards between the bispectral grid and the IPA test case was that not all of the test case values were exactly on a single curve. The maximum deviation however appears to result in an effective radius difference of less than one micron.

The results of the IPA test case illustrate the errors involved with the retrieval scheme due to the different computational standards between the BG and IPA test radiance calculations. The insensitivity of the reflectance function at 2.16 microns to changes in effective radius makes the retrieval of effective radius difficult at small optical depths. For this reason, effective radius retrievals for $\tau < 3$ are not likely to be reliable. (From a practical viewpoint, reflectances currently can only be measured to an accuracy of five percent (Nakajima and King, 1990) by airborne radiometers, and accurate R_e retrievals at small optical depths are not possible.) However, optical depth retrievals below this threshold are more reliable since the reflectance function at 0.75 microns is very sensitive to optical depth for thin clouds.

A similar set of bispectral grids are shown in Figures 6.3 and 6.4 for the retrievals using the 3.70 μm reflectances. Overall the retrievals at this wavelength were better because of the greater sensitivity of the reflectance function to changes in effective radius. For all sun/viewer geometries the domain average of the effective radius retrievals was always within one percent of 10 microns, and this suggests that the effective radius retrievals at 3.70 μm are not subject to much error from the coarser grids used in the RAMS cross section calculations. In Figure 6.5 the retrieved effective radius using the 3.70 μm reflectances is shown as a function of horizontal distance, and confirms that the retrievals are very good across most of the domain. The only significant discrepancies occur around

1.7 - 1.9 km, where the optical depth decreases below unity. At 2.16 μm, the domain average of the effective radius retrievals ranged from 8.87 to 9.65 microns across the different sun/viewing geometries and thus the relative error from the actual 10 micron radius ranged from 3.5 to 11.3 percent. The larger errors in the 2.16 μm were mainly caused by the insensitivity of the reflectance function at 2.16 μm to changes in effective radius amplifying the effect of the finite difference errors. Only the effective radius retrievals from the 3.70 μm reflectances are presented below since they appear to be more reliable. When the effective radii in the RAMS cross sections retrieved from the 2.16 μm reflectances were compared to those from the 3.70 μm reflectances, the 2.16 μm were systematically lower by a difference of roughly 1 to 1.5 microns.

Figures 6.6 and 6.7 show the retrieved and actual 0.75 μm optical depth (calculated from Mie theory) computed for the IPA test case for a range of sun and viewing angles. The effect of the coarser finite difference grid used in the RAMS cross section calculations is most evident at the largest optical depths where the accumulation of finite difference errors is largest and the sensitivity of the reflectance function to changes in optical depth is the smallest. For optical depths less than 10, the retrieved values are nearly identical to the actual values, while at larger optical depths the retrieval underestimates the true value by as much as 12 percent depending on the sun and viewing angles, with the errors increasing as the solar zenith angle becomes larger. The domain averaged retrieved optical depth range from 7.86 to 8.13, while the actual domain average value (not counting those regions where the optical depth falls below one) is 8.32. These differences are larger than the effective radius retrieval errors at 3.70 microns, and must be considered later in the optical depth retrievals from the RAMS cross sections.

6.3 Effects of the horizontal transport on optical property retrievals

For the results presented above, the effects of cloud geometry were neglected since both the bispectral grid and the IPA test case calculations assume a horizontally homogeneous atmosphere. In this section the effects of the horizontal transport of radiation on the retrievals of effective radius and optical depth will be considered. Unlike the results

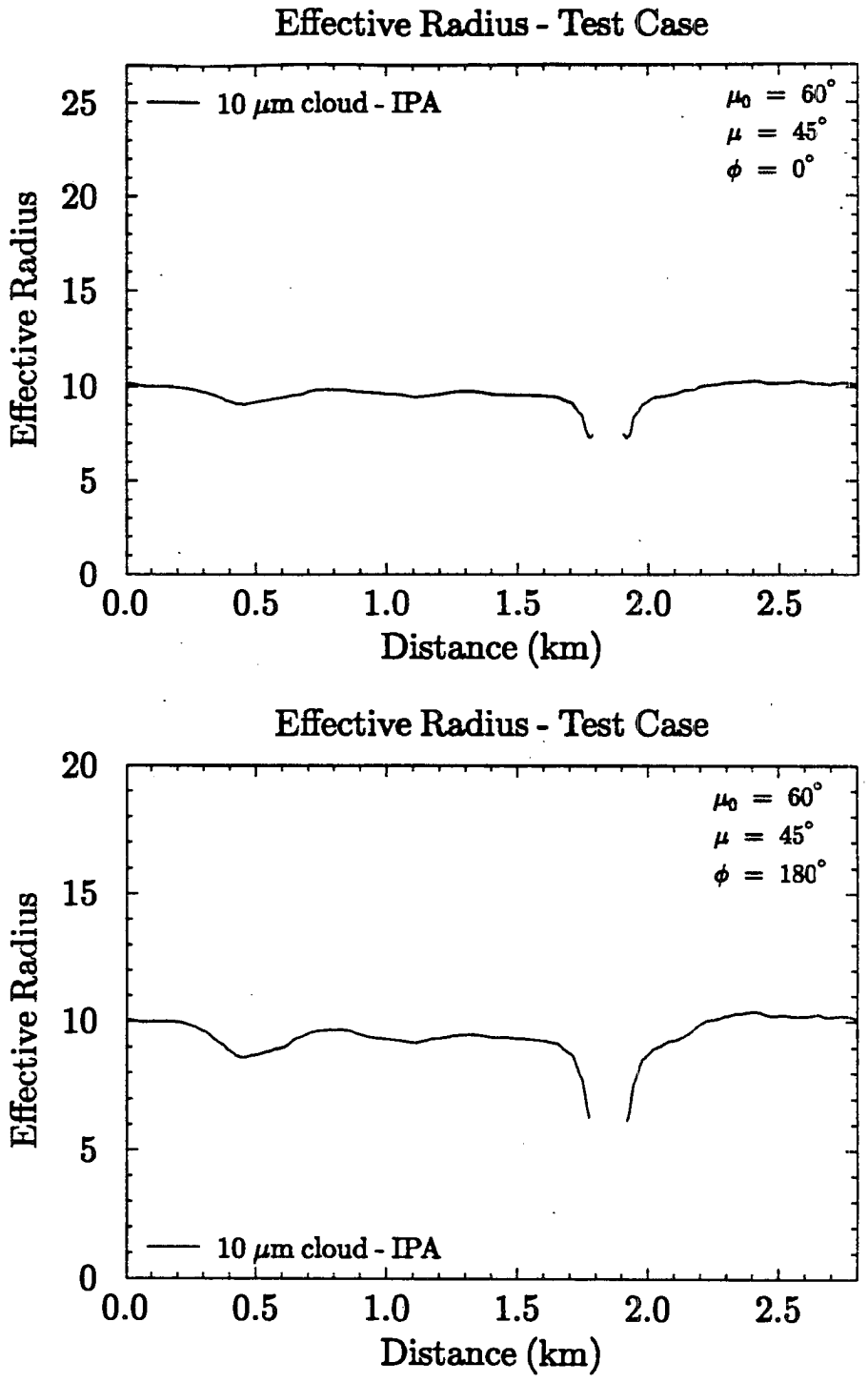

Figure 6.5: The effective radius retrieved from the IPA calculations of the test case at 0.75 μm and 3.70 μm for two sun/viewing geometries.

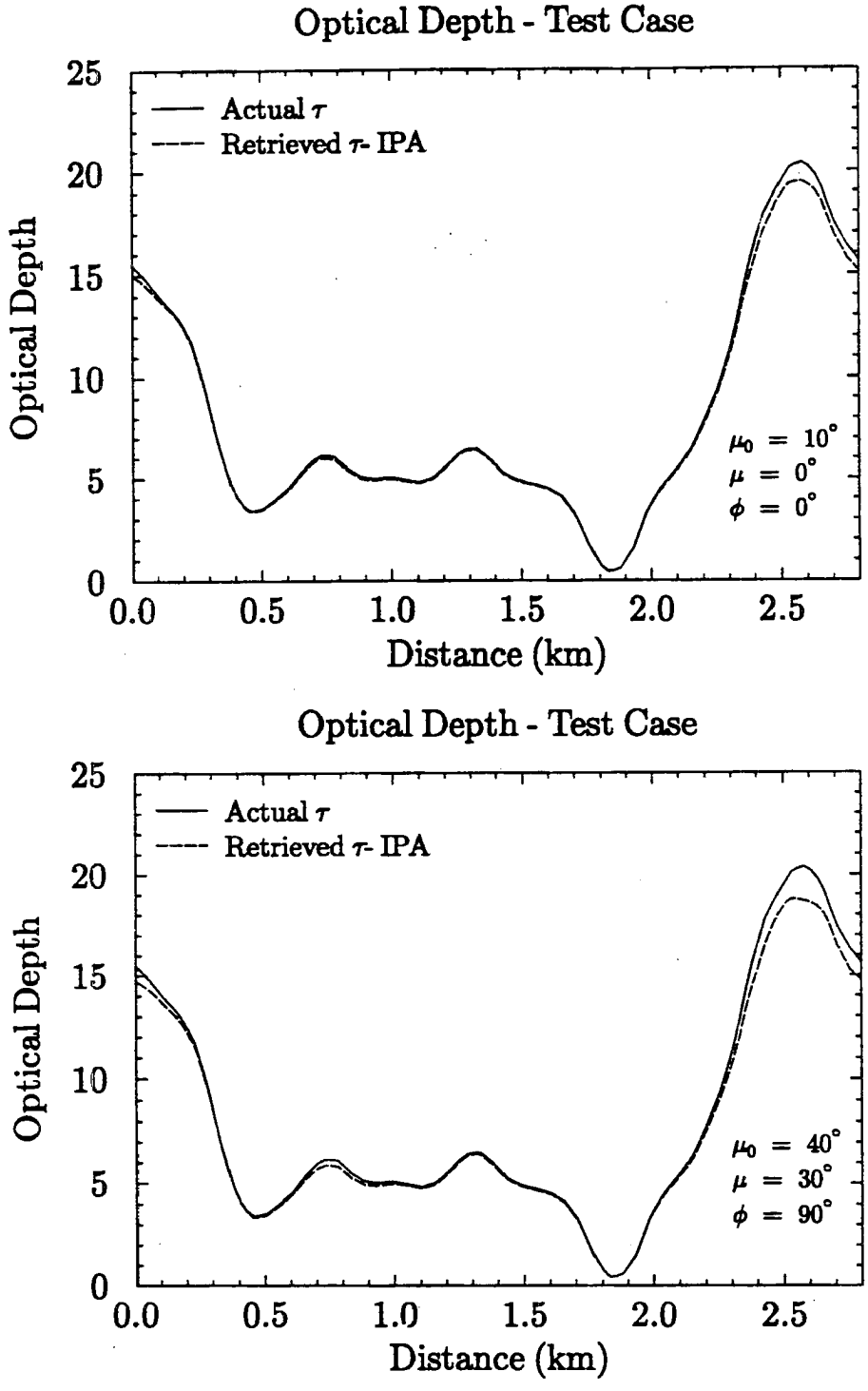

Figure 6.6: The actual 0.75 μm optical depth and the retrieved optical depth derived from the IPA calculations of the test case at 0.75 μm and 3.70 μm for $\mu = 0°, \mu_0 = 10°$, and $\phi = 0°$ and for $\mu = 30°, \mu_0 = 40°$, and $\phi = 90°$.

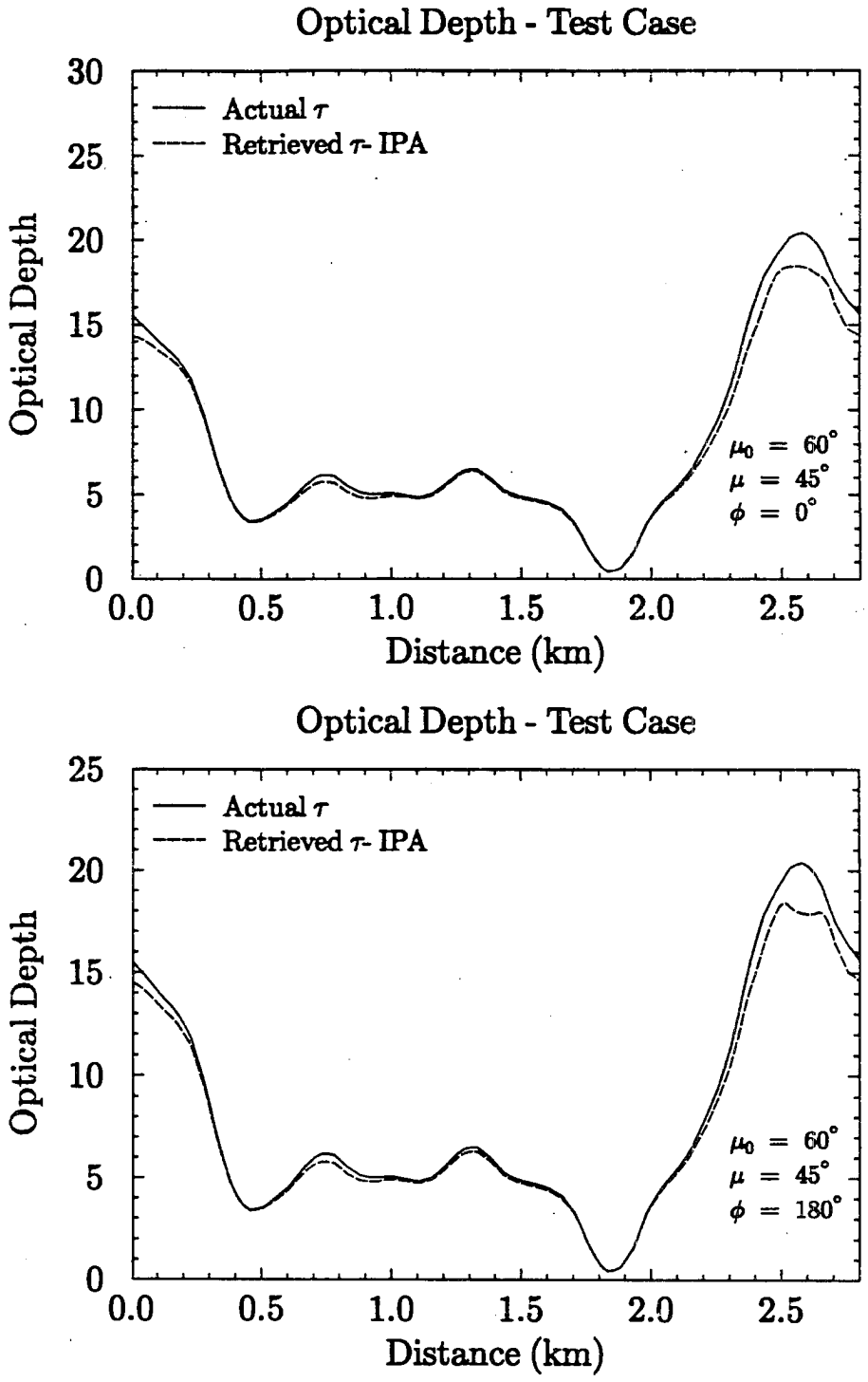

Figure 6.7: The same as Figure 6.6, but for $\mu = 45°, \mu_0 = 60°$, and $\phi = 0°$ and for $\mu = 45°, \mu_0 = 60°$, and $\phi = 180°$.

presented in the IPA test case, all of the following retrievals were done by computing the radiances in each cross section using the two dimensional SHSG model. This model, unlike the IPA mode of SHSG, computes the radiative transfer in a medium that can vary in two dimensions (instead of one), and horizontal transport of radiation can be explicitly computed and thus is a more realistic representation of the radiance fields. It is therefore expected that the point by point retrieval of cloud optical properties will vary from the actual properties since the retrieval grid is based on a horizontally (and vertically) homogeneous cloud and cannot account for any effects of the horizontal transport of radiation. Nearly all of the error that arises from these point by point retrievals results from the effects of the horizontal variability of the cloud optical properties.

6.3.1 Optical Depth Retrievals

Figure 6.8 shows the optical depth retrieval in Case 1a for two different viewing angles and a solar zenith angle of 60 degrees. These sun/viewer geometries were chosen because they most clearly illustrate the effects of the horizontal transport of radiation in the cloud. Unlike the previous results from the IPA test case, the discrepancies between the retrieved and actual optical depths are locally large. The close correspondence between the retrievals based on the 2D version of the test case and Case 1a show that the effects of the horizontal and vertical variability of effective radius (and thus the single scattering albedo and asymmetry factor) in Case 1a on the optical depth retrieval are minor. The correspondence is especially close since the domain averaged effective radius near the top of the cloud in Case 1a is close to 10 microns. Therefore, nearly all of the differences in the optical depth retrievals are due the effects of the horizontal variability of optical depth. Most noticeable in Figure 6.8a is the enhanced peak at 2.6 km and the large underestimation to the right of this peak. Figure 6.8b shows the radiance at an angle near the backscattering direction and clearly demonstrates the shading effects of the extinction peak at 2.6 km. Note that at some points near 2.0 km no value of retrieved optical depth is plotted even though the actual optical depth is clearly above unity. In these cases the effects of cloud geometry were such as to move the combination of the 0.75 μm and 3.70 μm reflection functions out of the area covered by the retrieval grid. The domain average

values of the retrieved optical depths in the test case using the 2D model to calculate the cross section radiances ranged from 7.19 to 8.36, depending on the sun/viewing geometry. When compared to the range using the IPA model (7.86 to 8.13), it is evident that the effect of the horizontal transport of photons is to make the domain average of the reflected radiances more sensitive to the sun/viewing geometry. Despite the large local errors in retrieved optical depth, the overall impact of the horizontal transport of photons on the domain average of all the retrievals is small. Except for Case 1a, the typical domain average value of the retrieved optical depth was generally within ±5 percent of the actual optical depth. Case 1a suffered the most of all the cross sections from the problem of the computed reflectance functions being outside the retrieval grid and produced a negative bias in the domain average of the retrieved optical depth.

6.3.2 Effective radius retrievals

Figures 6.9 and 6.10 show the retrieved effective radii as a function of distance along the cloud for Case 1a and the test case (2D version) cross sections. Unlike optical depth, no one value of effective radius can be assigned to each horizontal grid point in the model domain. Instead, two values of effective radius are shown corresponding to the maximum and minimum effective radius computed in the cloudy part of each column. A grid point was considered to be cloudy if the liquid water content at the point exceed 0.01 g m^{-3}. In the model cloud, the effective radius usually increased with height and the maximum and minimum values of effective radius correspond roughly with the cloud top and cloud base values of effective radius respectively. As expected, the effective radius retrievals are dependent on the variability of effective radius in the cloud. The cloud in Case 1a tended to be darker than the 2D test case cloud and mean of the retrieved R_e values was approximately 1.5 microns larger for any sun/viewing geometry. The largest differences between the retrievals in Case 1a and the test case occur where the maximum effective radii are largest. As the solar zenith and viewing angles increase, the effects of cloud inhomogeneity become more important in the reflected radiances. In Figure 6.10 the retrieved effective radii are often considerably larger than the maximum effective radius.

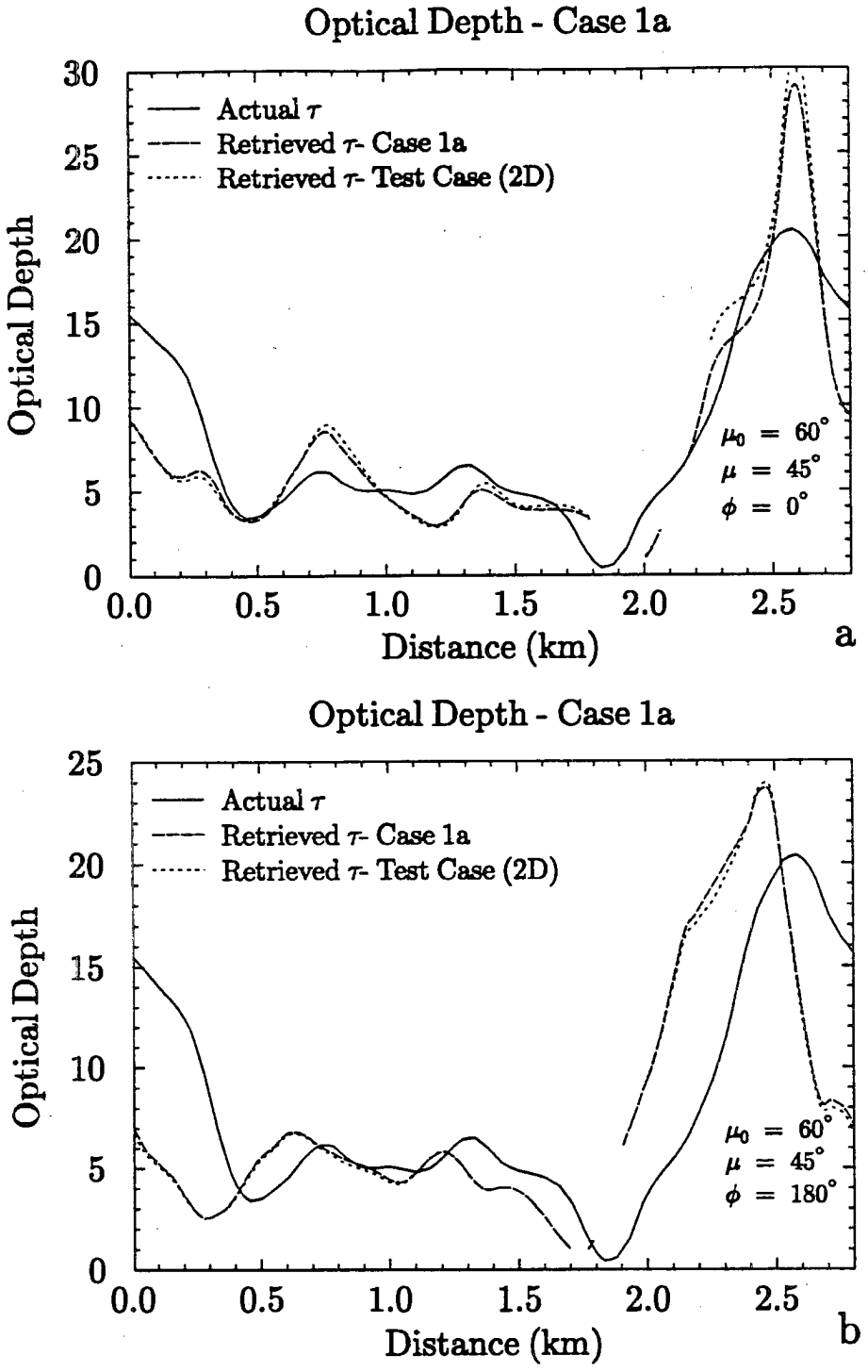

Figure 6.8: The actual 0.75 μm optical depth from Case 1a and the retrieved optical depth derived from the 2D calculations of the test case and Case 1a for two sun/viewing geometries.

This figure illustrates the difficulty in determining a relationship between a retrieved R_e and the effective radii distribution in the cloud. It is clear from the systematic differences between the retrievals in Case 1a and the 2D test case that the droplets near cloud top strongly influence the retrievals since the level of the 10 micron effective radius in the cloud was usually within the top 100 meters. Nakajima and King (1990) postulate that when the optical depth of the cloud is sufficiently large ($\tau > 8$ for 2.16 μm retrievals and $\tau > 5$ for 3.70 μm retrievals), the retrieved effective radius can be matched to the effective radius at some optical depth ($\hat{\tau}_{eq}$) within the cloud, and that this depth was relatively insensitive to the effects of vertical inhomogeneity. The optical depth can be calculated from a parameterization developed by Nakajima and King (1990) based on the retrieved effective radius and optical depth. The parameterization is as follows:

$$\hat{\tau}_{eq} = \min(0.365 - 0.145 \ln(k\tau_c), 0.5) \tag{6.2}$$

where τ_c is the optical depth of the cloud (which can be approximated by the retrieved optical depth) and k is a coefficient used in the asymptotic theory of Nakajima and King (1990). k can be approximated for the 2.16 μm retrievals (Nakajima and King, 1990) as

$$k = 4.92 \times 10^{-3} + 4.04 \times 10^{-2} \ln(R_e), \tag{6.3}$$

and for the 3.70 μm retrievals (Nakajima and Nakajima, 1994) as

$$k = 3.48 \times 10^{-2} + 9.62 \times 10^{-2} \ln(R_e), \tag{6.4}$$

where R_e is the retrieved effective radius. This equivalent effective radius will be referred to as the Nakajima-King effective radius (NK radius) and is nearly always between 85 to 90 percent of the maximum effective radius in the cloud for the 2.16 μm retrievals and slightly larger for the 3.70 μm retrievals.

It is also evident, however, that the reflected radiance at a point is influenced by the properties of the cloud surrounding the point and the sun/viewing geometry, as suggested by Figure 6.10. Thus, the retrieved effective radius is a function not only of the cloud microphysics locally but also of the surrounding cloud macrophysics. Like the optical

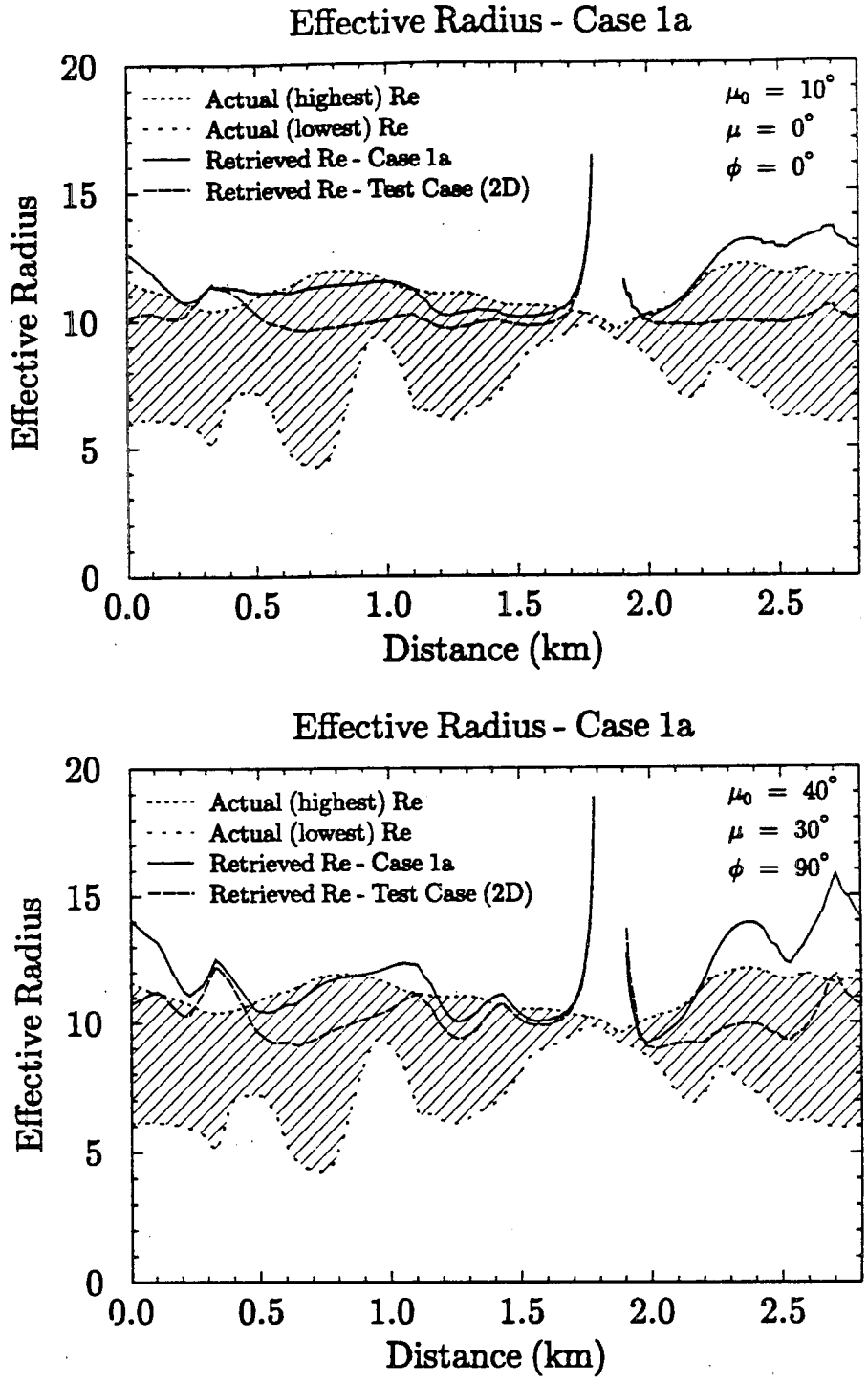

Figure 6.9: The effective radius retrieved from 2D radiances calculations at 0.75 μm and 3.70 μm of Case 1a and the test case as a function of distance. The shaded region indicates the range of effective radius computed at each point in Case 1a by Mie theory.

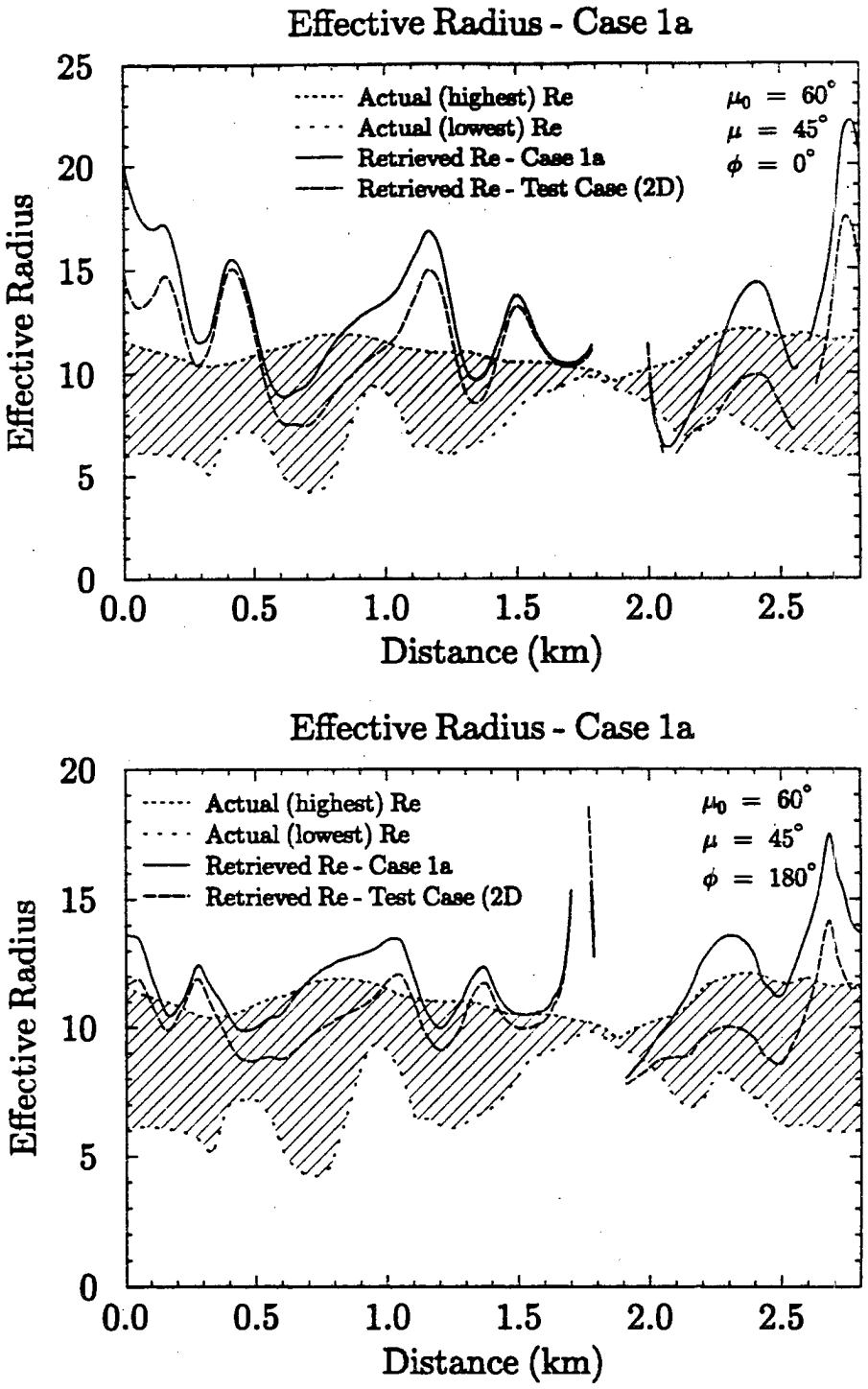

Figure 6.10: The same as Figure 6.9, but for a different set of sun/viewing geometries.

depth retrievals, the effect of the horizontal transport of photons on the retrievals is to make them more sensitive to changes in the sun/viewing geometry. The range in domain averaged retrieved R_e was 10.09 to 10.90 microns in the 2D version of the test case, compared to the 9.89 to 10.07 micron range in the IPA test case. In the R_e retrievals it also appears that the horizontal transport of radiation makes the clouds less reflective at 3.70 microns and the retrieved effect radius is systematically higher. This effect can also be seen in Table 6.2 (shown in a following section below) which compares the retrieved R_e with the domain mean of the maximum R_e for the RAMS cross sections Case 1a, 1b, 1c and 2c. In all of the cases the domain average of the retrievals exceeds the cloud's maximum R_e by an average of 2 (Case 2c) to 12 percent (Case 1b) depending on the cross section.

6.4 Effects of the variability in optical depth and effective radius

Although the results from the previous section highlight the effects of the horizontal transport of radiation on the optical property retrievals, the horizontal inhomogeneities in the cloud have another important effect on the retrievals. The spatial resolution of a satellite radiometer such as the AVHRR Local Area Coverage radiometer (Nakajima and Nakajima, 1994) is of the order of 1 to 6 km depending on the viewing angle. Thus the results of the point by point radiance calculations are much finer than is presently possible from most satellites. What the satellite will detect is an area-averaged radiance which is compared to the bispectral grid calculations. This averaging effect has many consequences on the subsequent satellite retrieval, and are enumerated below.

1. Since the satellite integrates the radiance over an area the point by point retrieval discrepancies produced by the horizontal transport of photons are averaged together and the overall dependence of the reflected radiances on sun/viewing geometry are diminished compared to the point by point radiances.

2. The area averaging introduces a bias similar in concept to the PPA albedo bias discussed in the last chapter. This bias can be demonstrated by an inspection of the bispectral grids in Figures 6.1 – 6.4. Any cloud area sampled by a satellite

radiometer will contain a range of optical depths due to the horizontal inhomogeneity of the field. Even if the effective radius throughout the area were nearly constant (as in the figures), the effective radius value retrieved from the mean reflection function at 0.75 μm and 3.70 μm would necessarily be larger than the value of the effective radius curve.

3. The magnitude of the bias depends not only on the variability of the optical properties in the satellite sample area (or satellite pixel), it also depends on the shape of the bispectral grid and thus the relationships between the reflectance functions and the retrieved cloud properties. This means that the biases will be different depending on the wavelengths used in the retrievals and the magnitude of the cloud's effective radius and optical depth. Some conclusions from this are:

   - Since the R_e curves based in the 3.70 micron reflection function are less convex than those at 2.16 microns, a generally smaller R_e area averaging bias would be expected for the 3.70 micron retrieval, especially for smaller effective radii. This result can be seen when the effective radii computed from the domain average of the point by point retrievals are compared with the effective radii computed from the domain mean reflectance function values for both the 2.16 micron and 3.70 micron retrievals. For example, in the IPA test case at 3.70 microns, the values computed from the mean of the point by point retrievals ranged from 9.89 to 10.07 microns and increased to a range of 10.55 to 10.92 microns for the values computed from the mean reflectance functions. At 2.16 microns, the corresponding effective radius ranges were 8.87 to 9.65 microns and 11.02 to 11.94 microns respectively.

   - The shape of the bispectral grids also indicate that while the effective radius curves become straighter for larger optical depths and effective radii (this would tend to reduce the overall bias), the spacing between the curves is nonlinear. This may lead to larger biases for large mean values of optical depth and effective radius, especially when the optical properties within the satellite pixel are

highly variable. In this case, the effects of the large point by point reflectance function fluctuations described in the last section would help to enhance the positive bias in retrieved effective radius. Similarly, the nonlinear relation between the 0.75 μm reflectance function and optical depth will introduce a negative bias in the satellite retrievals, which would become larger for larger optical depths. This effect may explain at least in part why the optical depth retrievals in Nakajima et al. (1991) underestimated optical depth when the optical depth became large.

By comparing both the domain averaged point by point retrievals (hereafter referred to as mean of retrievals or MOR) and the retrievals using the domain average reflectance functions (referred to as mean reflectance function or MRF) for all of the RAMS cross sections, estimates of many of the retrieval biases described above can be made for marine stratus clouds. Table 6.2 presents the maximum and minimum values of the MOR retrievals and the MRF retrievals computed over of all sun/viewing angles for all of the radiance simulations.

Table 6.2: Range in the domain averaged effective radius and optical depth retrievals for all radiance simulations. The retrieved values are computed from the domain average of the point by point retrievals (mean of retrievals) and the domain averaged reflectance functions (mean reflectance function). The actual domain averaged optical depth and the domain averaged maximum R_e are also presented for each simulation.

Case	Mean of retrievals		Mean Radiance		$\overline{\tau}$	max.
	$R_e(\mu m)$	τ	$R_e(\mu m)$	τ	(μm)	$\overline{R_e}$
IPA test	9.89 – 10.07	7.86 – 8.13	10.55 – 10.92	5.91 – 7.12	8.01	10.00
2D test	10.09 – 10.90	7.19 – 8.36	10.62 – 11.03	5.63 – 6.91	8.01	10.00
1a	11.41 – 12.68	7.18 – 8.11	12.11 – 12.83	5.57 – 6.83	8.01	11.09
1b	12.33 – 13.71	8.92 – 11.97	12.73 – 13.75	7.19 – 8.98	10.04	11.51
1c	11.82 – 13.03	5.95 – 6.67	12.35 – 13.18	5.13 – 5.89	6.41	11.58
2c	10.09 – 11.29	6.88 – 7.59	10.63 – 11.26	5.83 – 6.66	7.32	10.02

The differences between the MOR retrieved values from the corresponding MRF retrievals show the effects of a satellite's area averaging bias. The effects on the effective radius retrievals were to reduce the sensitivity of the retrievals to sun/viewing geometry.

The range in the MOR retrievals in Cases 1a, 1b, 1c and 2c were near 1.2 μm but only 0.6 to 1.0 μm for the MRF retrievals. For a given sun/viewer geometry the effective radius value in the MRF retrieval was an average of 0.3 to 0.4 microns larger than the corresponding MOR retrieval, with larger differences at smaller solar zenith angles and smaller differences at larger solar zenith angles. Since the mean effective radii in all four of the RAMS cross sections were similar in magnitude, the magnitude of the area averaging bias for clouds with larger R_e could not be assessed. The effect of the area averaging bias on the optical depth retrievals appears to be larger than that of the effective radius retrievals, and more sensitive to the horizontal variability of the optical properties in the domain. For a particular sun/viewing geometry, the MOR retrieved optical depths were 15 to 25 percent larger than the corresponding MRF retrievals. Part of this difference is due to the lower optical depth limit in the MOR retrievals elevating the domain averages. However, this effect was significant only in Case 1a, where it accounted for an optical depth difference of 0.3 in the domain average, which is twenty five percent of the mean difference between the MOR and MRF retrievals in the cross section. Most of the remaining optical depth increase (0.9) is attributed to the effects the area averaging bias and is 11 percent of the domain average optical depth in Case 1a. The mean differences between the MOR and MRF retrievals were larger in Cases 1a and 1b (1.2 and 1.6 respectively) than those in Cases 1c and 2c (0.5 and 0.7) and are likely the result of the greater variability in the optical depth distribution in those cross sections. The standard deviation of $\log \tau$ was 0.3294 and 0.3502 in Cases 1a and 1b respectively, and only 0.2370 and 0.2498 in Cases 1c and 2c.

6.5 Total impact of cloud inhomogeneity on retrievals

Given the results from Table 6.2, the total influence of cloud inhomogeneity on the retrieval of optical properties can be made. Table 6.3 presents the mean relative difference (summed over all sun/viewing geometries) between the actual domain average optical depth and domain average maximum effective radius from the domain averaged values obtained from the MOR and MRF retrieval methods for Cases 1a, 1b, 1c and 2c.

Table 6.3: Mean relative difference (summed over all sun/viewing angles) between the actual domain averaged optical depth and maximum effective radius from those computed from the MOR and MRF retrieval methods for Cases 1a, 1b, 1c and 2c.

Case	Mean of retrievals		Mean Radiance	
	$R_e(\mu m)$	τ	$R_e(\mu m)$	τ
1a	7 %	9 %	11 %	21 %
1b	12	0.5	15	17
1c	6	4	9	11
2c	2	3	7	12

The differences produced by the MOR method (from the actual values) result from the direct effects of cloud inhomogeneity on the point by point retrievals of cloud properties via the horizontal transport of radiation. Table 6.3 shows that in general these direct effects are less than five percent on the τ retrievals and from two to twelve percent on the R_e retrievals. The MRF retrieval represents what a satellite radiometer measures and includes the additional area averaging bias produced by the horizontal variability of the cloud optical properties in the satellite's sampling area and the nonlinear relationships between reflectance function and cloud optical properties. The difference between the MRF retrievals and the actual domain averaged values of τ and R_e show that the area averaging bias contributes an additional 3 or 4 percent to the effective radius errors and the majority of the optical depth errors. The mean relative differences in the MRF R_e retrievals ranged from 7 to 11 percent and the differences in the τ retrievals ranged from 11 to 21 percent. These relative errors in the retrieved cloud optical properties are significant when compared to the microphysical changes in the RAMS simulations due to the enhanced CCN concentrations. The mean optical depth increase across the entire domain (at a model time of 9000 seconds) was 12 percent in the first sensitivity run and the mean effective radius decrease was also 12 percent. The effects of cloud geometry thus have a significant impact on the satellite retrieval of cloud optical properties even in relatively uniform clouds like the 2D marine stratus considered in this study, and clearly these effects must be addressed before producing accurate retrievals. Some discussion on ways to correct for cloud inhomogeneity are presented in the next chapter.

6.6 Summary

A brief description of a two channel method used to compute cloud optical depth and effective radius from satellite reflectance measurements is presented. A simplified retrieval comparing the cloud top reflectances with tabulated results from plane parallel calculations show that the effects of cloud inhomogeneity produce local fluctuations in the reflected radiances that can be significantly different than those computed from plane parallel calculations. The mean computed relative errors produced by these fluctuations ranged from 2 to 12 percent in the domain average R_e retrievals and 0.5 to 9 percent in the domain average τ retrievals. Horizontal inhomogeneity within a satellite pixel will also affect the retrievals due to the nonlinear relationships between the reflectance functions and the retrieved optical properties. This additional bias produced an extra 3 to 4 percent error in the effective radius retrievals and an additional 7 to 16 percent error in the optical depth retrievals. These error values were averaged over a range of sun/viewing geometries. In general, the errors were smallest for high sun and near nadir viewing angles, although the area-averaging effects of a satellite radiance measurement tend to make the retrievals of effective radius and optical depth fairly insensitive to the range of sun/viewing geometries used in this dissertation.

Chapter 7

SUMMARY AND CONCLUSIONS

7.1 Summary

Recent estimates of the effects of increasing amounts of anthropogenic sulfate aerosol on the global climate have indicated that its impact on the radiative forcing of the atmosphere may be comparable to the effect from increases in CO_2 (Boucher and Rodhe, 1994; Jones et al., 1994). Much of this impact is expected from the indirect effects of the aerosol on global cloud microphysics and the subsequent impact on cloud albedo. Kim and Cess (1993) show higher values of low level cloud albedo in near coastal boundaries compared to similar mid-ocean clouds and attribute the difference to changes in aerosol concentrations. However, internal cloud inhomogeneity is known to reduce cloud albedo (Cahalan et al., 1994). In order to assess the overall impact of anthropogenic aerosol on the global climate, methods must be developed to separate the impacts of both cloud microphysics and the cloud's horizontal inhomogeneity on cloud albedo and other cloud radiative properties.

The Spherical Harmonic Spatial Grid (SHSG) method (Evans, 1993) was used to simulate the radiative transfer through a two dimensional cloudy atmosphere. The SHSG model was modified in order to compute broadband solar fluxes, and the k distribution method was used to account for gas absorption. By averaging the k distribution data over broader wavenumber and absorption coefficient ranges, the number of required computations were reduced from over 12,000 to 200, while the accuracy of the broadband albedo calculations (0.5%) were still nearly an order of magnitude smaller than the albedo changes resulting from cloud microphysical or macrophysical effects. Additional reduction of the number of calculations in the broadband model was limited by the problems associated with accurately accounting for the rapid variation in cloud droplet optical properties

with respect to wavenumber in the bands of the broadband model. For low altitude stratus simulations, several additional computations could be ignored since the strongest k distribution weights were associated with absorption above cloud top.

Three RAMS/LES simulations were produced to provide realistic cloud physics data for the radiative transfer simulations. A control run using thermodynamic and CCN data measured during FIRE was made in order to simulate a typical marine stratus field. In two sensitivity studies, the impact of increased amounts of CCN on cloud albedo were examined by introducing six times the typical marine CCN concentration of 120 cm^{-3} into the model cloud from above and below the cloud layer respectively. Two dimensional cross sections of the microphysical data from all three model simulations showed that the addition of CCN above the cloud top in the first sensitivity run resulted in a 50 to 100 percent increase in the cloud droplet concentrations and a reduction of the cloud top effective radius from over 11 microns to less than 10 microns. The enhanced CCN concentrations added below cloud base increased the cloud droplet concentrations up to 110 percent compared to the control run and decreased the effective radius of the cloud top droplets to 8.5 microns.

The results of the radiative transfer calculations indicated that in unbroken marine stratus clouds the *net* horizontal transport of photons over a domain of a few km was nearly zero, and the domain average broadband albedo computed in a two dimensional cross section was nearly identical to the domain average calculated from a series of independent pixel approximation (IPA) calculations of the same cross section. This matches the findings from Cahalan et al. (1994) for monochromatic calculations in a simple cloud model, and suggests that accurate computation of domain averaged albedos in unbroken marine stratus can be made using IPA calculations with one dimensional radiative transfer models. The horizontal inhomogeneity does affect the cloud albedo due to the nonlinear relationship between albedo and optical depth (Cahalan et al., 1994) and reduces the domain average total solar cloud albedo by a relative difference of five to six percent for unbroken clouds and fifteen percent for a more inhomogeneous cross section with broken cloudiness, when compared to a perfectly homogeneous cloud with the same mean optical properties.

Given the good agreement between the domain averaged albedos computed by the independent pixel approximation (IPA) and the multi-dimensional RTMs in this study and in Cahalan et al. (1994), computations of the mean albedo over portions of the entire three dimensional RAMS domain were made for all three RAMS simulations using IPA calculations from a two-stream model. Comparisons of the total solar albedos computed by this method between clouds with similar mean microphysics and different macrophysics show the relative difference in cloud albedo resulting from typical macrophysical differences in marine stratus were between three to five percent. The relative differences in cloud albedo due to microphysical changes resulting from the sixfold increase of CCN concentrations above cloud top ranged from six to nine percent. When the same increase in CCN concentration was introduced below the cloud layer, the increase in cloud albedo ranged from ten to fifteen percent, although some of the increase was due to cloud dynamical changes not associated with the effects of the additional CCN. The impact of microphysics on the cloud was greatest for small solar zenith angles.

Like the broadband albedos, local differences between the 2D and IPA computed heating rates were significant but the domain averages were very similar. The effects of PPA bias on the net flux convergence in the cloud were as large as 5 percent in the $\theta_0 = 10°$ simulations, but very small at $\theta_0 = 60°$. The effects of the microphysical changes on the mean net flux convergence were less than 2 percent.

Using a simplified two channel retrieval method that compared the cloud top reflectances computed from the two dimensional RAMS/LES cross sections with tabulated results from a set of plane parallel calculations, the cloud optical depth and effective radius were estimated and compared to the actual cloud properties. The results showed that the effects of cloud inhomogeneity produced local fluctuations in the reflected radiances that could be significantly different than those computed from plane parallel calculations. The mean computed relative errors produced by these fluctuations ranged from 2 to 12 percent in the domain average R_e retrievals and 0.5 to 9 percent in the domain average τ retrievals. Horizontal inhomogeneity within a satellite pixel will also affect the retrievals due to the nonlinear relationships between the reflectance functions and the retrieved optical properties. This additional bias produced an extra 3 to 4 percent error in the effective

radius retrievals and a 7 to 16 percent error in the optical depth retrievals. These error values were averaged over a range of sun/viewing geometries. In general, the errors were smallest for high sun and near nadir viewing angles, although the area-averaging effects of a satellite radiance measurement tend to make the retrievals of effective radius and optical depth fairly insensitive to the range of sun/viewing geometries used in this dissertation.

7.2 Conclusions and Recommendations for Future Research

This dissertation addresses the impacts of both cloud microphysics and cloud macrophysics on the radiative properties of marine stratus. Using a set of three RAMS/LES simulations of the 7 July 1987 FIRE-I case study day, the effects of enhanced CCN concentrations on the broadband solar albedos and heating rates were explored, as well as the effects of cloud structure on the retrieval of cloud properties from airborne reflectance measurements. The results of Chapters 5 and 6 show that the changes in cloud radiative properties due to the horizontal inhomogeneity of the cloud field were often comparable in magnitude to the changes resulting from indirect microphysical effects of the enhanced CCN concentrations.

The macrophysics of the cloud affect its radiative properties in two ways. Horizontal inhomogeneity in a cloud produces horizontal transport of solar radiation which is most apparent in the comparison between the heating rate fields computed by the 2D model and the IPA model in Chapter 5. For unbroken stratus and at small solar zenith angles, the *net* horizontal transport of photons were found to not affect the mean cloud albedo averaged over an area of at least a few square kilometers. This result permitted the use of the IPA domain average albedo alone to estimate the macrophysical and microphysical influences on marine stratus in Chapter 5. The conclusions of Gabriel and Evans (1994) indicate that the inaccuracy of the IPA method at large solar zenith angles and in broken cloudiness limits the applicability of IPA model to compute accurate domain average albedos in cloud systems. For most cloud systems, models must be developed that account for horizontal inhomogeneity.

The second effect of cloud inhomogeneity on radiative properties results from the nonlinear relationships between a cloud's albedo or reflectance and its optical properties.

Over a given averaging area, a cloud field will have a distribution of optical depth due to horizontal inhomogeneity. Since from plane parallel calculations the increase in cloud albedo in areas with above average optical depth will be less than the decrease in cloud albedo on areas with below average optical depth, the domain average albedo computed from IPA calculations will always be less than from PPA calculations that use the domain average optical properties of the cloud field. Similar biases in reflectance retrievals of effective radius and optical depth will occur since the reflectance functions are not linear functions of these cloud properties. It is clear that future retrievals of effective radius and optical depth must include knowledge of the sub-pixel scale variability of optical depth and effective radius.

Therefore, in order to account for the impact of cloud macrophysics on cloud radiative properties, improved RTMs to account for cloud inhomogeneity must be developed and information about the horizontal variability must be obtained. Given the large number of radiative transfer calculations necessary for cloud property retrievals, or for broadband calculations, further development in the speed and efficiency of multi-dimensional RTMs is necessary. Work by Barker (1992) and Gabriel and Evans (1994) show some promise in computing fluxes in multi-dimensional medium with modified one dimensional RTMs. Through the use of closure schemes that account for the effects of horizontal inhomogeneity on the propagation of direct solar radiation (through the pseudo-source term of the radiative transfer equation), Gabriel and Evans (1994) have developed methods to calculate domain averaged fluxes in broken cloud fields more accurately than the IPA or PPA models when compared to the 2D SHSG model. These closures, however, are not able to compute radiances as accurately as fluxes and more sophisticated closures may be necessary for satellite retrievals of effective radius and optical depth. Such improved models would be most helpful in the retrieval of effective radius since the results of Chapter 6 suggest that horizontal transport of solar radiation produces much of the error in this retrieval.

Regardless of the future multi-dimensional RTMs used to compute radiances and fluxes in an operational format, the PPA albedo bias in Chapter 5 and the area averaging bias in Chapter 6 demonstrate that information about the sub-pixel scale variability

of cloud optical properties must be known or estimated. The standard deviation of the logarithm of optical depth was found in this study to be a good measure of the magnitude of the PPA albedo bias, since on a logarithmic optical depth scale albedo becomes approximately linear (for plane parallel calculations), and the mean albedo of the optical depth distribution is approximately equal to the albedo of the mean logarithm of τ. This measure is also accurate for marine stratus since the net horizontal transport is small in these clouds and the IPA method is adequate for computing domain averaged albedos. It is likely however that other measures of cloud variability will be required for more heterogeneous cloud fields. One possible measure of cloud horizontal variability may be the scale of spatial homogeneity (SSH) presented in Feigelson (1984). The SSH of a quantity (such as optical depth) is defined as the horizontal length within which the quantity differs from the value at the beginning of the length by no more than a specified factor (usually two), and can be easily measured from aircraft data. Another way to quantify cloud inhomogeneity is to use simple statistical models of clouds like those presented in Barker (1992) or Cahalan et al. (1994). Cloud observations using millimetric radar reflectivity data could be fitted to a range of models of varying complexity. Information about the cloud structure could also be modeled directly by large eddy simulations of cloud systems simulations.

In addition to the development of a measure of cloud optical depth variability, relationships between the variability of cloud properties on different scales would be a valuable source of information for satellite retrievals of optical depth and effective radius. Thus, estimates of the sub-pixel variability of τ and R_e could be computed using information about the variability of surrounding pixels. These estimates could then be used in a satellite remote sensing algorithms to account for the area averaging bias described in Chapter 6, which accounted for much of the error in optical depth that was produced by horizontal inhomogeneity. This scaling information could be inferred from direct observations using millimetric radar data.

Bibliography

Albrecht, B. A., 1989: Aerosols, cloud microphysics, and fractional cloudiness. *Science*, **245**, 1227–1230.

Albrecht, B. A., D. A. Randall, and S. Nicholls, 1988: Observations of marine stratocumulus clouds during fire. *Bull, Amer. Meteor. Soc.*, **69**, 618–626.

Barker, H. W., 1992: Solar radiative transfer through clouds possessing isotropic variable extinction coefficient. *Q. J. R. Meteorol. Soc.*, **118**, 1145–1162.

Betts, A. K., 1989: The diurnal variation of california coastal stratocumulus from two days of boundary layer soundings. *Tellus*, **42A**, 302–304.

Betts, A. K. and R. Boers, 1990: A cloudiness transition in a marine boundary layer. *J. Atmos. Sci.*, **47**, 1480–1497.

Boucher, O. and H. Rodhe, 1994: Sensitivity of a gcm to changes in cloud droplet concentration. In *Department of Meteorology Report CM-83*, Stockholm University.

Cahalan, R. F., W. Ridgway, W. J. Wiscombe, T. L. Bell, and J. B. Snider, 1994: The albedo of fractal stratocumulus clouds. *J. Atmos. Sci.*, **51**, 2434–2455.

Cahalan, R. F., W. Ridgway, W. J. Wiscombe, S. Gollmer, and Harshvardhan, 1994: Independent pixel and monte carlo estimates of stratocumulus albedo. *J. Atmos. Sci.*, **51**, 2434–2455.

Charlson, R. J., J. E. Lovelock, M. O. Andreae, and S. G. Warren, 1987: Oceanic phytoplankton, atmospheric sulphur, cloud albedo and climate. *Nature*, **326**, 655–661.

Charlson, R. J., S. E. Schwartz, J. M. Hales, R. D. Cess, J. J. A. Coakley, J. E. Hansen, and D. J. Hofmann, 1992: Climate forcing by anthropogenic aerosols. *Science*, **255**, 423–430.

Chen, C. and W. R. Cotton, 1983: Numerical experiments with a one-dimensional higher order turbulence model: Simulation of the wangara day 33 case. *Boundary-Layer Meteorol.*, **27**, 375–404.

Chou, M. D., 1984: Broadband water vapor transmission functions for atmospheric ir flux computations. *J. Atmos. Sci.*, **41**, 1775–1778.

Chou, M. D., 1986: Atmospheric solar heating rate in the water vapor bands. *J. Clim. Appl. Meteor.*, **25**, 1532–1542.

Chou, M. D. and A. Arking, 1980: Computation of infrared cooling rates in the water vapor bands. *J. Atmos. Sci.*, **37**, 855–867.

Chou, M. D. and A. Arking, 1981: An efficient method for computing the absorption of solar radiation by water vapor. *J. Atmos. Sci.*, **38**, 798–807.

Chou, M. D. and L. Peng, 1983: A parameterization of the absorption in the 15 μm spectral region with application to climate sensitivity studies. *J. Atmos. Sci.*, **40**, 2183–2192.

Coakley, Jr., J. A., R. L. Bernstein, and P. A. Durkee, 1987: Ship tracks etc. *Science*, **237**, 1020.

Cotton, W. R., B. B. Stevens, G. Feingold, and R. L. Walko, 1992: A model for simulating the twomey effect. In *Report to the Third WMO Cloud Modeling Workshop.* WMO, Toronto, August 1992.

Curran, R. J. and M. L. C. Wu, 1982: Skylab near-infrared observations of clouds indicating supercooled liquid water droplets. *J. Atmos. Sci.*, **39**, 635–647.

Dave, J. V. and B. H. Armstrong, 1974: Smoothing of the intensity curve obtained from a solution of the spherical harmonics approximation to the transfer equation. *J. Atmos. Sci.*, **31**, 1934–1937.

Duda, D. P., G. L. Stephens, and S. K. Cox, 1991: Microphysical and radiative properties of marine stratocumulus from tethered balloon measurements. *J. Appl. Meteor.*, **30**, 170–186.

Evans, K. F., 1993: Two-dimensional radiative transfer in cloudy atmospheres: The spherical harmonic spatial grid method. *J. Atmos. Sci.*, **50**, 3111–3124.

Feigelson, E. M., 1984: *Radiation in a cloudy atmosphere*. D. Reidel, 293 pp.

Flatau, P. J., G. J. Tripoli, J. Verlinde, and W. R. Cotton, 1989: The csu-rams cloud microphysics module: General theory and code documentation. Technical Report Paper No. 451, Colorado State University, Dept. of Atmos. Sci., Fort Collins, CO, 200 pp.

Foot, J. S., 1988: Some observations of the optical properties of clouds. i: Stratocumulus. *Quart. J. Roy. Meteor. Soc.*, **114**, 129–144.

Gabriel, P. M. and K. F. Evans, 1994: Simple radiative transfer methods for calculation domain averaged solar fluxes in inhomogeneous clouds. *submitted to J. Atmos. Sci.*

Gabriel, P. M., S. C. Tsay, and G. L. Stephens, 1993: A fourier-riccati approach to radiative transfer. part i: Foundations. *J. Atmos. Sci.*, **50**, 3125–3147.

Han, Q., W. B. Rossow, and A. A. Lacis, 1994: Near-global survey of effective droplet radii in liquid water clouds using isccp data. *J. Climate*, **7**, 465–497.

Hegg, D. A., L. F. Radke, and P. V. Hobbs, 1990: Particle production associated with marine clouds. *J. Geophys. Res.*, **95**, 13917–13926.

Houghton, J. T., G. J. Jenkins, and J. J. E. (eds), 1990: Ipcc climate change: The ipcc scientific assessment. Technical report, Cambridge Univ. Press.

Hudson, J. G. and P. R. Frisbie, 1991: Cloud condensation nuclei near marine stratus. *J. Geophys. Res.*, **96**, 20795–20808.

Jones, A., D. L. Roberts, and A. Slingo, 1994: A climate model study of indirect radiative forcing by anthropogenic sulphate aerosols. *Nature*, **370**, 450–453.

Kim, Y. and R. D. Cess, 1993: Effect of anthropogenic sulfate aerosols on low-level cloud albedo over oceans. *J. Geophys. Res.*, **98**, 14883–14885.

King, M. D., 1983: Number of terms required in the fourier expansion of the reflection function for optically thick atmospheres. *J. Quant. Spectrosc. Radiat. Transfer*, **30**, 143–161.

King, M. D., 1987: Determination of the scaled optical thickness of clouds from reflected solar radiation measurements. *J. Atmos. Sci.*, **44**, 1734–1751.

Kourganoff, V., 1952: *Basic Methods in Transfer Problems.* Clarendon Press, 281 pp.

Lacis, A. A. and V. Oinas, 1991: A description of the correlated k distribution method for modeling nongray gaseous absorption, thermal emission, and multiple scattering in vertically inhomogeneous atmospheres. *J. Geophys. Res.*, **96**, 9027–9063.

Liou, K. N. and T. Sasamori, 1975: On the transfer of solar radiation in aerosol atmospheres. *J. Atmos. Sci.*, **32**, 2166–2177.

Louis, J. F., 1979: A parametric model of vertical eddy fluxes in the atmosphere. *Boundary-Layer Meteorol.*, **17**, 187–202.

Martin, G. M., D. W. Johnson, and A. Spice, 1994: The measurement and parameterization of effective radius of droplets in warm stratocumulus clouds. *J. Atmos. Sci.*, **51**, 1823–1842.

McClatchey, R. A., R. W. Fenn, J. E. A. Selby, F. E. Voltz, and J. S. Garing, 1972: Optical properties of the atmosphere, 3rd ed. Technical Report AFCRL-72-0497, Air Force Cambridge Research Laboratory, 108 pp.

Meszaros, E., 1988: On the possible role of the biosphere in the control of atmospheric clouds and precipitation. *Atmos. Environ.*, **22**, 423–424.

Nakajima, T. and M. D. King, 1990: Determination of the optical thickness and effective particle radius of clouds from reflected solar radiation measurements. part i: Theory. *J. Atmos. Sci.*, **47**, 1878–1893.

Nakajima, T., M. D. King, J. D. Spinhirne, and L. F. Radke, 1991: Determination of the optical thickness and effective particle radius of clouds from reflected solar radiation measurements. part ii: Marine stratocumulus observations. *J. Atmos. Sci.*, **48**, 728–750.

Nakajima, T. Y. and T. Nakajima, 1994: Wide-area determination of cloud microphysical properties from noaa avhrr measurements for fire and astex regions. *Accepted by J. Atmos. Sci.*

Paltridge, G. W. and C. M. R. Platt, 1976: *Radiative Processes in Meteorology and Climatology.* Elsevier, 318 pp.

Pielke, R. A., W. R. Cotton, R. L. Walko, C. J. Tremback, W. A. Lyons, L. D. Grasso, M. E. Nicholls, M. D. Moran, D. A. Wesley, T. J. Lee, and J. H. Copeland, 1992: A comprehensive meteorological modeling system – rams. *Meteorol. Atmos. Phys.*, **49**, 69–91.

Rossow, W. B., 1989: Measuring cloud properties from space: A review. *J. Climate*, **2**, 201–213.

Scott, N. A. and A. Chedin, 1981: A fast line by line method for atmospheric absorption computations: The automatized atmospheric absorption atlas (4a). *J. Appl. Meteor.*, **20**, 801–812.

Slingo, A., 1990: Sensitivity of the earth's radiation budget to changes in low clouds. *Nature*, **343**, 49–51.

Slingo, A. and H. M. Schrecker, 1982: On the shortwave properties of stratiform water clouds. *Quart. J. Roy. Meteor. Soc.*, **108**, 407–426.

Smith, G. L., J. T. Suttles, and N. Manalo, 1989: The erbe alongtrack scan experiment. In *IRS '88: Current Problems in Atmospheric Radiation*, Lenoble, J. and Geleyn, J. F., editors, A. Deepak, 242-244.

Stackhouse, Jr., P. W., 1989: A theoretical and observational comparison of cirrus cloud radiative properties. M. s. thesis, Colo. State Univ., Dept. of Atmos. Sci., Fort Collins, 120 pp.

Stackhouse, Jr., P. W., 1995: *The effects of two dimensional inhomogeneity on ice cloud radiative properties.* Ph. d. dissertation, Colo. State Univ., Dept. of Atmos. Sci., Fort Collins, 250 pp.

Stackhouse, Jr., P. W. and G. L. Stephens, 1994: The effects of ice cloud inhomogeneity on two-dimensional solar fluxes. *submitted to J. Atmos. Sci.*

Stamnes, K. and S. C. Tsay, 1990: Optimum spectral resolution for computing atmospheric heating and photodissociation rates. *Planet. Space Sci.*, **38**, 807–820.

Stephens, G. L., 1984: The parameterization of radiation for numerical weather prediction and climate models. *Mon. Wea. Rev.*, **112**, 826–867.

Stephens, G. L., 1988: Radiative transfer through arbitrarily shaped optical media. part i: A general method of solution. *J. Atmos. Sci.*, **45**, 1818–1836.

Stephens, G. L. and S. C. Tsay, 1990: On the cloud absorption anomaly. *Quart. J. Roy. Meteo. Soc.*, **116**, 671–704.

Stevens, B. B., W. R. Cotton, R. L. Walko, and G. Feingold, 1994: Large-eddy explicit microphysics simulation of an observed stratocumulus boundary layer. part i: model description. *J. Atmos. Sci., in preparation.*

Stuhlmann, R., P. Minnis, and G. L. Smith, 1985: Cloud bidirectional reflectance functions: A comparison of experimental and theoretical results. *Appl. Opt.*, **24**, 396–401.

Toon, O. B. and J. B. Pollack, 1976: A global average model of atmospheric aerosols for radiative transfer calculations. *J. Appl. Meteor.*, **15**, 225–246.

Twomey, S., 1959: The nuclei of natural cloud formation: the supersaturation in natural clouds and the variation of cloud droplet concentrations. *Geofis. Pura et appl.*, **43**, 243–249.

Twomey, S., 1977: The influence of pollution on the short wave albedo of clouds. *J. Atmos. Sci.*, **34**, 1149–1152.

Twomey, S. and T. Cocks, 1982: Spectral reflectance of clouds in the near-infrared: comparison of measurements and calculations. *J. Meteor. Soc. Japan*, **60**, 583–592.

Twomey, S. and T. Cocks, 1989: Remote sensing of cloud parameters from spectral reflectance in the near-infrared. *Beitr. Phys. Atmos.*, **62**, 172–179.

Tzivion, S., G. Feingold, and Z. Levin, 1987: An efficient numerical solution to the stochastic collection equation. *J. Atmos. Sci.*, **44**, 3139–3149.

Wielicki, B. A. and L. Parker, 1992: On the determination of cloud cover from satellite sensors: The effect of sensor spatial resolution. *J. Geophys. Res.*, **97**, 12799–12823.

Wielicki, B. A., J. T. Suttles, A. J. Heymsfield, R. M. Welch, J. D. Spinhirne, M. L. C. Wu, D. O. Starr, L. Parker, and R. F. Arduini, 1990: The 27-28 october 1986 fire ifo cirrus case study: Comparison of radiative transfer theory with observations by satellite and aircraft. *Mon. Wea. Rev.*, **118**, 2356–2376.

Wiscombe, W. J., 1977: The delta-m method: rapid yet accurate radiative flux calculations for strongly asymmetric phase functions. *J. Atmos. Sci.*, **34**, 1408–1422.

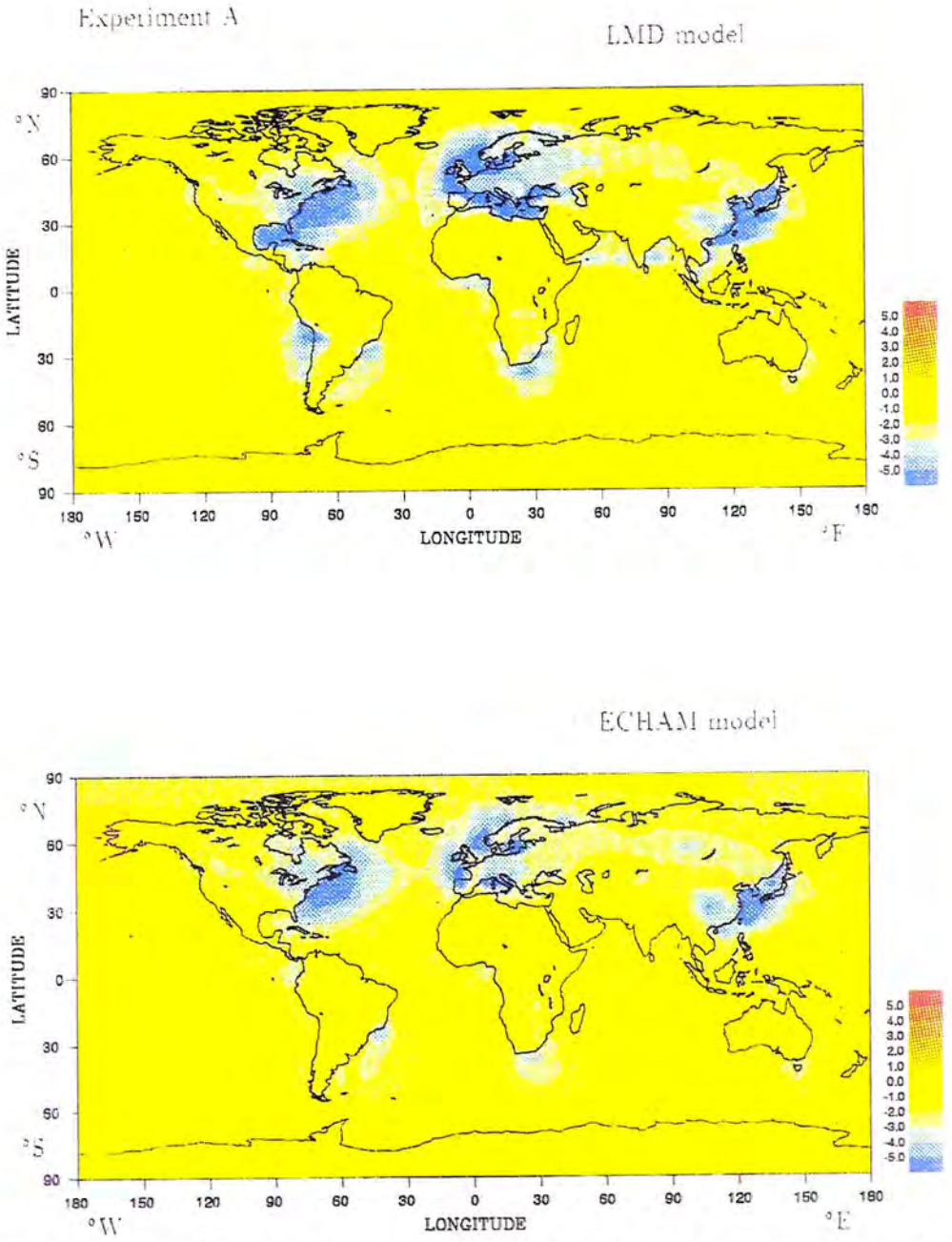

Figure 1.1: Maps of the top of atmosphere (TOA) radiative forcing in W m^{-2} due to the effects of anthropogenic aerosol on cloud albedo. (From Boucher and Rodhe (1994)).

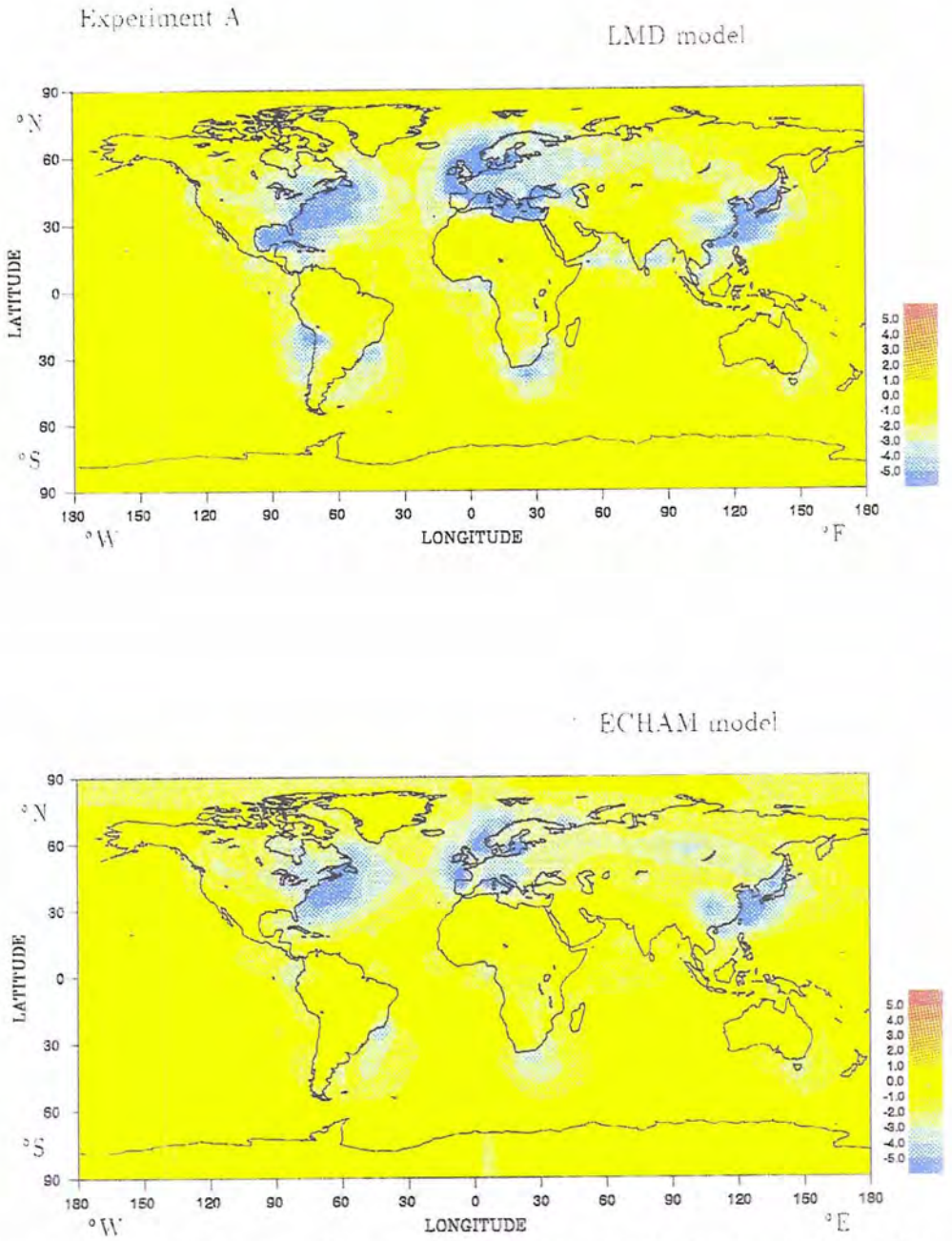

Figure 1.1: Maps of the top of atmosphere (TOA) radiative forcing in W m^{-2} due to the effects of anthropogenic aerosol on cloud albedo. (From Boucher and Rodhe (1994)).

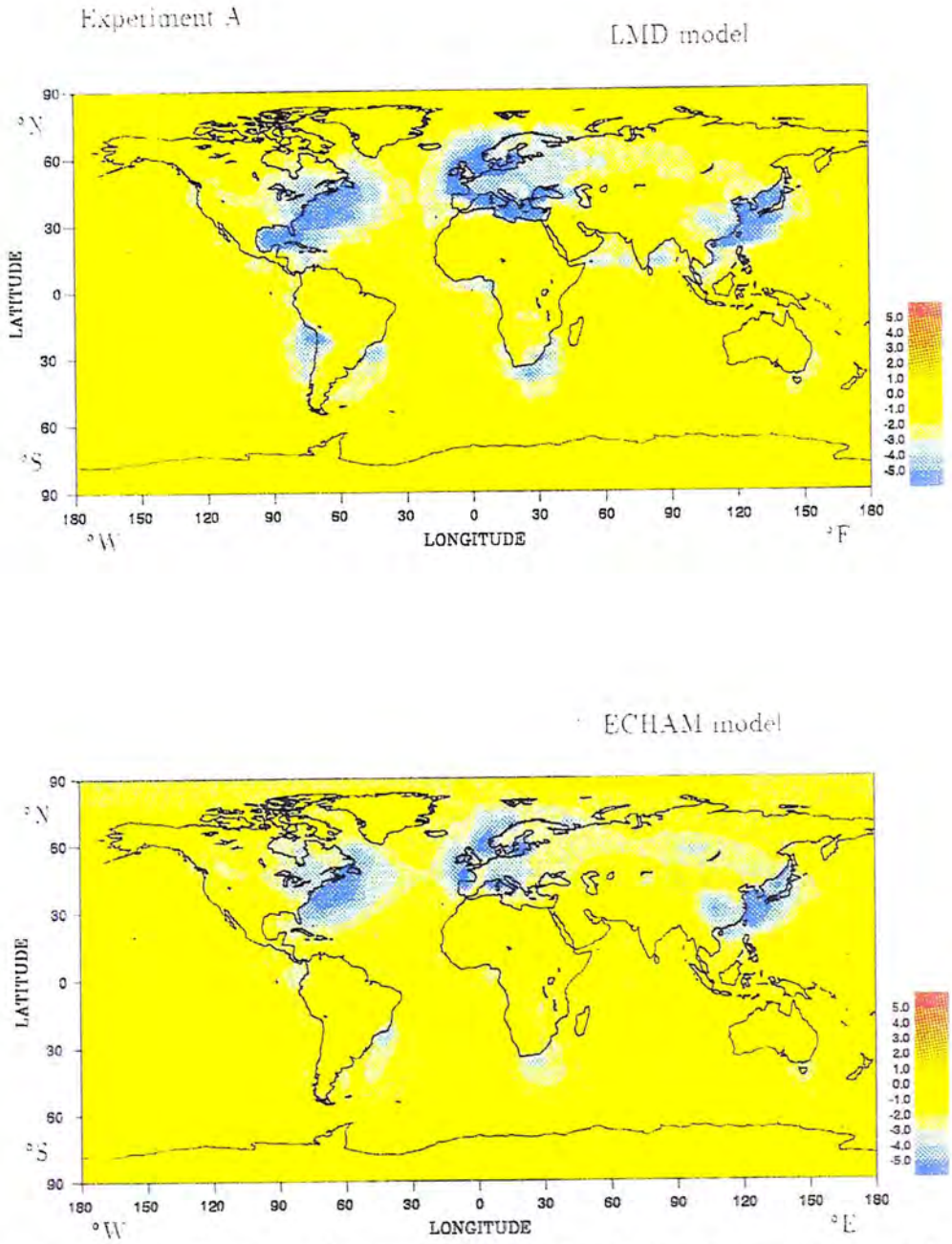

Figure 1.1: Maps of the top of atmosphere (TOA) radiative forcing in W m^{-2} due to the effects of anthropogenic aerosol on cloud albedo. (From Boucher and Rodhe (1994)).

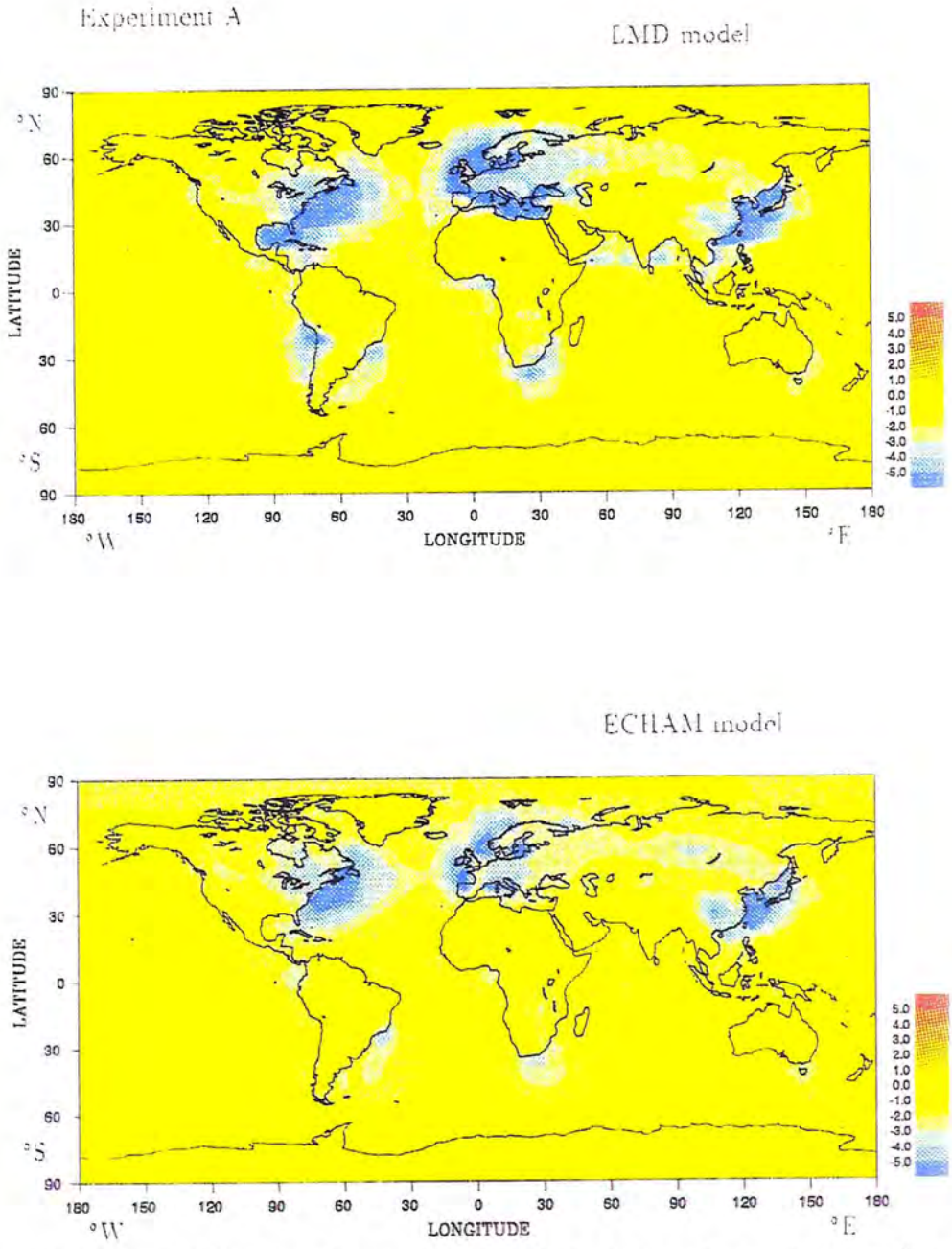

Figure 1.1: Maps of the top of atmosphere (TOA) radiative forcing in W m^{-2} due to the effects of anthropogenic aerosol on cloud albedo. (From Boucher and Rodhe (1994)).

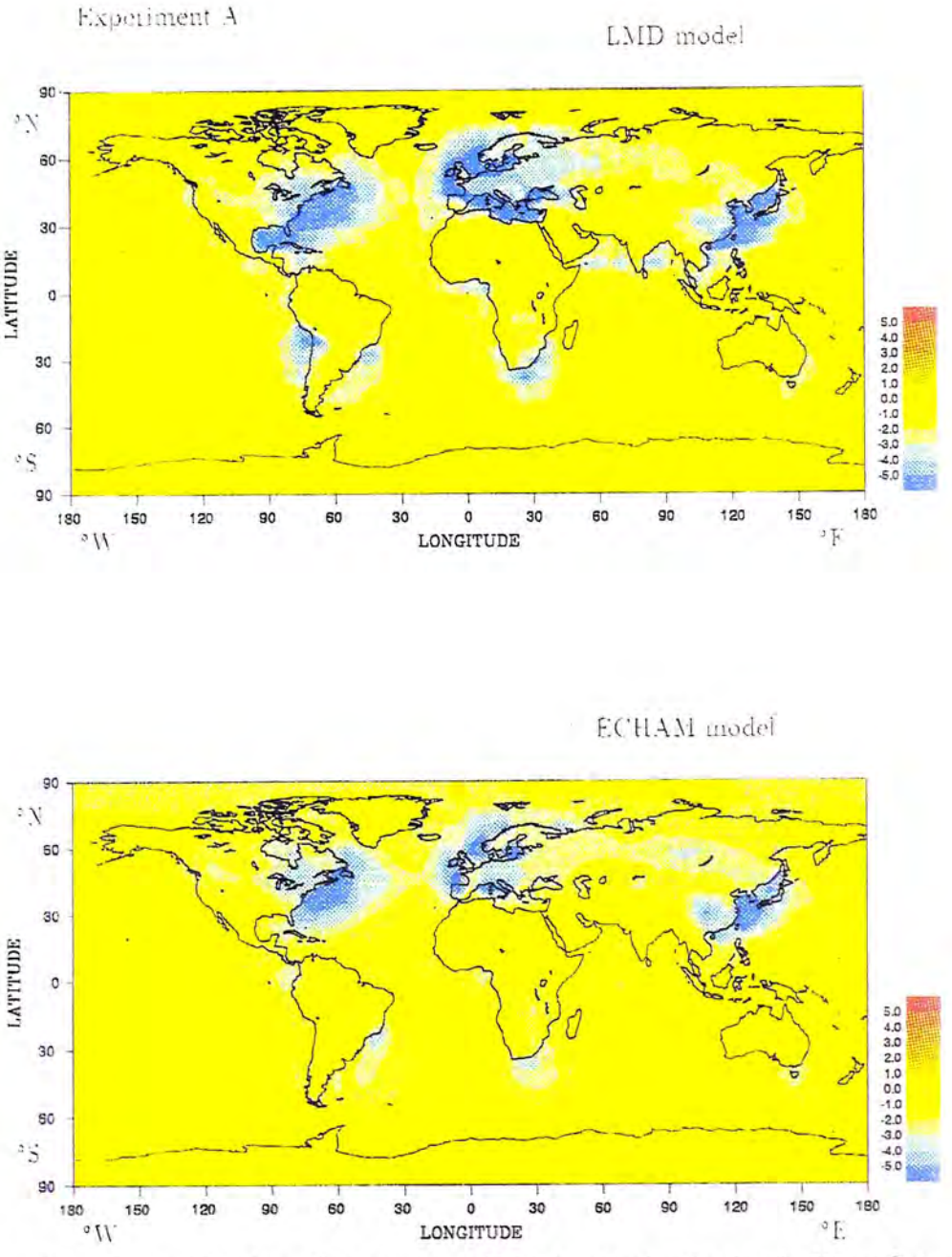

Figure 1.1: Maps of the top of atmosphere (TOA) radiative forcing in W m^{-2} due to the effects of anthropogenic aerosol on cloud albedo. (From Boucher and Rodhe (1994)).

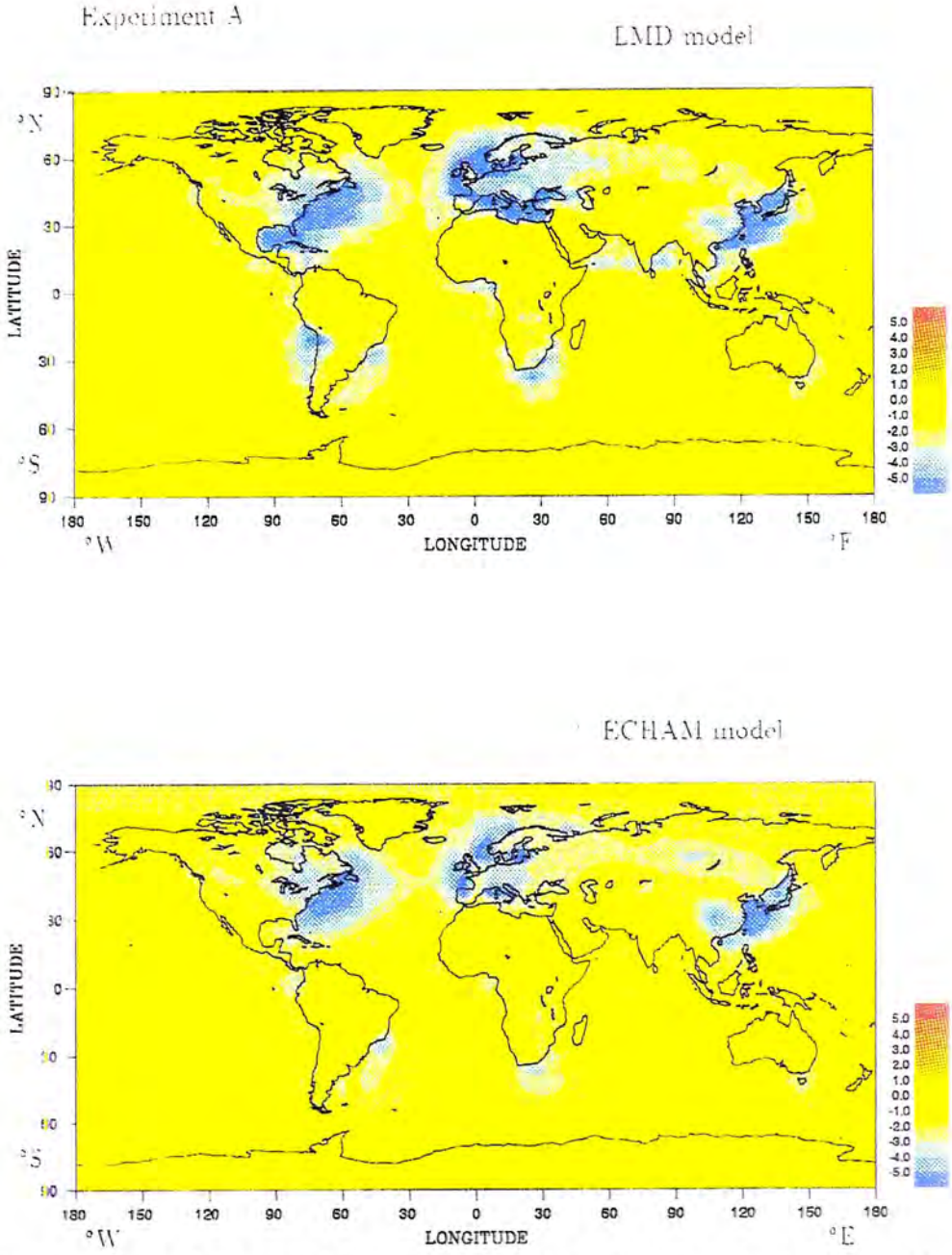

Figure 1.1: Maps of the top of atmosphere (TOA) radiative forcing in W m^{-2} due to the effects of anthropogenic aerosol on cloud albedo. (From Boucher and Rodhe (1994)).

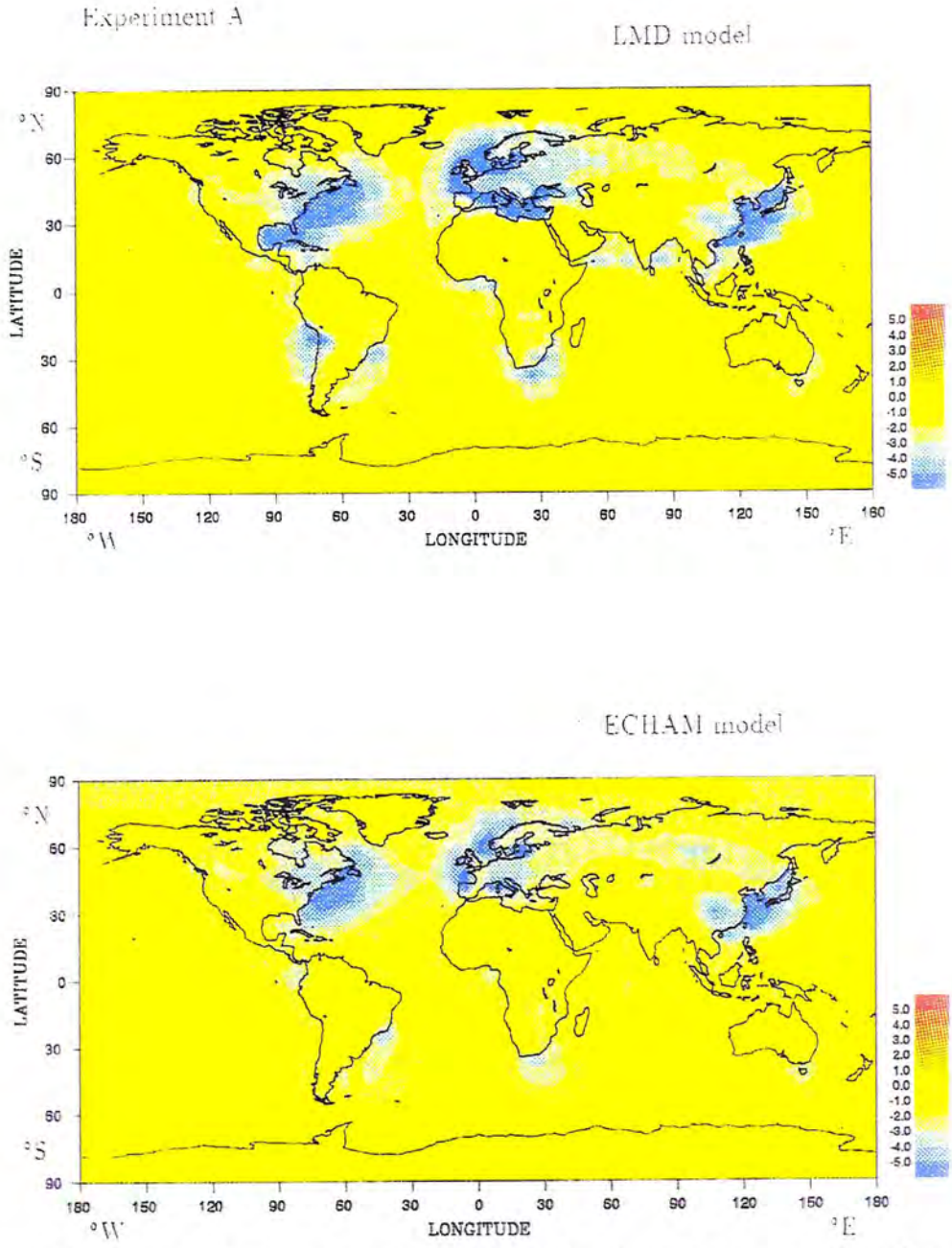

Figure 1.1: Maps of the top of atmosphere (TOA) radiative forcing in W m^{-2} due to the effects of anthropogenic aerosol on cloud albedo. (From Boucher and Rodhe (1994)).

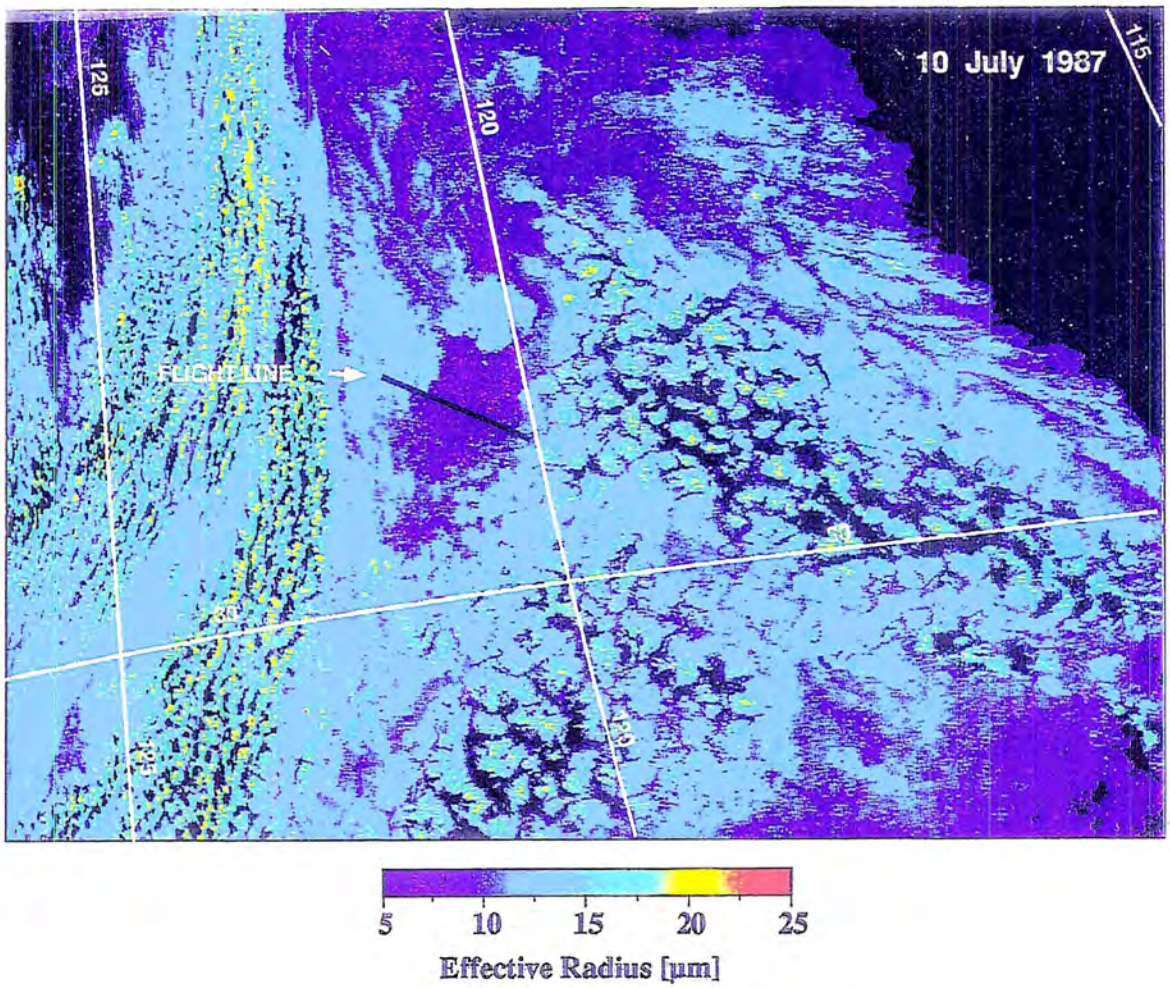

Figure 1.3: Same as Figure 1.2 but for the effective radius.

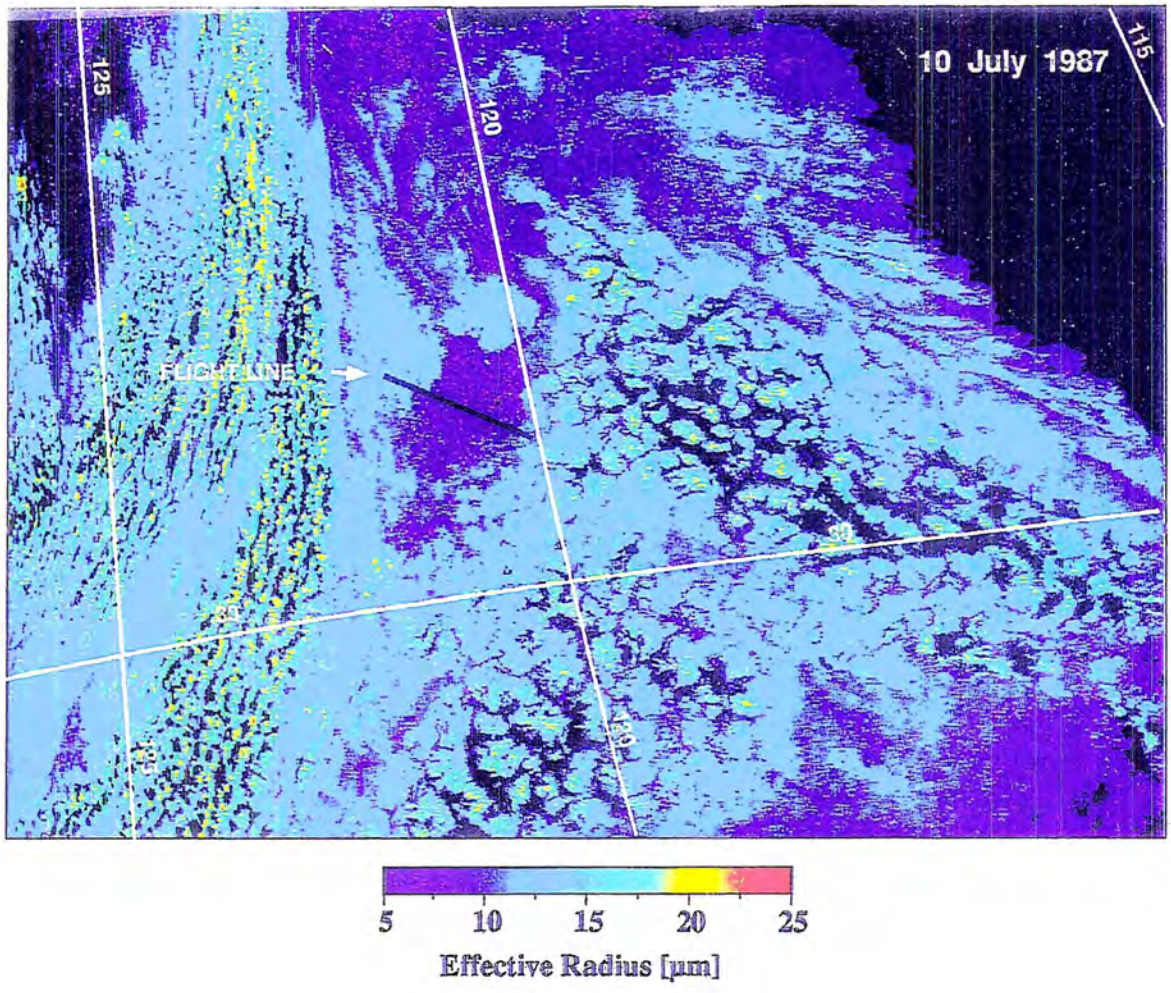

Figure 1.3: Same as Figure 1.2 but for the effective radius.

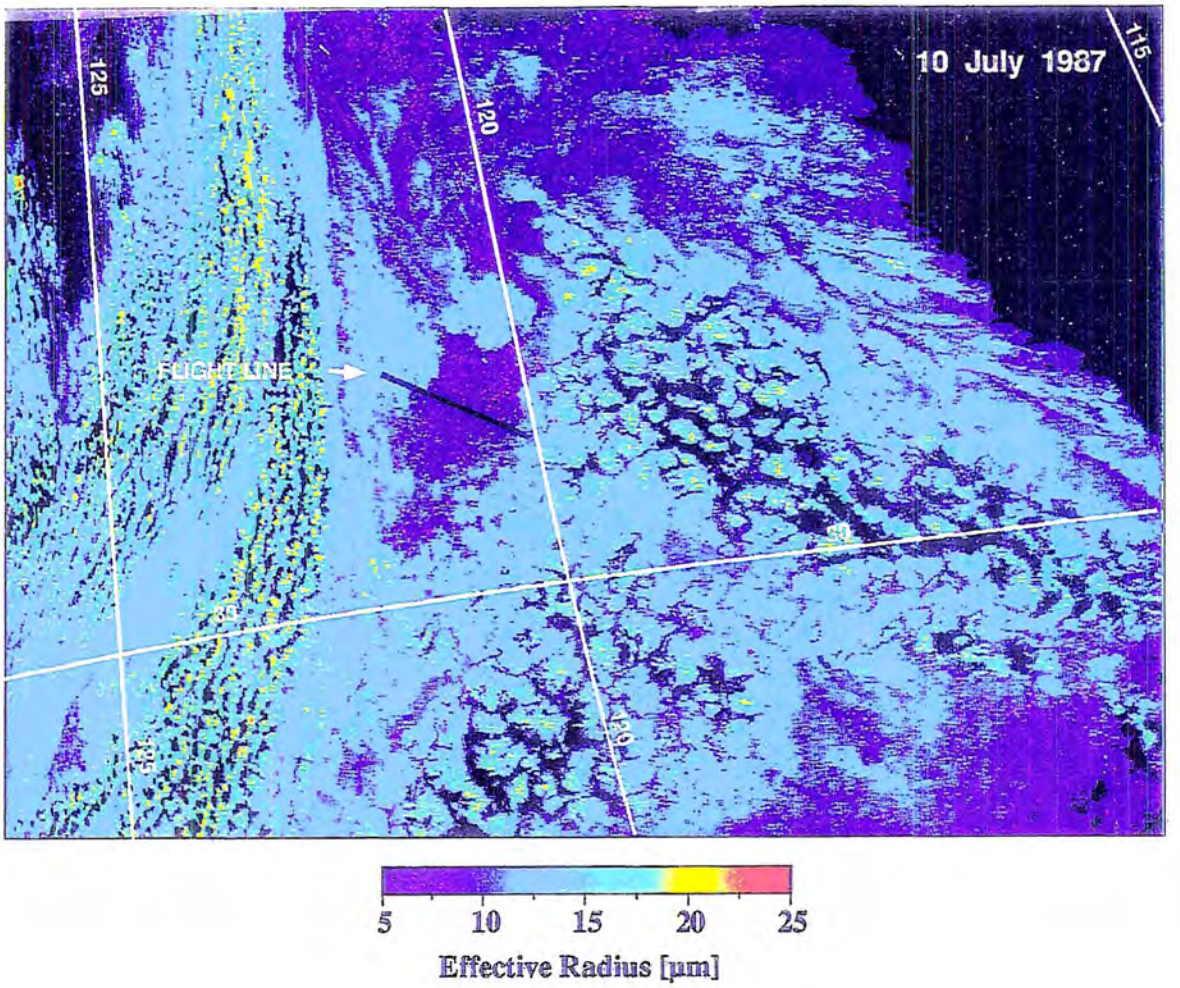

Figure 1.3: Same as Figure 1.2 but for the effective radius.

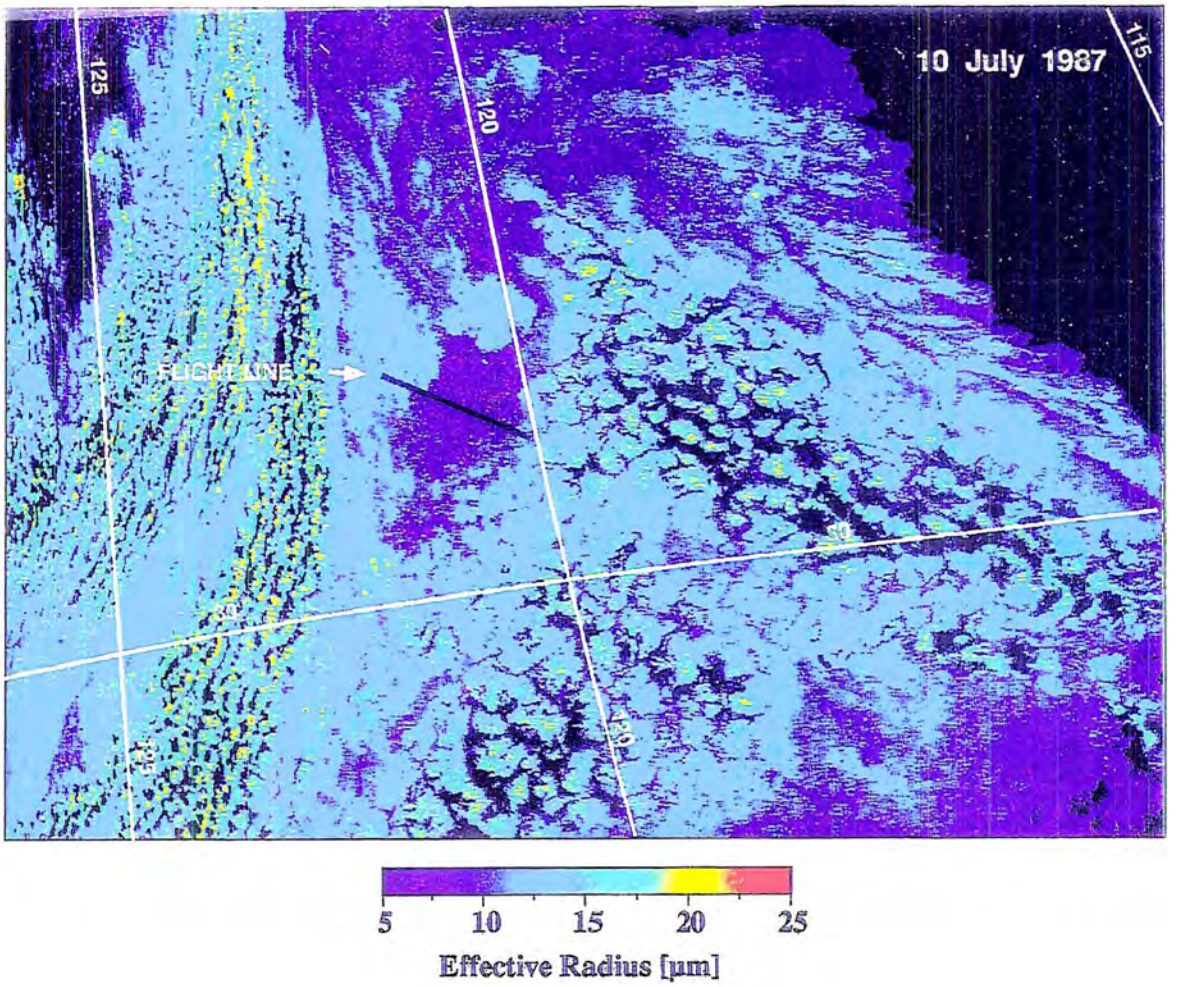

Figure 1.3: Same as Figure 1.2 but for the effective radius.

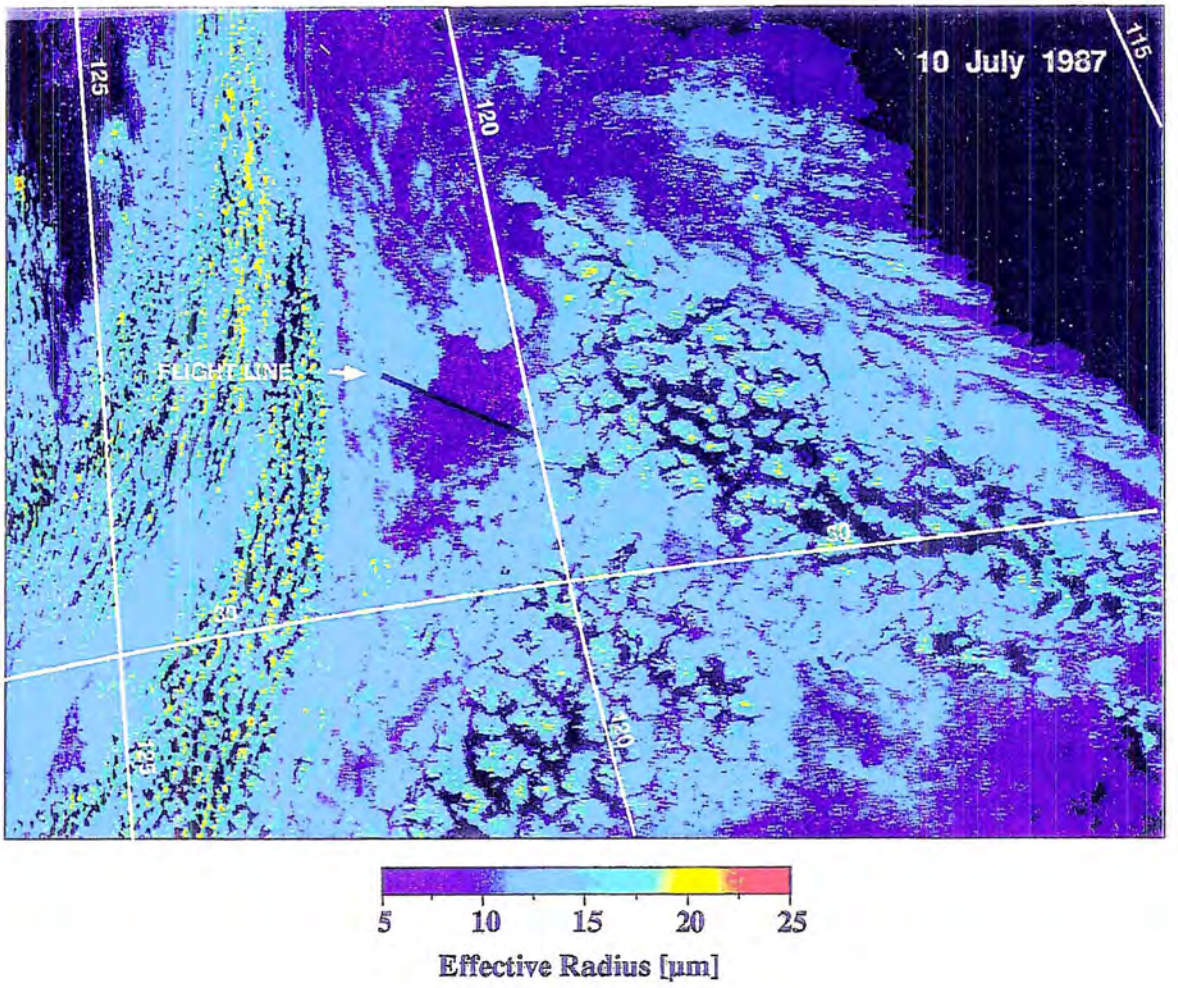

Figure 1.3: Same as Figure 1.2 but for the effective radius.

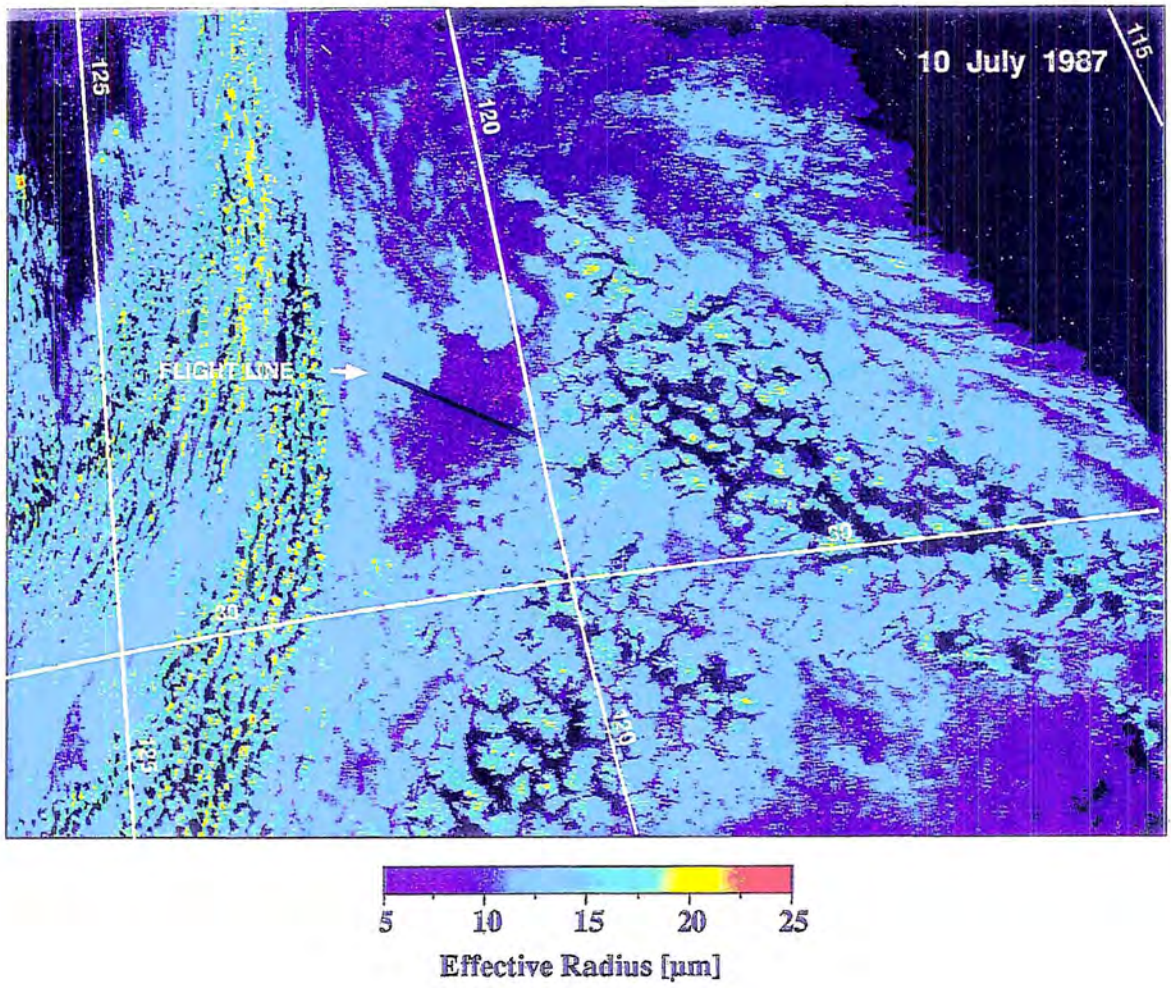

Figure 1.3: Same as Figure 1.2 but for the effective radius.

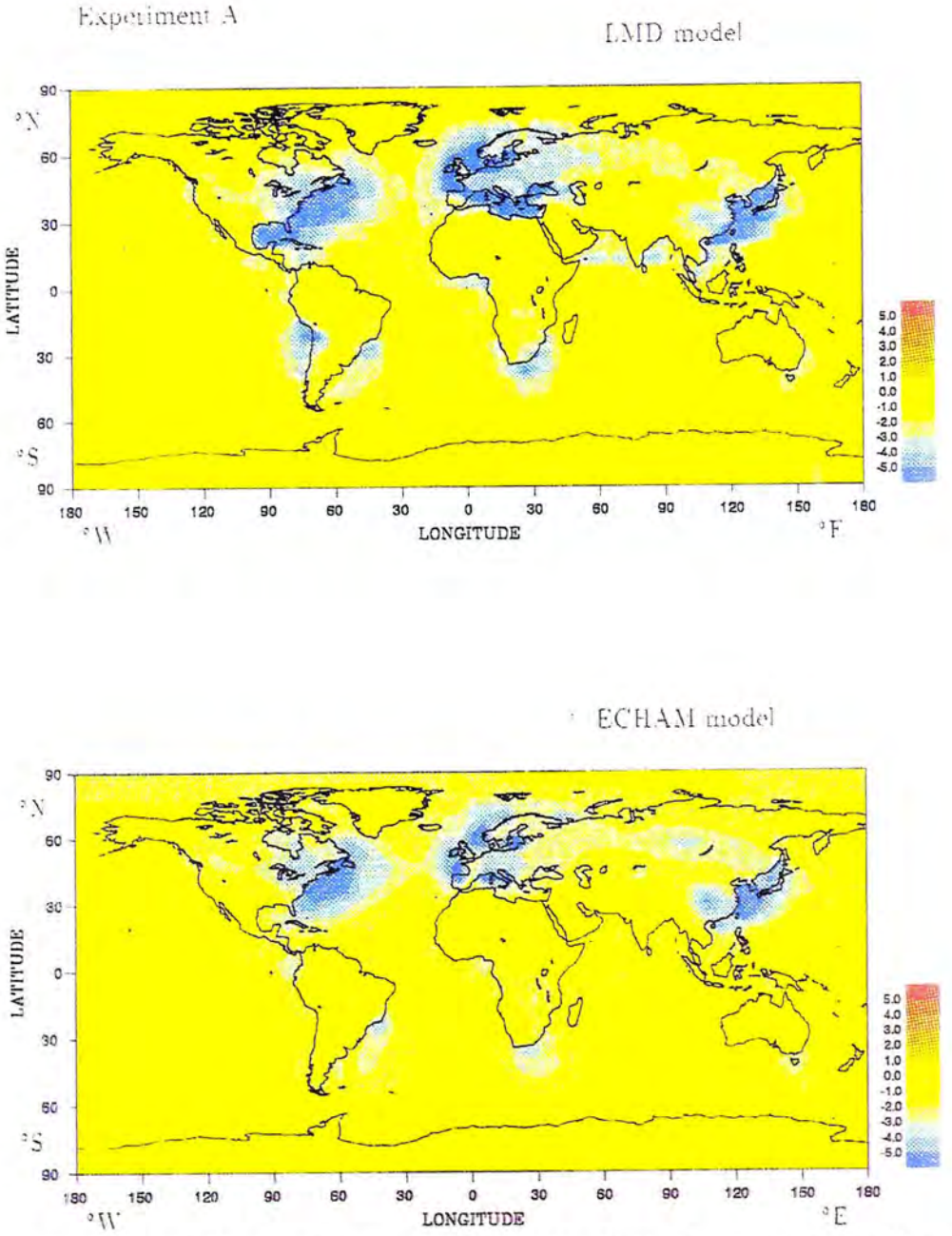

Figure 1.1: Maps of the top of atmosphere (TOA) radiative forcing in W m^{-2} due to the effects of anthropogenic aerosol on cloud albedo. (From Boucher and Rodhe (1994)).

Climatic impacts

Boucher & Rodhe (1994)
Jones *et al.* (1994)

Climate models – parameterize the effects of sulfate aerosol on clouds.

-1.3 W m^{-2} $\Longleftrightarrow$ 2 – 2.5 W m^{-2}

aerosols $\Longleftrightarrow$ CO_2

Experiment A

LMD model

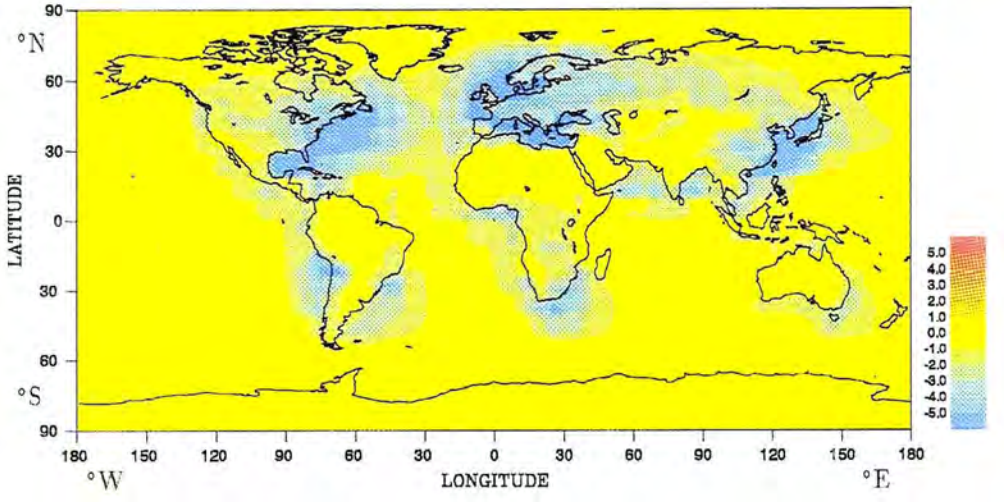

ECHAM model

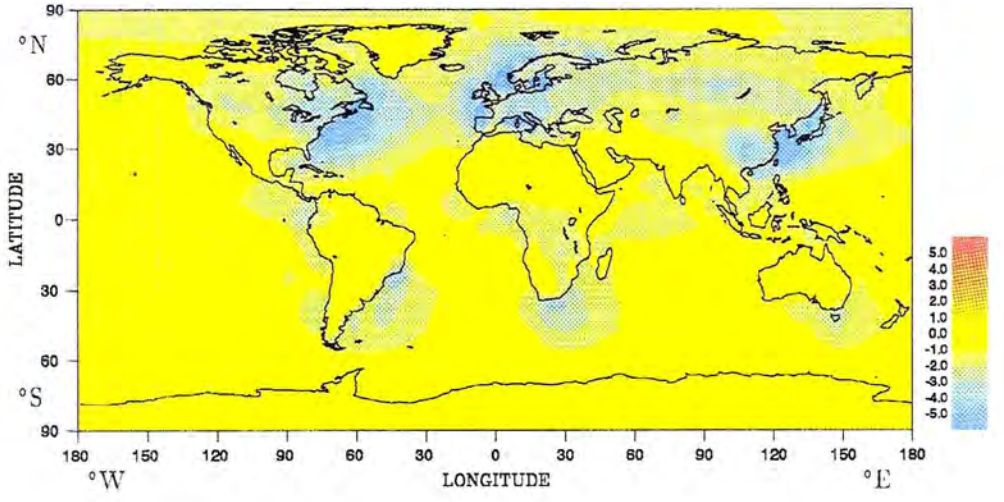

magnitude of the Twomey CCN/albedo effect if changes in microphysics due to increased CCN concentrations lead to changes in the macrophysics of the cloud.

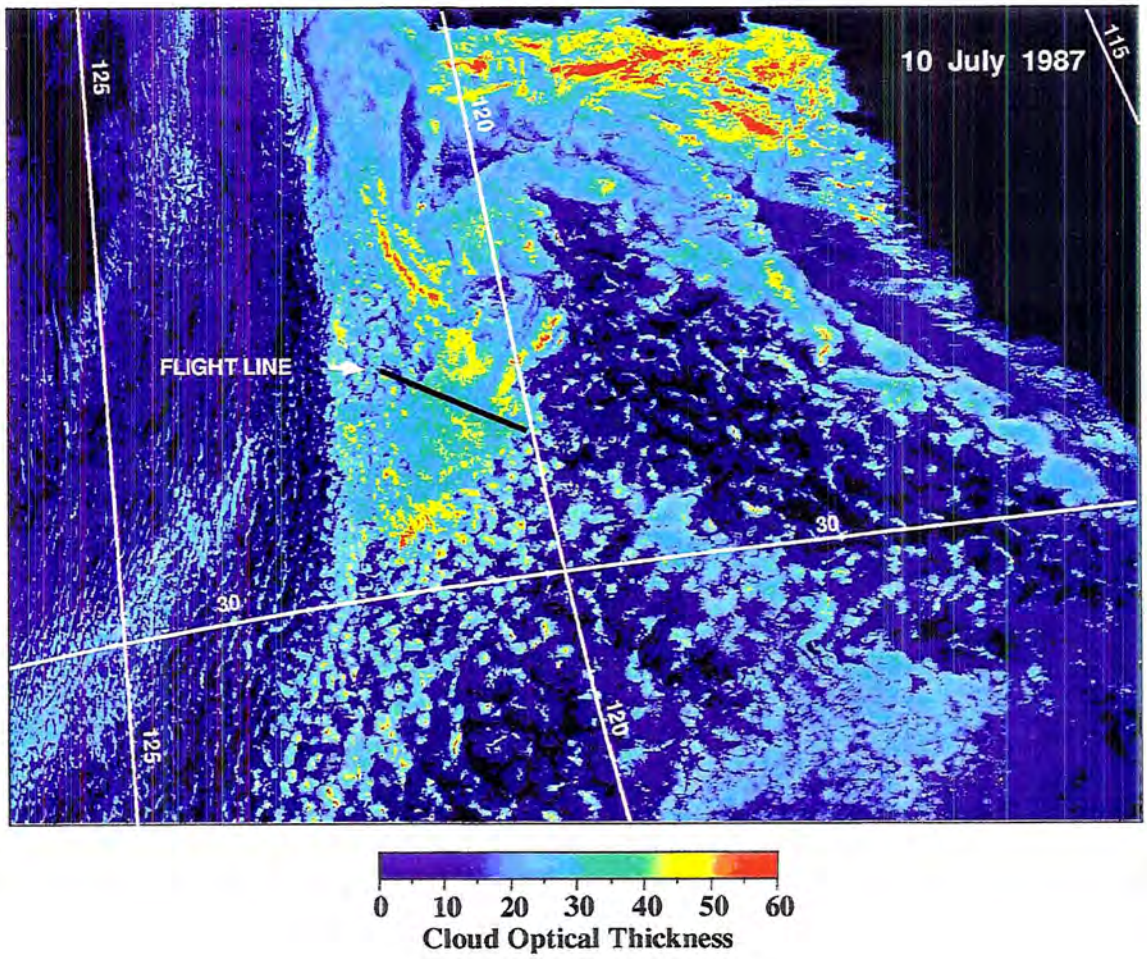

Figure 1.2: AVHRR-derived cloud optical thickness on 10 July 1987 in the FIRE-I IFO region. The solid line labeled *flight line* is the flight leg of the ER-2 and C-131A aircrafts. (From Nakajima and Nakajima (1994)).

Macrophysical properties must be studied with multi-dimensional RTMs, but despite the long history of research in the area, the use of such models to simulate marine stratus clouds has been limited. Computational expense has made such efforts unfeasible and few attempts were made to develop multi-dimensional models in the past. Monte Carlo methods have been used in the past two decades to study some basic cloud geometries (see-

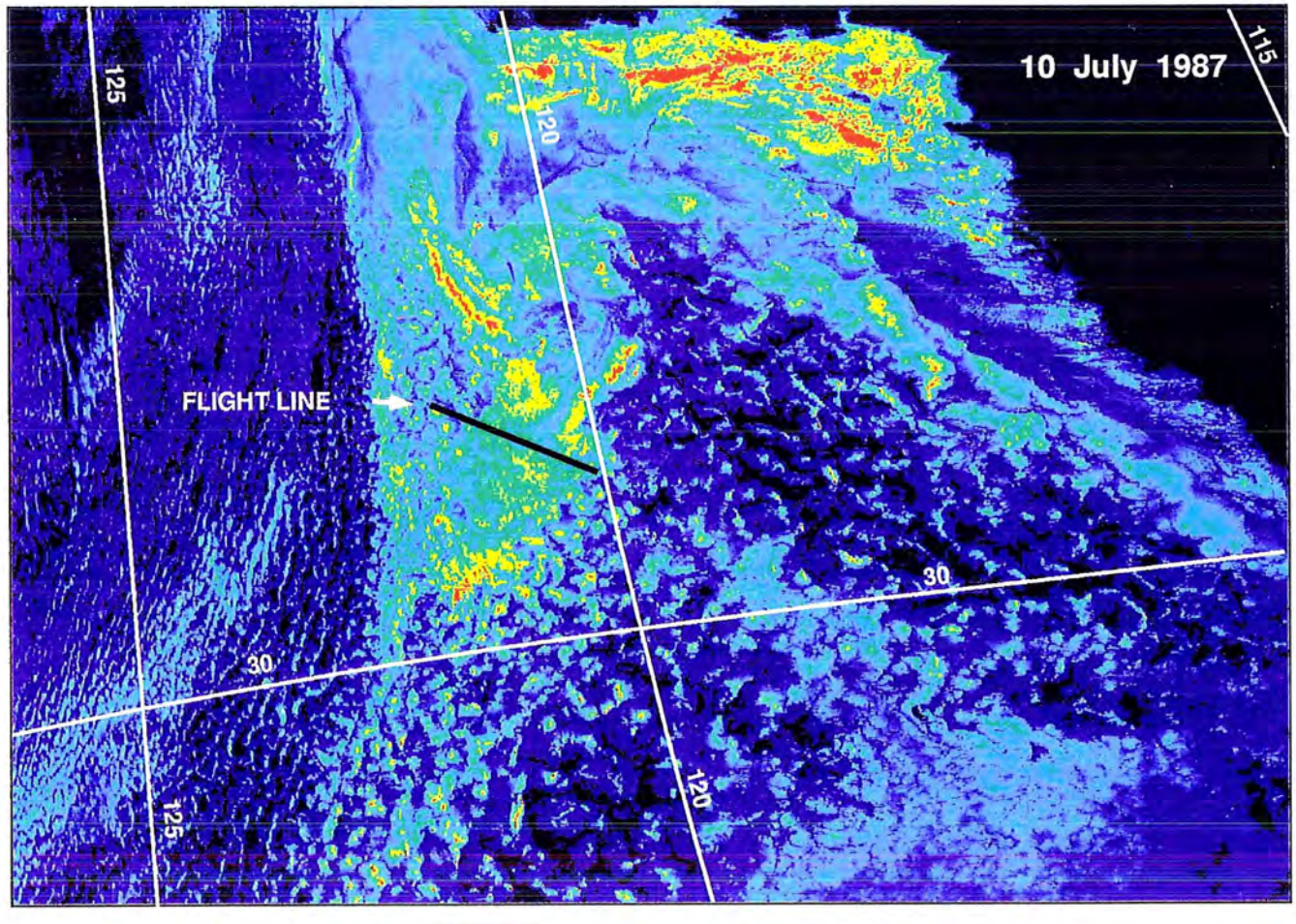
10 July 1987
FLIGHT LINE
125
120
115
30
30
125
120
0
10
20
30
40
50
60
Cloud Optical Thickness

Fig 7

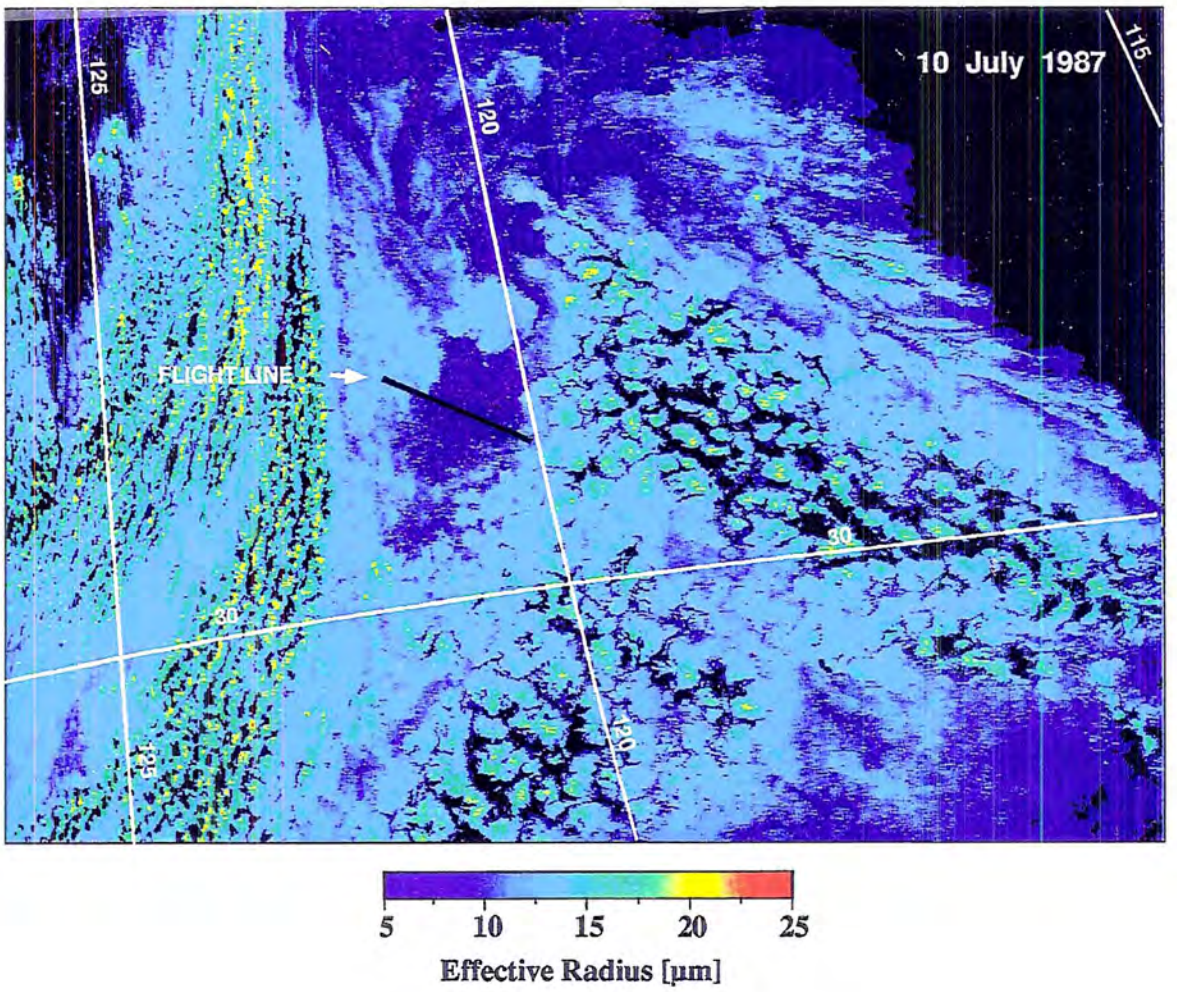

Figure 1.3: Same as Figure 1.2 but for the effective radius.

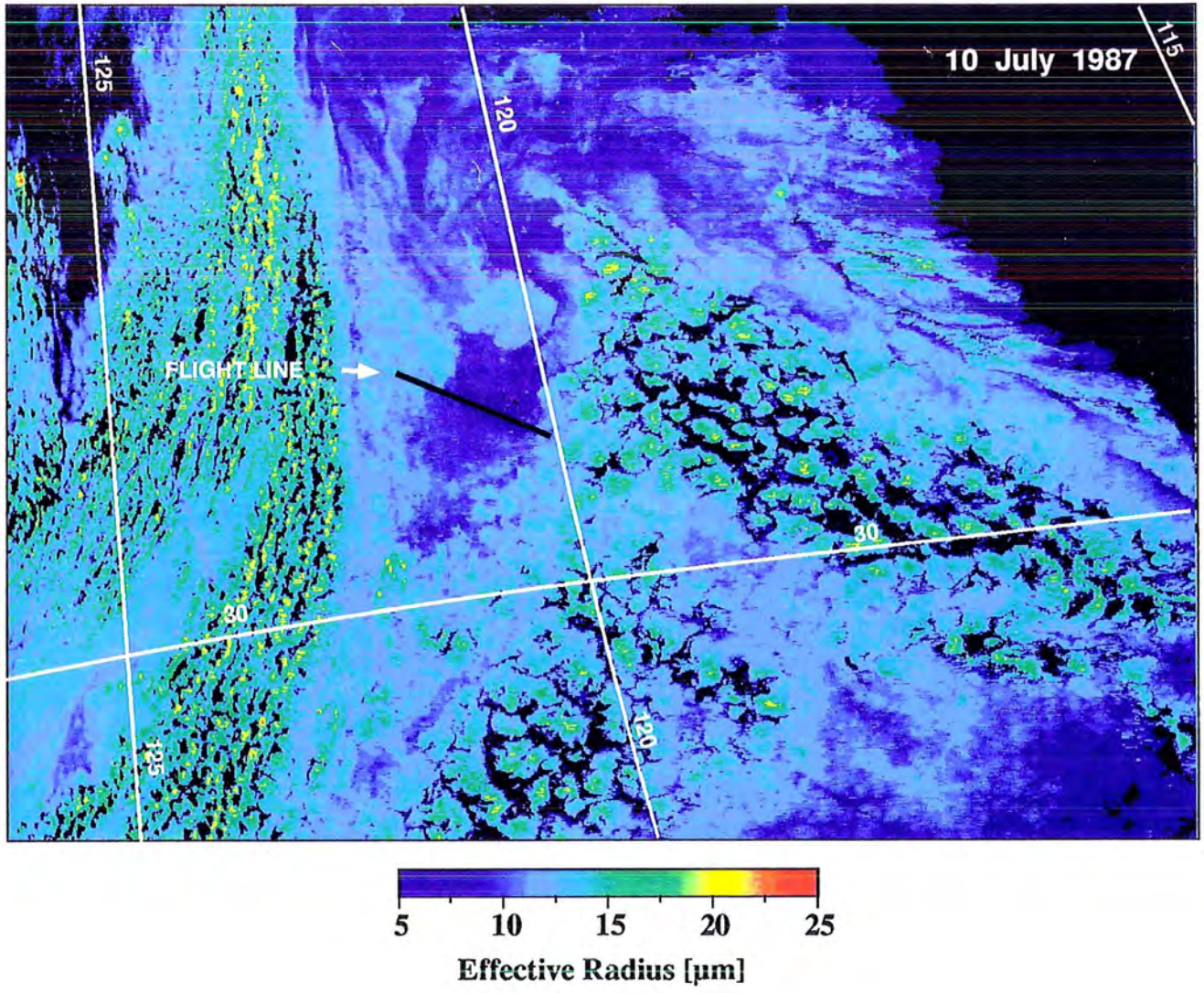
10 July 1987
125
120
115
FLIGHT LINE
30
30
125
120
5
10
15
20
25
Effective Radius [μm]

Fig 6